Low-Power and Miniaturized Medical Electronics for In-Vivo Localization and Tracking

Thesis by

Saransh Sharma

In Partial Fulfillment of the Requirements for

the Degree of

Doctor of Philosophy

CALIFORNIA INSTITUTE OF TECHNOLOGY

Pasadena, California

2023

Defended: May 15, 2023

Saransh Sharma
ORCID: 0000-0002-5052-4932

ACKNOWLEDGEMENTS

My journey of graduate studies at Caltech has been a very enriching experience that has led to tremendous academic and personal growth. This has been made possible by the wonderful people who have played quite indispensable roles in this journey and for that, I owe a great debt of gratitude to them.

First, I would like to sincerely thank my advisor Prof. Azita Emami. Her constant guidance, exemplary vision, and unwavering support throughout my graduate studies, have been the bedrock of all the research that I have done. She leads by example and has taught me the importance of having a strong foundation, of asking the right questions, of carefully and critically thinking about ideas, and of having a systematic and scientific approach towards problems. On a personal level, I have learned from her the importance and the need for empathy, generosity and inclusivity in our scientific community, which I find to be invaluable and constantly strive to imbibe. She has been a role model for me who I will always look up to for inspiration and advise. For her pivotal role in making my graduate life such a rewarding experience, I am profoundly grateful.

I feel honored and extremely grateful for our collaboration with Prof. Mikhail Shapiro. His unique perspective and ideas on the system and its application were crucial in defining our research projects. I have deep admiration for his breadth of knowledge, his constant curiosity, and his infectious enthusiasm, qualities that I wish to inculcate myself. I am also very grateful for our collaboration with Prof. Giovanni Traverso, which has been essential in demonstrating the impact of our research. His vast knowledge of biomedical engineering helped shape our system towards addressing highly relevant and pressing problems. These wonderful collaborations have broadened the horizons of my knowledge of biomedical applications that can benefit from advanced integrated circuits and systems.

I would like to thank the members of my candidacy and defense committee – Prof. P. P. Vaidyanathan, Prof. Alireza Marandi, and Prof. Axel Scherer, for taking the

time to evaluate my research and for their valuable inputs. I have had the privilege of taking Prof. PPV's classes at Caltech and absolutely enjoyed them.

I am immensely grateful to the present and past members of the Mixed-mode Integrated Circuits and Systems (MICS) lab for making our lab the absolutely best place to work. I thank Manuel Monge, Sahil Shah, Abhinav Agarwal, Kuan-Chang (Xavier) Chen, Arian Hashemi Talkhooncheh, Fatemeh Aghlmand (Fatima), Benyamin A. Haghi, Minwo Wang, William Wei-Ting Kuo, Lin Ma, Shawn Sheng, Steven Bulfer, Ting-Yu Cheng, and Hayward Melton. I am particularly grateful to Fatima, Xavier, and Arian for their tremendous help during chip tapeouts and measurements, and for the close friendships that made Caltech home for me. I would also like to thank members of the Shapiro lab Hunter Davis, Margaret Swift, Di Wu, and Dina Malounda; members of the Traverso lab Khalil B. Ramadi, Shriya Srinivasan, and Keiko Ishida; and members of the Caltech High-Speed Integrated Circuits (CHIC) lab Aroutin Khachaturian and Craig Ives. In the last few years of my graduate studies, I have been fortunate to work with Prof. Wei Gao and the members of his lab Jihong Ming, Changhao Xu, and Yiran Yang.

The strong undergraduate foundation that I received at the Indian Institute of Technology (IIT) Kharagpur was the basis for my graduate studies, and for that I sincerely thank Prof. Pradip Mandal, Prof. Anindya Sundar Dhar, Prof. Mrigank Sharad, Dr. Nijwm Wary, Prof. Indrajit Chakrabarti, Prof. Swapna Banerjee, Prof. P. P. Chakrabarti, Prof. Saswat Chakrabarti, Prof. Suvra Sekhar Das, and Prof. Amit Patra. I am also extremely grateful to my teachers at school and coaching institute—Meenu Rathore, Harsh Sharma, Preeti Pareek, Neelam Sonoo, Aastha Sinha, Binsu Paniker, Snehlata Gehlot, Varsha Gupta, O. P. Rai, Nitin Sharma, Kiran Sharma, Prabha Soni, Priyanka Roy, Pankaj Baluja, Suresh Dwivedi, Manish Samai, Manmohan Singh, Bablee Agarwal, and Archana Sharma.

The beautiful friendships of my childhood friends Himanshu Tatla, Kriti Garg, Saurav Maji, and Geetika Bhandari have been one of the most amazing parts of my life. I also cherish the friendships of Saion Roy, Manny Jain, Nikita Agarwal, Avilash

Mukherjee, Raj Vijayvargiya, Kuheli Pratihar, Ayush Gupta, Aditya Jhalani, Prashant Gautam, Himanshu Vyas, Adamya Dhakad, Riya Singla, Arkadev Roy, Anupama Lakshmanan, Armian Hanelli, Rathin Singha, Reza Hashemi, Connor McMahan, Srikanth Tenneti, Shriddha Chaitanya, Jiljo Moncy, Sagar Kumashi, and Corbin Chiodi.

The Philosophy of Yoga club at Caltech has been instrumental in helping me find a higher purpose in life, and for that, I thank Akshay Joshi, Guruprasad Raghavan, Kunal Mooley, Pranav Kulkarni, Shreya Anand, and Ashkan Rashedi.

I very much appreciate the support and assistance from the administrative staff Michelle Chen, Tanya Owen, Christine Garske, Angie Riley, Caroline Murphy, Mabby Howard, Chris Birtja, Dan Caballero; and from the Caltech International Student Programs (ISP) advisors Laura Flower Kim and Daniel Yoder.

I thank the amazing mentors during all the internships that I have had the privilege of learning from—Prof. Hossein Hashemi and the group at USC Sungwon Chung, Aria Samiei, Sushil Subramanian; Nick Hendrickson and the group at Medtronic Jon Thissen, Robert Mehregan, Shohan Hossain; Prof. Dipanajn Gope and the group at IISc Bangalore Harikiran Muniganti, Bhutesh, Sai Gunaranjan Pelluri, Arkaprovo Das, and Nikita Ambasana.

I am forever and infinitely grateful to my parents Mrs. Priti Sharma and Dr. Narendra Sharma, whose unconditional love and countless sacrifices have made me the person I am. To my sister Shivani Sharma, my uncles, aunts, cousins, nephews and nieces—I thank you all from the bottom of my heart.

Lastly, I am in eternal debt of the supreme almighty god, Krishna, to whom I owe everything that I have achieved in this life. My faith in Him has helped me persevere through the most difficult times of life, and has also been the constant source of guidance and wisdom that I turn to in times of need. For that, I dedicate this thesis to Him.

ABSTRACT

Medical electronic devices are an integral part of the healthcare system today. Significant advances have been made over the past few decades to yield highly miniaturized and low-power medical devices that are suitable for implantable, ingestible, or wearable applications. A key feature of medical devices that is central to their use in many applications is the capability to locate them precisely inside the body, and quite a lot of research effort has been expended in this direction. Location sensing is crucial for several applications: tracking pills in the GI tract, navigation during precision surgeries, endovascular procedures, robotic and minimally invasive surgery, and targeted therapy. The current gold-standard solutions for these procedures include invasive techniques such as endoscopy, or procedures that require repeated use of potentially harmful X-ray radiation such as CT scans. These techniques also require repeated evaluation in a hospital setting and are not conducive for non-clinical environments. While there are several alternative non-ionizing methods for imaging and localization based on electromagnetic tracking, radio-frequency, ultrasound, and optical tracking, none of them are able to simultaneously achieve a high field-of-view of tracking, high spatiotemporal resolution, fully wireless operation and miniaturization of the sensing devices, and system scalability with the number of devices. In this dissertation, we present a radiation-free system for high-precision localization and tracking of miniaturized wireless devices *in vivo*, using harmless magnetic field gradients.

First, we demonstrate our system for precision surgery applications. We designed highly miniaturized, wireless and battery-less microdevices, capable of measuring and transmitting their local magnetic field. One such device can be attached to an implant inside the body and another to a surgical tool, such that both can simultaneously measure and communicate the magnetic field at their respective locations to an external receiver. The relative location of the two devices on a real-time display can enable precise surgical navigation without using X-ray fluoroscopy. The prototype device consists of a micro-chip fabricated in 65nm

CMOS technology, a 3D magnetic sensor and an inductor-coil. The chip performs wireless power management, wireless bi-directional data-telemetry, and I2C communication with the sensor. Planar electromagnetic coils are designed for creating monotonically varying magnetic fields in the X, Y, and Z directions, resulting in field gradients that encode each spatial point with a unique magnetic field value. The concept of gradient-based spatial encoding is inspired by MRI. The system is tested *in vitro* to demonstrate a localization accuracy of <100μm in 3D, the highest reported to the best of our knowledge.

Second, we demonstrate our system for localization and tracking of ingestible microdevices in the GI tract, which is valuable for the diagnosis and treatment of GI disorders. We designed highly miniaturized, low-power, and wireless ingestible devices to sense and transmit their local magnetic field as they travel through the GI tract. These devices consist of a 3D magnetic sensor, a Bluetooth microprocessor and a 2.4GHz Bluetooth antenna for wireless communication, all packaged into a 000-size capsule. The magnetic field sensed by the devices is created by using high-efficiency planar electromagnetic coils that encode each spatial point with a distinct magnetic field magnitude, allowing us to track the location of the devices unambiguously. The system functionality is demonstrated *in vivo* in large animals under different chronic conditions and disease models to show 3D localization and tracking in real time and in non-clinical settings, with mm-scale spatial resolution, and without using any X-ray radiation. This has the potential for significant clinical benefit for quantitative assessment of GI transit-time, motility disorders, constipation, incontinence, medication adherence monitoring, anatomic targeting for drug delivery, and targeted stimulation therapy.

Third, in order to further miniaturize the devices developed for the above two applications and to make them even more low-power, we present a monolithic 3D magnetic sensor in 65nm CMOS technology that measures <5mm^2 in area and consumes 14.8μW in power while achieving <10μT$_{rms}$ noise. Our novel 3D

magnetic sensor overcomes the challenges faced by traditional magnetic sensors by being fully CMOS compatible and achieving high sensitivity with only μW-level power, which is in sharp contrast with Hall and Fluxgate sensors. The sensor is comprised of three orthogonal and highly dense metal coils implemented in the 65nm node, which generate a voltage signal in response to AC magnetic fields by electromagnetic induction. The EMF voltage signal is processed by on-chip circuitry that performs low-noise amplification, filtering, peak detection, and 12-bit digitization. Though the sensor can be used for a variety of applications that require AC field sensing, it is particularly useful for biomedical applications—tracking catheters and guidewires during endovascular procedures, minimally invasive surgeries, targeted radiotherapy, and for use as fiducial markers during preoperative planning. The proposed magnetic sensor is demonstrated for use in 3D tracking of catheters using the magnetic-field gradient-based spatial encoding scheme, and achieves 500μm of mean 3D localization accuracy.

PUBLISHED CONTENT AND CONTRIBUTIONS

S. Sharma, K. B. Ramadi, N. H. Poole, S. S. Srinivasan, K. Ishida, J. Kuosmanen, J. Jenkins, F. Aghlmand, M. B. Swift, M. G. Shapiro, G. Traverso, A. Emami, **"Location-aware smart-pills for wireless monitoring of gastrointestinal dynamics,"** *Nature Electronics*, vol. 6, pp 242-256, 2023. doi: 10.1038/s41928-023-00916-0.
S. S. participated in conceiving the ideas, designing the ingestible device and the electromagnetic gradient coils, performed the experiments, and co-wrote the manuscript.

S. Sharma, A. Telikicherla, G. Ding, F. Aghlmand, A. H. Talkhooncheh, M. G. Shapiro, A. Emami, **"Wireless 3D Surgical Navigation and Tracking System with 100µm Accuracy Using Magnetic-Field Gradient-Based Localization,"** *IEEE Transactions on Medical Imaging*, vol. 40, no. 8, pp. 2066-2079, Aug. 2021. doi: 10.1109/TMI.2021.3071120.
S. S. participated in conceiving the ideas, designing the CMOS chip, the implantable device and the electromagnetic gradient coils, performed the experiments, and co-wrote the manuscript.

S. Sharma, G. Ding, A. Telikicherla, F. Aghlmand, A. H. Talkhooncheh, M. Wang, M. G. Shapiro, A. Emami, **"3D Surgical Alignment with 100µm Resolution Using Magnetic-Field Gradient-Based Localization,"** *IEEE International Solid-State Circuits Conference (ISSCC)*, 2020, pp. 318-320.
doi: 10.1109/ISSCC19947.2020.9063108.
S. S. participated in conceiving the ideas, designing the CMOS chip, the implantable device and the electromagnetic gradient coils, performed the experiments, and co-wrote the manuscript.

S. Sharma, H. Melton, L. Edmonds, O. Addington, M. G. Shapiro, A. Emami, **"A Monolithic 3D Magnetic Sensor in 65nm CMOS with <10µT_{rms} Noise and 14.8µW Power,"** *2023 IEEE Custom Integrated Circuits Conference - (CICC)*, San Antonio, TX, USA, 2023, pp. 1-2.
S. S. participated in conceiving the ideas, designing the CMOS chip and the implantable device, performed the experiments, and co-wrote the manuscript.

S. Sharma, H. Melton, L. Edmonds, O. Addington, M. G. Shapiro, A. Emami, **"A 14.8µW Power and <10µT_{rms} Noise 3D Magnetic Sensor in CMOS for**

Biomedical Applications," *IEEE Journal of Solid-State Circuits, 2023* (to be submitted).
S. S. participated in conceiving the ideas, designing the CMOS chip and the implantable device, performed the experiments, and co-wrote the manuscript.

A. Emami and S. Sharma, **"3D Localization of Miniaturized Devices for Precision Medicine,"** *IEEE Solid-State Circuits Magazine*, Spring 2023.
S. S. participated in conceiving the ideas, designing the CMOS chip, designing the implantable and the ingestible devices, and the electromagnetic gradient coils, performed the experiments, and co-wrote the manuscript.

TABLE OF CONTENTS

LIST OF ILLUSTRATIONS

Number *Page*

LIST OF TABLES

Number *Page*

Chapter 1

INTRODUCTION

Medical electronics have become a ubiquitous part of the healthcare system today and are at the forefront of innovation in disease diagnosis and treatment. Their presence pervades both clinical and non-clinical environments as they are integral not only for standard clinical equipment such as magnetic resonance imaging (MRI) scanner, computed tomography (CT) scanner, robotic surgical tools, but also for more ambulatory and outside the clinic use cases such as wearable electronics, ingestible and implantable electronics, and consumer electronics for smart health (Fig. 1.1) [1]–[8]. Implantable medical electronic devices have enabled a broad set of capabilities including sensing and stimulation in different organs including the heart, the gastrointestinal (GI) tract, and the brain [2]–[5]. The creation of wearable electronics has enabled real-time interfacing of digital devices with the body to measure physiological parameters such as heart rate, respiration rate, oxygen saturation, blood pressure and glucose level [1]. Recent developments in ingestible electronics have demonstrated a myriad of functionalities by employing sensors for measuring the temperature, pH, pressure, gas, biomolecule types and concentration, camera for wireless imaging and endoscopy, drug delivery modules, and custom designed electronic chips for wireless communication [2]–[4]. With such a wide array of sensing modules added to these devices, doctors now have access to rich data sets collected from otherwise hard to access areas of the body, resulting in better diagnosis and treatment plans for the patient. Navigation in surgery is another important example of the impressive feat achieved by today's medical technology that has paved the way for less invasive and more user friendly surgical procedures with better outcomes [6]–[7].

These remarkable breakthroughs in medical electronics have been made possible by relentless research and development in different areas including integrated circuits

Fig. 1.1: Medical electronic devices for a variety of applications: (a) pacemaker, (b) eye implant for smart vision, (c) brain-machine interfaces, (d) cochlear implants, (e) smart electronic wristband, (f) PillCam for capsule endoscopy, (g) continuous blood glucose monitoring patch, (h) neural stimulator IC, and (i) smart watch for health monitoring.

technology, data science, material science, biological and chemical engineering, and advanced packaging to name a few. Focusing on the electronics side, we can very well appreciate the importance of Moore's law that has been a major driving force behind miniaturization and scaling of electronic circuits (Fig. 1.2), which medical devices have tremendously benefitted from [9][10]. With technology scaling, the average power demands of complementary metal-oxide-semiconductor (CMOS) technology have been decreasing, now reaching the nanowatt level [11]. Such low power numbers are a result of innovations across multiple layers of technology—(i)

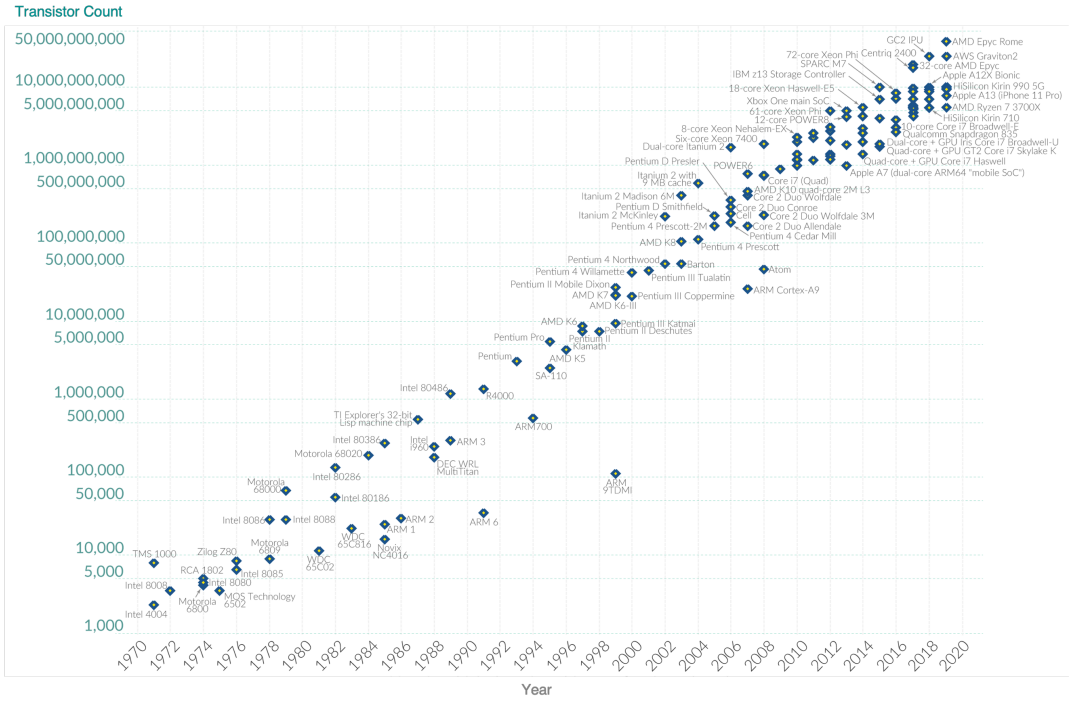

Fig. 1.2: Plot showing the number of transistors on integrated circuits from 1970 onwards [10]. Transistor counts have doubled approximately every two years, implying an exponential growth. This is in keeping with the Moore's law which has held true for more than 50 years now.

advanced circuit design techniques, (ii) higher level of integration in newer CMOS technologies, (iii) improved fabrication processes leading to higher reliability and yield, and (iv) advanced packaging techniques resulting in highly compact and low-power devices. Furthermore, low-power CMOS implementation of medical electronics is crucial for wireless power delivery, which can be accomplished using electromagnetic, ultrasound or piezoelectric power sources, or through the recently demonstrated energy harvesting techniques using the abundant biofluids in the body [8],[12],[13]. By co-designing the sensing electrodes with the electronic systems, a broad range of applications have emerged that were previously not possible due to bulky systems with discrete and power-hungry components. Taking another step forward, combining actuation and sensing capabilities on a single platform can lead

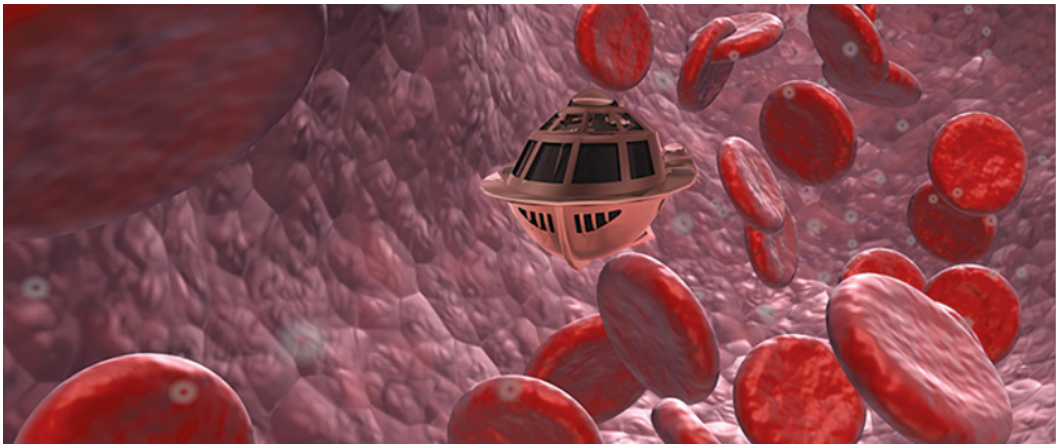

Fig. 1.3: Fantastic Voyage (1966) showing a microscopic submarine crew that venture into the body of an injured scientist to repair damage to his brain.

to the development of fully autonomous medical robots that can bring a dramatic shift to the current ways of health monitoring and treatment [5],[14].

1.1 Localization and navigation of medical devices *in-vivo*

One major feature of medical devices that is central to their use in many applications is the capability to locate them precisely inside the body. This idea of microscopic medical robots that can be controlled precisely to perform specific tasks at specific locations inside the body was made popular by the 1966 science fiction movie Fantastic Voyage. The movie shows a submarine crew who is shrunk to microscopic size and venture into the body of an injured scientist to repair damage to his brain (Fig. 1.3). Since then, quite a lot of research effort has been expended to make medical devices capable of sensing and transmitting their location when inside the body. Location sensing is crucial not only for the brain as demonstrated in the movie, but for many different medical applications. For instance, localization and tracking of wireless microdevices in the GI tract with high spatiotemporal accuracy has significant clinical value [2]–[4]. It can enable continuous monitoring and transit-time evaluation of the GI tract, which is essential for accurate diagnosis, treatment,

and management of GI motility disorders such as gastroparesis, ileus or constipation. GI motility disorders are also increasingly associated with a variety of metabolic and inflammatory disorders such as diabetes mellitus and inflammatory bowel disease. Together, these GI disorders affect more than one-third of the population globally and impose a considerable burden on healthcare systems [15]. High resolution and real-time tracking of wireless microdevices in the GI tract can also benefit anatomically-targeted sensing and therapy, localized drug delivery, medication adherence monitoring, selective electrical stimulation, disease localization for surgery, 3D mapping of GI anatomy for pre-operative planning, and minimally invasive GI procedures [2]–[4].

The current gold-standard solutions for these procedures include invasive techniques such as endoscopy and manometry, or procedures that require repeated use of potentially harmful X-ray radiation such as CT scans and scintigraphy (Fig. 1.4) [2]. These techniques also require repeated evaluation in a hospital setting, which can confound observations given the recognized variability in motility and activity. Alternative approaches—including video capsule endoscopy and wireless motility capsules—allow monitoring of the GI tract in real-world settings without interruption to daily activities [3]. However, these methods lack direct measurement of the capsule's location in the GI tract and have limited acquisition time. Commercial systems using electromagnetic-based tracking of sensors have also been developed but fail to simultaneously achieve a high field-of-view (FOV), high spatiotemporal resolution, fully wireless operation and miniaturization of the sensing devices, and system scalability with the number of devices [16]–[17].

Another major area that requires high-precision localization and real-time tracking of devices *in vivo* is precision surgery. A common example of that is orthopedic surgery in which long bone fractures are fixed by putting a metal rod into the bone and holding the two together using screws. It is crucial to know the precise location of the screw-holes before drilling into the fractured bone to put the screws in place

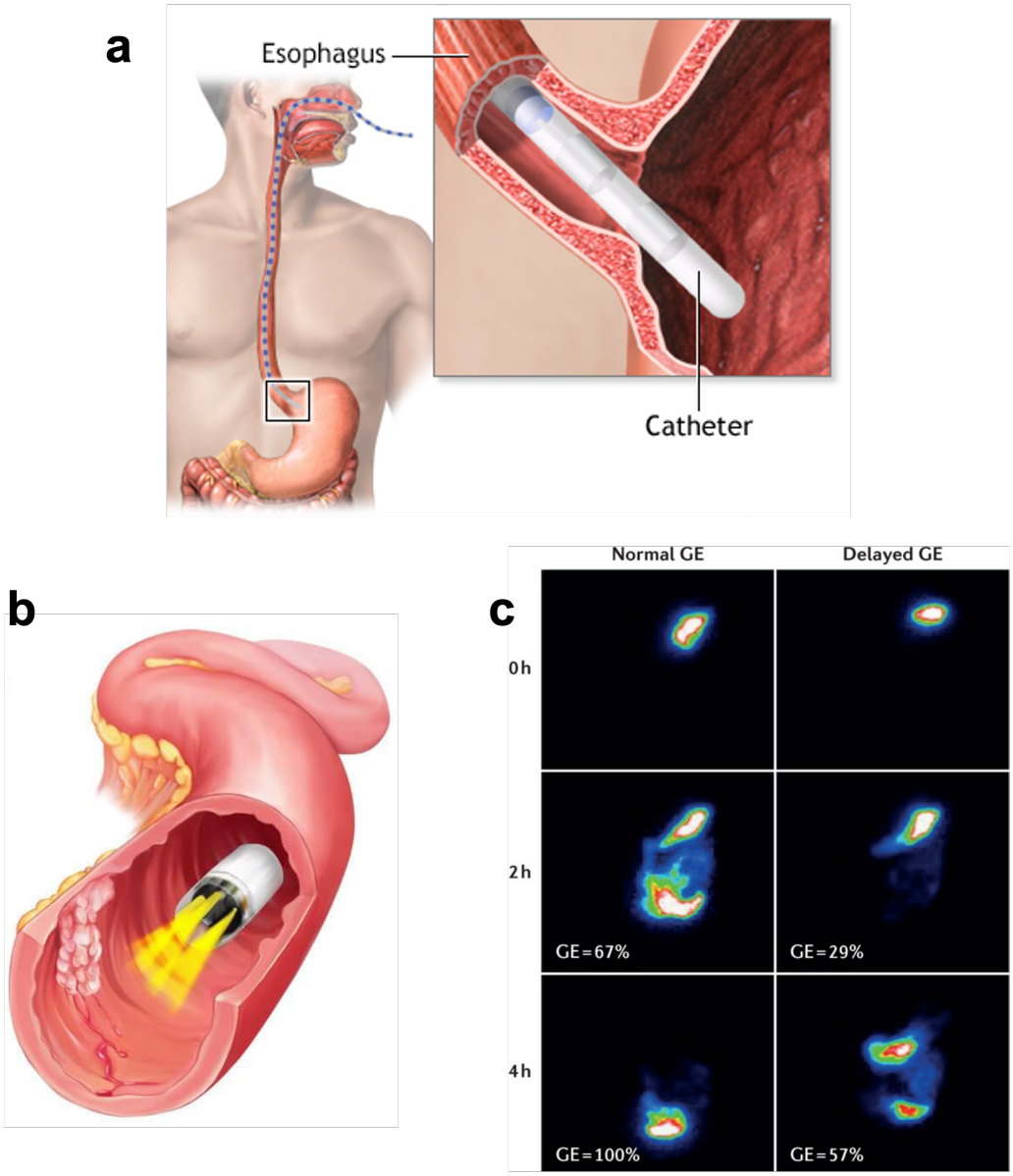

Fig. 1.4: Current clinical ways of GI tract monitoring: (a) wired endoscopy, (b) wireless capsule endoscopy, and (c) radiation-based scintigraphy.

[7]. Currently, multiple X-Ray images are taken to locate the screw-holes (Fig. 1.5). Other notable examples are robotic surgery, laparoscopic surgery and cardiovascular procedures, all of which require highly precise movement of surgical tools and devices inside the body, and currently rely heavily on potentially harmful X-Ray

Fig. 1.5: X-ray fluoroscopy being used during intramedullary nailing, a common orthopedic surgery to fix long bone fractures of the leg.

radiation. While there are several alternative non-ionizing methods for imaging and localization, none of them provide enough resolution and/or field-of-view (FOV) [16]. Most existing radio-frequency (RF) methods in the sub-GHz to several GHz of frequency range (as a trade-off between tissue-absorption loss and antenna-size of the implant), are based on the received signal strength, time of flight, time difference of arrival, angle of arrival and usage of RFID tags. However, such RF signals suffer very high attenuation when propagating through the human tissue. Severe multipath effects further limit their use for *in vivo* localization [18]. Ultrasound-based methods are most effective for soft tissues like muscles, tendons and internal organs, but have poor performance for bones and gas cavities, and require contact coupling to the subject [19]. Optical methods based on tracking infrared light, laser beam and fluorescence microscopy are limited by their low imaging depth due to light attenuation caused by absorption and scattering [20]. Optical methods are further limited by line-of-sight requirement.

1.2 Contribution

In this thesis, we present a radiation-free system for high-precision localization and tracking of miniaturized wireless devices *in vivo*, using harmless magnetic field

gradients. Our system overcomes several challenges faced by existing localization and tracking methods, and has the potential to replace harmful X-ray radiation used routinely for locating sensors and devices *in vivo*. Inspired by MRI, we generate monotonically varying magnetic fields in three orthogonal directions, resulting in gradients that encode each spatial point uniquely [21]–[22]. Highly miniaturized and wireless microdevices are designed to measure their local magnetic field magnitude and communicate it wirelessly to an external receiver. The receiver maps the field data to the respective spatial coordinates and displays the relative location of the microdevices in real time.

The first demonstration of our system is shown for precision surgery applications [23]–[24]. We designed highly miniaturized, wireless and battery-less microdevices, capable of measuring and transmitting their local magnetic field. One such device can be attached to an implant inside the body and another to a surgical tool, such that both can simultaneously measure and communicate the magnetic field at their respective locations to an external receiver. The relative location of the two devices on a real-time display can enable precise surgical navigation without using X-ray fluoroscopy. The prototype device consists of a micro-chip fabricated in 65nm CMOS technology, a 3D magnetic sensor and an inductor-coil. The Chip performs wireless power management at 13.56MHz using an active rectifier, boost-converter and regulators; wireless bi-directional data-telemetry; and I2C communication with the sensor. Planar electromagnetic coils are designed for creating monotonically varying magnetic fields in the X, Y, and Z directions, resulting in field gradients that encode each spatial point with a unique magnetic field value. We achieved un-ambiguous and orientation-independent spatial encoding in the FOV by: (i) using the gradient in the total field magnitude instead of only the Z-component; and (ii) using a combination of the gradient fields to correct for the non-linearity and non-monotonicity in X and Y gradients. The resultant X and Y FOV yield $\geq$ 90% utilization of their respective coil-span. The

system is tested *in vitro* to demonstrate a localization accuracy of <100μm in 3D, the highest reported to the best of our knowledge.

The second application where we demonstrate our system is in the localization and tracking of ingestible microdevices in the GI tract [25], which is valuable for the diagnosis and treatment of GI disorders. Such systems require a large field-of-view of tracking, high spatiotemporal resolution, wirelessly operated microdevices, and a non-obstructive field-generator that is safe to use in practical settings. We meet all of these requirements in our systems by designing—(i) highly miniaturized, low-power and wireless devices—termed ingestible microdevices for anatomic-mapping of gastrointestinal-tract (iMAG)—to sense and transmit their local magnetic field as they travel through the GI tract, and (ii) by creating 3D magnetic field gradients in the GI field-of-view using high-efficiency planar electromagnetic coils that encode each spatial point with a distinct magnetic field magnitude. The iMAG device consists of a 3D magnetic sensor for high-resolution field measurement, a Bluetooth Low Energy (BLE) microprocessor and a 2.4GHz Bluetooth antenna for wireless communication, and high-density coin-cell batteries for prolonged battery life while keeping a small form factor. The system functionality is demonstrated *in vivo* in large animals to show 3D localization and tracking of iMAG devices in real time and in non-clinical settings, with millimeter-scale spatial resolution, and without using any X-ray radiation. This has the potential for significant clinical benefit as quantitative assessment of GI transit-time is vital in the diagnosis and treatment of pathologies related to delayed or accelerated motility such as gastroparesis, Crohn's disease, functional dyspepsia, regurgitation, constipation, and incontinence. Other applications that could benefit from the high spatiotemporal accuracy of our system are therapeutic interventions like anatomic targeting for drug delivery, monitoring of medication adherence, delivery of macromolecules and electrical stimulation to specific regions of the GI tract in a wireless fashion [2]–[4].

Finally, in order to further miniaturize the devices developed for the above two applications and to make them even more low-power, we present a monolithic 3D magnetic sensor in 65nm CMOS technology that measures <5mm^2 in area and consumes 14.8µW in power while achieving <10µT$_{rms}$ noise [26]. Besides medical electronics, 3D magnetic sensors are an integral part of several fast-growing sectors such as automotive, navigation, robotics, power grids, industrial applications, consumer electronics and space equipment [27]. Due to their compatibility with the standard CMOS process, Hall magnetic sensors are widely used. However, one of the key challenges of CMOS-based Hall sensors is their relatively low sensitivity, which is inevitable given the low Hall coefficient of Si. For better sensitivity, Hall sensors are biased at higher current levels which hinders their widescale use in low-power bioelectronics and other power-constrained applications. Another challenge is the difficulty in implementing high-sensitivity vertical Hall elements in planar CMOS processes for 3D sensing. This is often overcome by using ferromagnetic materials that require additional and expensive steps during fabrication, thus increasing the cost [28]–[29]. Our novel 3D magnetic sensor overcomes all of these challenges as it is fully CMOS compatible and achieves high sensitivity with only µW-level power. The sensor is comprised of three orthogonal and highly dense metal coils implemented in the 65nm node, which generate a voltage in response to AC magnetic fields by electromagnetic induction. The 3D sensing coils are implemented using the available metal stack in the 65nm CMOS process. The EMF voltage signal is processed by on-chip circuitry that performs low-noise amplification, filtering, peak detection and 12-bit digitization while consuming only 14.8µW to yield µT-level sensitivity. Though the sensor can be used for a variety of applications that require AC field sensing, it is particularly useful for biomedical applications—tracking catheters and guidewires during endovascular procedures, minimally invasive surgeries, targeted radiotherapy, and for use as fiducial markers during preoperative planning. In this work, the proposed magnetic sensor is employed for 3D tracking of catheters using the magnetic field gradient based spatial encoding

scheme [23], and is demonstrated to achieve 500μm of mean 3D localization accuracy.

1.3 Organization

Chapter 2 provides a primer on the basic concepts of magnetic resonance imaging and the role of magnetic field gradients during image acquisition. We also provide an overview of Hall effect and Hall-based magnetic sensors since those are used for the implantable and ingestible microdevices developed in this work. Chapter 3 describes the system developed for navigation and tracking during precision surgeries, comprising the wireless and battery-less implantable device, the 3D magnetic field gradient-generating electromagnetic coils, and the localization algorithm. Measurement results for 3D localization *in vitro* and to study the effect of interference from different tools in the operation room are also presented.

Chapter 4 describes the system developed for continuous and real-time GI tract monitoring through ingestible microdevices. The design of the microdevice, the gradient generating electromagnetic coils, *in vitro* measurements, *in vivo* measurements in large animals for chronic studies and for different disease models in the gut are presented. In chapter 5, the design and implementation of the CMOS-based 3D magnetic sensor are described. System-level considerations, sensor design and requirements, details of the design and implementation of the processing circuit blocks, and measurement results for 3D tracking of catheters using our magnetic sensor in a phantom solution are presented. Finally, the conclusion of this work is presented in chapter 6, followed by the bibliography section.

Chapter 2

BACKGROUND

Since our 3D localization and navigation technique is inspired by MRI, we briefly describe the basic working principle of MRI in this chapter. The prototype magnetic-sensing devices developed for the precision surgery application and the GI tract monitoring application use a Hall-based magnetic sensor so we also describe the working mechanism of Hall sensors.

2.1 Magnetic Resonance Imaging (MRI)

MRI, one of the most successful medical imaging technologies of recent years, allows us to visualize the inside of the living organisms with great detail while using non-ionizing radiation [1]. It is widely used in research and diagnosis, with applications including: neuroimaging, soft tissue imaging, musculoskeletal imaging, brain activity studies, biomarker imaging, cancer studies, and many others. In contrast to X-Rays, RF, ultrasound and visible light, static magnetic fields (up to 5-10T) have negligible attenuation through the human body, no dependency on the tissue type, and no known harmful effects on cells [2]–[3]. These properties make MRI a very powerful and highly useful imaging tool. A common cylindrical-bore MRI scanner is shown in Fig. 2.1. There are three main magnetic fields in an MR imaging sequence: the strong polarizing magnetic field B_0 generated by a superconductive magnet; the RF excitation field B_1 generated by an RF coil; and the magnetic field gradients (G_X, G_Y and G_Z) generated by the gradient coils (Fig. 2.2). In a typical MRI sequence, first the static magnetic field B_0, commonly ranging from 1.5-7T, is applied to polarize the nuclear spins of hydrogen atoms. Our bodies are made of 80% water and each hydrogen atom in the water molecule has two subatomic particles: the nucleus called the proton (H^1); and an electron. The proton rotates around its own axis due to being electrically charged. The hydrogen atom is the most

Fig. 2.1: MRI setup used in clinics. The cylindrical bore has superconductive electromagnets to produce a Tesla-level static magnetic field (B_0) to polarize the hydrogen nuclei.

useful MRI source, as it is the most abundant element in the body. It is also the element with the highest gyromagnetic ratio, which is given as the ratio of its magnetic dipole moment to its angular momentum, which offers an advantage in MRI. Outside a magnetic field, the nuclei of hydrogen atoms are randomly oriented and provide a net magnetization of zero. However, when a subject is placed within a strong magnetic field of B_0, the nuclei tend to align in the direction of the field, producing a net magnetization (M) along the Z-axis, parallel to the scanner bore. This net magnetization is then manipulated to generate images.

After polarizing the nuclei, the RF frequency of f_0 (Larmor frequency), which corresponds to the RF field B_1, is applied to excite the hydrogen nuclei. Since the H

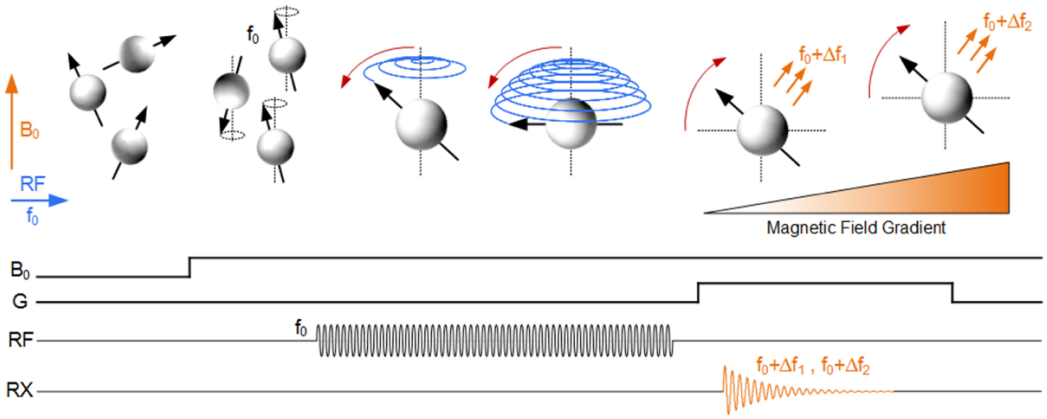

Fig. 2.2: Operating principle of MRI. Nuclear spins interact with a polarizing magnetic field B_0 and precess at their Larmor frequency f_0. They absorb and emit energy when an excitation RF signal is pulsed at the same resonance frequency f_0. By applying a magnetic field gradient during radiation, the location of spins are encoded in frequency shifts.

nuclei have a spin and a positive charge, they start *precessing* at the frequency of f_0 which is known as the Larmor frequency, and is defined as:

$$\omega = 2\pi\nu = \gamma B_0 \tag{2.1}$$

where γ is the gyromagnetic ratio of the nuclei. When the excitation RF pulse ends, the nuclei start relaxing, emitting a signal at the same frequency f_0 until they return to the resting state. This signal is known as the free induction decay (FID). To enable localization, a magnetic field gradient is applied after the RF pulse to expose nuclei at different locations to different magnetic fields, changing the frequency of their FID. The location information encoded in the oscillation frequency or frequency shift (Δf_1 and Δf_2 in Fig. 2.3) is then used to map the location of nuclei back in space. This approach is called frequency encoding.

Moving to three dimensions, MRI uses pulse sequences that involve slice selection, phase encoding and frequency encoding to image the target area of a patient. Slice selection is achieved by sending a *soft* RF pulse and applying the field gradient G_Z

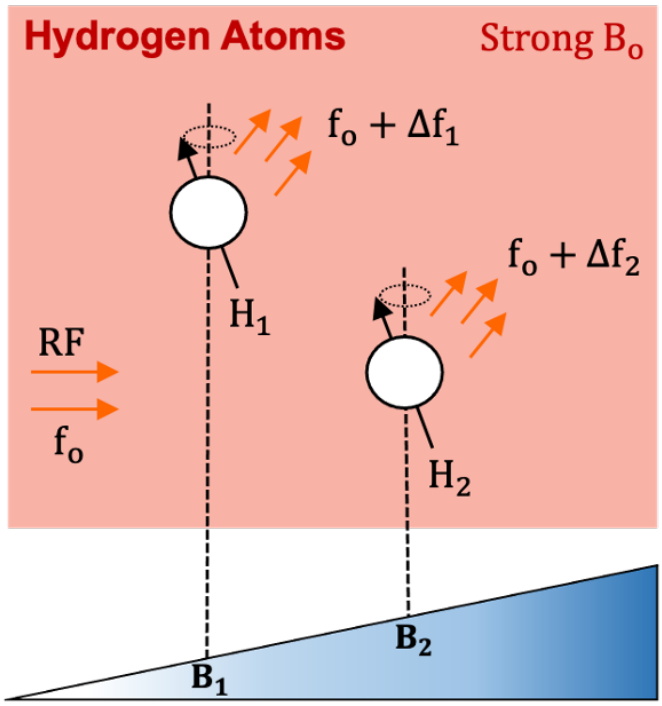

Fig. 2.3: Simplified overview of frequency encoding performed by H-atoms in MRI using magnetic field gradients. A strong and static Tesla-level magnetic field (B_0) is required in the background to polarize the nuclei before the gradient can be applied.

simultaneously to selectively excite only the nuclei from the target 2D slice. Phase encoding is then achieved by applying the field gradient G_Y to temporarily change the precessing frequency and de-phase nuclei at different locations. Finally, the field gradient G_X is applied during read-out to achieve frequency encoding.

The magnetic field gradient plays a crucial role in MRI and is discussed further. In the MRI context, a gradient is an additional magnetic field with a Z-component that varies linearly with position along some given direction (Fig. 2.4). For example, an X-axis gradient G_X would produce a total field along the Z-axis of:

$$B_Z^{tot} = B_0 + G_X x \tag{2.2}$$

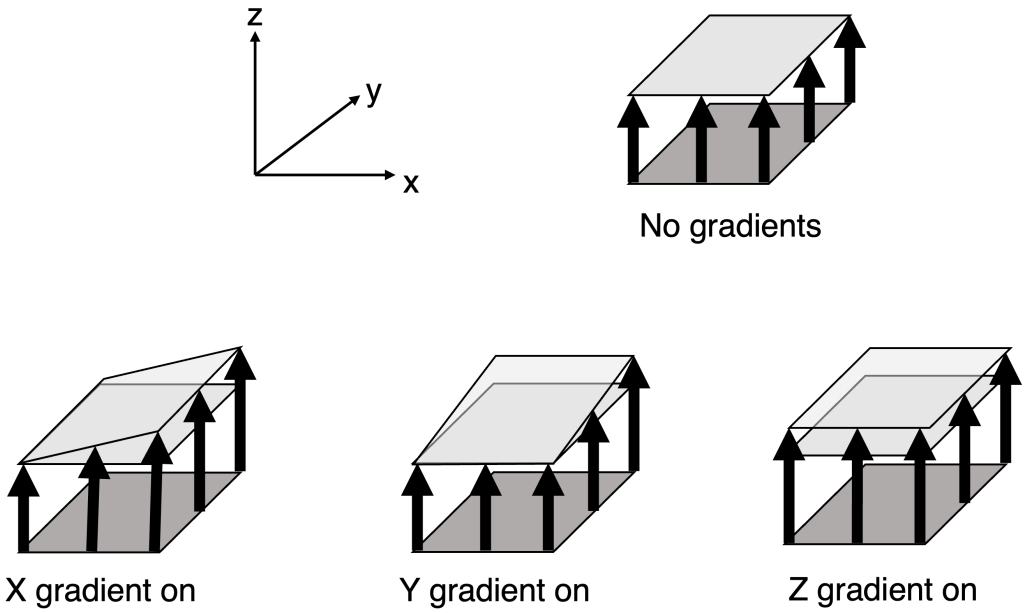

Fig. 2.4: Action of gradient fields. Note that the X and Y gradients do not generate transverse components that rotate/tip B_0 from side-to-side or up and down. The X and Y gradients act only to create in-plane "skewing" of the Z-components of B_0.

where B_0 is the main magnetic field. The gradient strength G_X is typically measured in units of mT/m and does not depend on position (although it may depend on time). In modern systems whole-body gradients have strengths of between 10-80 mT/m and can be switched on and off in less than one millisecond. The X, Y, and Z gradient generating coils used in typical closed-bore cylindrical MR scanners are shown in Fig. 2.5 [4][5].

In MRI acquisitions the receiver detects both the amplitude and phase of the signal so that we can write the signal at any given time *t* as:

$$S(t) = \iiint \rho(x,y,z)\, e^{-i\omega_0 - i\emptyset(x,y,z,t)} dx\, dy\, dz. \qquad (2.3)$$

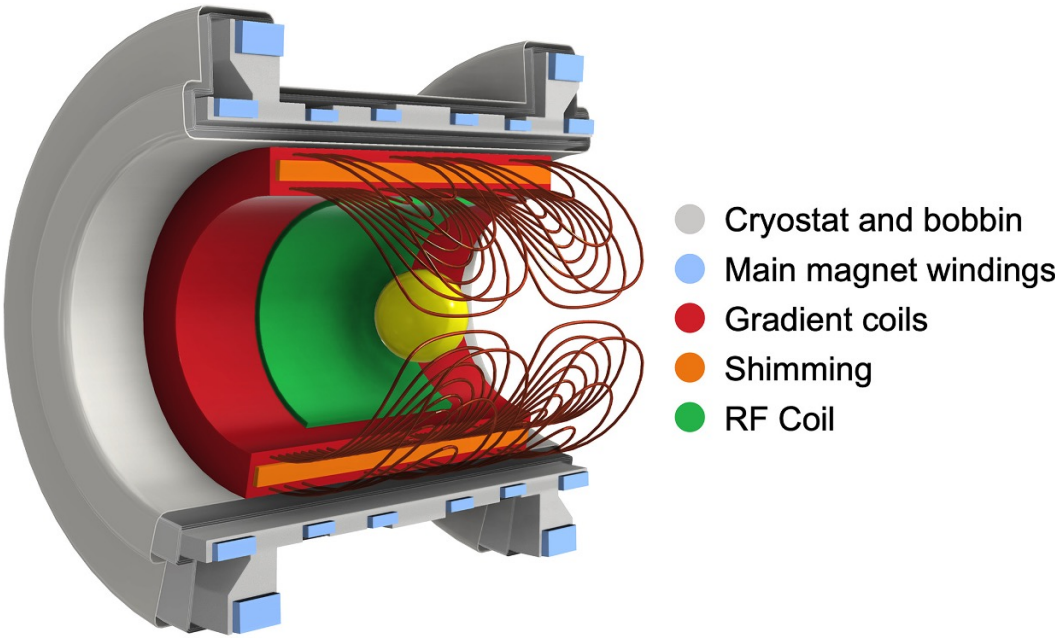

Fig. 2.5: Representative cross-section of a typical closed-bore MRI scanner showing the relative position of the RF coils, shimming coils, gradient coils, the superconductive electromagnetic coils (blue), and liquid helium chambers (gray) for cooling [5].

This is simply the sum, at time t, of the contributions over the field-of-view (FOV) of the receiver coils [6],[7]. We are using the standard complex (or phasor) representation to include the phase of the contributions, ρ is the position dependent proton spin density in the transverse plane, ω_0 is the Larmor precession frequency due to the main B_0 field and $\emptyset$ is the local phase offset induced by local variations in the axial field. For simplicity we are neglecting variations in the coil sensitivity across the FOV, which could be regarded as modifying ρ. The proton density ρ itself is assumed to be independent of time, which is true provided there is no subject motion during an acquisition.

As seen above, an MRI system uses switchable gradient fields parallel to and superimposed on the main B_0 field. The gradients are designed to be linear functions of position so that:

$$B_G(x, y, z, t) = G_X(t)x + G_Y(t)y + G_Z(t)z = \boldsymbol{G}(t).\boldsymbol{r}. \qquad (2.4)$$

In a modern system G_X, G_Y and G_Z will be typically up to 80 mT/m so that the resulting gradient field *G* will vary by up to ~40 mT across the imaging volume. It is important to understand that the terms in Eq. (2.4) are contributions to the field in the direction parallel to B_0. The Maxwell equation $\nabla.B = 0$ implies that field gradients in the Z direction must necessarily be accompanied by similar strength fields in the transverse plane. However, except in the case where B_0 itself is very small, these so-called concomitant fields can usually be ignored, but may need to be taken into account for certain cases.

The superconductive electromagnets that produce the static magnetic field of B_0 are a crucial component of an MR scanner. These instruments need liquid helium at 4K for the coils of commonly Nb-Ti alloy to be brought down to superconducting condition (Fig. 2.5). This is quite expensive and these instruments are usually very large because of the need for much insulation to keep the cryogen at low temperature. Another drawback is the large fringe field area, which can extend several meters in many directions. This is partly overcome by passive or active shielding of the magnet. For passive shielding, an MR room should have heavy iron plates in the walls, ceiling and floor. In active shielding, an additional coil carrying a counter current is situated outside the main coils minimizing the magnetic fields outside the bore.

2.2 Hall effect based magnetic sensor

A Hall sensor is a type of sensor which detects the presence and magnitude of a magnetic field using the Hall effect. The Hall effect is the production of a potential difference (the Hall voltage) across an electrical conductor that is transverse to an electric current in the conductor and to an applied magnetic field perpendicular to the current [8],[9]. It was discovered by Edwin Hall in 1879. The Hall effect is due to the nature of the current in a conductor. Current consists of the movement of many small charge carriers, typically electrons, holes and/or ions. When a magnetic field is present, these charges experience a force, called the Lorentz force. When such a magnetic field is absent, the charges follow approximately straight paths between collisions with impurities, phonons, etc. However, when a magnetic field with a perpendicular component is applied, their paths between collisions are curved, thus moving charges accumulate on one face of the material (Fig. 2.6). This leaves equal and opposite charges exposed on the other face, where there is a scarcity of mobile charges. The result is an asymmetric distribution of charge density across the Hall element, arising from a force that is perpendicular to both the straight path and the applied magnetic field. The separation of charge establishes an electric field that opposes the migration of further charge, so a steady electric potential is established for as long as the charge is flowing.

In order to derive equations for the Hall effect, let us consider a simple scenario. When we apply a magnetic field in a perpendicular direction to the applied field (which is driving the current), we find there is a transverse field in the sample that is perpendicular to the direction of both the applied field E_x and the magnetic field B_z, and is generated along the Y direction. Putting a voltmeter across the sample, as shown in Fig. 2.6, gives a voltage reading V_H. The applied field E_x drives a current J_x in the sample. The electrons move in the X direction, with a drift velocity v_{dx}. Because of the magnetic field, there is a Lorentz force acting on each electron and is given by:

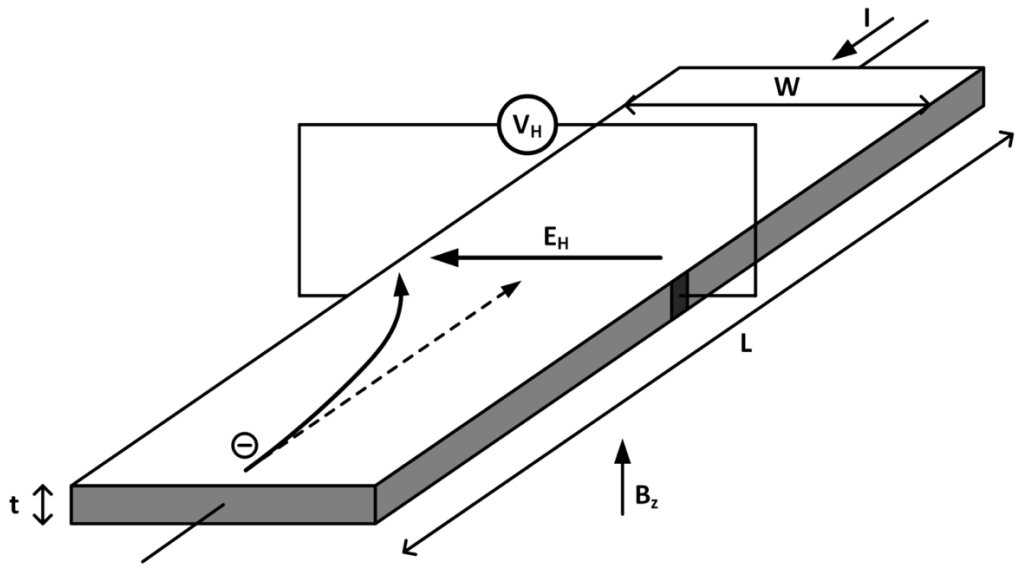

Fig. 2.6: Illustration of the Hall effect in a conductive media with a length L and a width W. An electric field E_H is generated by the carrier deflection and produces a maximum potential call the Hall voltage V_H .

$$F_y = -ev_{dx}B_z. \tag{2.5}$$

The direction of this Lorentz force is the Y direction, which we can show by applying the right hand thumb rule, because in vector notation, the force F acting on a charge q moving with a velocity v in a magnetic field B is given by the vector product:

$$F = qv \times B. \tag{2.6}$$

All moving charges experience the Lorentz force given by Eq. (2.6). In our example of a metal in Fig. 2.6, this Lorentz force is the Y direction, so it pushes the electrons leftward, as a result of which there is a negative charge accumulation near the left edge of the sample and a positive charge near the right edge of the sample.

The accumulation of electrons near the left edge results in an internal electric field E_H in the Y direction. This is called the Hall field and gives rise to a Hall voltage V_H between the left and right edges of the sample. Electron accumulation continues until the increase in E_H is sufficient to stop the further accumulation of electrons. When this happens, the magnetic field force $ev_{dx}B_z$ that pushes the electrons left just balances the force eE_H that prevents further accumulation. Therefore, in the steady state:

$$eE_H = ev_{dx}B_z. \tag{2.7}$$

However, $J_x = env_{dx}$. Therefore, we can substitute for v_{dx} to obtain:

$$eE_H = J_xB_z/n. \tag{2.8}$$

Simplifying this, we obtain:

$$E_H = \left(\frac{1}{en}\right)J_xB_z. \tag{2.9}$$

A useful parameter called the Hall coefficient R_H is defined as:

$$R_H = \frac{E_y}{J_xB_z}. \tag{2.10}$$

The quantity R_H measures the resulting Hall field, along Y, per unit transverse applied current and magnetic field. The larger R_H, the greater E_y for a given J_x and B_z. Therefore, R_H is a gauge of the magnitude of the Hall effect. A comparison of the Eq. (2.9) and (2.10) shows that for metals:

$$R_H = \frac{1}{en}. \tag{2.11}$$

Though R_H depends inversely on the free electron concentration, its value in metals is much less than that in semiconductors. In fact, Hall-effect devices (such as magnetometers) always employ a semiconductor material, simply because the R_H is larger. Since the conductivity is given by $\sigma = en\mu_d$, we can substitute for en in Eq. (11) to obtain:

$$R_H = \frac{\mu_d}{\sigma} \tag{2.12}$$

which can be simplified to:

$$\mu_d = R_H\sigma. \tag{2.13}$$

The drift mobility can thus be determined from R_H and σ. The product of R_H and σ is called the Hall mobility μ_H.

2.2.1 Hall effect in semiconductors

When a current-carrying semiconductor is kept in a magnetic field, the charge carriers of the semiconductor experience a force in a direction perpendicular to both the magnetic field and the current. At equilibrium, a voltage appears at the semiconductor edges.

The simple formula for the Hall coefficient given above is usually a good explanation when conduction is dominated by a single charge carrier. However, in semiconductors and many metals the theory is more complex, because in these materials conduction can involve significant, simultaneous contributions from both electrons and holes, which may be present in different concentrations and have different mobilities. For moderate magnetic fields the Hall coefficient is:

$$R_H = \frac{p\mu_h^2 - n\mu_e^2}{e(p\mu_h + n\mu_e)^2} \tag{2.14}$$

where n is the electron concentration, p the hole concentration, μ_e the electron mobility, μ_h the hole mobility and e the elementary charge. For large applied fields the simpler expression analogous to that for a single carrier type holds.

There are many instances when it is necessary to measure magnetic fields, and the Hall effect is ideally suited to such applications. Depending on the application, manufacturers use different semiconductors to obtain the desired sensitivity. Hall-effect semiconductor devices are generally inexpensive, small, and reliable. Typical commercial, linear Hall-effect sensor devices are capable of providing a Hall voltage of ~10 mV per mT of applied magnetic field. Hall effect sensors respond to static (non-changing) magnetic fields. This is a key difference from inductive sensors, which respond only to changes in fields. Hall sensors are commonly used for current sensing, position detection, and contactless switching applications.

Chapter 3

WIRELESS 3D SURGICAL NAVIGATION AND TRACKING USING MAGNETIC FIELD GRADIENTS

Localization and real-time tracking of devices *in vivo* with high precision are required during many surgical procedures and medical diagnostic techniques [1]-[3]. For instance, in orthopedic surgeries, long bone fractures are fixed by putting a metal rod into the bone and holding the two together using screws. It is crucial to know the precise location of the screw-holes before drilling into the fractured bone to put the screws in place [1]. Currently, the gold-standard for finding precise screw-hole locations relies heavily on potentially harmful X-Ray radiation. Typical imaging resolution of 200-500μm can be obtained by clinically used X-Ray imagers and computed tomography (CT) systems, which can be improved to <50μm using high radiation doses [4]. Multiple 2D X-Ray images can be used to provide detailed, 360^0 cross-sectional images, using CT [3].

In this work, we focus on orthopedic surgery, a major class of medical procedures performed on millions of patients per year [5]. Orthopedic surgeries are performed for the repair, reconstruction, and replacement of various bones and joints. Intramedullary (IM) nailing is a common example of high-precision orthopedic surgery, which requires insertion of a Titanium (Ti) metal rod into the medullary canal of a fractured bone, followed by locking screws [1]. The screws are installed at the proximal and distal end of the bone with the help of a surgical drill, to hold the bone and rod together. X-Ray fluoroscopy is performed over the desired region to precisely locate the screw-holes and their axis, before drilling manually. This is called the free-hand technique. Fluoroscopy is used because it can produce real-time images on a screen by using continuous X-Ray beams, which provide real-time feedback to the surgeon during the procedure [6]. The total duration of fluoroscopy can vary from 1-15 min per patient and is highly dependent on the skills of the surgeon [7]. This

can cause high levels of radiation exposure to the patient, surgeon and staff. Despite the drawback, the freehand technique using X-Ray fluoroscopy remains the gold standard for localizing screw-holes in bone implants, achieving 100-200μm of accuracy, depending on the radiation dose [3]-[4]. Handheld mechanical tools are also available for screw-hole localization. However, they work well for proximal holes but not for distal holes because of the high axial deformation (≈15mm) of the metal rod as it goes inside the bone [7], which cannot be compensated by the mechanical guide. Other medical procedures requiring precise alignment and positioning of surgical tools and implants, almost exclusively use X-Ray fluoroscopy instead of 2D X-Ray images, the latter being more common for diagnosis and snapshots [3].

3.1 System overview for wireless 3D surgical navigation

We present a radiation-free system for high-precision surgical alignment, navigation and tracking, using magnetic-field gradient-based localization of micro-scale devices. Our localization technique is inspired by MRI, a simplified view of which is shown in Fig. 3.1 (a), but does not require the strong and static B_0 (ranging from 1.5-7T in typical MR scanners) used in MRI. The high cost of MRI equipment (mainly because of the very strong B_0) and its incompatibility with many metals, make it an impractical modality to be used in real time during orthopedic procedures. As shown in [8], micro-chip devices can be designed to mimic the behavior of nuclear spins inside the body, and frequency encoding can be performed with these artificial atoms, similar to MRI. A simplified view of the system in [8] is shown in Fig. 3.1 (b), wherein devices D_1 and D_2 are excited using an RF frequency of f_0, and transmit a frequency-encoded signal during their read-out phase. The absence of strong background B_0 in [8] is a major difference from MRI, which reduces the cost of implementation significantly. Such a system is particularly useful when communicating with a large number of devices simultaneously over different frequency bands.

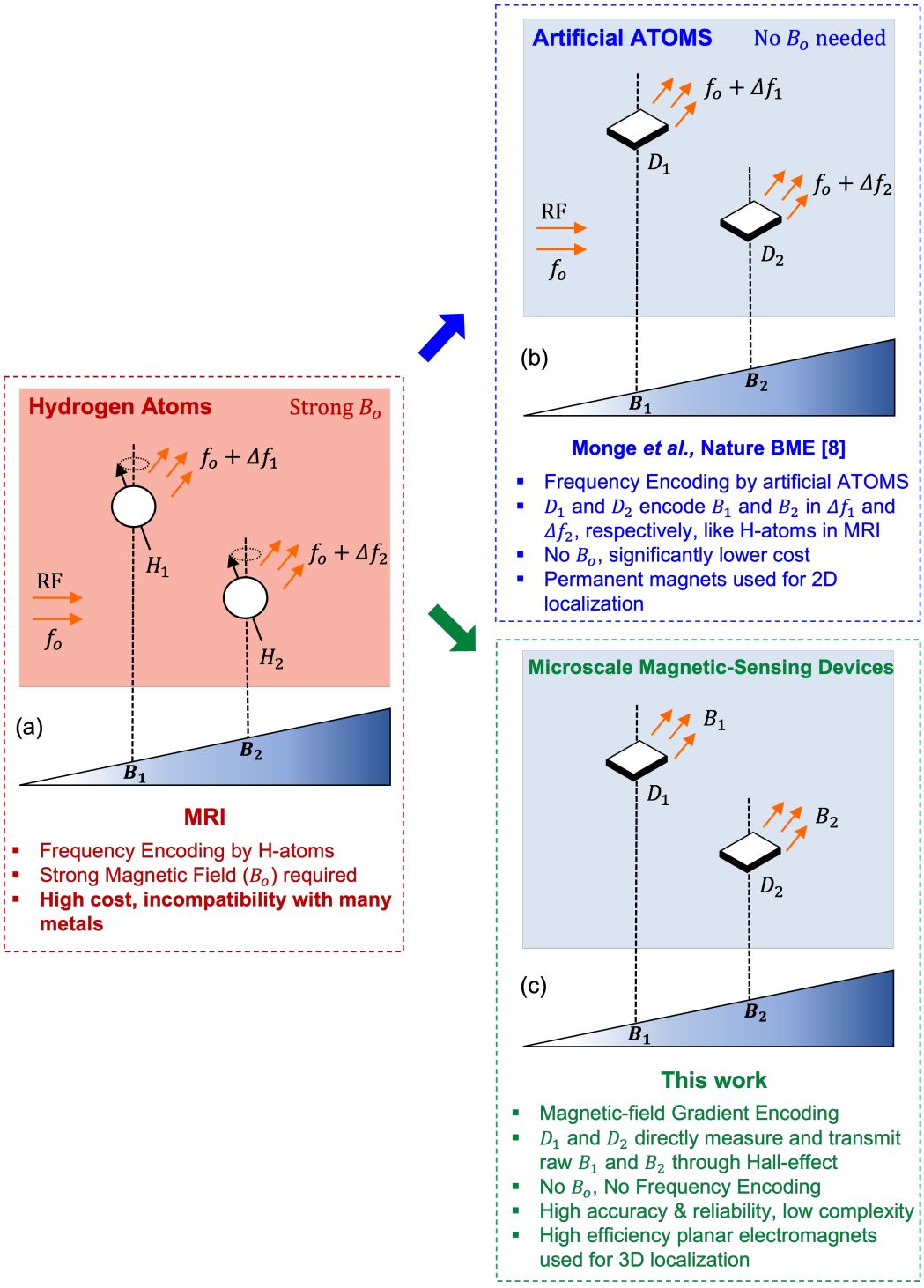

Fig. 3.1: 3D localization system. (a) Frequency encoding performed in MRI using hydrogen atoms. (b) Micro-chips working as artificial atoms to perform frequency encoding without any B_0 [8]. (c) Micro-chips localized using magnetic-field gradient encoding, eliminating both B_0 and frequency encoding in this work.

In this work, we describe an approach focused on achieving higher precision while communicating with a small number of wireless devices, as required in surgical applications. Rather than relying on analog frequency encoding, this approach uses digital reporting of the total magnetic field value at the devices' location, in combination with 3D field gradients, to precisely and robustly track the location of wireless devices. Micro-chip devices D_1 and D_2 are designed to *directly* measure, digitize, and transmit their local magnetic fields B_1 and B_2, respectively, through the Hall-effect, as shown is shown in Fig. 3.1 (c). Direct measurement of the raw field value at the devices' location eliminates the conversion complexity (required in frequency encoding), improves the accuracy, and enhances the reliability of the system. Other advantages of our system compared to [8] and other EM-based tracking techniques in [9], are the completely wireless operation of the devices D_1 and D_2, scalable and high FOV using efficient planar-electromagnets, and 3D localization with 100μm accuracy, as detailed below.

The complete system overview and the principle of operation of the proposed localization technique are shown in Fig. 3.2 and Fig. 3.3, respectively. In a surgical procedure, the patient's leg with a Ti metal rod inside is placed on top of a bed. Our system is designed such that a small electronic device (shown in green) can be attached right next to the screw-hole at a known position on the rod. Another identical device can be installed on the surgical drill. A planar electromagnetic assembly, consisting of magnetic field gradient generating coils for X, Y, and Z is placed beneath the surgical bed. The electromagnets produce monotonically varying magnetic fields, resulting in a known gradient in the three orthogonal directions. Fig. 3.3 shows the magnetic field gradient in the X-direction. The two devices can simultaneously sense the magnetic field at their respective locations and communicate it wirelessly to an external receiver. The receiver maps the field-data to spatial coordinates, and the relative locations of the devices are then displayed on a computer screen in real time. This can enable the surgical team to maneuver to screw-hole locations without using any X-Ray fluoroscopy [10]. In addition to the

3D position, orientation information of the devices can be critical for certain surgical procedures, such as the one shown in Fig. 3.2, and is discussed later. It is also to be noted that the relative position of the hole, with respect to the drill, will be obtained after calibration to compensate for the known location-offset between the hole and the device. If the device-location with respect to anatomical features (like specific bones, muscles or other internal body parts) is desired, which might be valuable for certain surgical applications, it can be obtained by using existing imaging modalities like X-Ray and MRI in conjunction with our system.

The wireless and battery-less devices D1 and D2 in Figs. 3.2–3.3 consist of a 3D magnetic sensor, an ASIC (Controller-Chip) designed in 65nm CMOS process, and an inductor-coil wound along the edges of the device. The Controller-Chip consists of a Power-Management-Unit (PMU) to convert AC power into regulated DC power, an RF Wake-up (RFW) block to perform wireless data communication, and a Data-Acquisition-Unit (DAU) to interface with the sensor. For this prototype device, we have used AK09970N as the 3D magnetic sensor, which communicates with the Chip over the I2C protocol [11]. The sensor is based on Hall-effect, has 16-bit data out for each of the 3-axis magnetic components, high sensitivity (1.1-3.1μT/LSB) and measurement range (± 36mT), and a footprint of 3x3x0.75mm^3. The spatial localization resolution (Δx) obtained by the system, in each of the three dimensions, is given by Eq. (3.1).

$$\Delta x = \frac{\Delta B_{eff}}{G}\left\{1 + \sqrt{\left(\frac{\delta G_i}{G}\right)^2 + \left(\frac{\delta G_s}{G}\right)^2}\right\} \tag{3.1}$$

$$\Delta B_{eff} = \sqrt{(\Delta B_i)^2 + (\Delta B_j)^2 + (\Delta B_k)^2} \tag{3.2}$$

ΔB_{eff} is the effective resolution that the sensor can achieve while performing a magnetic field measurement. It is dictated by the noise of the sensing and processing

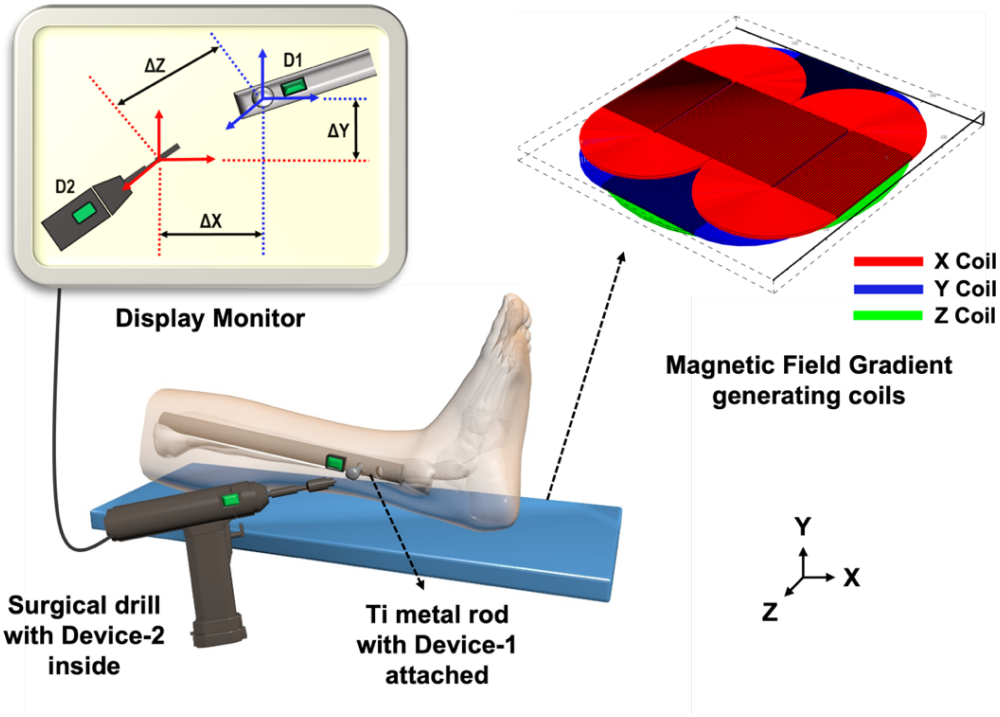

Fig. 3.2: Complete overview of the localization technique. Devices 1 and 2 measure the magnetic field at their respective locations, generated by the gradient coils, and their relative position is displayed in real time.

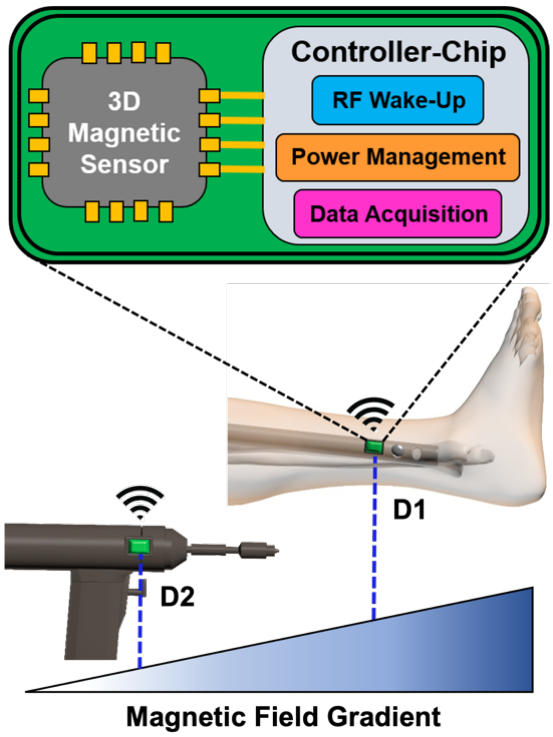

Fig. 3.3: Principle of opeartion of the gradient-based localization of devices.

units, the most dominant being the quantization noise. Since the sensor measures three orthogonal components (denoted by i, j, k) of the magnetic field, ΔB_{eff} is composed of the error in each component, as given by Eq. (3.2). G is the applied magnetic field gradient, which is determined by the current in the electromagnets and their geometrical structure. Two major noise sources have been identified in G: (i) δG_i—error caused by field interpolation; and (ii) δG_s—error caused by variations in supply current. Since δG_i and δG_s are independent and uncorrelated, they add in quadrature. The goal is to keep the contributions by these two error sources below 1% so that RHS in Eq. (3.1) reduces to $\approx \Delta B_{eff}/G$. With G = 30mT/m and ΔB_{eff} < 3μT, the system can achieve Δx < 100μm, as discussed later in detail.

3.2 Wireless and battery-less implantable microdevice

One of the most important aspects of the device is to be completely wireless, such that it can be hermetically sealed and sterilized to be used with surgical implants inside the body. Wireless operation is achieved through the CMOS Controller-Chip, which is at the core of the implantable device. A detailed overview of the Chip is shown in Fig. 3.4. Ultra-low power and high-efficiency circuit blocks are designed for the PMU, RFW and DAU, as described in the following sub-sections.

3.2.1 Rectifier

The rectifier constitutes the analog front-end of the PMU by converting the incoming RF signal at 13.56MHz to DC signal for all other circuit blocks. A full-wave rectifier is chosen over half-wave topologies due to larger average DC output voltage. Active-diodes are used as the four switches of these rectifiers to maximize the voltage conversion ratio by reducing the total voltage drop along the conduction path. The complete circuit schematic of the rectifier is shown in Fig. 3.5. The inductive link generates a sinusoidal voltage V_{In} which is given as input to the rectifier. Power-

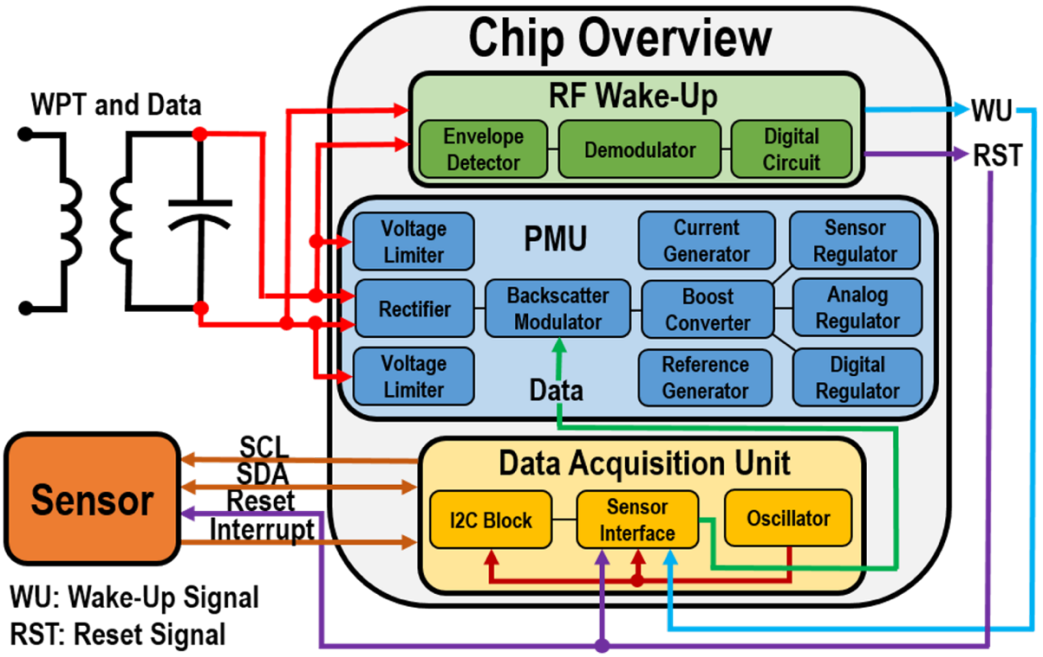

Fig. 3.4: Complete Controller-Chip overview with the external indcutor coil and magnetic sensor.

transistors M_{n1}, M_{n2}, M_{p1} and M_{p2} are sized to have 30 fingers of 10µm each (width) to allow sourcing of 2mA of output current while keeping the V_{ds} drop to a minimum across each transistor. The lengths are 60nm each to ensure fast switching. Unbalanced-biased comparators are used to switch M_{n1} and M_{n2} to reduce reverse leakage from C_L back into the rectifier [12]. In the absence of unbalance voltage ΔV, there exists a leakage current when V_{In2} (V_{In1}) increases to 0V and V_{In1} (V_{In2}) decreases to V_{Out} This is because when these voltages occur, Comparator 2 (Comparator 1) needs to discharge the large gate capacitance of M_{n2} (M_{n1}) to turn it off, thereby causing a delay during which both M_{n2} (M_{n1}) and M_{p1} (M_{p2}) are turned on. To circumvent this problem, M_{n2} needs to be turned off earlier to provide enough time for the gate capacitance to be discharged. Choosing ΔV appropriately, as given by Eq. 3.3, allows an early turn-off to reduce the reverse leakage significantly. R_1 and R_2 are chosen to be 500Ω and 30kΩ, respectively. K is 0.5 times V_{ov} of M_{n3}.

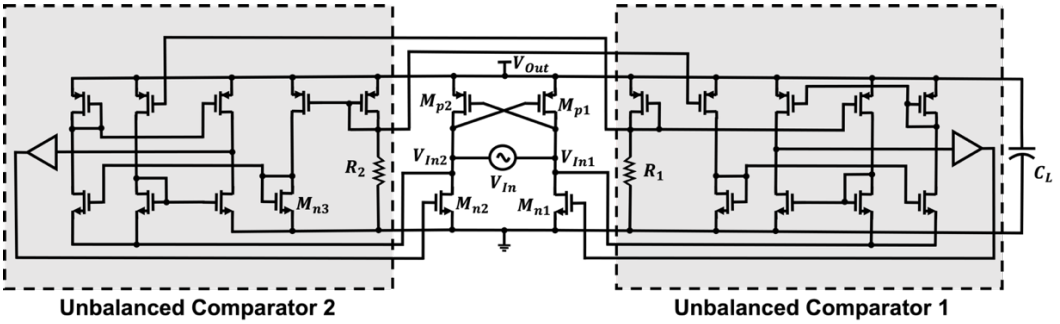

Fig. 3.5: Circuit schematic of the rectifier, highlighting the two unbalanced comparators.

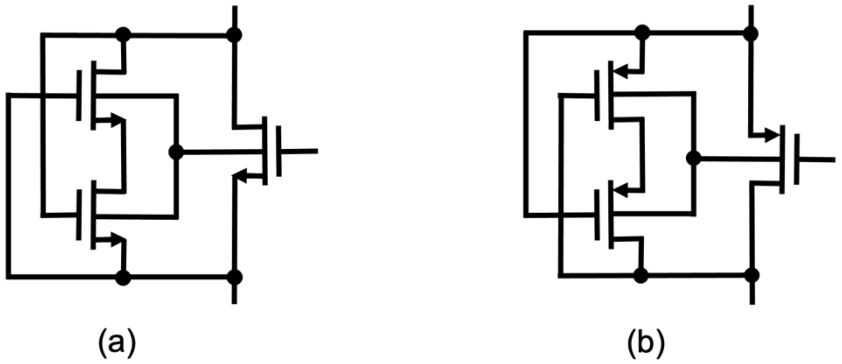

Fig. 3.6: Dynamic body-biasing for (a) NMOS M_{n1} and M_{n2}; and (b) PMOS M_{p1} and M_{p2}.

$$\Delta V = K\left(\sqrt{R_2/R_1} - 1\right) \tag{3.3}$$

The rectifier is capable of self-startup under low input amplitudes. In order to prevent latch-up phenomena during startup and steady state, it is crucial to bias the body terminals of M_{n1} (M_{p1}) and M_{n2} (M_{p2}) to the lowest (highest) available voltage. Since ground (V_{Out}) is not the lowest (highest) voltage during the entire operation, the body terminals of the power transistors are biased dynamically, as shown in Fig. 3.6 [13]. The rectifier thus achieves 84% voltage conversion efficiency for $1V_{pp}$ sinusoidal signal at 13.56MHz, under no-load condition. This drops to 80% when providing 2mA of load current, hence giving an average efficiency of 82%.

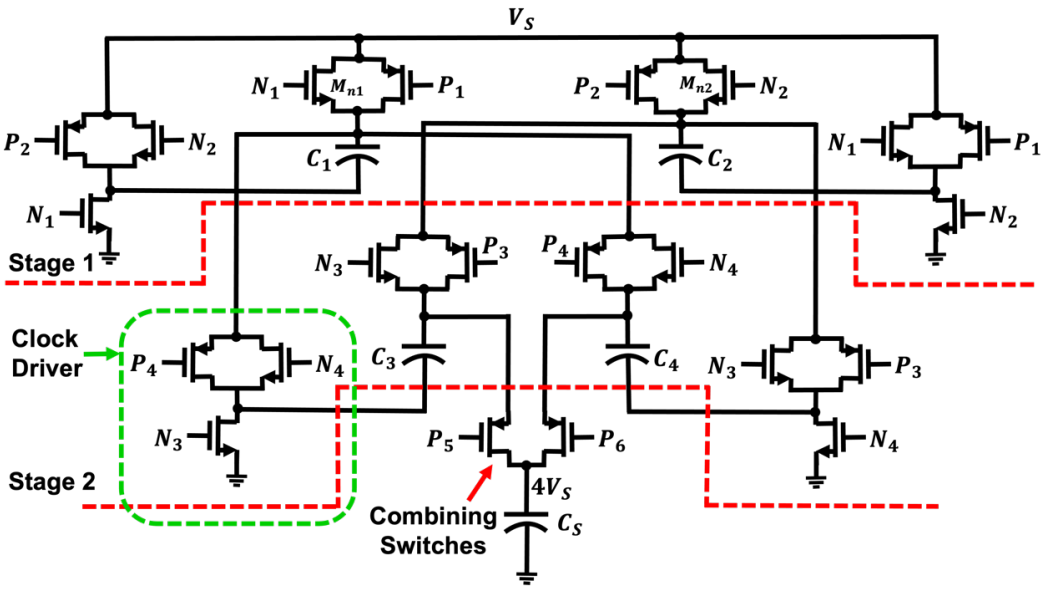

Fig. 3.7: Circuit schematic of the boost-converter showing the two interleaved stages. Clock drivers are on the extreme left and right of each stage.

3.2.2 Boost-converter

The rectified DC voltage is boosted to 4× by a two-stage interleaved switched-capacitor DC-DC boost-converter, as shown in Fig. 3.7. Each stage is a voltage doubler, which results in an overall conversion-ratio of 4 at the output. Traditional Dickson charge-pumps employ cross-coupled self-switched NMOS transistors M_{n1} and M_{n2}, which increase the conduction resistance and cause shoot-through current, resulting in a degraded efficiency [14]. To eliminate that, each stage of the boost-converter is switched using non-overlapping (NOL) complementary clocks [15]. For Stage 1, when N_1 (P_1) is high (low), C_1 is charged to V_S, which increases to $2V_S$ when N_2 (P_2) becomes high (low). The $2V_S$ is fed as input to Stage 2 and by the same doubling process, $4V_S$ appears across C_3 and C_4, which is then combined to appear across a single capacitor C_S. Complementary PMOS switches are used in both stages to aid during startup since the initially low output of boost-converter is sufficient to

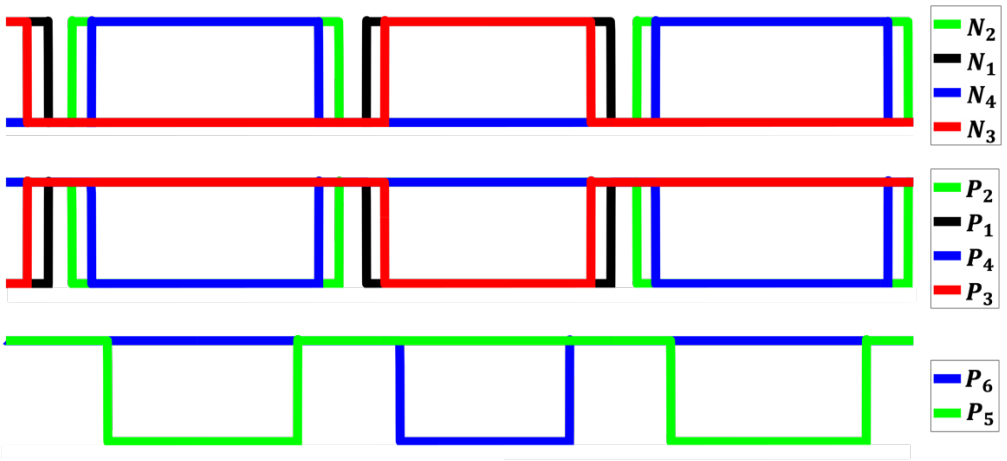

Fig. 3.8: NOL clock waveforms used for swicthing all the transistor swicthes of boost-converter.

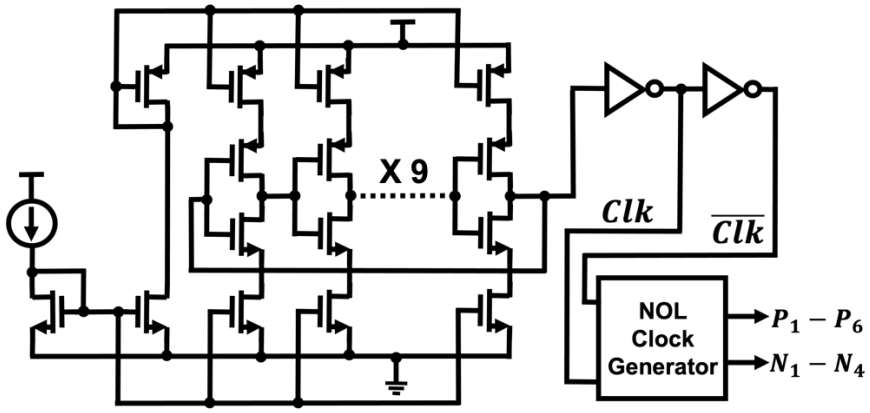

Fig. 3.9: Current-starved ring-oscillator used for genertaing a single 1MHz clock phase.

turn the PMOS on [16]. The lower side of clock drivers (green dotted box) should not contain a PMOS to initially isolate the input and output nodes from ground. The interconnecting fly capacitors (C_1-C_4), called C_f, control the effective impedance of the boost-converter, along with the switching frequency F_S, as described in Eq. (3.4) [15]. To reduce losses in the conduction path, it is desirable to choose high values of both C_f and F_S. However, an arbitrarily large C_f causes a huge area penalty while a high F_S results in more switching losses. As a trade-off, C_f and F_S were chosen to be 1nF (off-chip) and 1MHz, respectively.

$$Z_{BC} = 1/F_s C_f \quad (3.4)$$

The NOL clock waveforms, shown in Fig. 3.8, eliminate the shoot-through current and charge-sharing losses. A single 1MHz clock pulse is generated from a 9-stage current-starved ring-oscillator operated in the sub-threshold region (0.5V supply), shown in Fig. 3.9. The NOL clock generating block consists of delay lines in the feedback path [16] and digital combination blocks to generate the required clock phases, all at 0.5V supply. The waveforms are then scaled appropriately using a chain of level-shifters, supplied by the regulators. A single level-shifter block is shown in Fig. 3.10 (a). Since the max NOL clock voltage of $4V_S$ is targeted to be around 2.5V, the boost-converter and level-shifter consist of 2.5V I/O transistors. The overall voltage boosting efficiency is 96% with no-load and 65% when peak current is driven by regulators, the drop being due to the resistive losses by switches in the conduction path.

3.2.3 Regulators, reference-generators, back-scattering, and voltage-limiters

The output voltage of the boost-converter ($4V_S$) is provided to three regulators, each of which is designed as shown in Fig. 3.10 (b). It consists of a single-stage amplifier with a feedback loop to regulate the output node [17]. Each regulator has a different value of the reference voltage (V_{REF}) and R_1/R_2, depending on the desired output voltage. The sensor regulator provides 2.5V and a peak current of 2mA for ≈1ms to the sensor during measurement phase, which is the most power hungry phenomena. It consists of an external 100uF capacitor for energy storage to avoid a significant drop in the output voltage when 2mA of load current is driven. The sensor can function reliably down to 1.8V, which gives enough time for the capacitor to charge back to 2.5V. The analog and digital regulators provide 1V and 0.5V to the entire Chip, respectively.

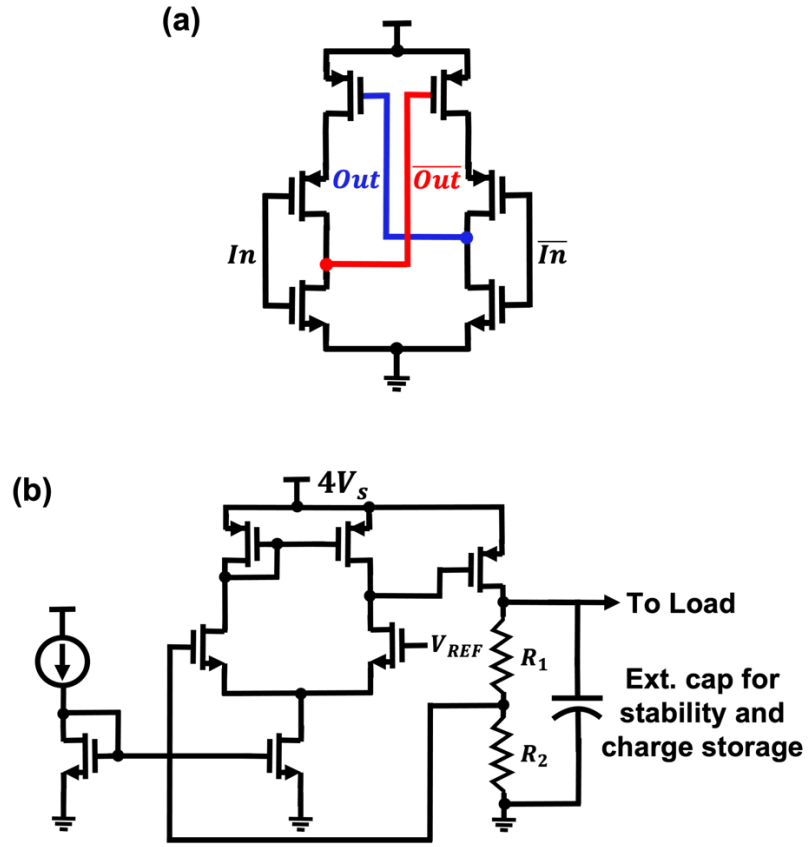

Fig. 3.10: Circuit schematics of (a) a single level-shifter block; and (b) regulator using external capacitor.

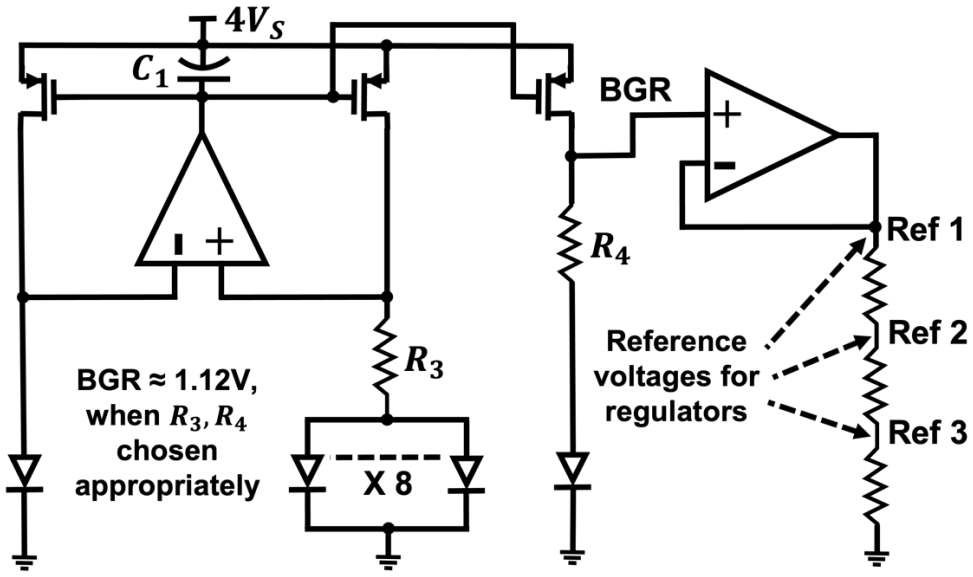

Fig. 3.11: Circuit schematic of the bandgap voltage reference generator.

The reference voltages for regulators are derived from the bandgap reference generator (BGR) and a resistive divider, as shown in Fig. 3.11. The values of R_1 and R_2 are 10MΩ and 120MΩ, respectively, which result in a BGR output ≈ 1.12V, independent of the supply voltage and temperature [18].

The back-scatter modulator shorts the rectifier's output with the boost-converter's input during normal mode of operation, without causing any power loss. In the transmit mode, it performs Load-Shift-Keying at the rectifier's output, based on the digital data stream to be transmitted. This results in modulation of the reflected RF signal on the inductor coil, which is decoded externally to extract the data.

Voltage limiters are connected at RF inputs to clamp the voltage to 1.2V, which prevents over-stressing of the front-end transistors. Implementation details of the back-scatter switch and voltage limiters are described in [19].

3.2.4 Start-up circuit

Since the rectifier has self-startup capability, it does not require any auxiliary circuit during the initial transient. However, for a target input (V_S) of ≈ 600mV to the boost-converter, its complementary PMOS switches fail to perform self-startup. This is because during the initial rising phase of the entire PMU, the supply voltage of oscillator in Fig. 3.9 is 0V since it is the output of digital-regulator. For the regulator voltage to rise, the boost-converter's output has to rise, which does not happen sufficiently enough (stops at ≈ 300mV) in the absence of clock, thus creating a global deadlock. To bring the PMU out of this initial-zero condition, the supply voltage of oscillator is switched such that when lower than an on-chip reference of 400mV, it gets supplied by the rectifier's DC output. This bypasses the regulators' output during startup and causes the boost-converter's output to rise, thus bringing the PMU out of deadlock. The level-shifters, which provide NOL waveforms to the clock-drivers, are

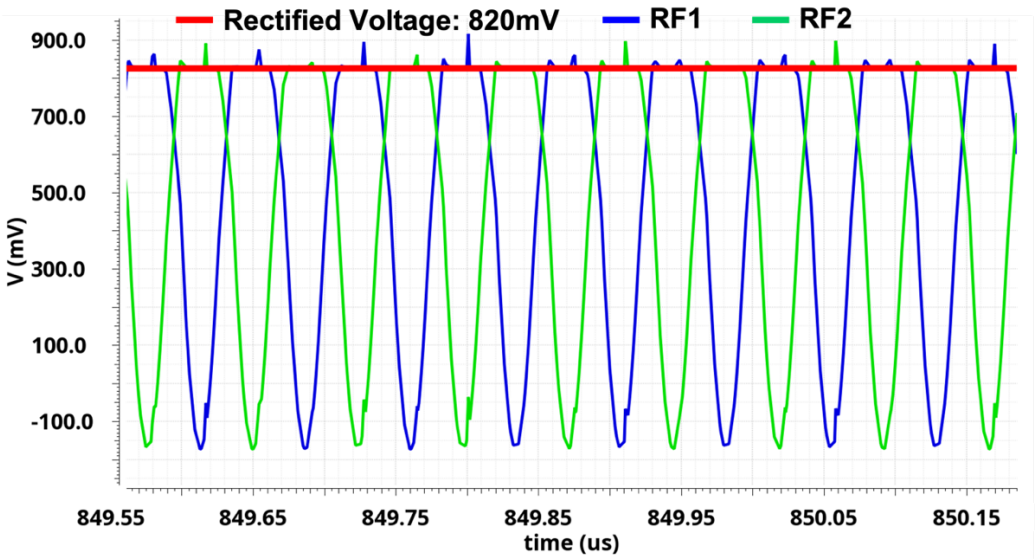

Fig. 3.12: Input RF voltages (13.56MHz) to rectifier and output DC voltage.

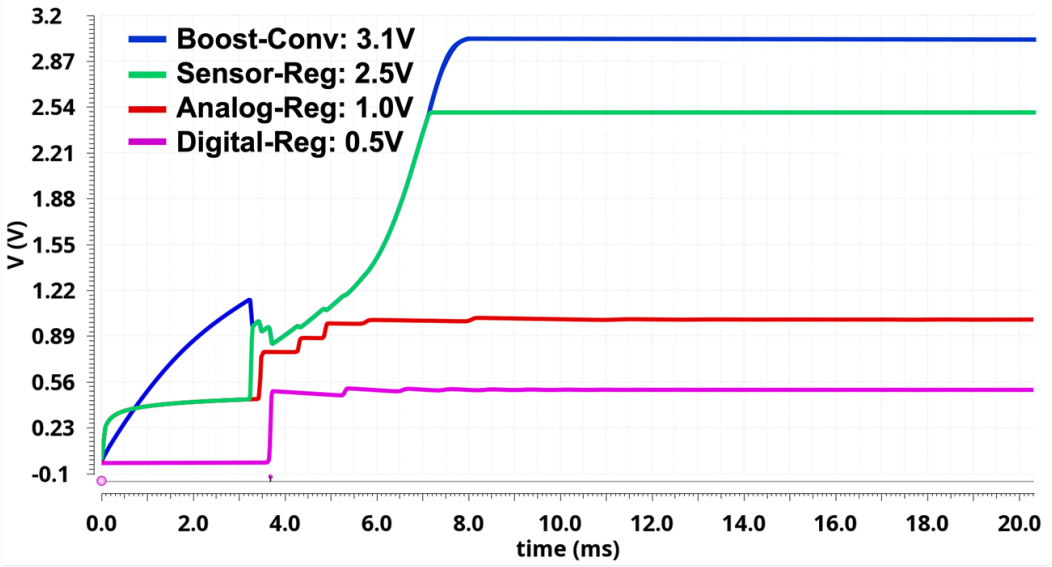

Fig. 3.13: Output voltages of boost-converter and the three regulators.

also supplied initially with the rectifier's output and later switched to regulated outputs, thus kick-starting the PMU.

Since the Chip was designed for a conservative scenario with the rectifier input of ≈ 800mV_{pp}, the analog and digital regulators were also supplied with boost-converter's

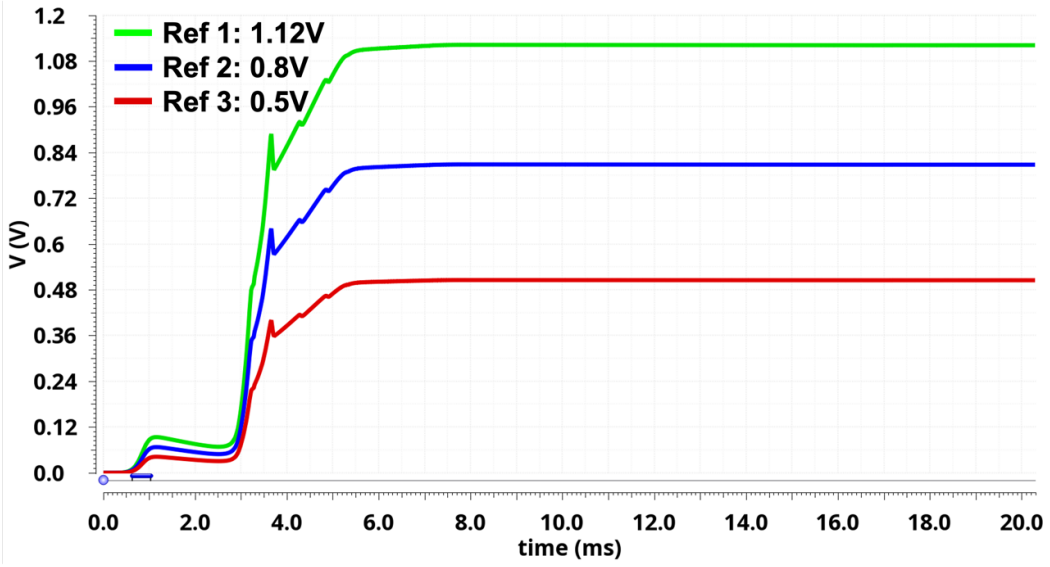

Fig. 3.14: Output voltage of the BGR circuit and the derived reference voltages.

output. However, owing to the high efficiency of the wireless power-transfer link and the PMU front-end, $1.2V_{pp}$ was easily generated at the rectifier's input during testing, producing 1V DC at its output. This is sufficient to supply the analog and digital regulators, which can instead be connected directly to the rectifier's output and reduce loading of the boost-converter. This would also eliminate the initial global-deadlock. Voltage boosting is essential only for the sensor-regulator which needs to provide 2.5V to the sensor. The entire PMU is simulated with $1V_{pp}$ 13.56MHz RF input, which is converted to 820mV DC by the rectifier (Fig. 3.12). The boost-converter produces 3.1V, which is given to the voltage and current reference generators, and the regulators (Fig. 3.13). The three outputs of BGR, shown in Fig. 3.14, serve as V_{REF} for the three regulators.

3.2.5 RF wake-up (RFW)

The ping signals for reset and wake-up are transmitted as Amplitude-Shift-Keying signals on top of a 13.56MHz carrier. An envelope detector (ED) at the front-end of RFW detects the presence of low-level zero signal on the carrier (Fig. 3.15). The ED

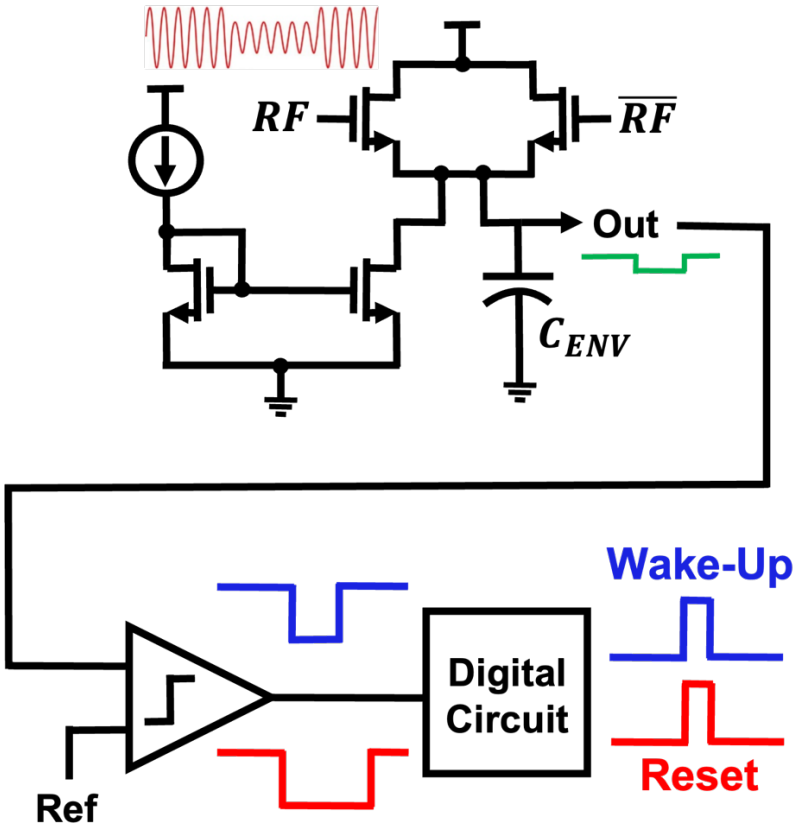

Fig. 3.15: Overview of the RF wake-up block.

is implemented as a source-follower topology, biased at 10nA and C_{ENV} = 25fF, such that it can separate the low-frequency message signal from the high-frequency carrier. The reset signal is a 50µs long pulse of zeros whereas wake-up is 25µs long. Both the zero-lengths are sufficiently short to not affect the wireless power transfer (WPT) efficiency. The output of ED is only 200mV_{pp} for a 1V_{pp} modulated RF signal, which is quite low for the digital circuit block to process. A comparator stage is thus added to convert the ED's output rail-to-rail. This is fed to a digital decoder circuit which compares the zero-length with pre-set thresholds to decode reset/wake-up unambiguously. The final decoded signals are sent to the DAU.

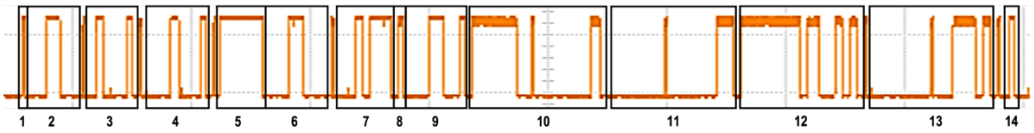

1. Start condition.
2. Sensor address (0001100) with write mode bit (0): 00011000. This allows values to be written on SDA by the chip.
3. Control register (21H) address: 00100001. Value written into this register makes the sensor go into measurement mode with different settings.
4. Control register value: 00010001. This sets the sensor to do a single measurement in low power mode.
5. Measurement phase. When this gets over, ODINT pin it pulled down by the sensor and the chip is notified.
6. The sensor now has to read the measured data. For that, it first has to go into write mode to write the data register value on SDA. Hence, 00011000 again.
7. Data register (17H) address: 00010111. This stores 64 bit data: 1st 16 are status bits, next 16 are Z data, then Y and then X data. All data values are vectors with first bit being the sign bit.
8. Start condition for read operation.
9. Sensor address with read mode bit (1): 00011001. This allows values to be read from SDA by the chip.
10. 16 bits of status register. The last bit being 1 signifies that data is stored successfully from the measurement and is ready to be read.
11. 16 bits of Z field data.
12. 16 bits of Y field data.
13. 16 bits of X field data.
14. Stop condition.

Fig. 3.16: Complete digital data-flow from the Chip to the sensor, captured from SDA line.

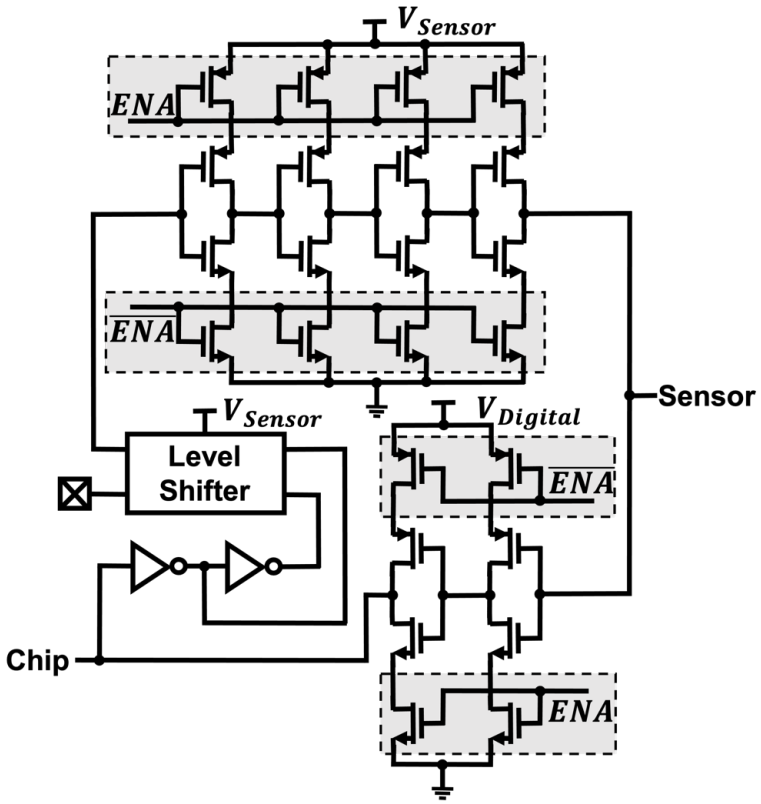

Fig. 3.17: Circuit schematic of the bidirectional level-shifter used for SDA.

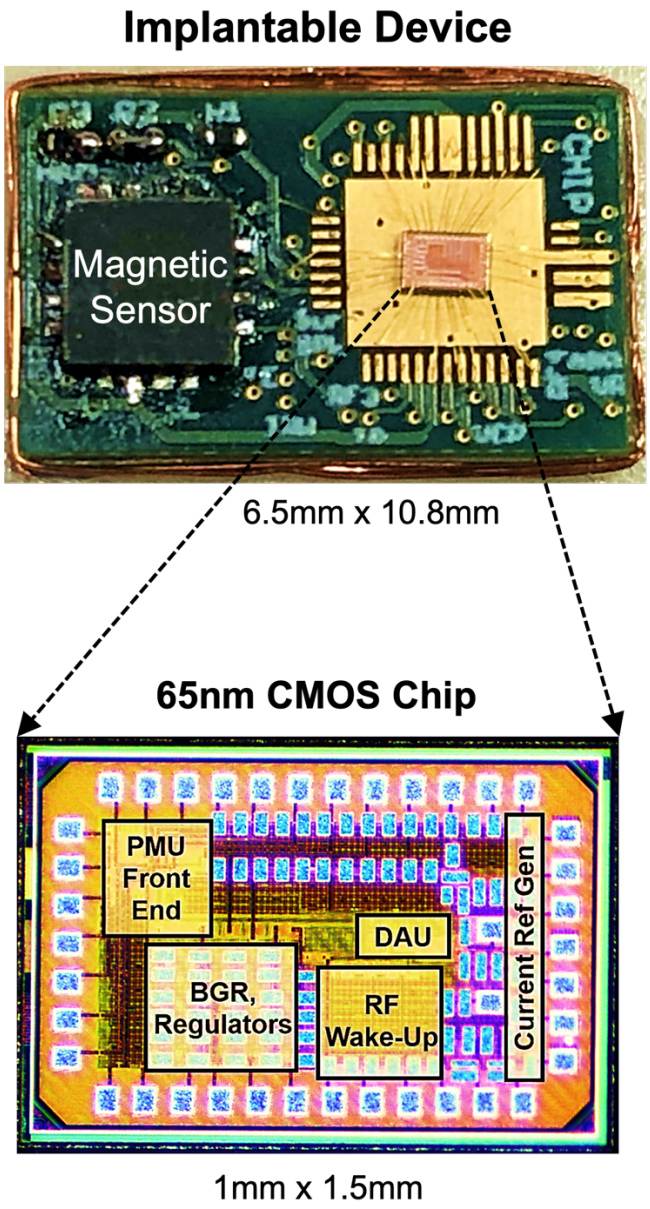

Fig. 3.18: The assembled implantable device and the fabricated 65nm CMOS chip.

3.2.6 Data acquisition unit (DAU)

The DAU forms the interface between the Controller-Chip and the external magnetic sensor. It consists of 2 major digital circuit blocks—Sensor Interface (SI) and I2C block. The digital clock is derived from the ring-oscillator discussed before. The I2C

block is at the front-end of interface with the sensor and provides the serial-clock (SCL) and serial-data (SDA) interconnections, as shown in Fig. 3.4. To begin magnetic field measurement by the sensor, a wireless reset is first sent to the Chip, which is decoded by the RFW and serves as a global reset. The wake-up signal triggers a measurement phase, during which the SI block provides all the required digital bits. After a measurement interrupt occurs, the I2C block reads the 16-bit long data stream for each of X, Y, and Z from the SDA line and sends to the back-scatter modulator for transmission. A detailed digital flow of the complete measurement and communication phase is shown in Fig. 3.16.

The unidirectional interfaces with the sensor (SCL, reset and interrupt) require a one-way level-shifter, implemented as Fig. 3.10 (a). However, the SDA is bidirectional, requiring data flow from the Chip to the sensor and vice-versa. To achieve that, a bidirectional level-shifter is designed as shown in Fig. 3.17. When the ENA signal is low (logic 0), data flow is from the Chip to the sensor, after appropriately level shifting the 0.5V Chip signal to 2.5V sensor signal. When ENA is high (logic 1), the data flow is opposite, which can be handled by a simple buffer with supply voltage of $V_{Digital}$. The digital codes for I2C and SI blocks are written in Verilog and synthesized using standard cells in 65nm CMOS process.

The prototype implantable device is assembled on an FR4 PCB measuring 10.8mm × 6.5mm (Fig. 3.18). The 3D magnetic sensor and Controller-Chip are placed on top and all the capacitors for regulators, rectifier, boost-converter and inductor resonance, are placed on the bottom of PCB. The Chip measures 1.5mm × 1mm and is fabricated in 65nm CMOS process. The secondary inductor coil is wound along the PCB edges. When the device is used as an actual implant in a surgical space, it would need to be encapsulated by poly-dimethyl siloxane (PDMS) and sealed hermetically. The device functionality is unaffected by such encapsulation.

3.3 Electromagnetic gradient-generating coils

A simplified view of the magnetic field gradients used for encoding the device location is shown in Fig. 3.19. Three devices D_1, D_2, and D_3 are located in the FOV. To localize the devices along the X-axis, a monotonically varying magnetic field B_X is generated that has a gradient in its *total magnitude* along the same axis. The gradient ensures that no two points along the axis have the same value of the magnetic field magnitude. This implies that the relationship described by Eq. (3.5) holds

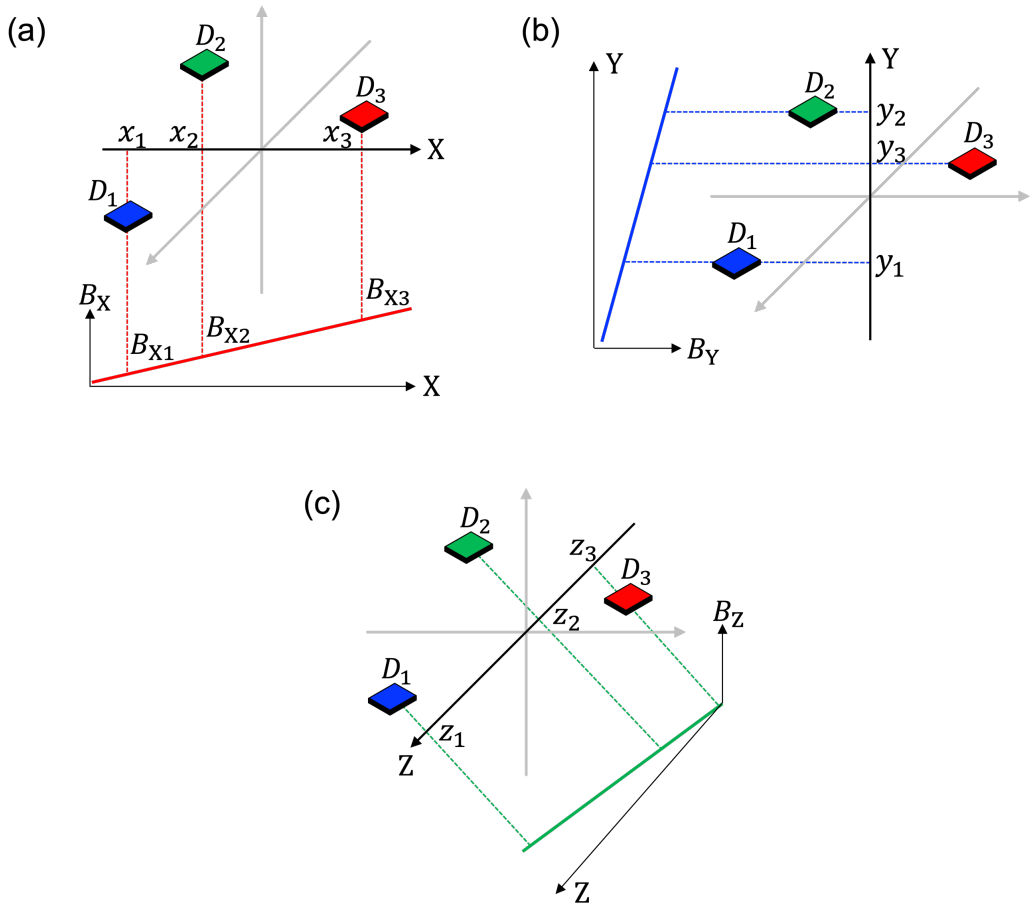

Fig. 3.19: Conceptual overview of 3D localization of devices $D_1 - D_3$. (a) For the X-direction, a monotonically varying magnetic field is created to result in a field gradient. Each device measures the total field magnitude at its location, which is unique for each point along the X-axis. This process is repeated for localization in (b) Y and (c) Z direction.

between the magnitude of the field measured by the three devices, denoted by B_{X1}, B_{X2}, and B_{X3}, as shown in Fig. 3.19 (a). The three orthogonal components of the field ($\hat{x}B_X, \hat{y}B_X, \hat{z}B_X$) measured by each device, are used for computing the field magnitude at the device's location, as described in Eq. (3.6).

$$\|B_{\mathrm{X1}}\| < \|B_{\mathrm{X2}}\| < \|B_{\mathrm{X3}}\| \tag{3.5}$$

$$\left\|B_{\mathrm{X}i,\ i=1,2,3}\right\| = \sqrt{(\hat{x}B_{\mathrm{X}i})^2 + (\hat{y}B_{\mathrm{X}i})^2 + (\hat{z}B_{\mathrm{X}i})^2} \tag{3.6}$$

For the X-dimension, since the magnetic field B_X has a net gradient in its magnitude along the X-axis, G_X is defined as the derivative of $\|B_{\mathrm{X}}\|$ with respect to x, as given by Eq. (3.7).

$$\mathrm{X-Gradient} = G_{\mathrm{X}} = \partial\|B_{\mathrm{X}}\|/\partial x \tag{3.7}$$

Similarly, to localize the devices along the Y and Z axis, a monotonically varying magnetic field is generated that has a gradient along the same axis, and the corresponding field magnitude is measured by the devices (Fig. 3.19). Using the field measurements along the three orthogonal axes, the complete 3D position of all the devices can be decoded unambiguously. Since the gradient manifests in the *magnitude of the magnetic field* along each axis, this localization technique is immune to potential inaccuracies caused by device misalignment and orientation mismatch relative to any specific coordinate system. As the orientation changes, the measured individual field components might change from those in Eq. (3.6), but the overall magnitude remains the same, thus reinforcing Eq. (3.5). This is also evident from Eq. (3.2), as the sensor may have its relative coordinates of $\hat{\imath}, \hat{\jmath}, \hat{k}$ different from the $\hat{x}, \hat{y}, \hat{z}$ in Eq. (3.6), but the magnitude remains unchanged.

3.3.1 Gradient coils design specifications

The gradient required along each axis is described by Eq. (3.7). Special emphasis needs to be paid to the magnitude function since it implies that all three orthogonal components of the vector field contribute to the gradient. It would be ideal to have a single field polarization, suitably in $\hat{z}$, that could produce a field gradient along the required axis of either X, Y, or Z. However, such a field is not a solution of Maxwell's equations and thus cannot be produced by a real field-generator. The problem is compounded by the flatness requirement of the field-generator, which rules out volume-enclosing architectures used in closed-bore cylindrical MRI scanners. Summarizing all the crucial specifications governing the design of our electro-magnetic gradient coils: (i) completely planar coils that can easily slide beneath the patient's bed to ensure no inhibition to the surgeon's movement from the top; (ii) enhanced FOV to allow sufficient room for surgical navigation and alignment; (iii) high gradient strength G to achieve high resolution; (iv) high current efficiency to make the maximum use of current drawn by the gradient coils; (v) low coil-length to have less inductance (for fast switching) and less resistance (for lower heating); and (vi) absence of bulky permanent magnets producing a strong magnetic field, due to their incompatibility and safety issues with nearby metals [20],[21].

The gradient coil efficiency η is defined as the ratio of the magnetic field gradient (G) produced by the coil to the current drawn (I). To study and confirm the magnetic field profiles and the gradients generated by the coils, static magnetic field simulations were carried out in a magneto-static software Radia. The geometrical design parameters of the coils were also optimized in Radia. The target FOV was initially set to be 15x15x10cm^3. The value of G discussed in the following sections is the average value, in order to keep the DC current selection straightforward. The magnetic field notations used in this work are described below. Field vectors generated by each coil with their components along the three orthogonal axes:

$$\begin{matrix}\mathrm{X}-\mathrm{Coil}\\ \mathrm{Y}-\mathrm{Coil}\\ \mathrm{Z}-\mathrm{Coil}\end{matrix}\begin{bmatrix}B_{\mathrm{X}}\\ B_{\mathrm{Y}}\\ B_{\mathrm{Z}}\end{bmatrix}=\begin{bmatrix}\hat{x}B_{\mathrm{X}} & \hat{y}B_{\mathrm{X}} & \hat{z}B_{\mathrm{X}}\\ \hat{x}B_{\mathrm{Y}} & \hat{y}B_{\mathrm{Y}} & \hat{z}B_{\mathrm{Y}}\\ \hat{x}B_{\mathrm{Z}} & \hat{y}B_{\mathrm{Z}} & \hat{z}B_{\mathrm{Z}}\end{bmatrix}. \tag{3.8}$$

X-Coil's (similarly others) field plotted along different axes:

$$\begin{bmatrix}\hat{x}B_{\mathrm{X}(x)} & \hat{x}B_{\mathrm{X}(y)} & \hat{x}B_{\mathrm{X}(z)}\\ \hat{y}B_{\mathrm{X}(x)} & \hat{y}B_{\mathrm{X}(y)} & \hat{y}B_{\mathrm{X}(z)}\\ \hat{z}B_{\mathrm{X}(x)} & \hat{z}B_{\mathrm{X}(y)} & \hat{z}B_{\mathrm{X}(z)}\end{bmatrix}. \tag{3.9}$$

where $\hat{z}B_{X(y)}$ denotes the Z-component of the X-Coil's vector field B_{X}, plotted along the Y-axis.

3.3.2 Z-gradient coil

The generation of Z gradient is relatively simpler than that of X and Y. This is because the magnetic field strength produced by a coil decreases monotonically as the distance from the surface is increased, irrespective of the coil geometry. Hence, to create a Z-axis gradient in the magnetic field magnitude, a planar circular coil carrying current in a counter-clockwise direction suffices, as shown in Fig. 3.20. The center of the coil produces a magnetic field pointing upward. The field magnitude ($\|B_Z\|$) thus generated along the Z-axis is plotted in Fig. 3.20 for varying values of X at Y=0. Since the coil is symmetric about X and Y, an identical plot is obtained while varying the Y-coordinate at X=0. The 10cm Z-FOV is plotted from 1cm above the coil surface, to a height of 11cm. The gradient strength G is 46mT/m at X=0, reaches a maximum of 67mT/m at X=$\pm$5cm, and comes down to 48mT/m at X=$\pm$10cm, thus ensuring G > 30mT/m over a span of 20cm along the X-axis (same along the Y-axis). The DC current used in the Z-Coil is 12.5A, which results in an average value of η to be 4.3mT/m/A. The 10cm cavity at the center of the Z-Coil is particularly important when the coil's field is used for enhancing the X and Y

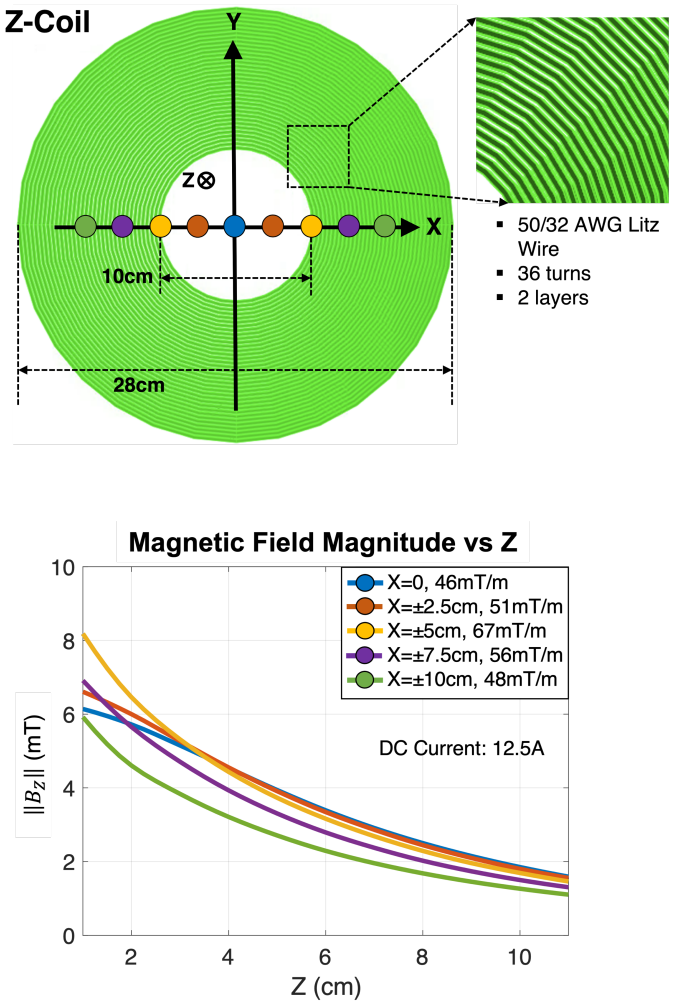

Fig. 3.20: Z-Coil (top). Measured magnetic field magnitude $\|B_Z\|$ along the Z-axis (bottom), plotted for different values of X (at Y=0).

gradients' FOV, as discussed in the following section. It also enhances the linearity of the Z-Coil's field magnitude, which is more exponential in the absence of the cavity.

3.3.3 X-gradient coil

In order to create a gradient in the magnetic field along the X-direction using planar electromagnetic coils, the most common technique is to place two identical coils,

carrying currents in opposite directions, right next to each other [22]. The prototype X-Coil designed in this work is shown in Fig. 3.21. The physical coil-span should be higher than or equal to the required FOV of 15cm, which is the reason for designing the coil with a 30cm span along the X-axis. The clockwise current-carrying half (left) produces a magnetic field B_X that has a Z-component ($\hat{z}B_X$) pointing into the plane, denoted by negative values. The counter-clockwise current-carrying half (right) produces $\hat{z}B_X$ pointing out of the plane, denoted by positive values. This creates a monotonically varying Z-component in B_X along the X-axis, i.e., $\hat{z}B_{X(x)}$, between the centers of the two coils, as shown in Fig. 3.22 (a). The elongation of the two spirals of the X-Coil is kept to be 15cm so as to keep the X-gradient homogenous across the required Y-FOV. The Y-Coil is designed identically to X, but rotated by 90º to align the gradient along the Y-axis.

Generating a gradient in the Z-component of B_X is not sufficient for the localization shown in Fig. 3.19. As described by Eqs. (3.5)–(3.7), the *magnitude* of the magnetic field needs to be monotonically varying, which implies that the gradient should manifest in $\|B_X\|$. Fig. 3.21 shows $\|B_X\|$ generated by the X-Coil and plotted along the X-axis. The highly non-linear nature of this plot is due to the following reasons: (a) the addition of non-zero and non-linear X and Y components ($\hat{x}B_X$ and $\hat{y}B_X$) to $\hat{z}B_X$, (b) non-linearity of the magnitude function, which flips the negative half of the field to result in an even-function centered at X=15cm. In order to circumvent this problem, one possible solution, as employed in MRI, is to have a significantly higher static background field B_0, which points in the Z-direction. Using $B_0 \geq 0.5$T, it is observed that $\|B_X\|$ is dominated by $\hat{z}B_X$ and the field profile closely resembles Fig. 3.22 (a). The high value of B_0 is necessary to suppress the contributions from the non-linear and undesirable $\hat{x}B_X$ and $\hat{y}B_X$, and to provide a high positive offset to $\hat{z}B_X$ which can accentuate its value in the field magnitude plot. However, generating B_0 of such a high value defeats the purpose of this work since it requires either a strong and bulky permanent magnet, or electromagnets carrying very high DC currents. We employ a different technique, described in the following section, for creating the

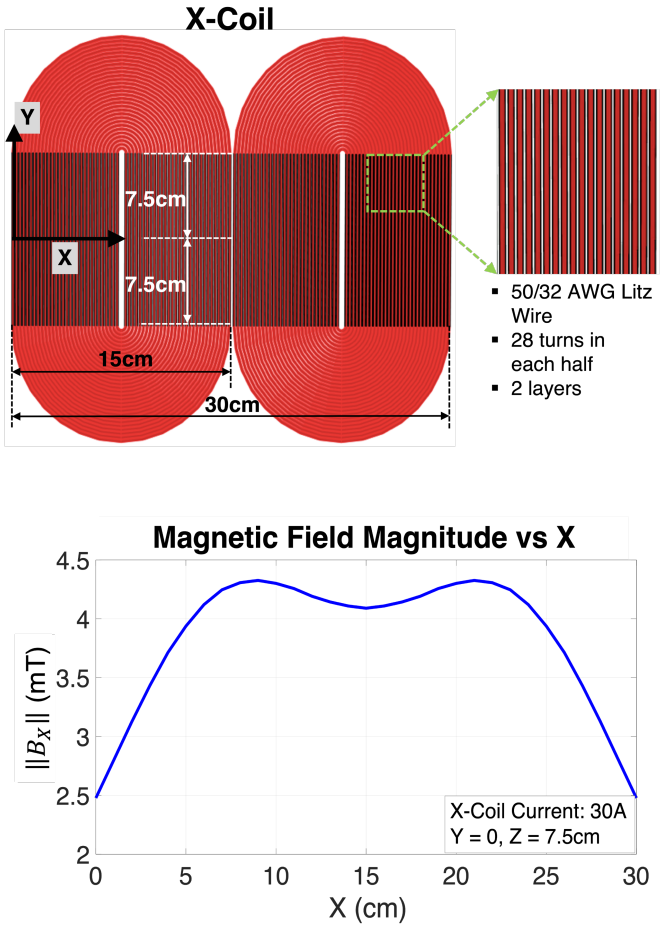

Fig. 3.21: X-Coil consisting of two spirals placed next to each other (top). Measured magnetic field magnitude $\|B_X\|$ along the X-axis (bottom).

required gradient in $\|B_X\|$ along the X-axis, while achieving a sufficiently high X-FOV.

3.3.4 X and Y FOV enhancement

The non-zero magnetic field components of the X-Coil along the X-axis (at Y=0, Z=7.5cm), denoted by $\hat{z}B_{X(x)}$ and $\hat{x}B_{X(x)}$, are shown in Fig. 3.22 (a) and (b), respectively. Combining these two gives a highly non-linear magnitude plot for $\|B_X\|$, as was shown in Fig. 3.21. The Z-Coil's field is then evaluated in more detail.

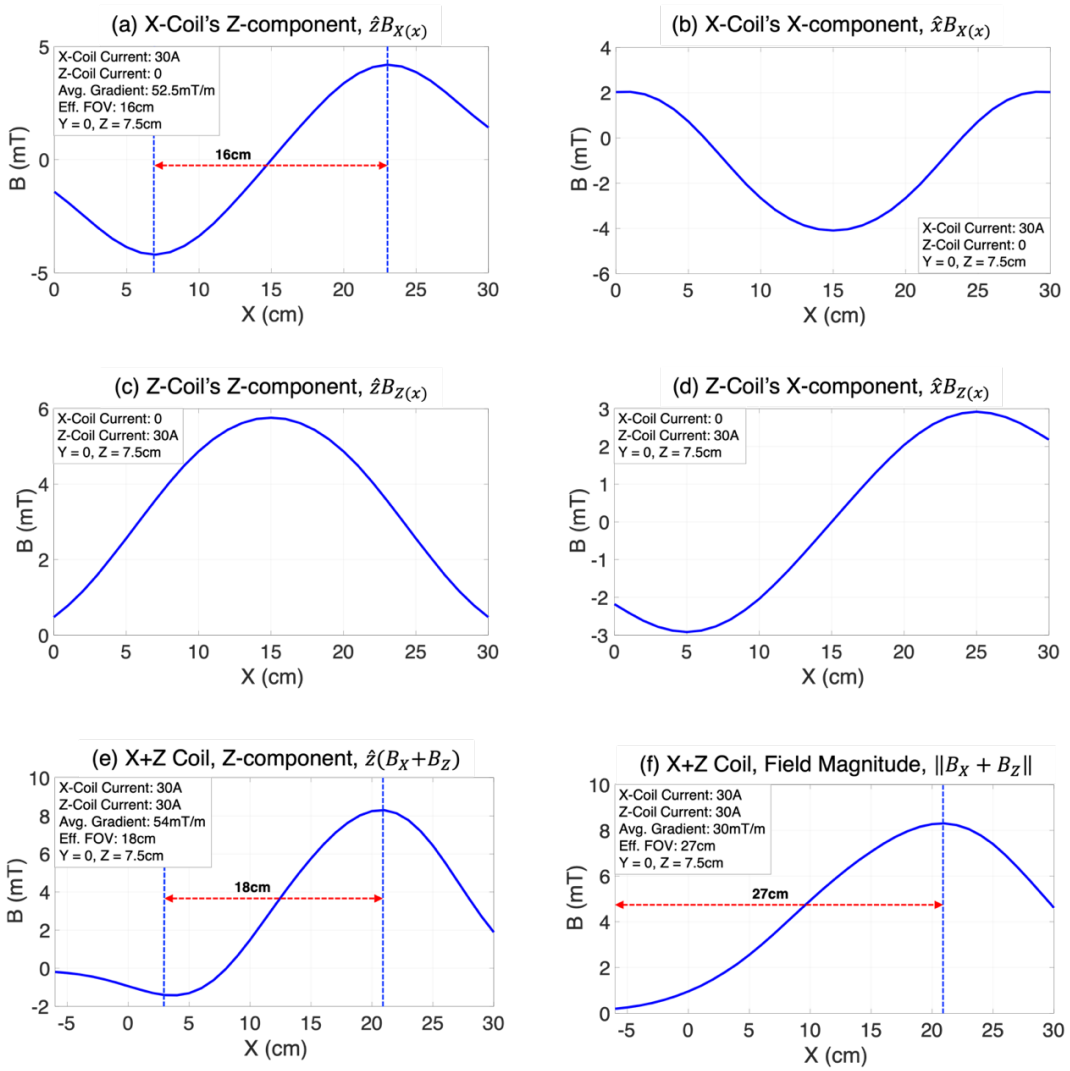

Fig. 3.22: Achieving magnetic field gradient along the X-axis. (a) Simulated Z-component and (b) X-component of X-Coil's magnetic field along the X-axis. (c) Z-component and (d) X-component of Z-Coil's magnetic field plotted along the X-axis. (e) Z-component and (f) complete magnetic field magnitude when both X and Z coils are on together.

The non-zero magnetic field components produced by the Z-Coil along the X-axis (at Y=0, Z=7.5cm), are $\hat{z}B_{Z(x)}$ and $\hat{x}B_{Z(x)}$, as shown in Fig. 3.22 (c) and (d) respectively. The strictly positive and monotonic nature in either half of $\hat{z}B_{Z(x)}$ makes it an appropriate candidate for offsetting the negative half of $\hat{z}B_{X(x)}$. Additionally, $\hat{x}B_{Z(x)}$ exhibits a highly linear behavior from 5cm to 25cm, the

predominant region of non-linearity in $\hat{x}B_{X(x)}$, indicating that a superposition of the two would be relatively more linear than the latter alone.

The Z-Coil is then positioned right beneath the X-Coil and both are turned on simultaneously. The resulting magnetic field profile along the X-axis is plotted in Fig. 3.22 (e) and (f). Fig. 3.22 (f) highlights that the magnitude of the resultant magnetic field produced by the coil combination, when plotted along the X-axis, is strictly positive *and* monotonic from -6cm to 21cm, generating an effective FOV of 27cm and displaying high linearity. The negative position coordinates simply imply that the region is beyond the physical location of the coils. Compared to the physical horizontal-span of the X-Coil (30cm), the X-FOV measures 27cm with this new combination, yielding an effectively useful coil-span of 90%. For off-center regions where Y≠0, the Y-component of the X and Z coils is also present and contributes to the magnitude of the field generated by the two coils. Nonetheless, the qualitative nature of the field profile resembles Fig. 3.22 (f) in all the cases, as discussed below.

3.3.5 Gradient variation in FOV

To evaluate the homogeneity of the X-gradient resulting from employing both the X and Z coils in tandem, the gradient profile is studied for a varying range of Y-coordinates. In Fig. 3.23 (a), the field magnitude generated by only the X-Coil is plotted along the X-axis, while varying Y from -10 to 10cm and keeping Z=7.5cm. Next, in Fig. 3.23 (b), the field magnitude generated by only the Z-Coil is plotted along the X-axis, while varying Y from -10 to 10cm and keeping Z=7.5cm. Due to the circular nature of the Z-Coil, its field magnitude (along X-axis) is non-homogenous across Y-coordinates, with the center (Y=0) having the highest field gradient that gradually falls as Y is increased to ±10cm. This effect also manifests in the field profile when both the coils are turned on simultaneously, the magnitude of which is plotted in Fig. 3.23 (c) for Y from -10 to 10cm and Z=7.5cm. The gradient G reduces monotonically from 37mT/m at Y=0 to 24mT/m at Y=±10cm, while

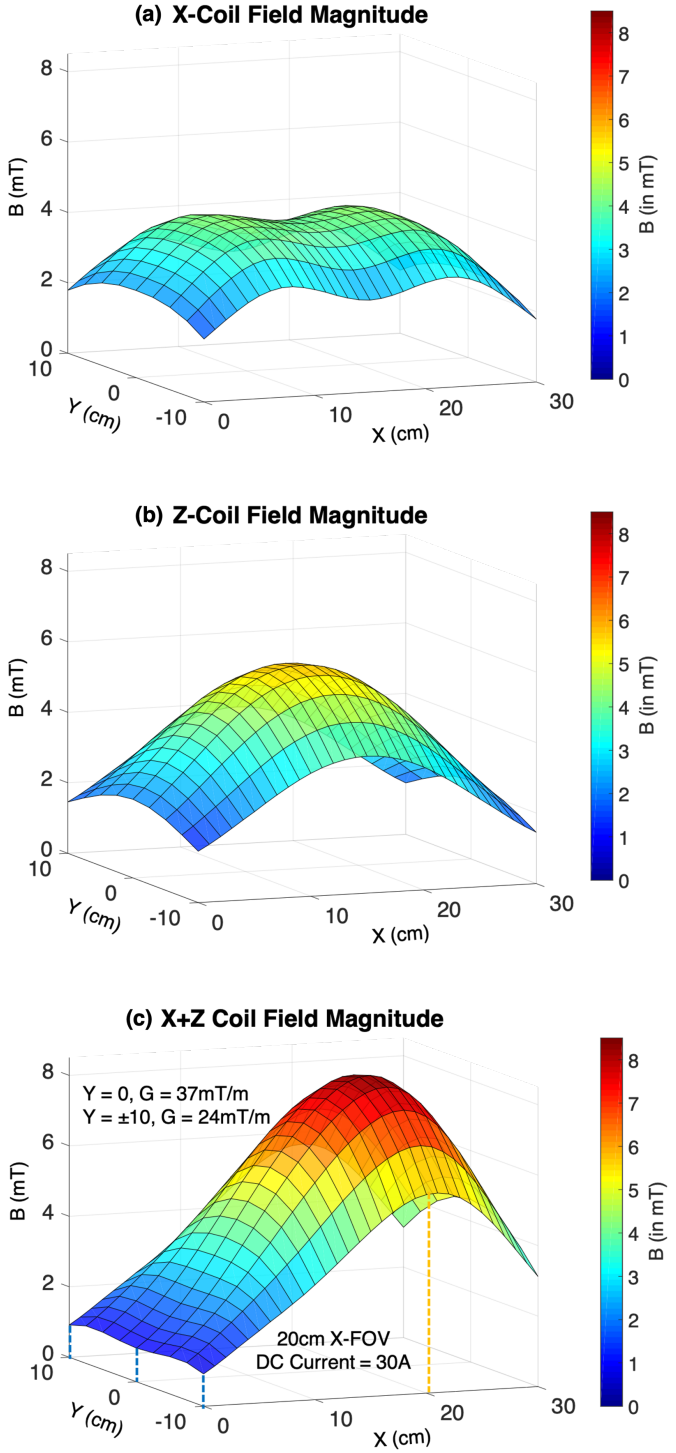

Fig. 3.23: Measured magnetic field magnitude when (a) only X-Coil is on, (b) only Z-Coil is on, and (c) both X and Z coils are on simultaneously. The Y-coordinate is varied from -10 to 10cm with Z=7.5cm. Gradient *G* in (c) attains the highest value at Y=0 (center) and gradually decreases at Y=±10cm.

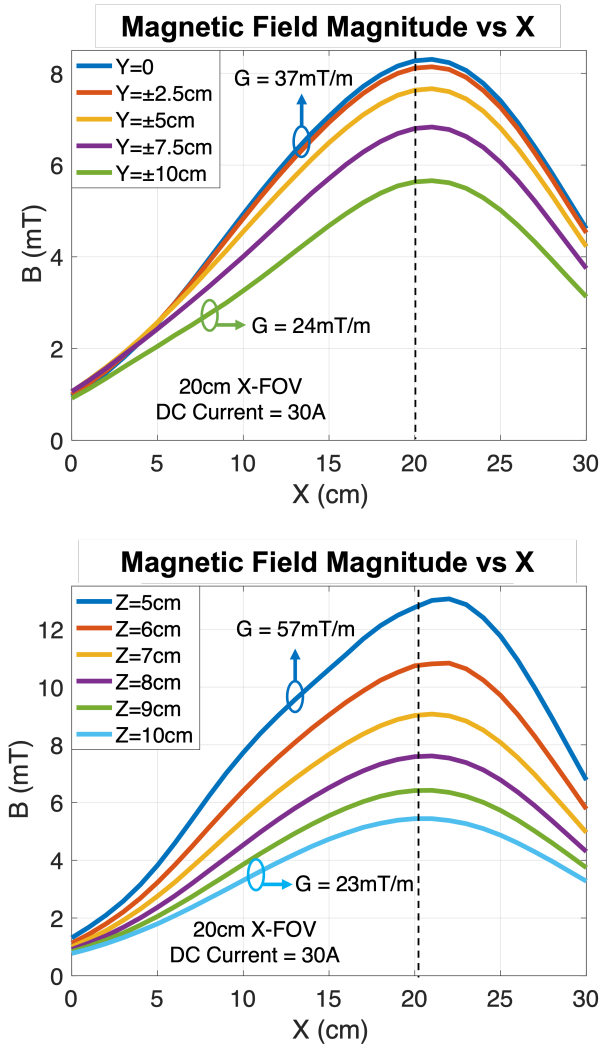

Fig. 3.24: X gradient variation as the Y coordinate is varied (top) and Z coordinate is varied (bottom).

maintaining a 20cm X-FOV throughout. Similarly, the value of *G* reduces monotonically as the Z-coordinate is increased (57mT/m at Z=5cm, Y=0, to 23mT/m at Z=10cm, Y=0), which is expected because the field strength falls as the height from the coil-surface is increased, irrespective of the coil-geometry. 2D gradient variation plots are shown in Fig. 3.24.

This implies that for a given sensor resolution in Eq. (3.1), the obtained position resolution would be higher as the devices move closer to the center of the FOV spanning 20x20x10cm^3 in X, Y, and Z, respectively, as the gradient *G* is higher in the center-region. To improve the position resolution obtained at the boundary planes of the FOV, either the DC current in coils should be increased (resulting in a stronger gradient), or the sensor resolution should be higher. Keeping the maximum current as 30A in this work, we employ the sensor in low-noise mode towards the boundary planes where the gradient strength is <30mT/m. In the low-noise mode, the sensor has a resolution of 1μT, requiring only 10mT/m to achieve 100μm of position error. However, the current consumption in low-noise mode is 2.2mA for 850μs, compared to 1.5mA for 250μs in the low-power mode (3μT). With the extra power penalty on the sensor side, the desired position resolution of 100μm can be achieved in the entire FOV. This is the primary reason for designing the PMU and other circuit blocks in the Controller-Chip with very high efficiency—to wirelessly send comparatively higher power to the sensor when operated in the low-noise mode.

Extending the same principle to Y-gradient, both the Y and Z-Coils are turned on simultaneously for a monotonic Y-FOV. Similar to X, this also leads to a 27cm long Y-FOV with a highly homogenous, monotonic and linear magnetic field profile. Since the 30A of DC current is sufficient to ensure a gradient strength of ≥10mT/m at all the boundary planes of a 20x20x10cm^3 volume, we restrict the FOV to points inside this volume. Each point inside the FOV corresponds to a unique set of magnetic field values obtained from the three orthogonal gradients, as summarized by the following equations:

Magnetic field during X-gradient (X + Z-Coil On):

$$\|B_X + B_Z\| = \sqrt{(\hat{x}B_{\mathrm{X}} + \hat{x}B_{\mathrm{Z}})^2 + (\hat{y}B_{\mathrm{X}} + \hat{y}B_{\mathrm{Z}})^2 + (\hat{z}B_{\mathrm{X}} + \hat{z}B_{\mathrm{Z}})^2} \qquad (3.10)$$

Magnetic field during Y-gradient (Y + Z-Coil On):

$$\|B_Y + B_Z\| = \sqrt{(\hat{x}B_{\mathrm{Y}} + \hat{x}B_{\mathrm{Z}})^2 + (\hat{y}B_{\mathrm{Y}} + \hat{y}B_{\mathrm{Z}})^2 + (\hat{z}B_{\mathrm{Y}} + \hat{z}B_{\mathrm{Z}})^2} \quad (3.11)$$

Magnetic field during Z-gradient (Z-Coil On):

$$\|B_Z\| = \sqrt{(\hat{x}B_{\mathrm{Z}})^2 + (\hat{y}B_{\mathrm{Z}})^2 + (\hat{z}B_{\mathrm{Z}})^2}. \quad (3.12)$$

Another advantage of this technique is the utilization of the X and Y components of the magnetic field produced by the X and Z coils, as seen in Fig. 3.22. The magnetic field magnitude plotted in Fig. 3.22 (f) consists of contributions from the X and Y components as well, which are otherwise non-desirable and eventually wasted in MRI. Hence, our technique leverages the gradient coils to their maximum utilization by using *all* the field components produced by the X and Z coils, to yield a ≥ 90% usable FOV without using any additional resources.

3.3.6 Gradient coils assembly

The three gradient coils are assembled using a 50 stranded, 32 AWG Litz wire (50/32). Single-stranded equivalent AWG wires are not an appropriate choice here because of—(i) their mechanical rigidity, which makes them difficult to be cast into circular coils; and (ii) their increased resistance at high frequencies (during gradient switching) due to skin-effect. These factors make multi-stranded Litz wire an appropriate choice for the coils. The Z-Coil consists of 2 layers, each with 36 turns. Each elongated half of the X and Y coils consists of 2 layers, with 28 turns/layer. Finally, the three coils are stacked together concentrically to give a single planar structure with the X-Coil on top, Y-Coil in the middle, and Z-Coil on the bottom (Fig. 3.25). The complete coil-stack measures 30x30x1cm^3. Fig. 3.26 shows the fully assembled coils and Table-I lists their individual parameters.

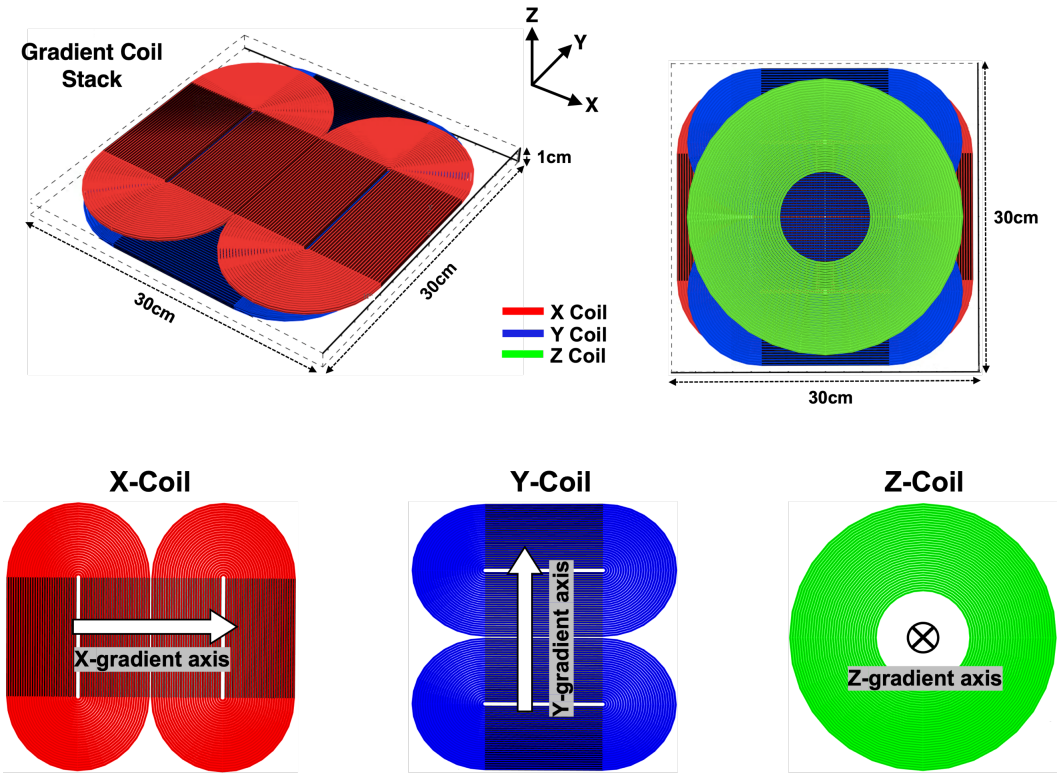

Fig. 3.25: Gradient coils stack showing the planar form factor of the assembled coils (top). Individual coils and their respective gradient axis (bottom).

For applications requiring bigger FOV, the physical dimensions can be correspondingly scaled for all the coils. More layers can be added to generate a proportionately higher FOV and/or gradient since the plots in Fig. 3.20 to Fig. 3.24 correspond to only two layers of windings for each of the coils. The DC current is another parameter for scaling the FOV vertically. With a DC current of 30A in both the X and Z coils, the average value of η for the X-gradient is 588μT/m/A. Heating of the coils is discussed in the following sub-section G. The field magnitudes plotted in Figs. 3.20, 3.21, 3.23, and 3.24 are all measured values during the characterization phase described in the next sub-section. Fig. 3.22 consists of simulated plots in Radia to show the individual components of the field and the intuition behind combining them in a specific order. The simulated and measured field profiles have an excellent agreement (<1% error).

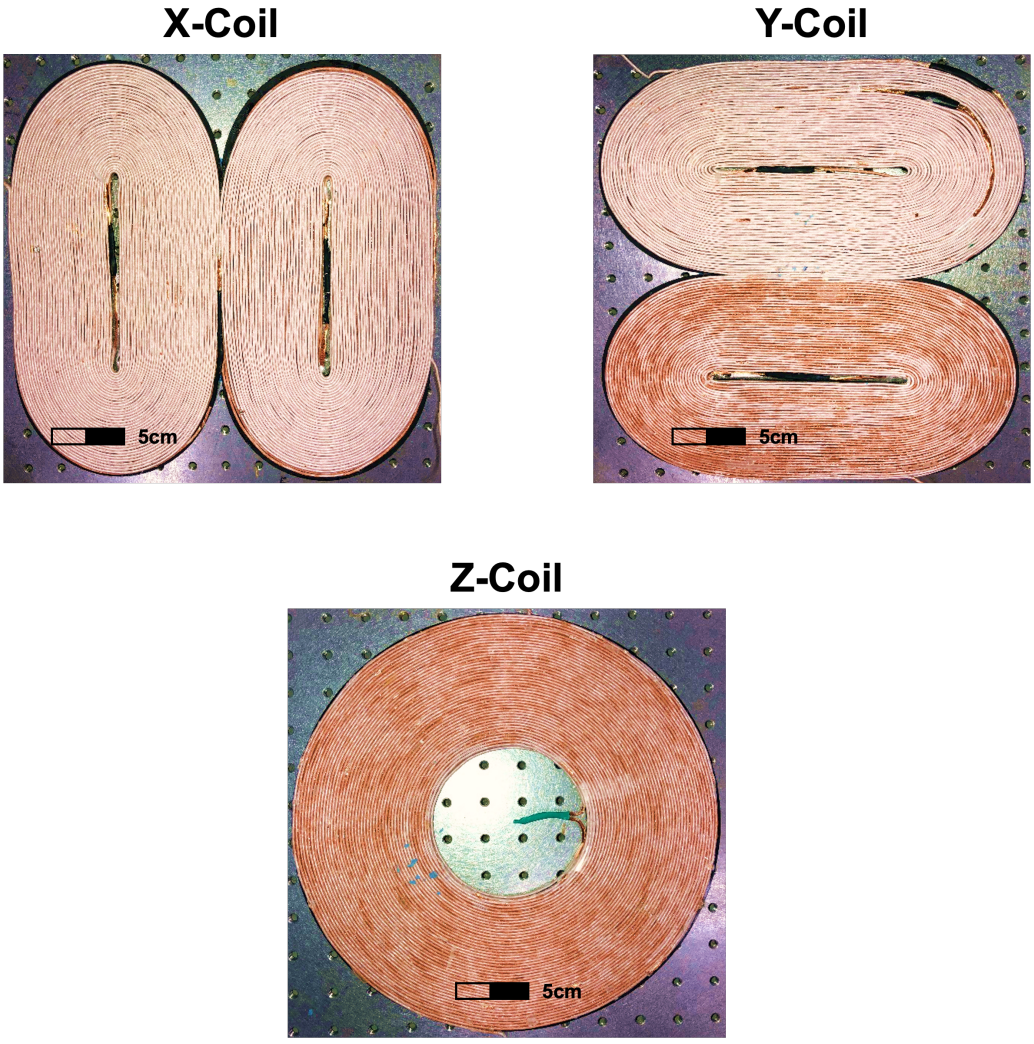

Fig. 3.26: Fully assembled X, Y, and Z coils using 50/32 AWG Litz wire.

Parameter	Z Coil	X & Y Coils
FOV Used	10cm	20cm
DC Current	12.5A	30A
Avg. η	4.3mT/m/A	588μT/m/A
Inductance	1.64mH	1.5mH
Resistance	1Ω	950mΩ

Table 1.1: Gradient coils specifications.

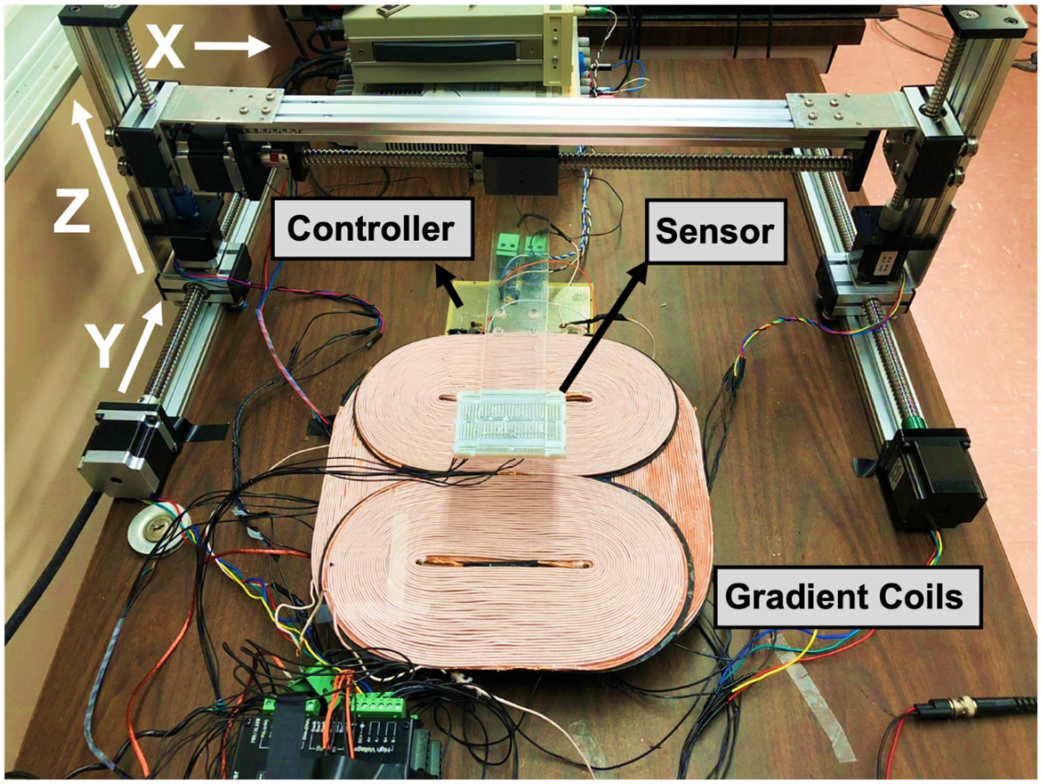

Fig. 3.27: Automated 3D-stage consisting of X, Y, and Z actuators for characterizing the FOV of gradient coils.

3.3.7 Gradient characterization in FOV

The FOV above the coil surface needs to be characterized by measuring magnetic field values and storing them in a lookup table (LUT), such that they can be retrieved for position decoding after measurements by the device. For robotically wound coils with consistent spacing between the turns, it is possible to model them accurately in Radia. Thereafter, the magnetic field at 100µm (or lower) increments in the 20x20x10 cm^3 FOV can be measured by simulations in Radia and stored in the LUT. The increment step should be at least equal to or less than the desired value of Δx in Eq. (3.1), to ensure that the error is not limited by characterization. However, the increments cannot be arbitrarily small since they require a proportionately higher simulation time. With 100µm increments, the estimated simulation time on a high-

performance server for completely characterizing the current FOV is less than a few hours. Also, this needs to be performed *only once* for a given set of coils since the magnetic field values for an arbitrary DC current can be obtained by linearly scaling the field values stored in the LUT.

Since the prototype coils developed in this work are hand-wound, the undesirable minute gaps between the turns are not exactly consistent, thus making it difficult to accurately model the coils in Radia. As a result, the coils were characterized externally by the setup shown in Fig. 3.27 since the required resolution of 100μm cannot be achieved using the Radia-based characterization for these coils. The setup comprises linear actuators that move in the X, Y, and Z directions and measure the magnetic field at every 2.5mm step. Points in between the 2.5mm steps are interpolated using Makima, a piecewise cubic Hermite interpolation in MATLAB. This results in an ultra-finely characterized FOV with steps of 10μm in X, Y, and Z, such that the interpolation error of δG_i described in Eq. (3.1), causes <1% variation in G. An increase in the step size from 2.5mm causes δG_i to increase proportionately. The 3D magnetic sensor (AK09970N) is mounted on a fiberglass arm and makes a field measurement at every position step. Arduino is used as the global micro-controller to simultaneously control the movement of the actuators and interfacing with the sensor. To reduce the effect of the sensor noise from 15μT_{pp} (measured in the lab) to ≤ 1μT_{PP}, the sensor averages 200 measurements at each location. The earth's ambient magnetic field is also measured at each location and subtracted from the gradient coil's field. The corrected field values are then stored in the LUT. Each step consisting of all the measurements and the movement of the actuators takes <10s, requiring 15days to completely characterize the 20x20x10cm^3 FOV with 2.5mm increments. For future versions of the coils that are robotically assembled, the total time for characterization can be reduced significantly using Radia.

It is crucial to have a constant DC current from the power supply into the coils, i.e., minimize δG_s in Eq. (3.1), since variations in current cause field-offsets that directly

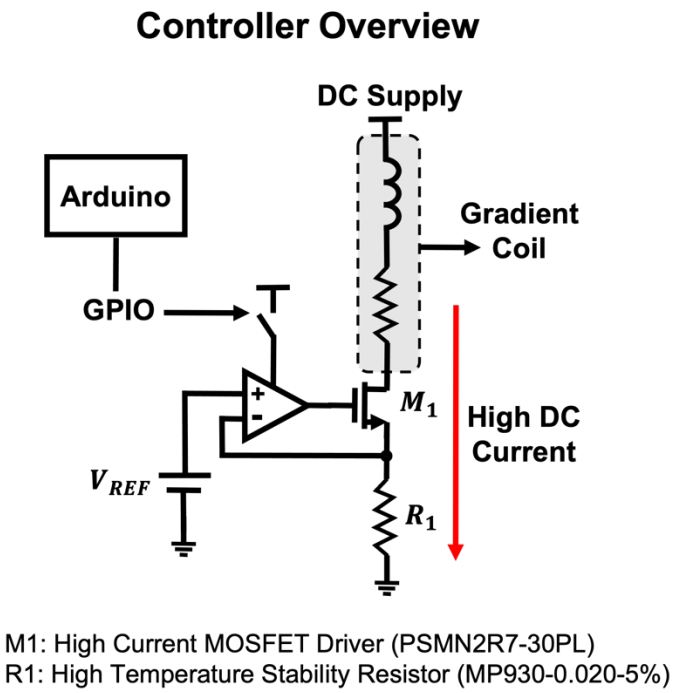

Fig. 3.28: Schematic overview of the controller-board used for driving the coils.

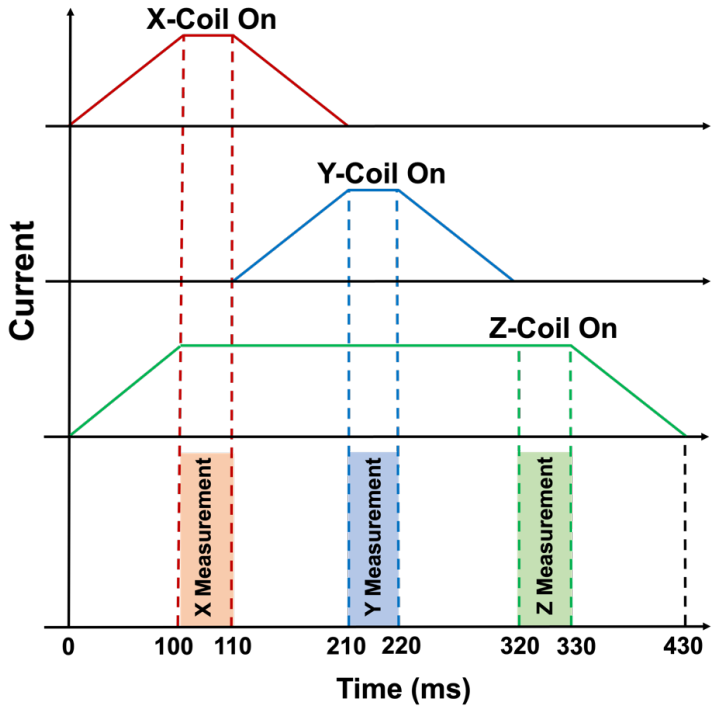

Fig. 3.29: Global timing diagram of the gradient coil on/off time-instants along with the field-measurement phases.

translate to position error. Therefore, a controller-board is designed to precisely control the DC current into the gradient coils so as to get $\delta G_s \approx 0$. A high-level schematic of the board is shown in Fig. 3.28. V_{REF} and R_1 together set the value of the DC current since $I_{DC} = V_{REF}/R_1$. An N-channel MOSFET driver M_1 (PSMN2R7-30PL) rated for 100A is used for handling the high DC current coming into the coils. R_1 is chosen with high temperature stability (MP930-0.020-5%) to ensure a thermally stable current value. All of these steps ensure that the contributions from δG_i and δG_s in Eq. (3.1) are kept ≤1%.

The global timing diagram is shown in Fig. 3.29. Measurement phases are synchronized to occur during the 10ms time-window when the DC currents in the coils are stable. The 10ms span is sufficient for the 25 measurements that are performed during the normal operation of the device, as will be discussed in the following section. Since the number of measurements at each step during the characterization phase are much higher, a 100ms span is required instead. The relatively high ramp-up/down time of 100ms is primarily due to the DC current supplies used for this application, which limits the number of measurements to 7 in 1s. The high rise/fall time also causes 85% of the total power dissipated as heat, and only 15% is contributed by the 10ms measurement time-window for each of the X, Y, and Z measurements shown in Fig. 3.29. The use of high-efficiency DC supplies like [23]–[24] can reduce the heat loss by almost 80% by significantly reducing the high rise/fall times. The entire duty-cycled operation of the coils, shown in Fig. 3.29, results in ≈300W of average power lost as heat with the current DC supplies. For continuous localization carried out over 1 minute, this produces 18kJ of energy in the coils, resulting in 3.4^0C rise in the surface temperature. For procedures requiring a longer localization time, cooling pads or thermal insulators may be used above and below the coils to dissipate the heat faster.

A more energy-efficient approach for designing future versions of the gradient coils with larger FOV would be to use more layers of windings (instead of two used in the

first prototype here), rather than increasing the DC current that has square-dependence on heat-loss (I^2R). The former approach increases the heat linearly and also provides a larger coil volume for heat dissipation. The extra layers will increase the thickness of the coil-stack, which is not a problem since the stack is completely planar and can easily slide beneath the surgical bed. For the switching speed, it can be seen from Table 1.1 that the L/R time constant for X and Y Coils is 1.58ms and for Z-Coil is 1.64ms. Both of these are significantly less than the 100ms rise/fall times of the DC supply and therefore have a negligible effect on switching speed.

3.4 Measurement results

The complete measurement setup for the localization system is shown in Fig. 3.30. The magnetic field gradient coil stack is placed on the bottom with the primary wireless power transfer (WPT) inductor-coil on top. A 5cm high saline tank separates the device from the WPT coil. The device consisting of the Silicon-Chip, 3D magnetic sensor, inductor-coil and FR4 PCB, is completely bio-compatible. When the device is used as an actual implant in a surgical space, it would need to be encapsulated by poly-dimethyl siloxane (PDMS) and sealed hermetically [25]. The device functionality is unaffected by such encapsulation. After wirelessly powering up the Chip, a wake-up signal is sent to trigger magnetic field measurement by the sensor. The decoded wake-up pulses are shown in Figs. 3.31–3.32. These are synchronized with the gradient on/off signal to allow high DC current in the coils only during the measurement phase. The sensor generates a 16-bit digital data stream for each of the X, Y, and Z components of the field. Fig. 3.31 shows the zoomed measurement when the gradient coils are off, thus making the Chip measure the earth's magnetic field (±30μT to ±60μT), so as to cancel its effect from the gradient coil's field. The first 8 bits of all the vectors are either 0 or 1, indicating a very small value. The field vectors have significantly higher and strictly positive values, as shown in Fig. 3.32, once the gradient coils are turned on. After the Chip finishes a measurement, the data is backscattered wirelessly at 100kHz,

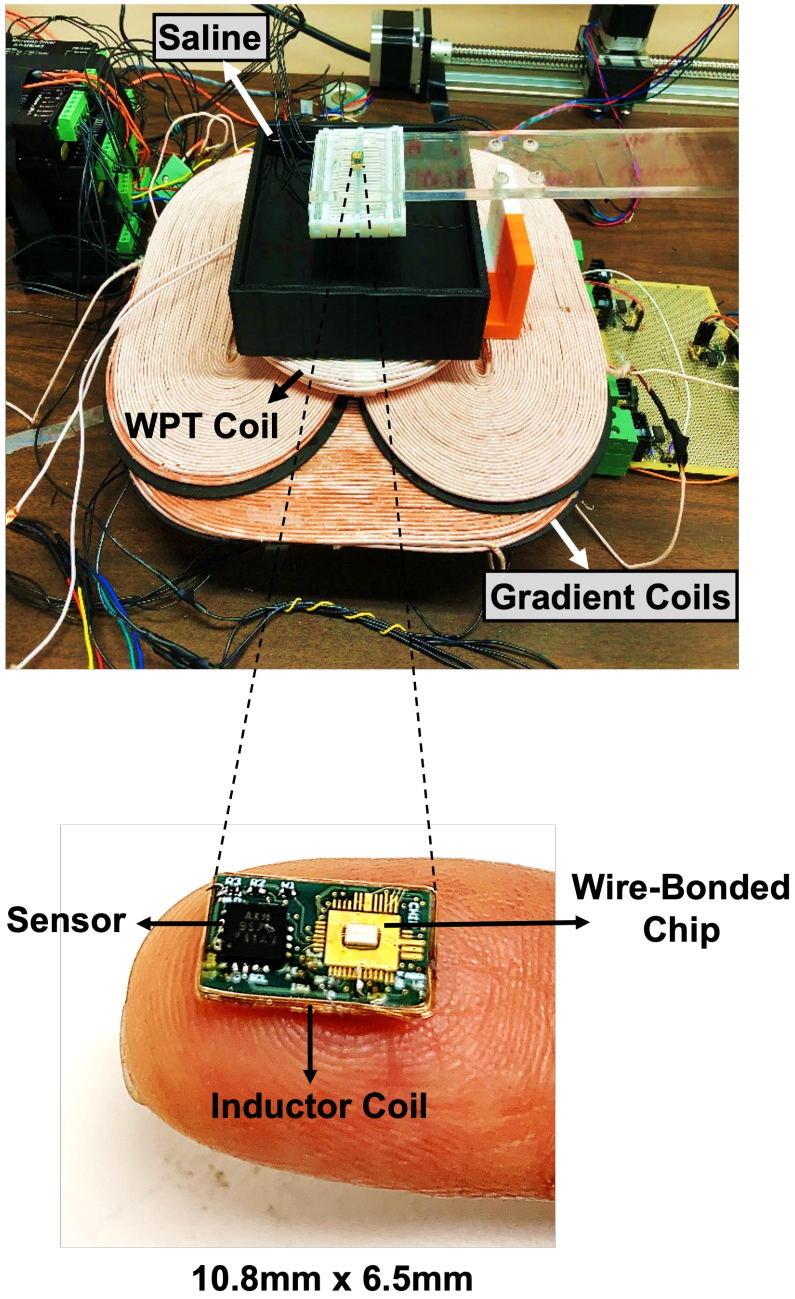

Fig. 3.30: Measurement setup for localization consisting of the compleetly assembled device and magnetic field gradient coils.

requiring <1ms for transmission to the external reader module (Fig. 3.33). Offset cancellation and position decoding take <10ms, causing the total latency between the field measurement and position-display to be ≈10ms. However, this gives only

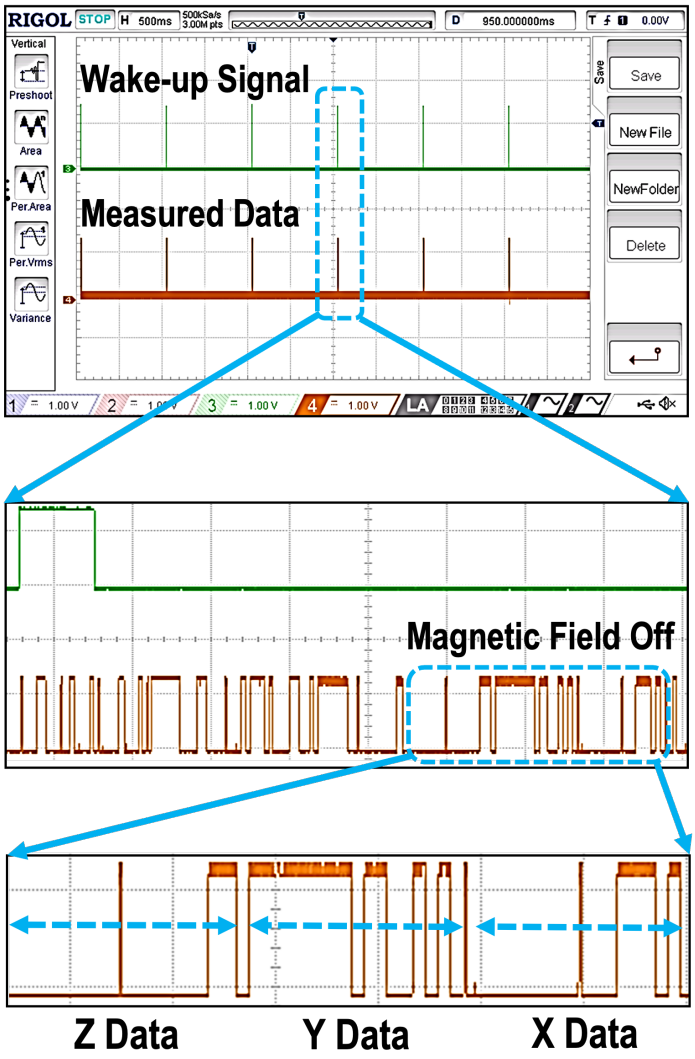

Fig. 3.31: Measurement results for the CMOS chip showing the decoded wake-up signal and the measured 16-bit data vectors for each of X, Y, and Z in the absence of gradient coil's magnetic field, thus measuring the earth's field.

one coordinate position and in order to decode the X, Y, and Z position, there is an extra 100ms of wait time due to the rise/fall time requirement of the DC current in the gradient coils, as was shown in Fig. 3.29. The rise/fall time constraint can be relaxed with the use of more efficient DC supplies [23]–[24] such that the overall latency for a 3D position update is <50ms, with 10ms each for the X, Y, and Z measurements, 10ms for decoding and the remaining 10ms for rise/fall time

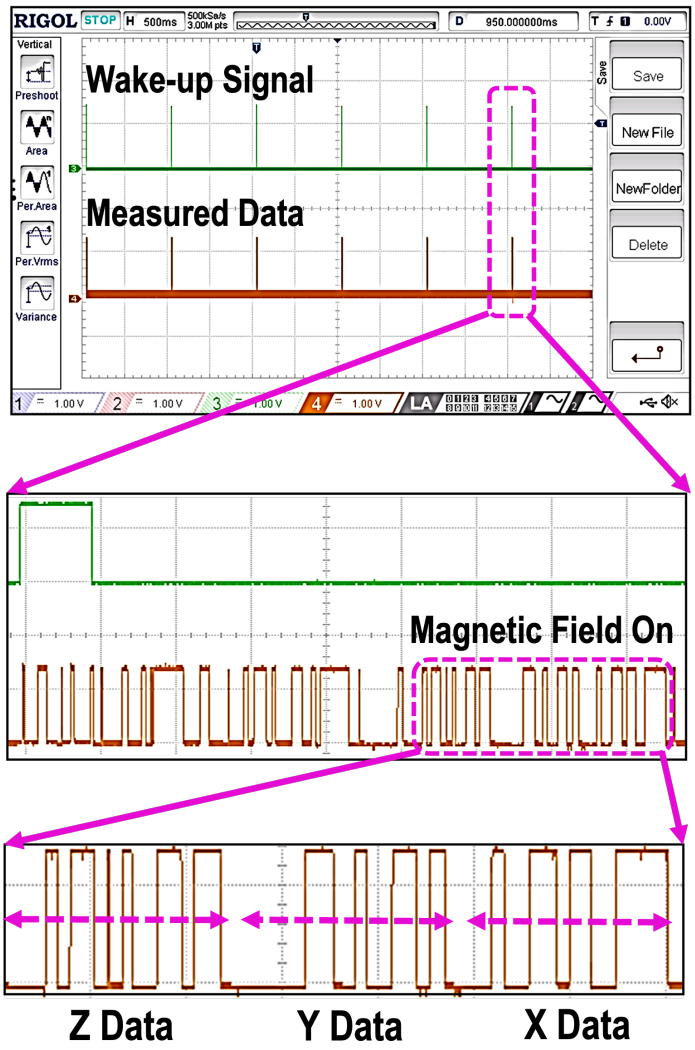

Fig. 3.32: Measurement results for the CMOS chip showing the 16-bit data vectors for each of X, Y, and Z in the presence of magnetic field generated by the gradient coils.

overhead. The latency can be further reduced by decreasing the number of measurements from 25 (which require 10ms for each coordinate) to a single measurement, at the cost of ≤500µm of 3D position error.

Three points in the gradient coils' FOV are chosen, corresponding to three distinct spatial coordinates: (i) X1, Y1, Z1 in the region with G=50mT/m; (ii) X2, Y2, Z2 in the region with G=30mT/m; and (iii) X3, Y3, Z3 in the region with G=10mT/m.

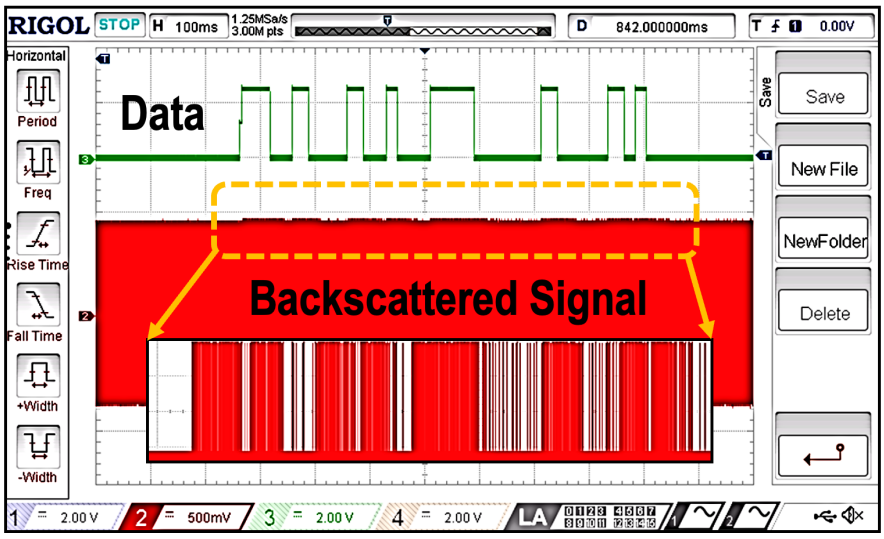

Fig. 3.33: Measured backscatter signal shown with much lower data speed for clarity.

The demodulated field values measured at each point, denoted by B_{xi}, B_{yi}, B_{zi}, are given as input to the 3D Search-Algorithm implemented in MATLAB, which outputs the corresponding closest position coordinate (Fig. 3.34). In Step 1, B_{xi} is compared with all the magnetic field magnitudes stored in the B_X column of the Main-LUT (created during the characterization phase) and a smaller LUT-X is created dynamically that contains all entries of the Main-LUT within $\pm\Delta B$ of B_{xi}. ΔB is chosen to be 100μT to ensure high accuracy by eliminating all false positives. Since B_{xi} corresponds to a large number of B_X values located in the 3D volume above the coil surface, there is more than one row in LUT-X. In Step 2, a similar process is repeated for B_Y using B_{yi}. The intersection of the B_{xi} and B_{yi} planes results in an array of points spread across various planes parallel to the coil surface. B_{zi} is used for the search in Step 3 and finally, the output coordinates are the x_i, y_i, z_i (shown as the 567th entry in Fig. 3.34) from LUT-Z that correspond to magnetic field values having the smallest Euclidean difference from B_{xi}, B_{yi}, B_{zi}.

The actual position of the Chip, measured from a global reference point on the gradient coils, is known precisely since it is placed on the robotic micro-positioner.

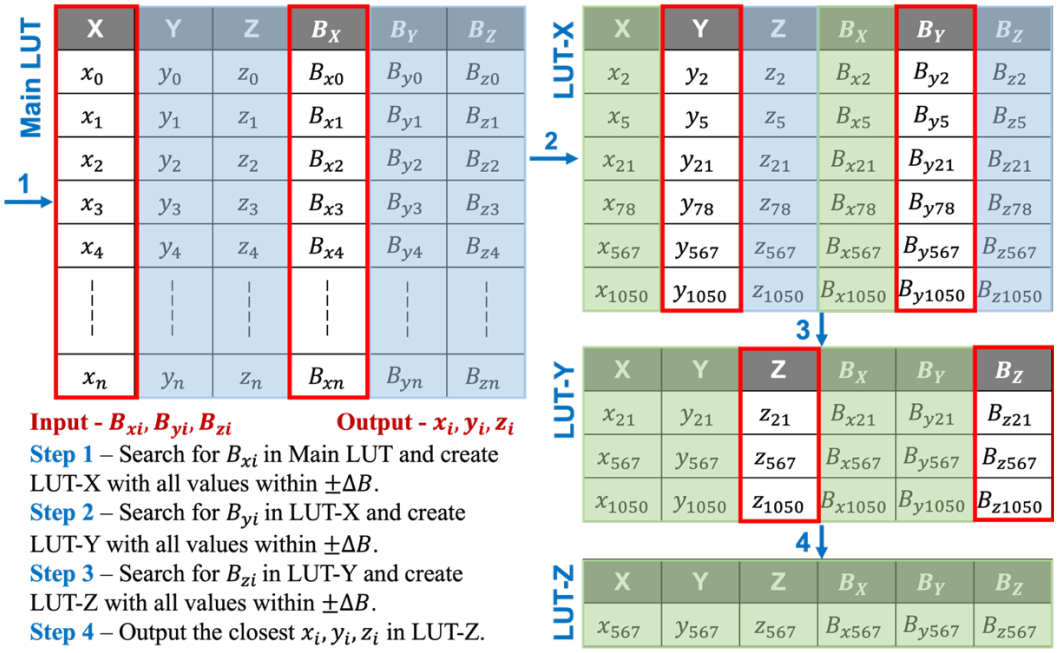

Fig. 3.34: Overview of the 3D Search-Algorithm for position decoding from the magnetic field values measured by the device.

The predicted position is the output of the Search-Algorithm discussed above and is also referenced to the same global point on the coils. The error is defined as the difference between the actual and the predicted position and is plotted against the number of measurements (taken at the same position) in Fig. 3.35. The accuracy is defined qualitatively as the inverse of the error and therefore, a smaller error implies a larger accuracy. In the high gradient regions (≥30mT/m), the sensor is operated in low-power mode which has a sensitivity of 3μT/LSB. Given the error due to δG_s and δG_i is ≤1%, this should ideally produce a peak error of <100μm, as per Eq. (3.1). However, the error plots in Fig. 3.35 show that the peak position error from a single measurement can be 500μm. This is attributed to the random noise of the sensor, which has a peak measured value of 15μT. To mitigate the effect of sensor noise on the position error, averaging of several measurements is performed for a given position. As seen from the plots in Fig. 3.35, with increasing the number of measurements, the peak error gradually decreases. It is found that with averaging

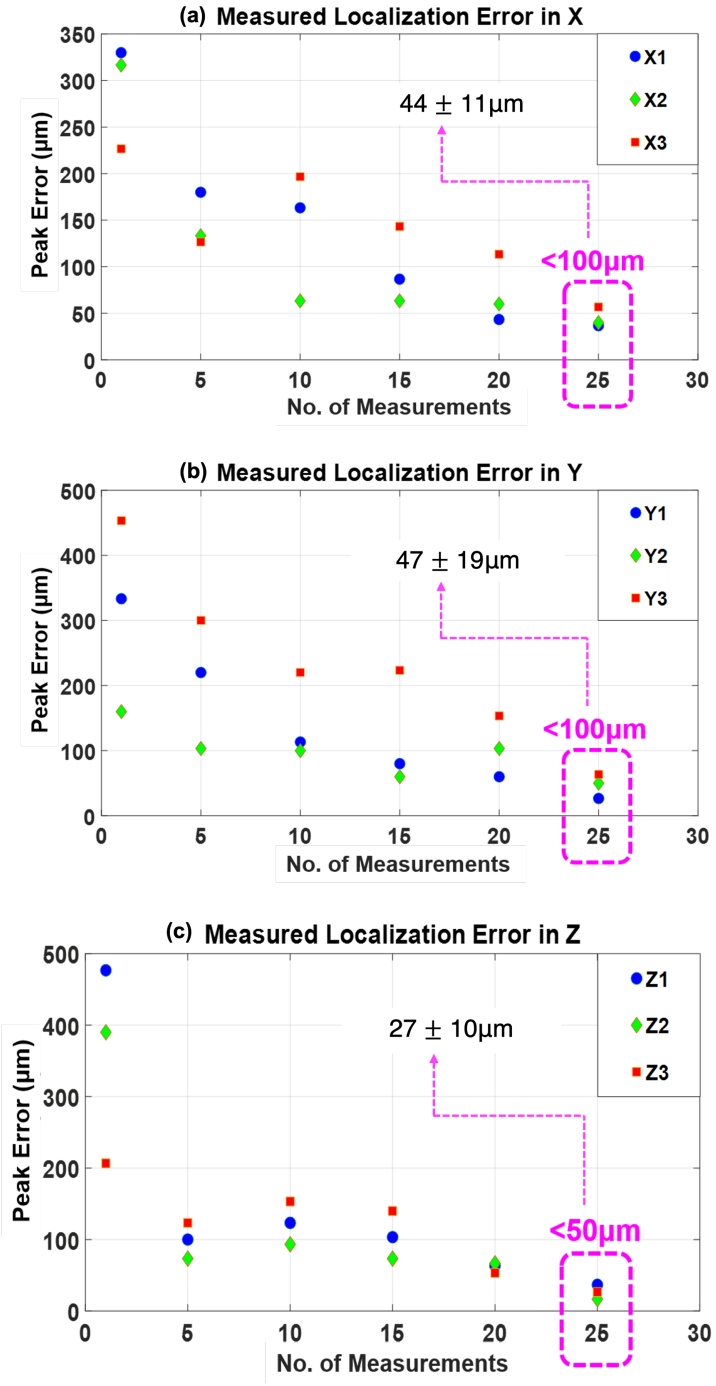

Fig. 3.35: Measured localization error for (a) X, (b) Y, and (c) Z direction. Peak error, which is the difference between the predicted position (output of the Search-Algorithm) and the actual position (measured from a global reference point on the gradient coils), is plotted vs the number of measurements averaged. An ensemble of ≥25 measurements is averaged at each position to get the peak error of <100µm in all three dimensions.

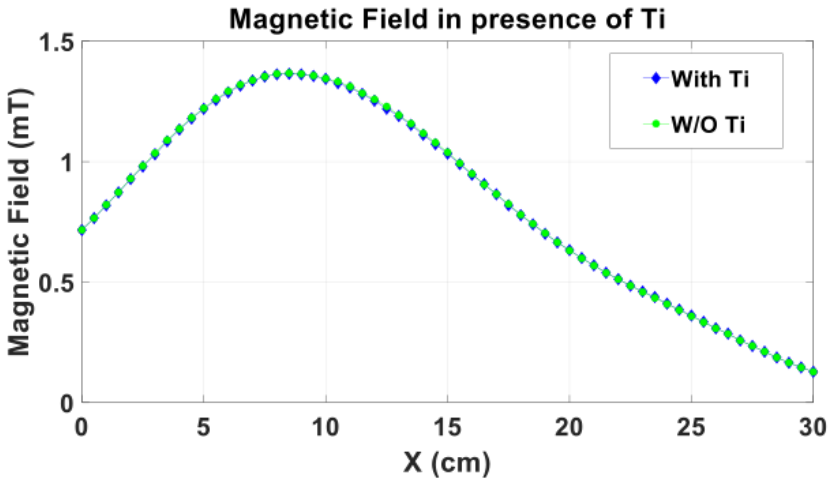

Fig. 3.36: Measurement results showing lack of field distortion in the presence of Ti.

an ensemble of ≥25 measurements, the peak error reduces to <100μm. The averaging window can be relaxed for: (i) a sensor with higher sensitivity and lower noise, thus reducing ΔB_{eff} in Eq. (3.1); and/or (ii) higher field gradient to increase G. In the low gradient region (G<30mT/m), the sensor is operated in the low-noise mode, achieving a sensitivity of 1μT/LSB that results in <100μm of position error.

Thus, by selectively operating the sensor in low-power or low-noise mode, the desired error threshold of 100μm is maintained in the entire FOV. The mean and std. deviation of the error obtained at the three different points (with averaging 25 measurements) shown in Fig. 3.35 is: (i) X: 44 $\pm$ 11μm, (ii) Y: 47 $\pm$ 19μm, and (iii) Z: 27 $\pm$ 10μm. Note that such a high resolution is necessary only when the surgeon is very close to the screw-hole, and can be relaxed during the initial maneuvering to quickly navigate to the approximate hole location, without performing any averaging. With positioning the approximate hole-location close to the center-region of the FOV, operation of the sensor in low-noise mode can be avoided.

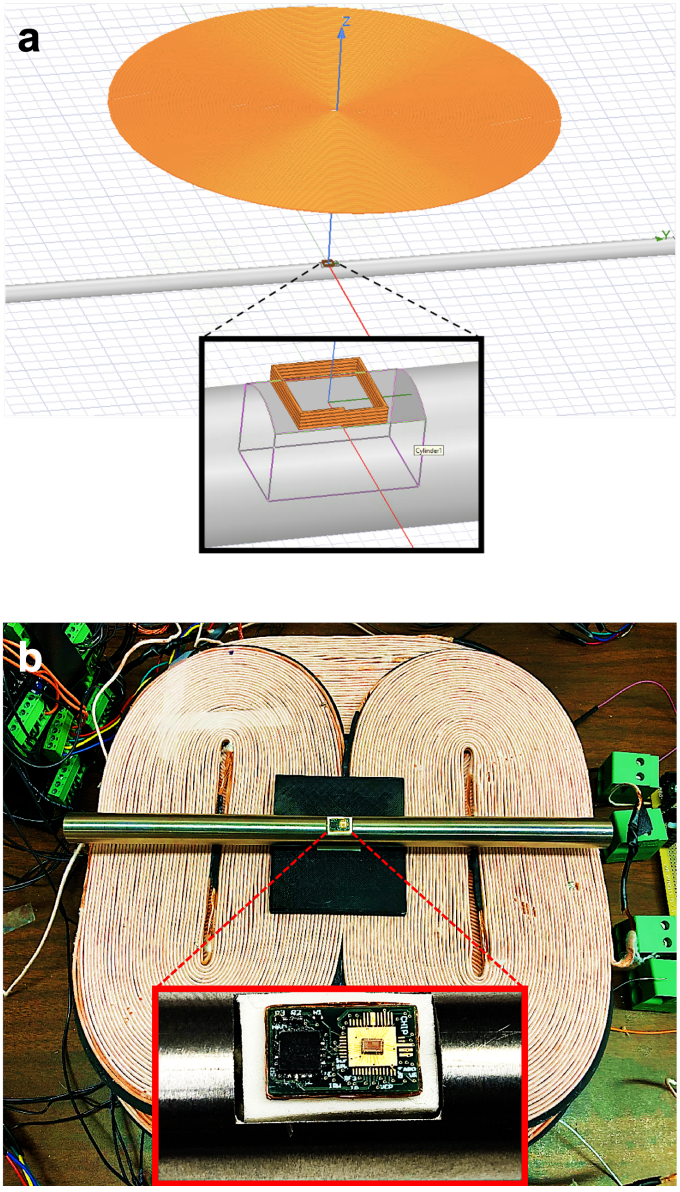

Fig. 3.37: Measurements in the presence of Ti rod. (a) Simulation setup in HFSS to determine the cavity depth. (b) Measurement setup with the device placed on top of a PDMS-filled cavity.

The system is further evaluated in the presence of a Ti rod. Due to the extremely low magnetic susceptibility of Ti, there is practically no distortion (<0.1%) of the magnetic field in its presence, as evident from Fig. 3.36. However, due to the presence of Ti metal right beneath the device (Fig. 3.37), the WPT efficiency gets

degraded due to the induced eddy currents in the metal. To improve the efficiency so as to keep the transmitted power well within the SAR standard of 1.6W/kg, a 6mm deep cavity is drilled from the surface of the rod and filled with PDMS (non-metallic, non-magnetic), inset in Fig. 3.37. This achieves safe and robust power delivery up to an angular rotation of ±15º of the rod, which is the maximum deformation that can occur during flexion and torsion during orthopedic surgeries [7]. The depth of the cavity was optimized using simulations in HFSS, as shown in Fig. 3.37.

The effect of interference from surgical tools and implants in the operation room (OR) is studied next. All tools can be classified as either magnetic (having high susceptibility of χ) or non-magnetic ($\chi \approx 0$), where the former cause distortion in the magnetic field gradient generated by the coils but the latter do not. Several localization experiments were conducted in the presence of both kinds of tools. For all non-magnetic tools, the error in the decoded position is independent of their presence, as shown in Fig. 3.38 for one such type, and is thus <100μm. Most implants are non-magnetic and surgical tools made from non-magnetic materials are used routinely in the OR. For magnetic tools, the error is significant (2–8cm) only when the tools are in 1cm of proximity to the device. As the distance from the tools increases to 5cm, the error decreases to 1–5mm and falls below the 100μm threshold when the tools are ≥15cm away from the device. The results for one such tool are shown in Fig. 3.38. Hence, the accuracy of our localization system is uncompromised in the presence of all non-magnetic surgical tools and implants and can be retained if all the magnetic tools are kept ≥15cm away from the device during the navigation and tracking phase.

Regarding medical safety in the OR, it is important to study the effect of magnetic force and magnetic torque on magnetic surgical tools when used in close proximity to our system. During the interference studies described above, no mechanical movement was observed in any of the magnetic surgical tools, even when placed

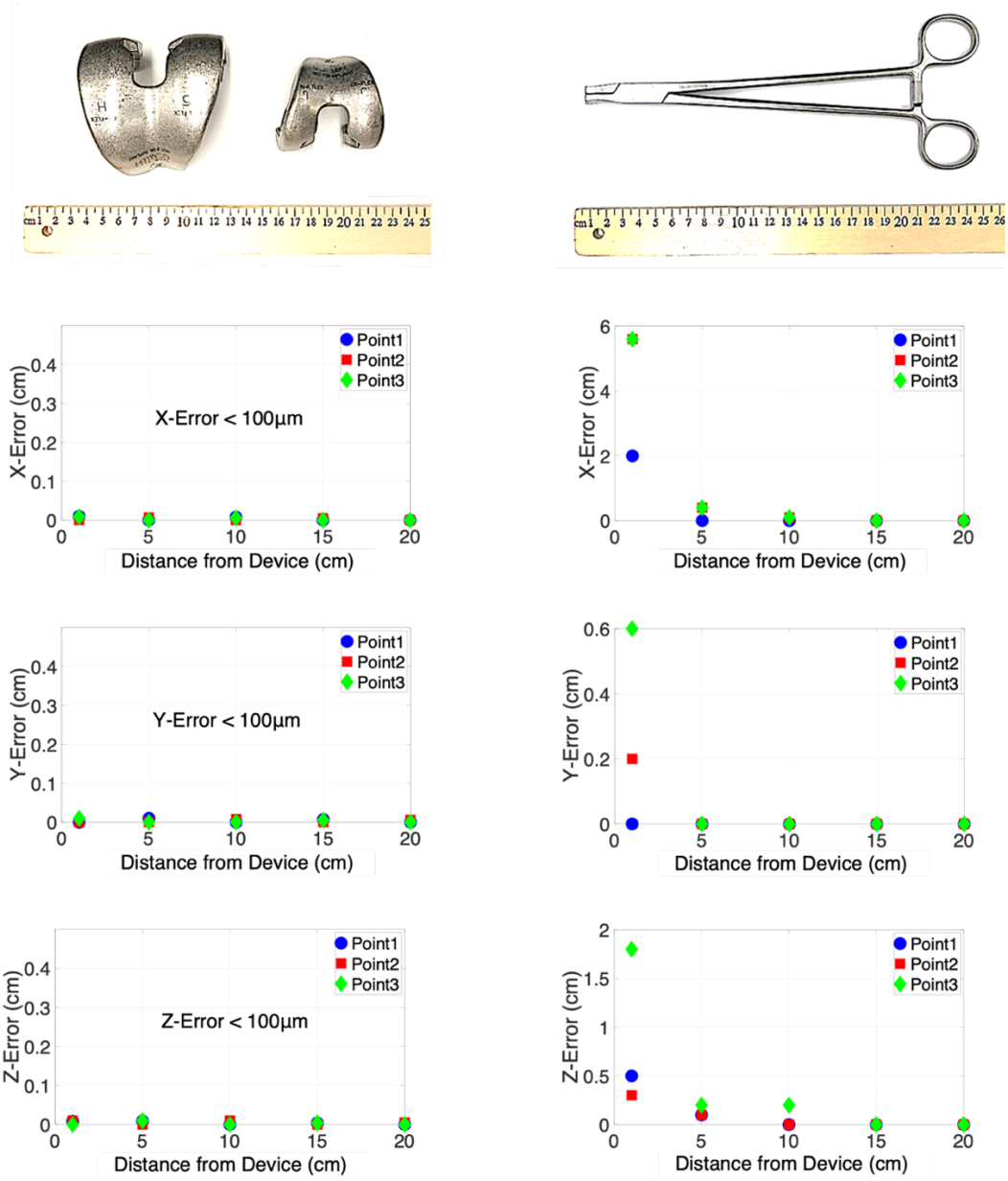

Fig. 3.38: Non-magnetic surgical implant used for studying the effect of interference (left). Peak error in the decoded position (at 3 different points) is plotted for X, Y, and Z as the distance of the implant from the device is varied. Same experiment is performed for a magnetic surgical tool (right), where the error goes to <100µm when the tool is ≥15cm away from the device.

right next to the device. This was the case both during the 100ms rise-time and the 10ms stable-time of the gradients, none of which led to any mechanical motion in the

magnetic tools or the electrical equipment used. To verify this observation theoretically using the formulation described in [26], it is calculated that for Stainless Steel (used commonly for making surgical tools) with saturation magnetization M_s of 1.65T, the ratio of magnetic force to gravitational force and the ratio of magnetic torque to gravitational torque, are both less than 1 when the tools are kept ≥10cm away from the gradient coils. Magnetic forces and torques that are less than those produced by gravity are not expected to pose added risk to the patient [27]. It is expected that magnetic tools would be kept at least 15cm away from the coils and the devices, to retain the system's accuracy. At such distances, all magnetic tools and equipment can be safely used concurrently with our system.

For medical safety considerations, it is also important to study the effect of Peripheral Nerve Stimulation (PNS) due to gradient-switching performed by the coils. The 100ms rise-time for the gradients used in this work is significantly slower than the 0.1-1ms rise-time used in fast MRI scanners. PNS threshold is most commonly defined as the peak $d|B|/dt$, reported to be 43-57T/s in [28], which is sufficiently higher than our peak value of 0.4T/s (B≤40mT and 100ms rise-time). It is also worth noting that PNS effects are of concern when switching times are in 0.1ms to ≈1ms range and are negligible when switching time is >5ms, given $|B|$<100mT [29]. Considering the rise-time along with the peak $d|B|/dt$ value, the International Electrotechnical Commission (IEC) thresholds for PNS and Cardiac Stimulations have a common asymptotic value of 20T/s at long rise-times (>5ms), thus implying complete safety of the gradient-switching employed in this work [30].

The system in this work is also capable of measuring the angular orientation of the device, which can be found after decoding the 3D location using field magnitudes. As the sensor transmits all the three orthogonal components (with sign information) of the magnetic field vector at its location, described by Eq. (3.6), the individual components can be compared one-to-one with those stored in the LUT to find the

angular difference from the orientation used during characterization. This will provide complete position and orientation information of the devices relative to each other, which are critical for some surgical procedures. Authors in [31] have reported angular as well as position measurements for their magnetic tracking system, where localization of a magnet-robot is performed using an external array of 64 Hall-effect sensors. EndoScout developed by Robin Medical [32] uses a wired sensor ($1cm^3$ volume) that has an induced EMF in response to a known external magnetic field gradient. The gradient is produced by an MRI scanner since the system was developed primarily to localize sensors during MRI. However, the resolution of the system is limited to a few mm [33], mainly because of the large sensor volume and lack of integrated data processing. Also, the sensor is not wireless and is maneuvered using a catheter inside the body. Similarly, commercial systems using AC/DC EM-based tracking of sensors have been reported in the past [9] by NDI *Aurora*, Calypso, Polhemus and Ascension, but the requirements of high localization resolution, high FOV, high penetration depth, an integrated sensor with data-processing, wireless operation of the sensor, small size of the sensor, high sampling rate for real-time feedback, planarity and efficiency of the field-generator, safety and compatibility with metals—these are some of the crucial aspects that have not yet been met by any one single system. As a result, very few such systems have been clinically approved to be used as or along with implants during surgical navigation.

Table 1.2 shows the performance summary and comparison of our system with state-of-the-art localization techniques. The first part of the table compares our system-level specifications with other techniques used for localizing sensors and devices deep inside the body, based on X-Ray, Fluorescence, Optical, Ultrasound, RF, Laser, magnetic tracking, EM, and MRI-inspired. The second part compares our device-level specifications with other implantable/ingestible sensors and devices, most of which are AC/DC EM or RF-based, used for navigation and tracking *in vivo*. To the best of our knowledge, the resolution obtained by this system has the highest value to be reported. The FOV and penetration depth are

also unprecedentedly high. The complete wireless operation of a device of this scale has not been shown before for localization applications. The sampling frequency of 7 Hz is currently limited by the ramp-up time of DC currents in the gradient coils. Future work would be to increase the sampling frequency and thus reduce the latency, perform angular orientation measurements in addition to the position (6D), and reduce the overall power and footprint of the implantable device by using a CMOS integrated 3D magnetic sensor.

System Specifications	This work	TMI 2020 [34]	TMI 2019 [35]	SIGCOMM 2018 [36]	Nat. BME 2017 [8]	TMI 2017 [37]	ASME 2016 [31]	TBME 2013 [38]	US Patent 2003 [32]
Localization Dimension	**3D**	3D	3D	3D	2D	3D	5D *	3D	6D *
Localization Resolution	**100µm**	600µm	2.8mm	1.4cm	500µm	2.23mm	2.1mm	1.5-4.44mm	2mm
Localization Modality	**Magnetic Field Gradient**	Radioactive & Fluorescence	Optical & Ultrasound	RF-based Backscatter	MRI Inspired	Ultrasound & Filtering	Magnetic Tracking	Laser & Conoprobe	MRI Gradients
Sample Rate	**7Hz**	17mHz	1Hz	N.R.	N.R.	N.R.	200Hz	30Hz	16Hz
Penetration Depth	**10cm**	2cm **	N.R.	8cm	1.2cm	N.R.	5cm	N.R.	Sensor dependent *#
Field of View	**20cm x 20cm x 10cm #**	14cm x 14cm x 2cm	24cm x 30cm x 8cm	8cm ##	1.2cm $	16.5cm x 22cm $$	7cm x 7cm x 5cm	N.R.	30cm from center

Device Specifications	This work	SIGCOMM 2018 [36]	Nat. BME 2017 [8]	US Patent 2003 [32]
CMOS Technology	**Yes (65nm)**	No	Yes (180nm)	No
Wireless Power	**Yes**	Yes	No	No
Wireless Data	**Yes**	Yes	Yes	No
Frequency	**13.56MHz**	830, 870MHz	500MHz #$	N/A
CMOS Chip Area	**1.5mm^2**	N/A	2.16mm^2	N/A
Avg. Power	**1mW *$**	N.R.	339uW	N.R.

* Angular orientation is also reported (3D+2/3D)
** For fluorescence-based method
*# Depends on penetration depth of the wired sensor
Can be enhanced by using bigger gradient coils
Only depth-FOV is relevant for RF
$ Reported for a single axis
$$ Reported for 2D US image area
#$ Center frequency
*$ Includes external sensor power
N.R.: Not Reported
N/A: Not Applicable

Table 1.2: Performance summary and comparison table.

3.5 Conclusion

This work presented a wireless 3D surgical navigation and tracking system that achieves <100μm localization error in 3D and in real time, using safe magnetic field gradients. The completely wireless operation of the implantable device and the significantly enhanced and scalable FOV, make the system highly suited for navigation during various high-precision surgeries and diagnostic procedures, thus eliminating the need for potentially harmful X-Ray fluoroscopy.

Chapter 4

LOCATION-AWARE INGESTIBLE MICRODEVICES FOR WIRELESS MONITORING OF GASTROINTESTINAL DYNAMICS

Localization and tracking of wireless microdevices in the gastrointestinal (GI) tract with high spatiotemporal accuracy is of high clinical value [1]. It can enable continuous monitoring and transit-time evaluation of the GI tract, which is essential for accurate diagnosis, treatment, and management of GI motility disorders such as gastroparesis, ileus or constipation [2–3]. GI motility disorders are also increasingly associated with a variety of metabolic and inflammatory disorders such as diabetes mellitus and inflammatory bowel disease. Together, these GI disorders affect more than one-third of the population globally and impose a considerable burden on healthcare systems [3]. High resolution and real-time tracking of wireless microdevices in the GI tract can also benefit anatomically-targeted sensing and therapy, localized drug delivery, medication adherence monitoring, selective electrical stimulation, disease localization for surgery, 3D mapping of GI anatomy for pre-operative planning, and minimally invasive GI procedures [1–4].

The current gold-standard solutions for these procedures include invasive techniques such as endoscopy and manometry, or procedures that require repeated use of potentially harmful X-ray radiation such as computerized tomography (CT) and scintigraphy [1–5]. These techniques also require repeated evaluation in a hospital setting, which can confound observations given the recognized variability in motility and activity. Ideally, GI monitoring would be carried out in real-world ambulatory settings through portable and non-invasive procedures without causing patient discomfort. Alternative approaches—including video capsule endoscopy (VCE) and wireless motility capsules—allow monitoring of the GI tract in real-world settings without interruption to daily activities [6–11]. Wireless motility capsules are orally administered and track the pH, pressure and temperature along the GI tract, while

VCE can augment the measurements by also acquiring video. However, these methods lack direct measurement of the capsule's location in the GI tract which needs to be inferred from the acquired data, thus allowing only large-scale organ mapping [6–8]. X-ray radiographs, in comparison, can measure the ingested capsule's real-time location with an accuracy of around 500μm [12]. Another drawback of VCE is the limited acquisition time of 12 hours, which is significantly shorter than the total GI transit-time (around 24–72 hours) [6–8].

Electromagnetic (EM) field-based tracking approaches have also been reported for localization of sensors and devices *in vivo*. 2D localization of a magnetic sensor in a field-of-view (FOV) spanning less than 2cm has been achieved using magnetic field gradients generated by bulky permanent magnets [13]. However, the sub-Tesla level magnetic field produced by the permanent magnets in this approach poses a high safety risk when magnetic materials are used in the vicinity. Alternative approaches that localize a magnet moving through the GI tract using an external array of magnetic sensors have also been explored [14–18], but have insufficient FOV and poor spatial resolution which degrades sharply with using multiple magnets. Commercial systems using EM-based tracking of sensors have also been developed [19–20]. However, the simultaneous requirements of high FOV, planarity and efficiency of the field-generator, safety with magnetic materials and metals, fully wireless operation and miniaturization of the devices, high spatiotemporal resolution, automized and real-time data analysis, and system scalability with the number of devices have not been met by existing systems in the context of GI monitoring.

In this work, we report a platform for localizing and tracking wireless microdevices inside the GI tract in real time and in non-clinical settings, with millimeter-scale spatial resolution, and without using any X-ray radiation. This is achieved by creating 3D magnetic field gradients in the desired FOV using high-efficiency planar coils, which encode each spatial point uniquely. It is particularly challenging to generate 3D field gradients using planar electromagnetic coils in the absence of a strong

background field. We overcame this by employing gradients in the total magnitude of magnetic field instead of only the Z-component, and by using a combination of gradient fields to produce monotonically varying field magnitudes in a large and scalable FOV. We designed highly miniaturized and wireless devices—termed ingestible microdevices for anatomic-mapping of gastrointestinal-tract (iMAG)—to

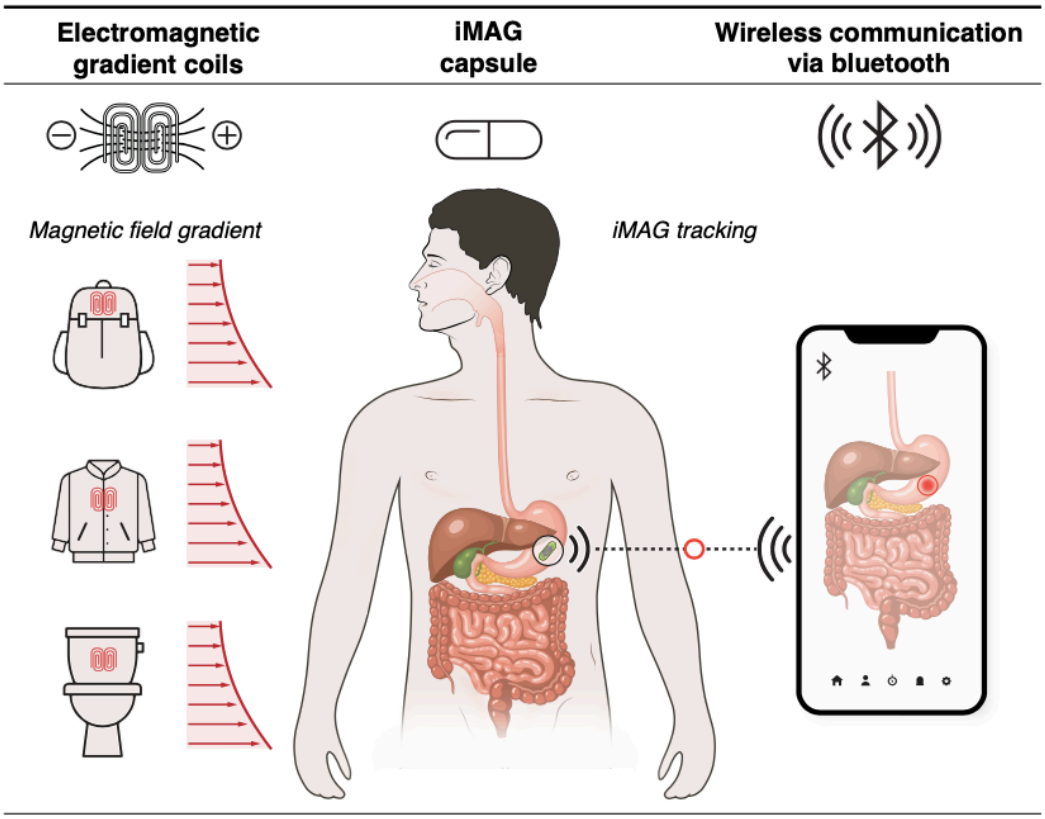

Fig. 4.1: Overview of the complete magnetic-field gradient-based tracking system is shown. A wireless ingestible microdevice for anatomic-mapping of gastrointestinal-tract (iMAG) is shown inside the patient. An external smartphone/receiver sends a wireless ping signal to iMAG to measure its local magnetic field. The measured field value is transmitted by iMAG to the receiver which maps it to the corresponding spatial coordinates and displays the 3D location in real time. The magnetic field is generated by planar electromagnetic coils placed behind the patient's back, which can be customized to form a wearable jacket, or put into a backpack with batteries, or attached to a toilet seat for continuous GI tract monitoring. The field generated by the electromagnets is strictly monotonic in nature, resulting in a magnetic field gradient that encodes each spatial point uniquely.

sense and transmit their local magnetic field to an external receiver. The receiver maps the field data to the corresponding spatial location, allowing real-time position tracking of the iMAG devices as they move through the GI tract. While the concept of frequency encoding similar to MRI has been explored previously [13], we use direct spatial encoding with magnetic field gradients to create a more accurate and energy-efficient system.

4.1 System concept

Our system uses high efficiency planar electromagnetic coils to generate 3D magnetic field gradients in a FOV spanning the entire GI tract (Fig. 4.1). The field gradients are generated in a time-multiplexed sequence such that at any given time, the principal magnetic field gradient occurs along a single axis. Using the field measurements along three orthogonal axes, the 3D position of the device can be decoded unambiguously. The complete iMAG system can be readily deployed in various non-clinical settings such as smart-toilets, wearable jackets or portable backpacks, thus allowing real-time GI tract monitoring without disrupting daily activities of a patient. A prototype animal-chute with the gradient coils is designed in this work for evaluation in large animal models, as discussed later. Another prototype with the gradient coils attached to a toilet-seat is designed for an at-home system, as shown later, demonstrating the use of our technology for chronic and non-invasive human applications.

The spatial localization resolution obtained by our system in each dimension (Δx) is given by:

$$\Delta x = \Delta B / G \tag{4.1}$$

where ΔB is iMAG's field-measurement resolution, and G is the applied magnetic field gradient along the corresponding axis. The goal for iMAG is to have ΔB = 3μT

and G > 3mT/m across the entire FOV to achieve a localization resolution of 1mm. To localize the devices along each axis (Fig. 4.2 (a)), a monotonically varying magnetic field is generated that has a gradient in its total magnitude along the same axis. A simplified view for the X-axis is shown in Fig. 4.2 (b) that results in Eq. (4.2). The three orthogonal components of the field $(\hat{x}B_X, \hat{y}B_X, \hat{z}B_X)$ measured by each device in Fig. 4.2 (b) are used for computing the field magnitude at the device's location, as described in Eq. (4.3). The field magnitude can then be mapped to the corresponding spatial coordinate.

$$\|B_{X1}\| < \|B_{X2}\| < \|B_{X3}\| \tag{4.2}$$

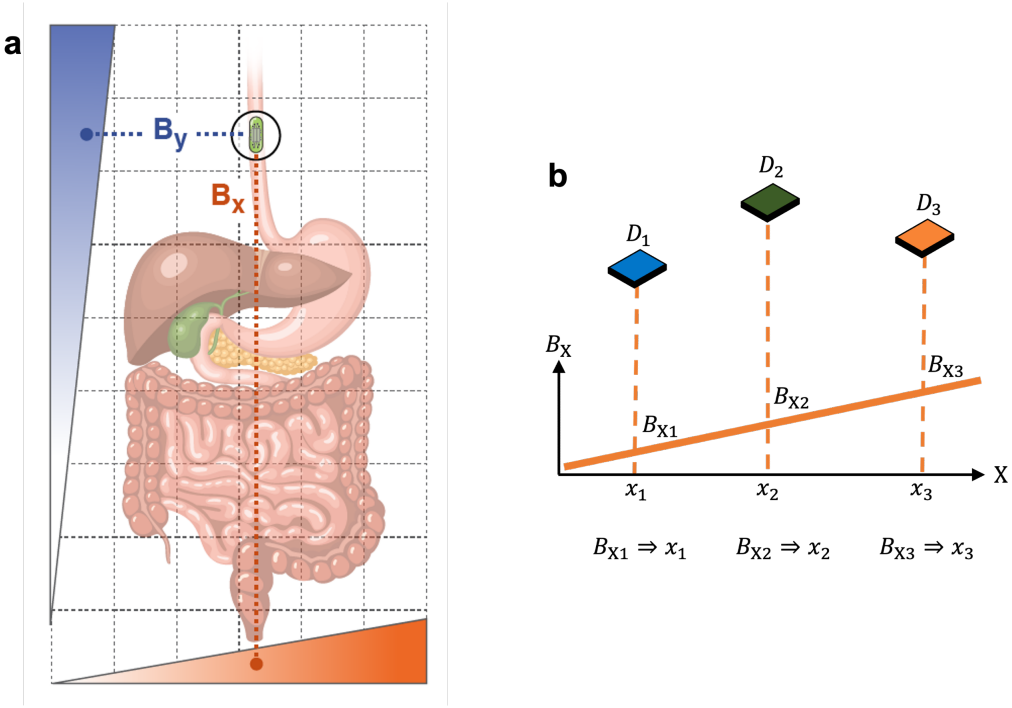

Fig. 4.2: Localization principle. (a) iMAG device is shown inside the patient's GI tract with magnetic field gradients present along the three axes (shown only along X and Y for simplicity). (b) Conceptual overview of the 3D localization of magnetic sensing devices $D_1 - D_3$. Monotonically varying magnetic field is generated to result in a field gradient along the X-axis. Each device measures the total field magnitude at its location which is unique for each point, thus allowing one-to-one mapping from field to position. This process is repeated for localization along the Y and Z axes.

$$\left\|B_{Xi,\ i=1,2,3}\right\| = \sqrt{(\hat{x}B_{Xi})^2 + (\hat{y}B_{Xi})^2 + (\hat{z}B_{Xi})^2} \quad (4.3)$$

Since the magnetic field B_X has a net gradient in its magnitude along the X-axis, G_X is defined as:

$$X - Gradient = G_X = \partial\|B_X\|/\partial x. \quad (4.4)$$

The process is then repeated for the Y and Z axes to localize the devices along them. By employing gradients in the magnitude of the field along each axis, our localization technique is immune to potential inaccuracies caused by device misalignment relative to any coordinate system.

4.2 iMAG design and characterization

We designed the 3D magnetic field sensing iMAG devices with the following specifications: (i) high resolution field-measurement (3μT/LSB); (ii) wireless operation at 2.4GHz Bluetooth frequency; (iii) ultra-low power for prolonged battery-life (2–4 weeks); (iv) small form-factor (20mm length, 8mm diameter); (v) bio-compatibility. The iMAG device (Fig. 4.3) consists of a 3D magnetic sensor that can measure and digitize magnetic field values to a 16-bit digital vector with 3μT accuracy (see Methods). A Bluetooth Low Energy (BLE) micro-processor interfaces with the sensor over the inter-integrated circuits (I2C) protocol. The digitized field-vectors received by the micro-processor are sent to a 2.4GHz Bluetooth antenna for wireless transmission to the external receiver. Coin-cell batteries are used for power. iMAG is fabricated by assembling these low-cost and commercially available components on a custom-designed printed circuit board (PCB), packaged into a biocompatible poly-dimethyl siloxane (PDMS) mold with the size of an ingestible 000-capsule (Fig. 4.3 (d)). Methods section summarizes the power consumption of iMAG under different operating modes. The TX power was set to 4dBm to ensure maximal connectivity with the receiver. An advertising rate of 2.5s and a connection

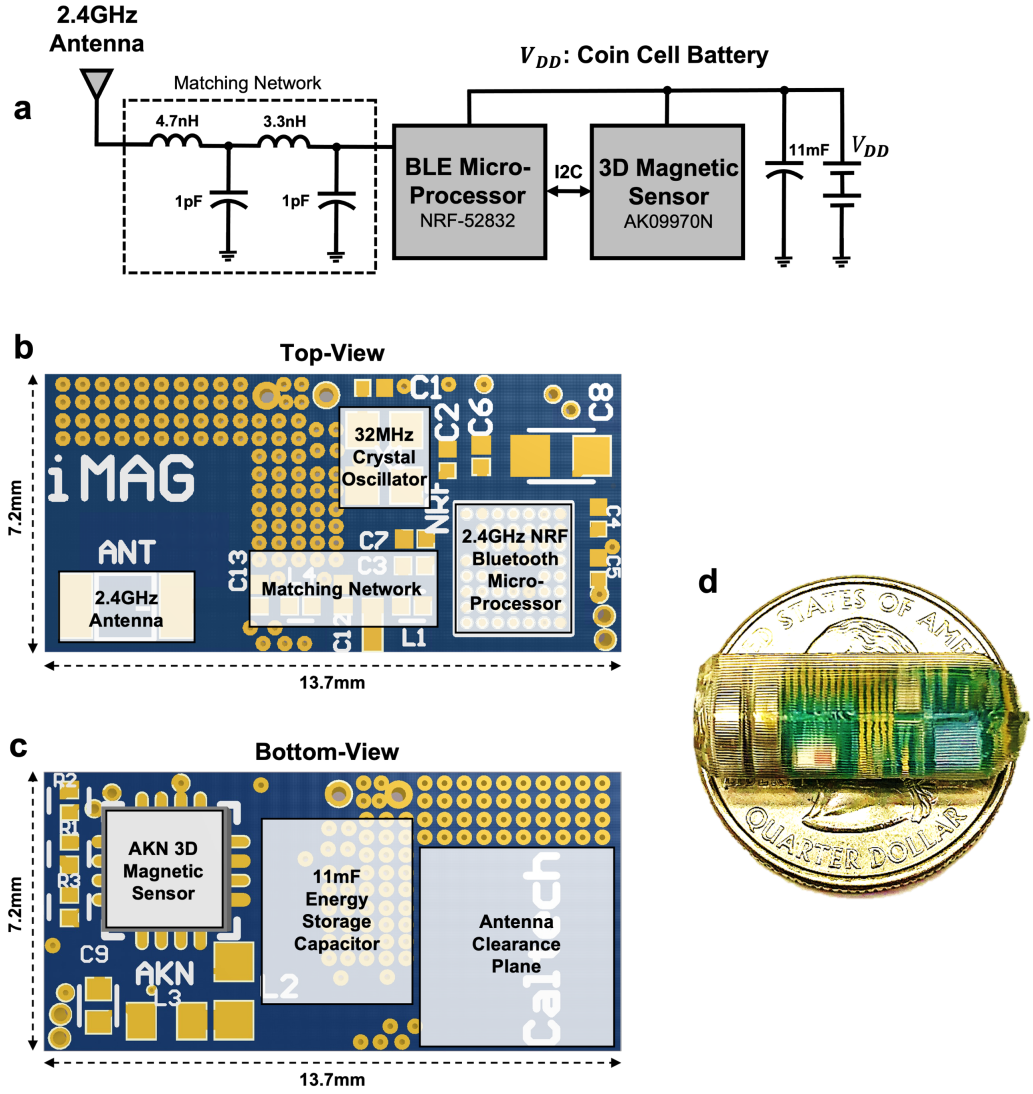

Fig. 4.3: iMAG device overview. (a) iMAG consists of a 3D magnetic sensor, a BLE micro-processor to communicate with the sensor, an antenna to communicate with the external receiver and coin-cell batteries for power. (b) Top and (c) bottom views of the iMAG PCB board showing the placement of critical circuit blocks. (d) iMAG is encapsulated into a cylindrical pill measuring 20mm (length) and 8mm (diameter).

interval of 50ms were chosen as a compromise between the connection speed, stability and battery-life. All non-necessary peripherals were deactivated to ensure that the maximum continuous current was within the discharge limits of the battery.

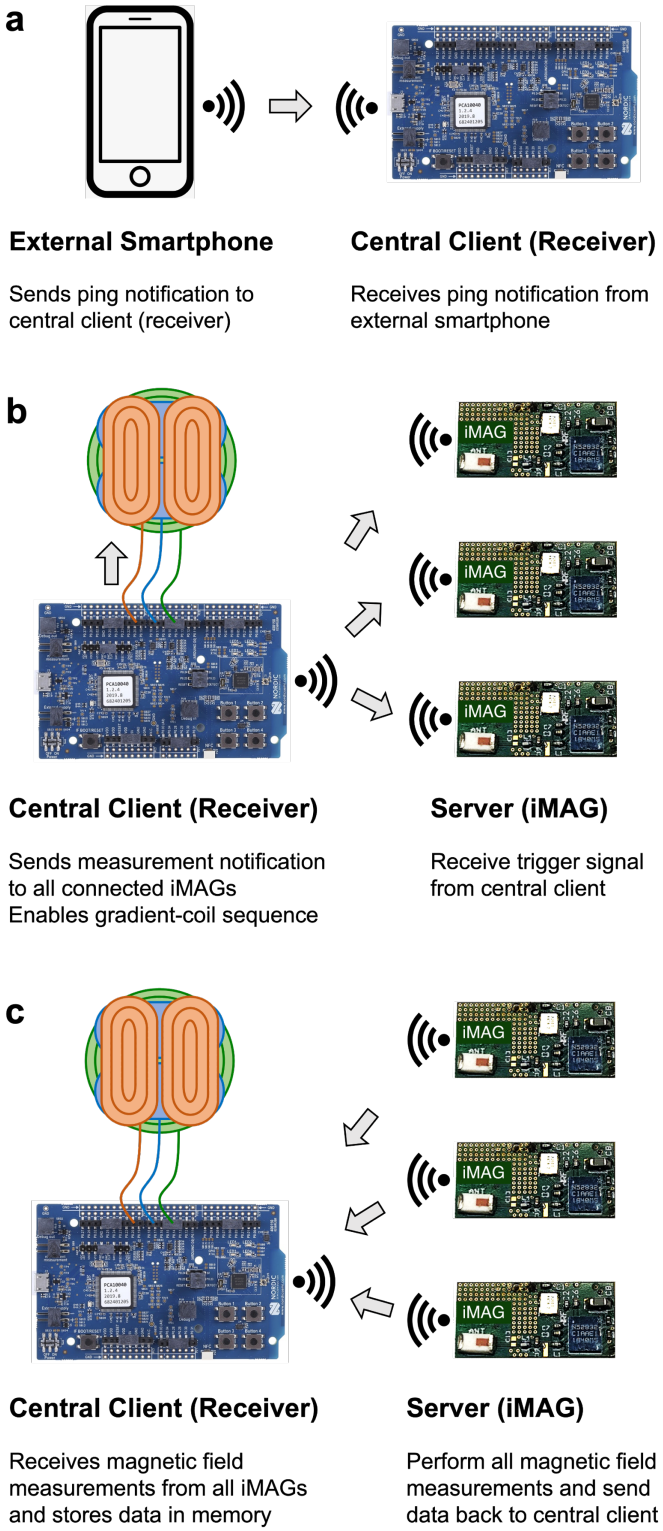

Fig. 4.4: The complete communication protocol between the smartphone, receiver board, iMAG devices and the gradient coils is illustrated.

To measure the 3D location of iMAG, an external smartphone sends a wireless ping signal to an NRF52 development board, used as the receiver in this work (Fig. 4.4 (a)). The ping signal is relayed by the receiver to the iMAG devices to trigger magnetic field measurements at their appropriate times (Fig. 4.4 (b)). With its I/O pins connected to the gradient coils' ENA (enable) switches, the receiver also activates the required sequence of coil combinations to generate the magnetic field gradients. Upon reception of the measured magnetic field data values from the connected iMAGs (Fig. 4.4 (c)), the receiver displays them on a computer screen using a UART protocol. The receiver concurrently runs a search algorithm to retrieve the 3D spatial coordinates corresponding to the magnetic field data (see Methods). The magnetic field value at each point in the FOV is measured and stored in a look-up table (LUT) during a prior characterization phase (see Methods). The search algorithm uses the LUT from the characterization phase for position retrieval.

The communication range is defined as the longest distance between iMAG and the receiver before losing connection (received signal strength <–96dBm at the receiver), and is evaluated under various *in vitro* settings. First, the iMAG was submerged in an HCl solution to mimic the acidic and fluid-filled gastric cavity. For a pH of 2–6, the range was >1m (Fig. 4.5 (a)). For a typical gastric pH of 1.2–3.5, the range varied from 30cm to >1m, respectively. At lower pH values, the concentration of the freely dissociated H^+ and Cl^- ions increases exponentially in the solution. These ions absorb the 2.4GHz RF signal, with the absorption being proportional to the ionic concentration, and lead to a lower signal strength at the receiver [21]. Intestinal pH is 4.5–6.5, for which the range was >1m. Second, the range was tested in different concentrations of NaCl solution (saline). For an NaCl concentration of 0.2% w/v, similar to gastric fluid, the range was >1m (Fig. 4.5 (b)). For an NaCl concentrations of 0.6-1% w/v, similar to intestinal fluid, the range varied from 60cm to >1m. Third, the range obtained in simulated gastric fluid (SGF) was >50cm up to 250ml of SGF (Fig. 4.5 (c)). Finally, the range in simulated intestinal fluid (SIF) was >1m for up to 250ml of SIF (Fig. 4.5 (d)), (see Methods for preparation). The 250ml of SGF and

SIF are chosen as they represent the mean gastrointestinal fluid volume under fasting and fed conditions [22–23]. We could similarly communicate with iMAG over 1m away when placed in 250ml of porcine gastric juice. The next step is to evaluate the communication range under *in vivo* settings in the presence of several layers of body tissue—skin, fat, muscle, and organs, which not only cause absorption of the RF signal by the ionic and dipole concentrations in these layers, but also multipath reflections due to the heterogeneous nature of the tissue [24]. The range *in*

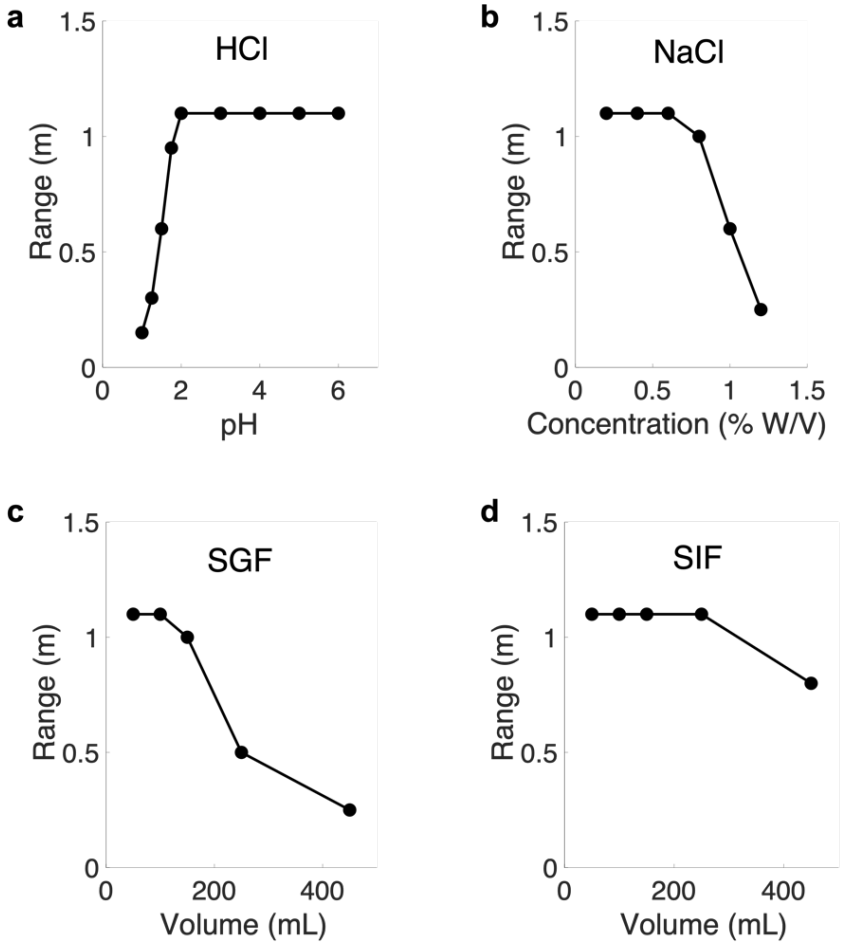

Fig. 4.5: *In vitro* characterization of the communication range between iMAG and the receiver board. The range was measured for: (a) 250ml HCl with varying pH; (b) 500ml NaCl solution with varying salt concentration; (c) Simulated Gastric Fluid (SGF); and (d) Simulated Intestinal Fluid (SIF) with varying quantity. All range values >1m are labeled as 1.1m since that is sufficient range here.

vivo when iMAG was placed endoscopically in the gastric cavity of an anesthetized pig was >1m. Thus, iMAG achieves sufficient communication range for evaluation in a large animal model. For evaluating the communication time, iMAG was submerged in an HCl solution (pH = 1.5) for two weeks which is towards the higher end of GI transit-time in pigs, and was communicated with within every few hours (see Methods).

4.3 Electromagnetic coils for 3D magnetic field gradients

We designed electromagnetic coils to generate the gradients G_X, G_Y and G_Z to be ≥ 3mT/m across the entire FOV (40x40x20cm^3, Fig. 4.6) to ensure a resolution of 1mm across all three spatial dimensions. To create a Z-axis gradient in the magnetic field magnitude, a planar circular coil is designed to carry current in counter-clockwise direction (Z-Coil in Fig. 4.6), producing a monotonically decaying magnetic field magnitude as the Z-distance from the coil is increased (Fig. 4.7 (a)). The DC current is chosen as 15A to get G_Z > 3mT/m at all boundary planes of the FOV.

The X-Coil (Fig. 4.6) consists of two halves carrying currents in opposite directions to produce a magnetic field B_X that points into (right, negative) and out of (left, positive) the plane. While computing $\|B_X\|$, the sign information is lost and results in identical values from both the halves, shown below the X-Coil in Fig. 4.6, making 75% of the coil area unusable. Since the Z-Coil produces an always-positive field (Fig. 4.7 (a)), it can be used to correct for the non-monotonicity in the X-Coil's field [25] (see Methods). With both the coils powered simultaneously during the X-measurement phase, the resultant magnetic field along the X-axis is strictly monotonic over the entire X-FOV (Fig. 4.7 (b-c)). Variations of the X-gradient in the FOV are explained in the Methods Section. The Y-Coil is identical to the X-Coil (Fig. 4.6) except for a 90^0 rotation. During the Y-measurement phase, both the Y and Z coils are powered simultaneously (Fig. 4.8). Fig. 4.9 shows the fully assembled gradient coils. The Z-Coil consists of 2 layers, each with 80 turns, and each elongated

half of the X and Y coils consists of 2 layers, with 68 turns/layer (Embodiment-1 in Fig. 4.11 and Table 2.1).

A major safety consideration of our system is the potential for peripheral nerve stimulation (PNS) resulting from gradient-switching by the coils. The 10ms rise-time for the gradients (Fig. 4.8) used in this work is significantly slower than the 0.1-1ms rise-time used in fast MRI scanners. PNS threshold is commonly defined as the peak $d|B|/dt$ value, reported to be 43-57T/s [26], which is more than an order of magnitude higher than our peak value of 1.5T/s (Fig. 4.10). In addition,

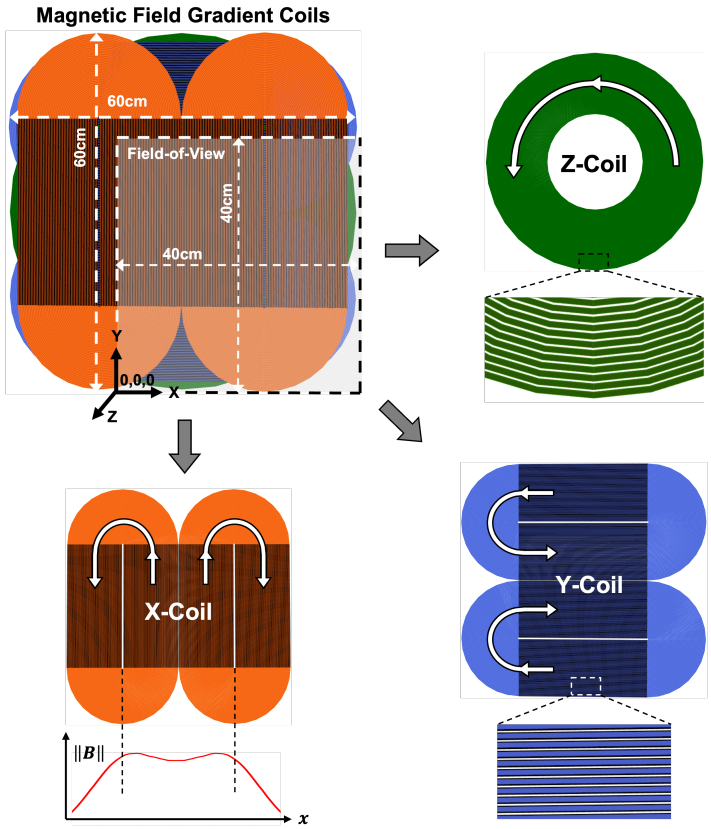

Fig. 4.6: Magnetic field gradient generating coils for X, Y, and Z are shown. Z-Coil consists of a single spiral carrying current in one direction. X-Coil consists of two elongated spirals carrying currents in opposite directions. The magnitude function causes both the spirals to produce identical field values. Y-Coil is identical and orthogonal to X. All three coils are stacked together concentrically, resulting in a planar coil structure with an effective FOV of 40x40x20cm^3.

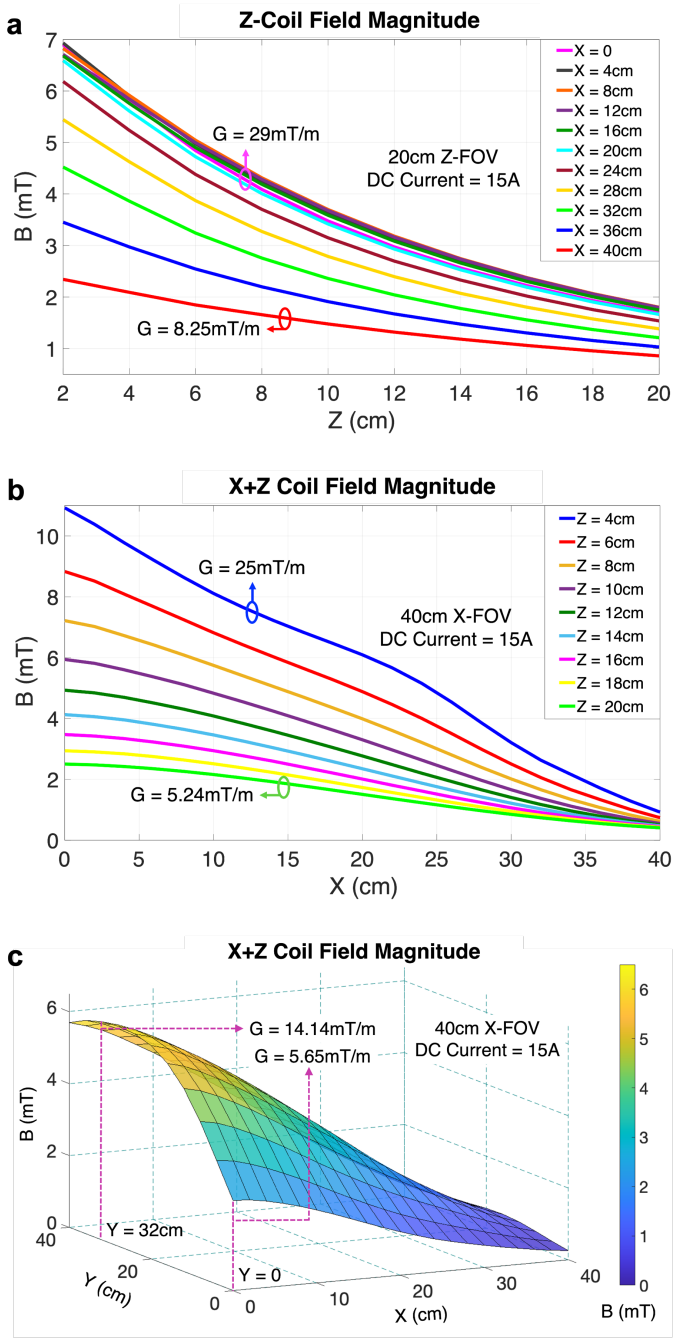

Fig. 4.7: Magnetic field variation. (a) Field profile produced by the Z-coil, plotted along the Z-axis while varying the X-coordinate (at Y=20cm). Identical plots are obtained as the Y-coordinate is varied since the field is symmetric about the X and Y directions. (b) X-axis magnetic field profile, plotted for a varying Z-coordinate (at Y=20cm), when both the X and Z coils are on together. (c) X-axis field profile as the Y-coordinate is varied (at Z=10cm). Similar plots are obtained along the Y-axis when both Y and Z coils are on together.

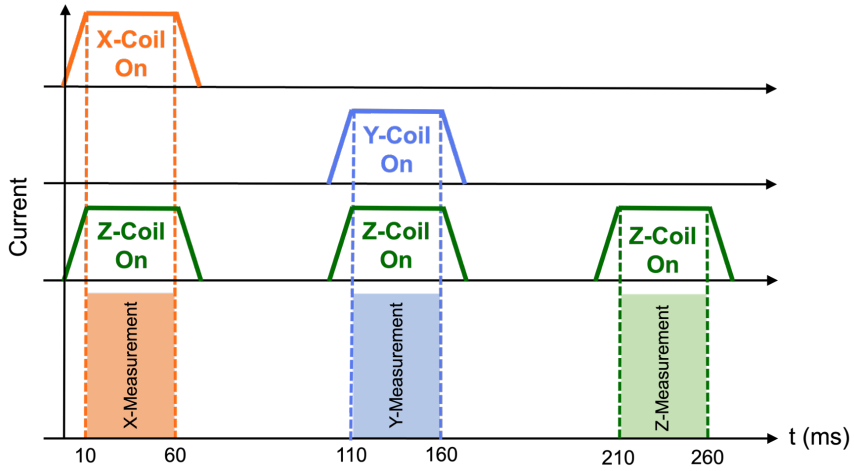

Fig. 4.8: Global timing diagram showing the measurement phases with the gradient coils on/off times. Z-coil is kept on during the X and Y measurements to produce monotonically varying magnetic field magnitudes along the respective axes.

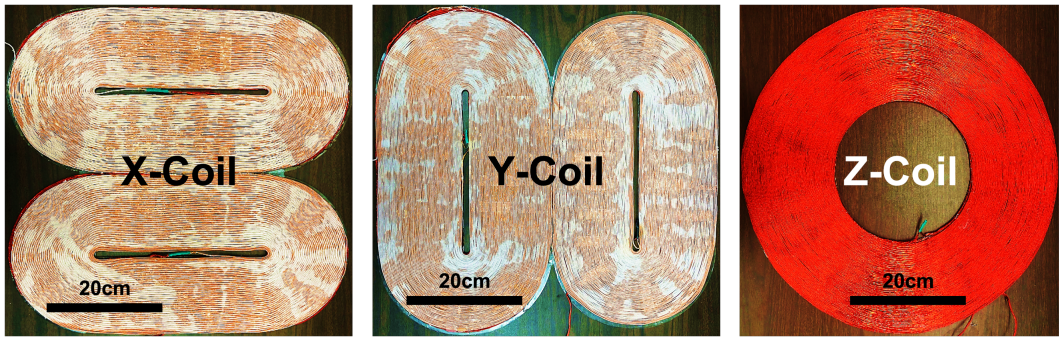

Fig. 4.9: Fully assembled X, Y, and Z gradient coils using 50/32 AWG Litz wire.

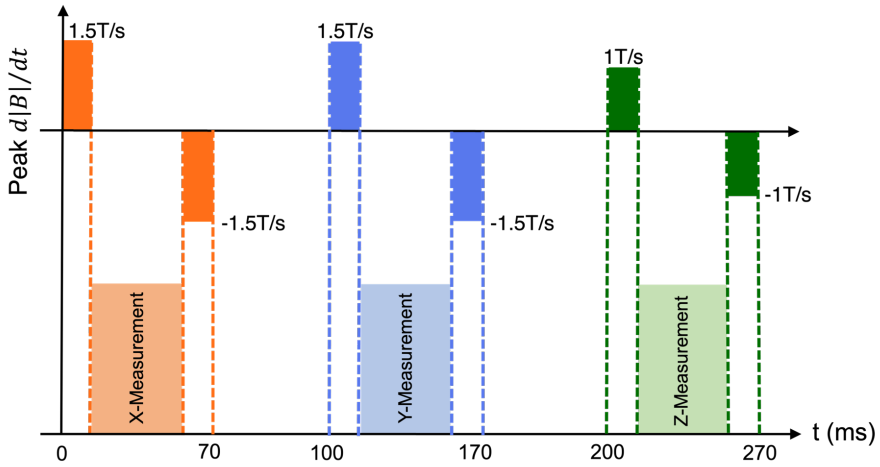

Fig. 4.10: Peak $d|B|/dt$ values plotted for the entire measurement phase. All values are significantly less than the recommended safety threshold of 20T/s.

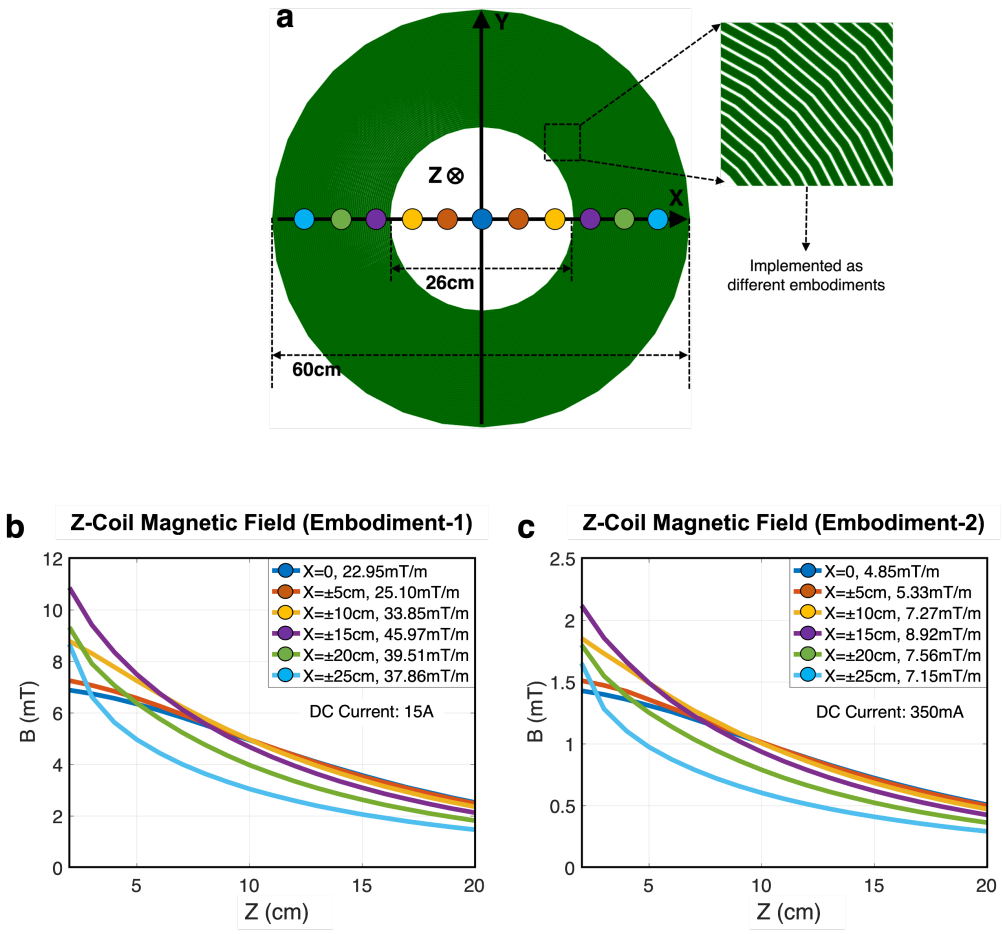

Fig. 4.11: Different coil embodiments. (a) The flat-spiral Z-coil is shown and is made using several loops of copper wire beginning from an inner diameter of 26cm and extending to an outer diameter of 60cm. Using different diameters of the copper wire, different embodiments of the Z-coil (and similarly the X and Y coils) can be realized. (b) Gradient profiles generated by the Z-coil of Embodiment-1 carrying 15A of DC current. The prototype used in this work is an implementation of Embodiment-1. (c) Gradient profiles generated by the Z-coil of Embodiment-2 carrying 350mA of DC current. The gradient in Embodiment-2 is only 5x lower than the gradient in Embodiment-1, while the DC current is 43x lower. This is achieved by using a much smaller diameter of the copper wire for Embodiment-2 that results in ≈9x increase in the number of turns that can be fitted in the same coil footprint.

PNS effects are considered negligible when switching time is >5ms and $|B| <$ 100mT [27]. Both of these metrics are satisfied by our system. Considering the rise-time along with the peak $d|B|/dt$ value, the International Electrotechnical

Commission (IEC) thresholds for PNS and cardiac stimulations have a common asymptotic value of 20T/s at long rise-times (>5ms) [28], which is significantly higher than the 1.5T/s gradient-switching employed here. Additionally, no mechanical movement was observed in any of the magnetic equipment placed in the vicinity of the coils, ensuring minimal risk due to the induced magnetic force and torque.

Another safety consideration for the gradient coils is the heat generated during measurements. From Fig. 4.8, it can be seen that a single measurement cycle lasts less than 300ms. Given the several-hour long transit through the stomach, small

Comparison between different Coil-Embodiments

Specification	Embodiment-1	Embodiment-2
Wire Diameter	2.2mm	0.25mm
Number of Turns	68 (X, Y-Coil), 80 (Z-Coil)	590 (X, Y-Coil), 670 (Z-Coil)
Number of Layers	2 (X, Y, Z-Coil)	2 (X, Y, Z-Coil)
Coil Resistance	3.7Ω (X, Y-Coil), 3.2Ω (Z-Coil)	565Ω (X, Y-Coil), 486Ω (Z-Coil)
Coil Inductance	8.8mH (X, Y-Coil, measured) 9.7mH (Z-Coil, measured)	621mH (X, Y-Coil, simulated) 683mH (Z-Coil, simulated)
DC Current	15A	350mA
Power Required During Measurement	800W	60W
Average Heat Dissipation	3.3W (for once per minute)	0.25W (for once per minute)
Mean Position Resolution	1.5mm	7.5mm
Coil Weight	18kg	1.2kg
Battery Weight	N/A	< 200g
Use-Case	Coils on Wall / Toilet Seat	Coils in Jacket / Backpack

Table 2.1: Comparison of the two embodiments shown in Fig. 4.11. The 350mA of current in Embodiment-2 leads to only 0.25W of heat (corresponding to $<0.1^0$C increase in the surface temperature of the coils) for a measurement done every minute, which is sufficient for monitoring the GI transit-time and motility. For applications requiring a higher sampling rate (maximum achievable 3.3Hz by the current system), thermal insulators can be used around the coils to alleviate the heating. The 7.5mm of mean position resolution for Embodiment-2 is acceptable for localization in the GI tract. The total weight of the coils in Embodiment-2 and the required battery for powering the coils is suitable for portable prototypes such as jackets or backpacks.

intestines and colon [2–3,7–8], and 1–2 contractions per minute in each of these organs on an average [8], one measurement per minute is sufficient for accurate monitoring of transit-time and motility. For such sparse measurements, the average heat produced in the coils is only 3.3W, which is easily dissipated by the large coil area. The power, heat, weight and other specifications of the coils are listed under Embodiment-1 in Table 2.1. Though the heat generated is negligible, the transient power during each measurement is 800W, which is not suitable for portable prototypes. Another challenge for portability is the high weight of the coils. To circumvent these, a more portable-friendly prototype (Embodiment-2 in Fig. 4.11 and Table 2.1) can be fabricated. Using a copper wire with 0.25mm diameter, ≈9x more turns can be fitted into the same footprint as the current prototype. The large number of turns relax the current requirement significantly, with only 350mA of DC current and 0.25W of heat for Embodiment-2, which leads to $<0.1^0$C rise in the surface temperature during measurements. However, the mean position resolution is lowered to 7.5mm, which is still acceptable for localization in the GI tract. For stationary prototypes used in walls or toilet seats, the 15A current carrying Embodiment-1 can be used for higher accuracy of localization. The coils can also be operated at the theoretically maximum sampling frequency of 3.3Hz (1/300ms) for applications requiring a higher refresh rate, and the heat generated can be alleviated by using thermal insulators around the coils.

4.4 Spatiotemporal resolution and system characterization

The value of ΔB found experimentally using the 3D magnetic sensor is 15μT, which corresponds to Δx ranging from <1mm (when G > 15mT/m) to 5mm (when G = 3mT/m). iMAG's lowest resolution of 5mm occurs only at the boundary planes of the FOV and is 1-2mm elsewhere, resulting in a volume-averaged mean value of 1.5mm (Fig. 4.12). The precision and repeatability of the gradients play an important role in the error performance. We achieved <5% error in the gradients during each measurement by custom designing a coil controller (see Methods) and extensive

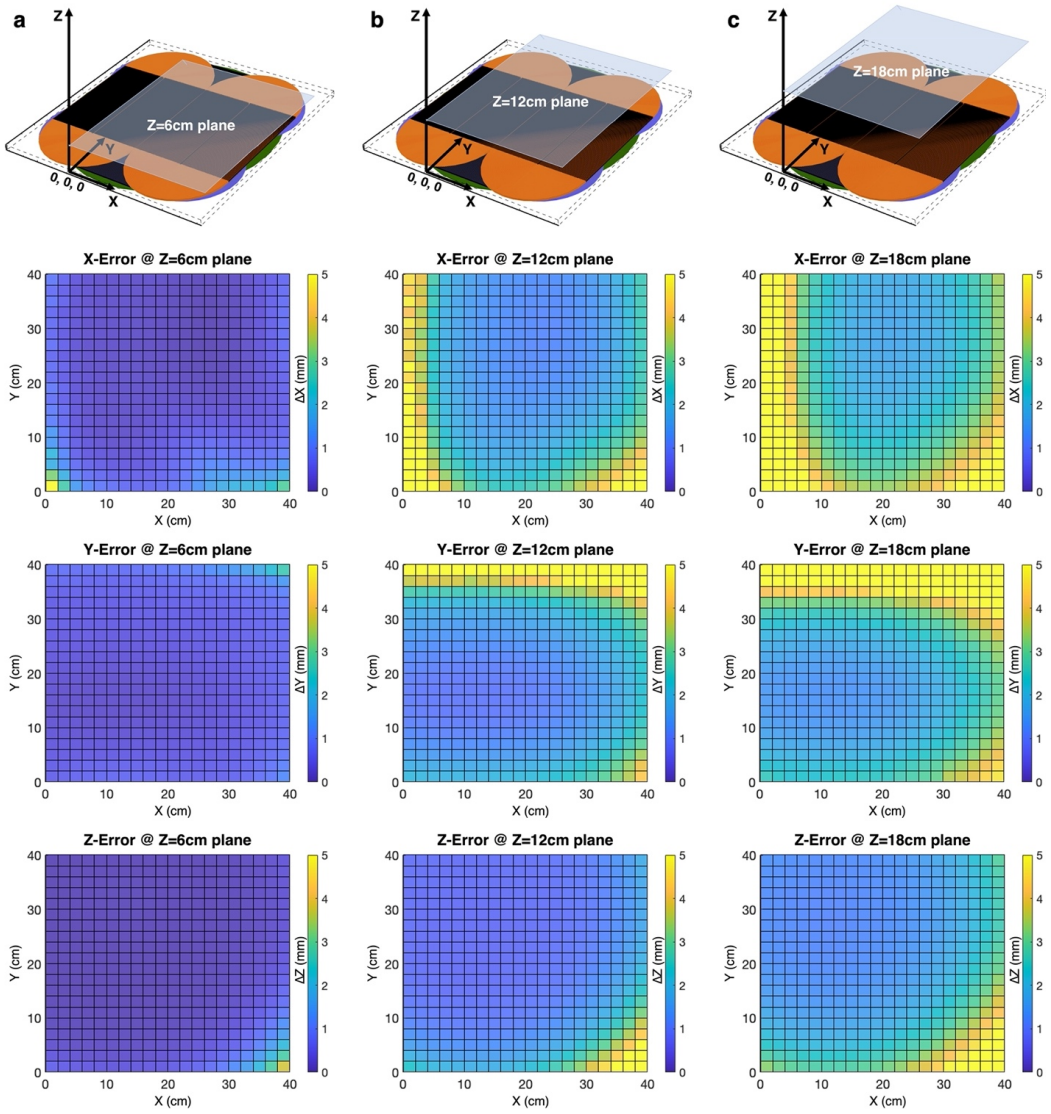

Fig. 4.12: The spatial error while localizing a single iMAG relative to the gradient coils is plotted. (a) For Z=6cm plane. The X, Y and Z errors (shown below the coil-setup) are close to the lower error-bound of the system (≈1mm). (b) The spatial errors are plotted for Z=12cm plane and the errors in most regions of the FOV are in 1–2mm range. The transition to the higher error-bound of the system (≈5mm) is visible at the boundary planes of the FOV. (c) The spatial errors are plotted for Z=18cm plane and the presence of the higher error-bound of the system (yellow regions) is more prominent at the boundary planes of the FOV compared to the Z=12cm plane. The FOV ends at Z=20cm and the remaining half of the 40x40x40cm^3 FOV is covered by the other set of the gradient coils shown in Fig. 4.6.

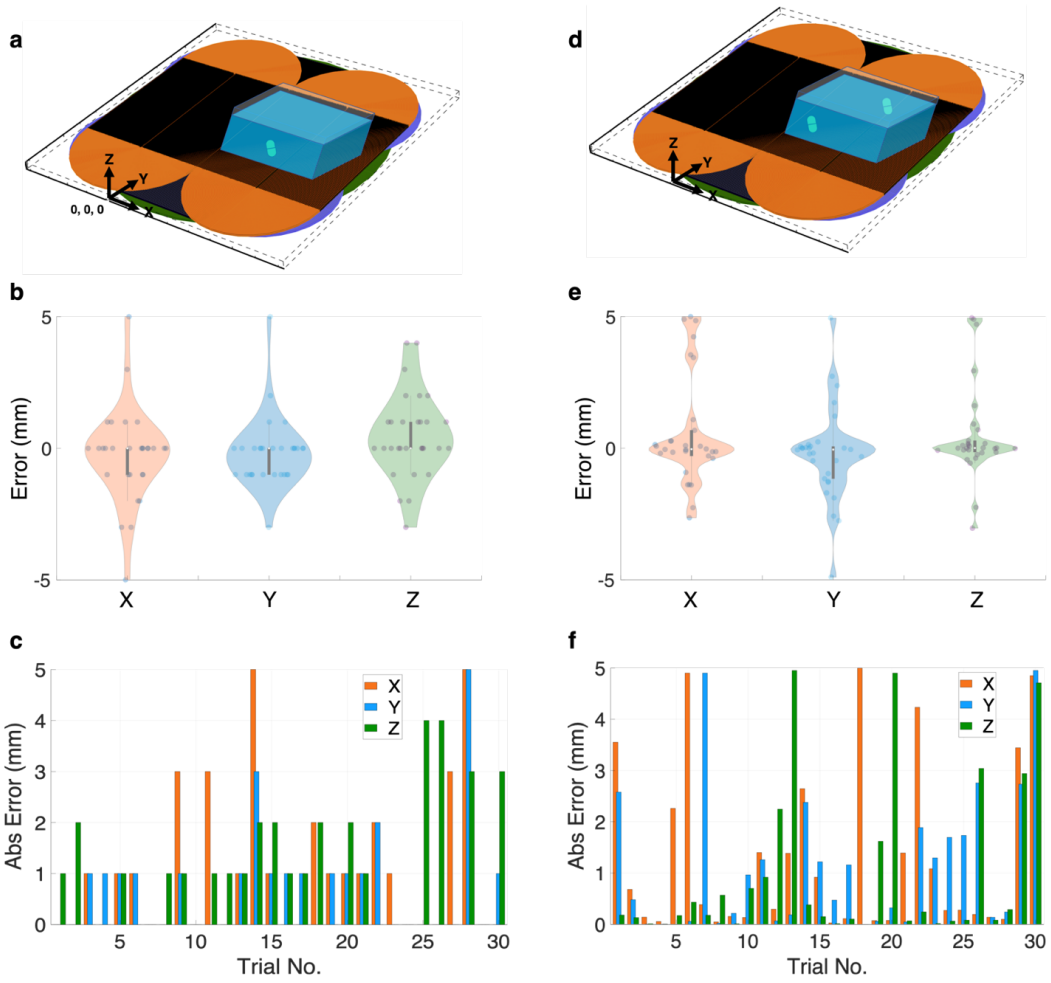

Fig. 4.13: *In vitro* characterization. (a) Localization of a single iMAG with respect to the global origin (0,0,0) of the coils at n=30 different locations chosen uniformly in the FOV. (b) Errors at all 30 locations clustered together. (c) Error at each location is plotted separately. Reported as mean ± std: 1.07 ± 1.44mm (X), 0.77 ± 1.07mm (Y), 1.13 ± 1.20mm (Z). (d) *In vitro* localization of iMAG with respect to another iMAG at a known location serving as a relative reference. This eliminates the need for a global reference point. n=30 different locations were chosen uniformly in the FOV. (e), (f) Error in the decoded position of iMAG localized with respect to a reference iMAG. Error as mean ± std: 1.34 ± 1.68mm (X), 1.13 ± 1.38mm (Y), 0.97 ± 1.55mm (Z).

characterization (see Methods). For applications requiring a higher spatial resolution, several measurements at a single location can be averaged to reduce the effect of the sensor-noise [25,29]. The same can be achieved by increasing the gradient G at the

cost of higher current and/or more layers of coils. For GI monitoring applications, sub-cm of resolution is acceptable since the GI system exhibits cm-scale of relative motion even under still external conditions [30]. The temporal resolution of iMAG is dictated by the total delay between sending a wireless ping and completion of the 3D position decoding, which is <300ms (Fig. 4.8), providing sufficiently real-time position update for applications in this work.

We first tested the system *in vitro* to demonstrate functionality and verify the theoretical localization resolution. The 3D position of a single iMAG submerged in a saline-tank was found with respect to the global origin of the coils (0,0,0 in Fig. 4.6). The error is defined as the difference between the actual and the decoded position. The absolute peak and mean error magnitudes in X, Y and Z (Fig. 4.13 (a-c)) were ≤5mm and ≤1.2mm respectively, as the location of iMAG was varied uniformly in the FOV. To eliminate the fixed reference (global origin), we added another iMAG at a known location in the tank (Fig. 4.13 (d)) to serve as a relative reference for the main iMAG. The peak and mean errors in the decoded distance between the main and reference iMAG were ≤5mm and ≤1.4mm respectively at all the locations (Fig. 4.13 (e-f)).

We performed *in vivo* testing and characterization in porcine models as they represent a reliable analogue for the human application, given their anatomy and size [31]. A custom wooden chute was designed with two sets of gradient coils, each comprising the X, Y, and Z coils (Fig. 4.14 (a)). The two coil-sets are needed to generate 40x40x40cm^3 of FOV spanning the porcine GI tract. Unwanted interference between the fields produced by the two coil-sets was eliminated by sequential powering. We tested the system's accuracy *in vivo* using a test fixture (Fig. 4.14 (b)) with two iMAG devices positioned a fixed distance apart (81.12mm). The fixture was deployed endoscopically into the gastric cavity (Fig. 4.14 (c)). The decoded distance between the two devices was 83.6 ± 0.7 mm, falling within our desired error margin of 5mm (Fig. 4.14 (d-e)).

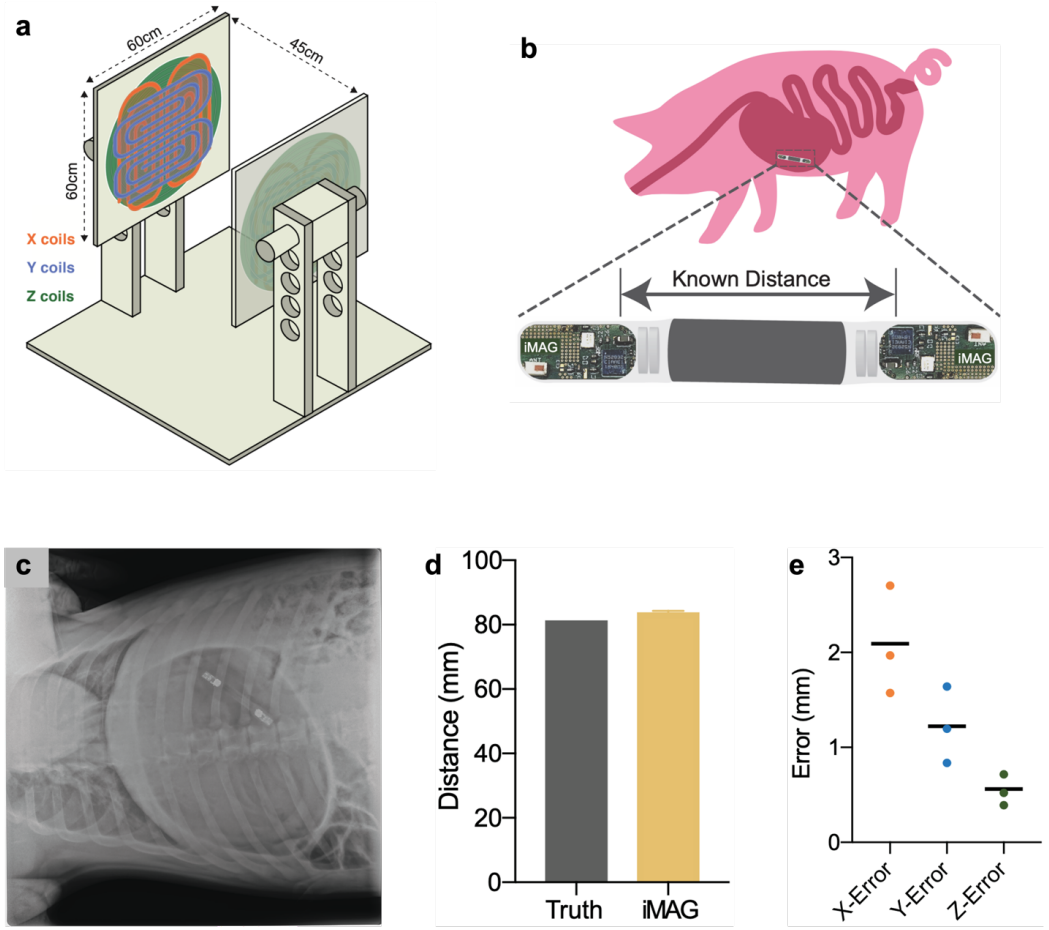

Fig. 4.14: *In vivo* characterization. (a) Custom designed wooden chute with two sets of gradient coils on each side to provide a 40x40x40cm^3 FOV with adjustable height. (b) Test fixture with two iMAG devices positioned a fixed distance apart and lodged into the gastric cavity of the pig. (c) X-ray scan of the animal showing the position of the test fixture. (d) The decoded inter-device distance from iMAG is 83.6 $\pm$ 0.7mm (mean $\pm$ std), plotted alongside the ground-truth distance of 81.12mm. (e) Individual errors in the X, Y, and Z components of the decoded distance are plotted.

4.5 *In vivo* evaluation

We first sought to emulate a real-world setting where an iMAG would be ingested and its position would be tracked relative to a reference iMAG located externally on the skin of the ambulatory animal. The iMAG was administered endoscopically (Fig.

4.15 (a)) and evaluated upon passage to assess electrical and mechanical integrity. The signal strength detected by the receiver while localizing the ingested iMAG is

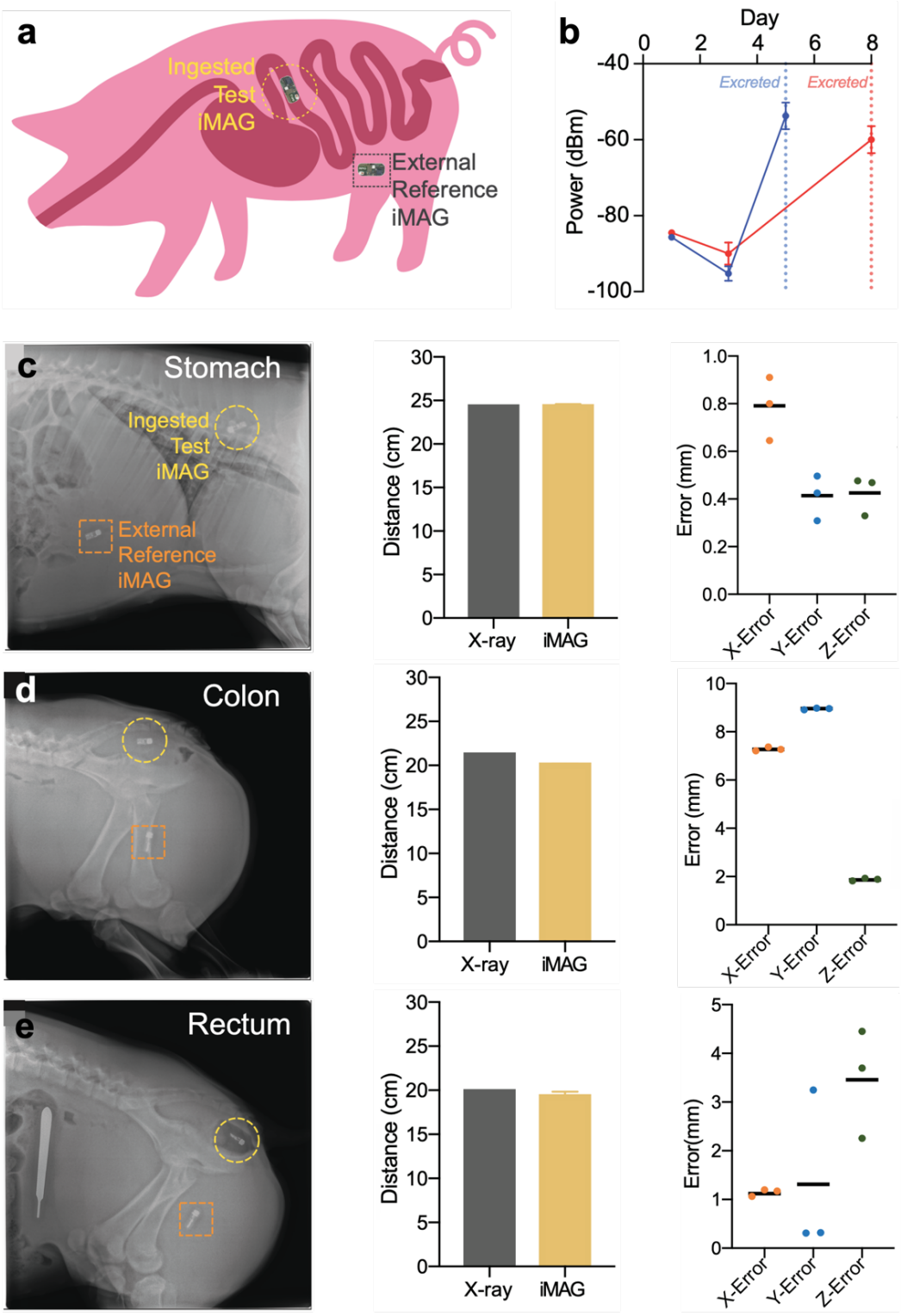

Fig. 4.15: Chronic *in vivo* studies. (a) Two iMAG devices are used with one serving as the ingested test iMAG, and the other attached externally on the skin in the abdominal region to serve as the reference iMAG. Localization of the two devices is performed on each test-day (M/W/F). (b) Signal strength (plotted as mean ± std) detected by the receiver while localizing the ingested iMAG on different test days. When located in the stomach and SI, the signal strength is -80 to -100dBm, which increases to -70dBm or higher when located in the colon or rectum. To compare the decoded distance of the ingested iMAG from the reference, X-ray scans were conducted when iMAG was located in the: (c) stomach; (d) colon; and (e) rectum. The position of the external reference iMAG is shown in each scan. The error between the distance given by the X-ray and iMAG is found to be (reported as mean ± std): 0.54 ± 0.21 mm for stomach; 6.04 ± 3.70 mm for colon; and 1.97 ± 1.30 mm for rectum. The iMAG devices remained fully functional upon excretion, confirming their long-term viability in a chronic setting. All iMAG decoded distance bars are plotted as mean ± std. n=3 for all the distance and error measurements. n=4 for all the signal strength measurements.

plotted in Fig. 4.15 (b). The signal strength when iMAG is located in the stomach and small-intestines (SI) is –80 to –100dBm, approaching the noise-floor of the receiver when less than -95dBm. The signal strength increased to over –70dBm when located in the colon or rectum. The ingested iMAG was localized in different regions of the GI tract: (i) stomach (Fig. 4.15 (c)); (ii) colon (Fig. 4.15 (d)); and (iii) rectum (Fig. 4.15 (e)). The error in the decoded distance between the ingested and the reference iMAG devices, when compared with the distance obtained from the X-ray scans, was found to be <5mm for the stomach (Fig. 4.15 (c)) and rectum (Fig. 4.15 (e)), and <10mm for the colon (Fig. 4.15 (e)). The *in vivo* error values reported here are over-estimations, as explained in the Methods section. The ingested iMAG devices remained functional upon excretion (signal strength >–60dBm), thus confirming their applicability for chronic use.

We next investigated the utility of our system in a fecal incontinence (FI) model [32]. To monitor the movement of feces in the distal colon, our FI model comprised a freely moving iMAG in the lumen of the distal colon and a reference iMAG located

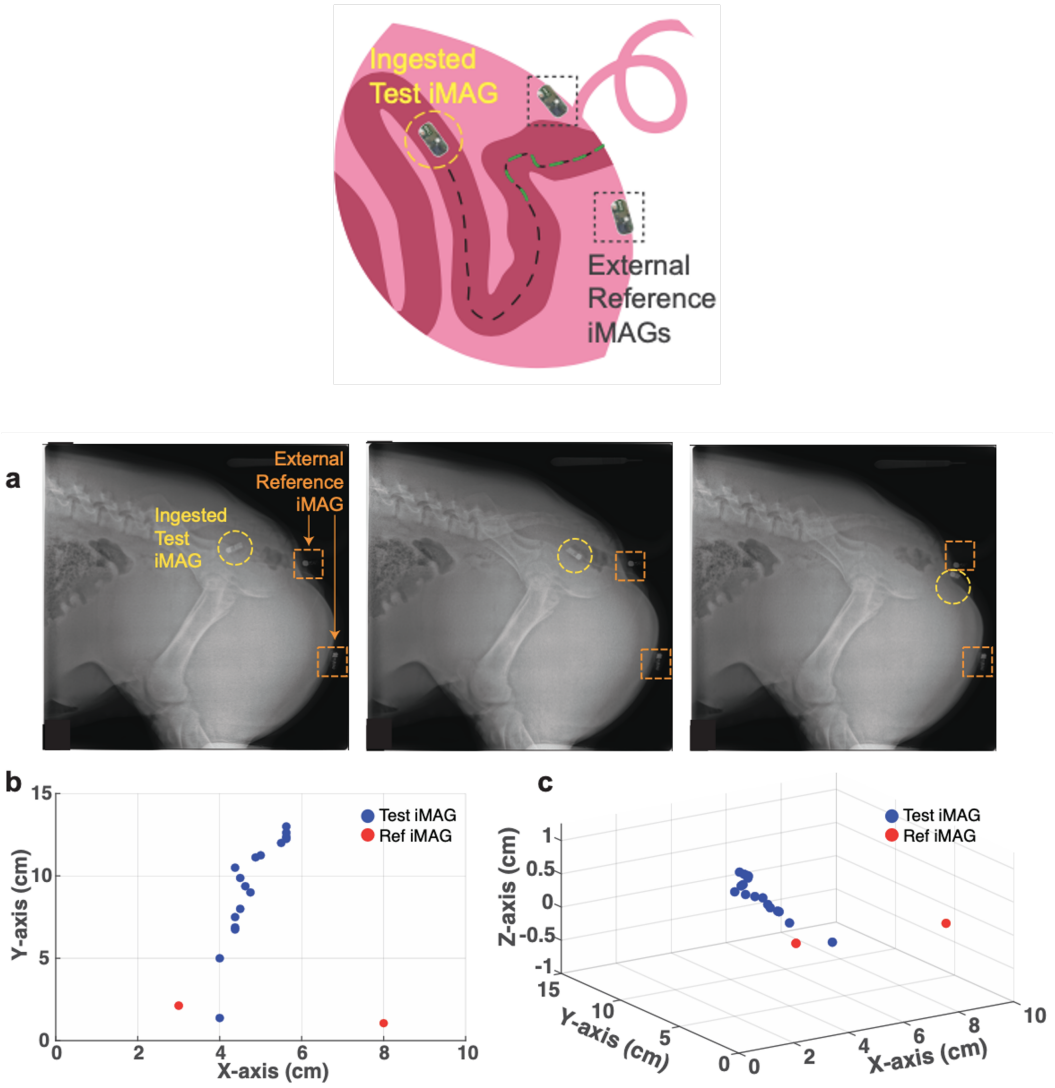

Fig. 4.16: iMAG for fecal incontinence monitoring. (a) iMAG placed 16cm proximal to the anal verge of the pig using a catheter and two reference iMAG devices fixed externally on the skin. The iMAG was pulled out in increments of 5mm and a measurement was made at every step to reconstruct the trajectory. (b) Top-view and (c) side-view of the reconstructed 3D trajectory which was successfully mapped to the colonic anatomy. On comparing the decoded distance traversed by the iMAG with the actual distance moved by the catheter, our system serves as an accurate (>97%) indicator of defecation.

on the skin surface near the anal sphincter. The objective was to detect the presence of the moving iMAG when within a specific distance (chosen here as 10cm) of the

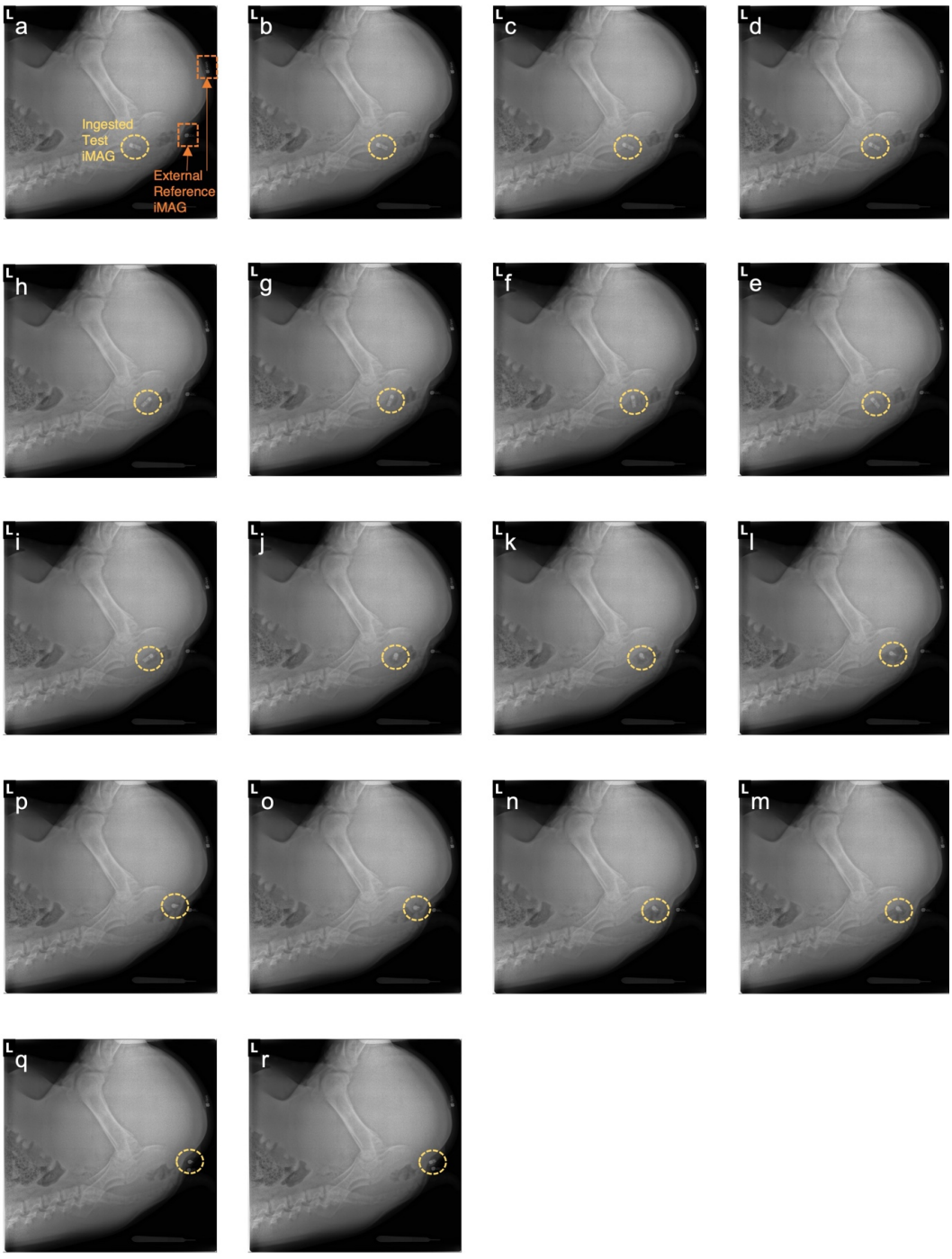

Fig. 4.17: Consecutive X-ray scans obtained while moving the iMAG (connected to a catheter) out of the anal sphincter in steps of 5mm during the fecal incontinence study (a)-(r). Detailed results shown in Fig. 4.16.

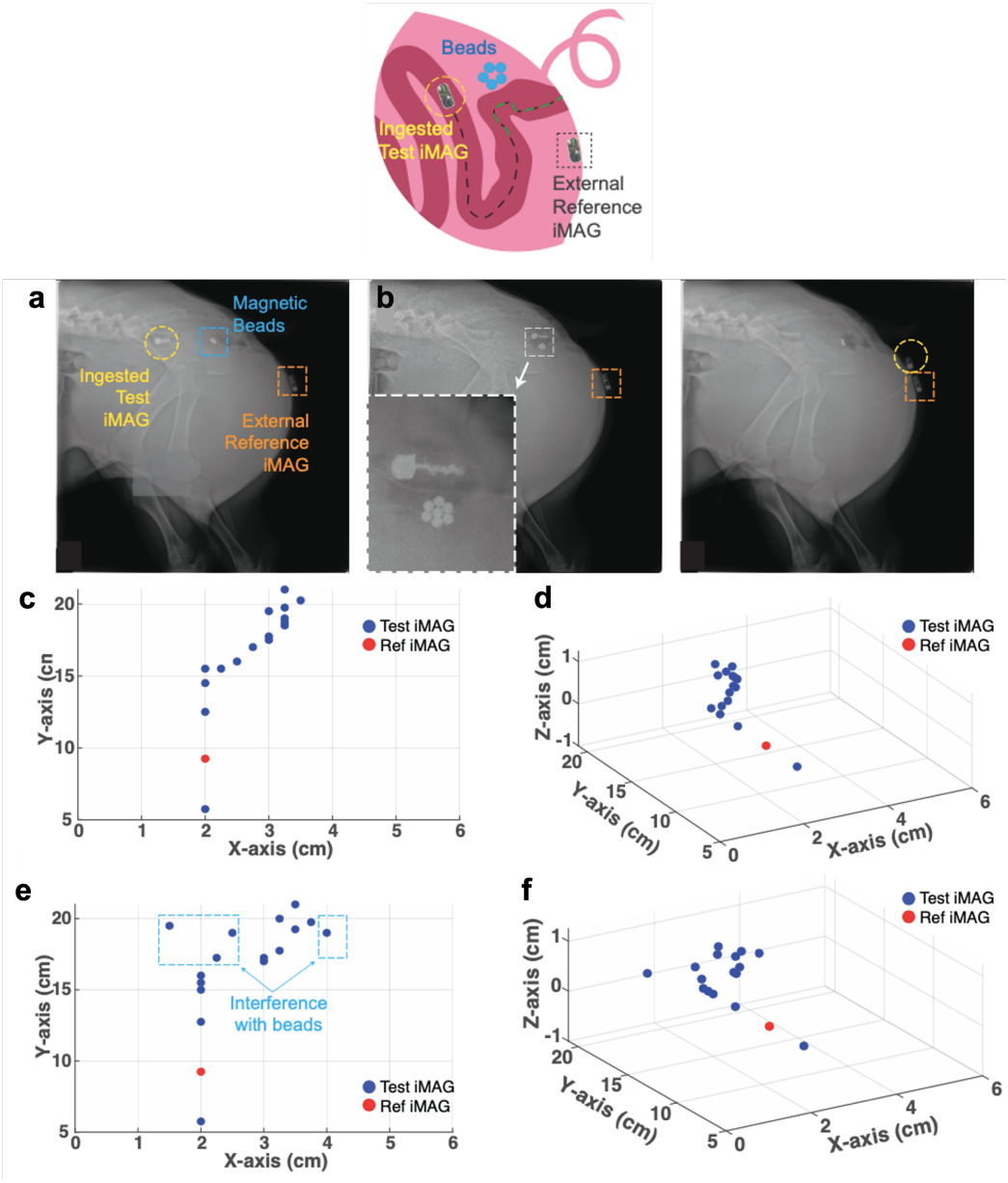

Fig. 4.18: Colonic passage study of iMAG in the presence of magnetic barium beads. (a)-(b) Placement of barium beads inside colon. (c) Top-view and (d) side-view of iMAG's trajectory in the absence of barium beads, showing close resemblance to the reconstructed colonic anatomy in Fig. 4.16 for a different pig. (e) Top-view and (f) side-view of the trajectory in the presence of barium beads, distinctly showing the errors in the decoded position due to the distortion of magnetic field when the beads are in close proximity (<5cm) to iMAG. This shows that not only is our system sensitive to the presence of magnetic labels, but also immune to them when located sufficiently away (>5cm in this case) from the iMAG being localized.

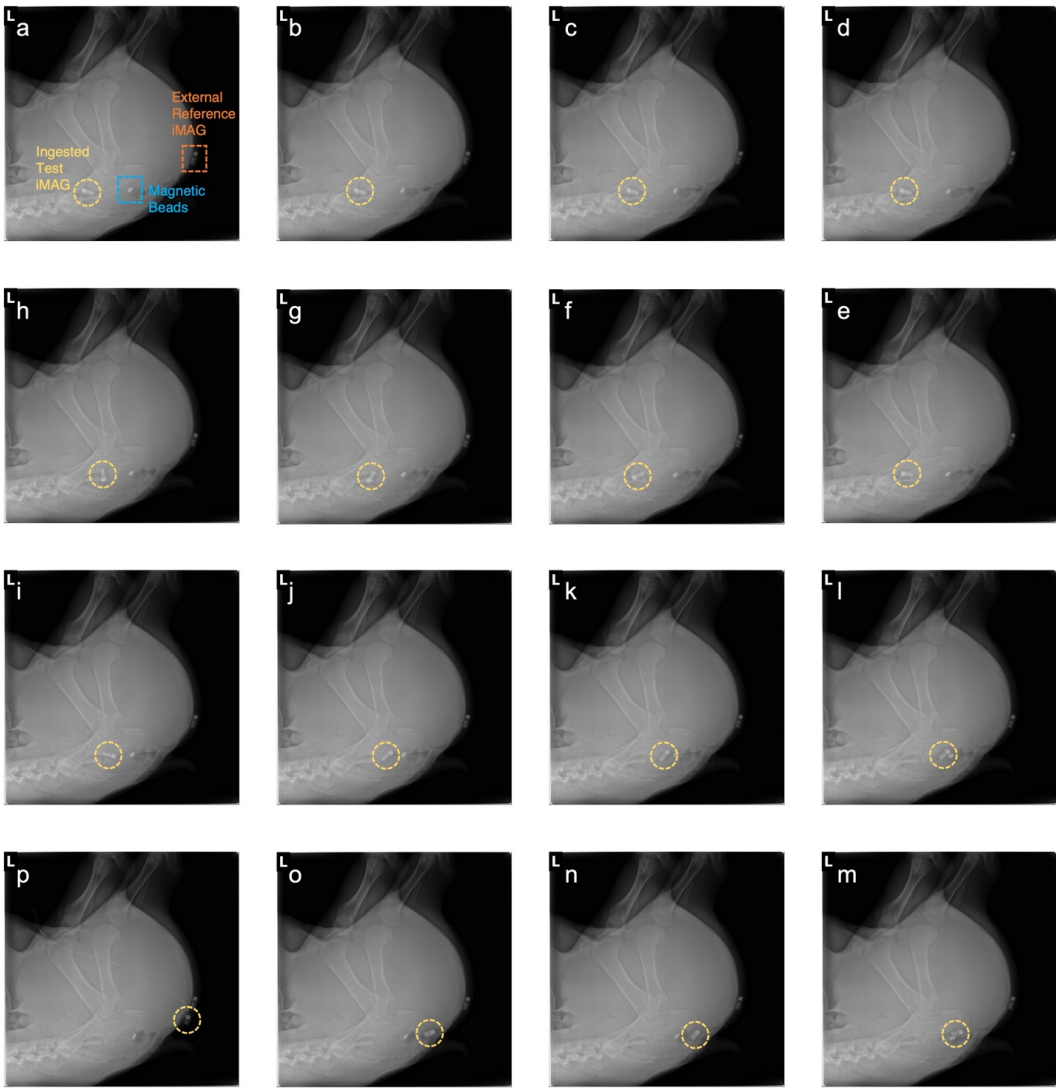

Fig. 4.19: Consecutive X-ray scans obtained while moving the iMAG (connected to a catheter) out of the anal sphincter in steps of 5mm during the magnetic label (barium beads) tracking study (a)-(p). Detailed results shown in Fig. 4.18.

and fixed two reference iMAG devices externally (Fig. 4.16 (a)). The iMAG was pulled out in increments of 5mm, with a measurement being made at every step and the reconstructed trajectory shown in Fig. 4.16 (b–c). The consecutive X-ray scans performed during the measurements are shown in Fig. 4.17. When the iMAG was 10cm inside, the error in the distance between the reference and the moving iMAG was <3mm, which validates the functionality of the system as an accurate (>97%)

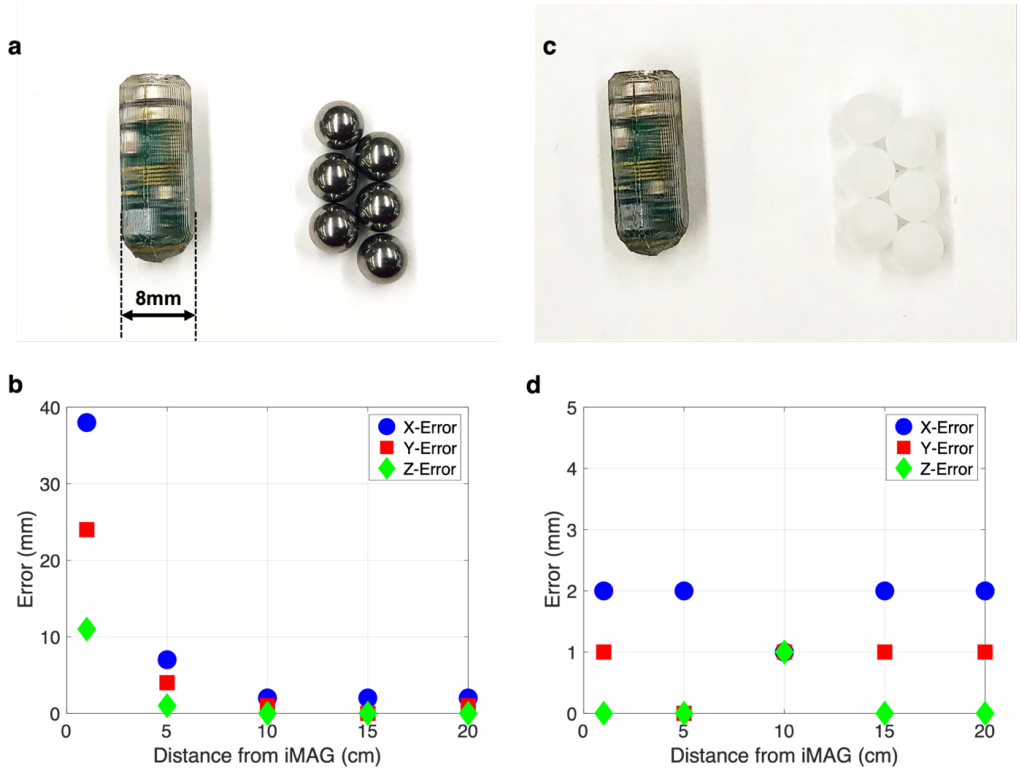

Fig. 4.20: Magnetic interference characterization performed by localizing an iMAG device in the presence of magnetic vs non-magnetic beads. (a) iMAG device shown next to highly magnetic barium beads used during the magnetic-label tracking study performed in this work (Figs. 4.18–19). (b) Localization error of iMAG plotted vs distance from the barium beads. When the beads are very close to iMAG (<5cm), the error is significantly higher than the 5mm error-threshold of the system due to the distortion caused in the magnetic field by the beads. As the distance of the beads from the iMAG is increased to 10cm or higher, the error falls within the threshold limit which signifies the system's immunity to distortion caused by magnetic objects when located sufficiently away. (c) iMAG device shown next to non-magnetic polyethylene beads used as a negative control to compare against the interference caused by the magnetic barium beads. (d) Localization error of iMAG as the distance of the polyethylene beads is varied from iMAG. As seen, the error values are independent of the proximity from the beads and are within the error-threshold, highlighting the specificity of our system toward magnetic objects.

indicator of defecation. We were also able to map the iMAG trajectory to successfully reconstruct colonic anatomy (Fig. 4.18 and Fig. 4.21) across multiple animals.

Finally, we evaluated the use of iMAG as an *in vivo* sensor of pre-labeled locations within the GI tract. We placed magnetic barium beads at a specific location in the colon (Fig. 4.18 (a)) and used our system to sense when the ingested iMAG passed this location (Fig. 4.18 (b)). We then mapped the iMAG's trajectory without (Fig. 4.18 (c-d)) and with (Fig. 4.18 (e-f)) the barium beads. The highly magnetic beads interfere with the local magnetic field, thus impacting magnetic field readings by iMAG. The error in the decoded position was significant (>1cm, Fig. 4.18 (e-f)) when iMAG was within 5cm of the beads, thus demonstrating our system's specificity to magnetic labels. The consecutive X-ray scans performed during the measurements are shown in Fig. 4.19. In a clinical scenario where the location of such labels is unknown, iMAG can make an additional measurement each time before the gradient coils are switched on. The magnetic field produced by the labels can be sensed by iMAG and distinguished from the relatively-low background earth's field (<60μT). A prior anatomy-map obtained from an existing imaging modality (X-ray/MRI/CT) that shows the relative location of the labels can be used as an additional reference. We have also evaluated the effect of interference using non-magnetic polyethylene beads for negative control and compared with the interference caused by the magnetic barium beads (Fig. 4.20).

4.6 Clinical Applications

The real-time and mm-scale localization resolution of iMAG holds the potential for significant clinical benefit. Quantitative assessment of GI transit-time is vital in the diagnosis and treatment of pathologies related to delayed or accelerated motility such as gastroparesis, Crohn's disease, functional dyspepsia, regurgitation, constipation, and incontinence [1–4]. Other applications that could benefit from the high spatiotemporal accuracy of our system are therapeutic interventions like anatomic targeting for drug delivery, monitoring of medication adherence, delivery of macromolecules and electrical stimulation to specific regions of the GI tract in a wireless fashion [11,33–34].

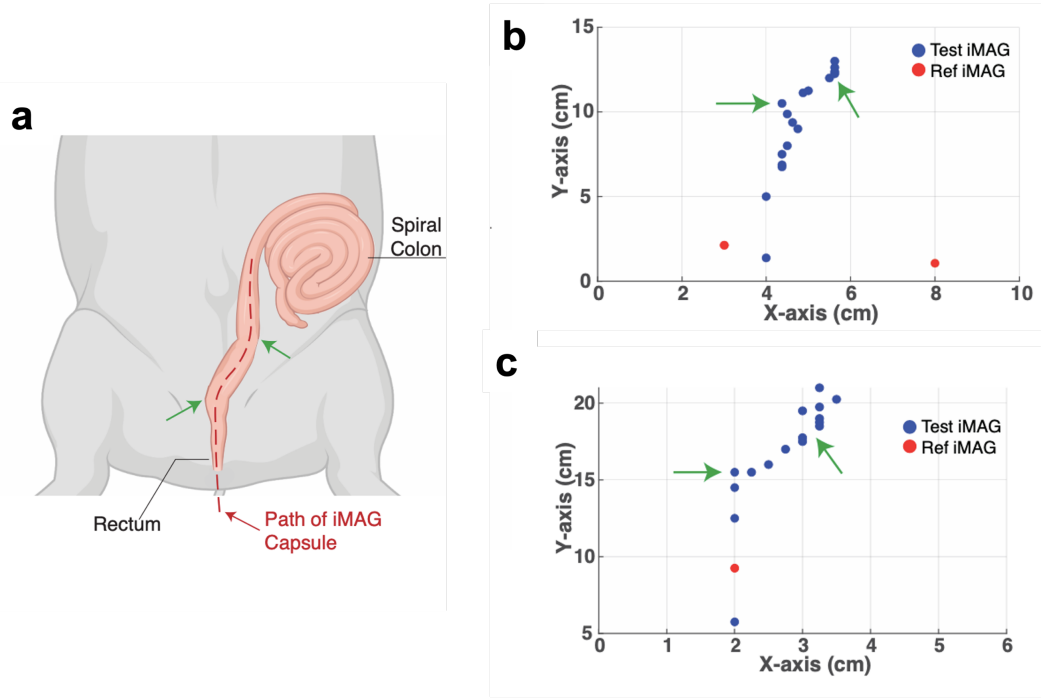

Fig. 4.21: iMAG for anatomic mapping. (a) Pig's colon shown for comparison. (b) iMAG trajectory from the fecal incontinence monitoring study. (c) iMAG trajectory from the magnetic label tracking study. The two sharp bends in the rectum are prominently visible (highlighted by green arrows) in (a) and are captured by both the iMAG trajectories shown in (b) and (c). This shows that our technology can distinguish anatomical features for organs that are retroperitoneally fixed in the GI tract, like colon. The trajectory maps in (b) and (c) are created by plotting together all the decoded position coordinates of iMAG using the magnetic field measurements performed by it as it moves along the colon.

We have shown our system to be a highly accurate indicator of defecation, which is of clinical significance for patients suffering from FI. An iMAG pill could be ingested with each meal to track its progress through the GI tract in patients with FI. The reference iMAG could be incorporated into 'smart' clothing for monitoring the bowel movements. The successful reconstruction of colonic anatomy (Fig. 4.21) also shows that iMAG can delineate complex and curved trajectories of the retroperitoneally fixed parts of the GI tract, which are hard to acquire through other imaging modalities (X-ray/CT). To localize the moving iMAG with respect to the patient's anatomical

features (like bones, muscles or other relatively-fixed internal body parts), a prior scan of the patient with the reference iMAG attached at a known external location, can be conducted using the existing imaging modalities such as MRI, CT, or X-ray scans. Using this one-time scan, the location of internal organs with respect to the reference iMAG can be known. The reference iMAG can be attached to the patient's skin using a Tegaderm™ patch (or other adhesives) anywhere in the abdominal region. The water-resistant patch will ensure that the reference iMAG stays at its location for the duration of the internal iMAG's passage.

We have also demonstrated iMAG's usage as an *in vivo* sensor to detect the location of magnetic particles and beads. This approach can be used to label injection sites, polyps, fistulas, stomas, or strictures requiring localized therapy, using anatomic markers such as magnetic beads or staples. Additional capabilities could be added to the iMAG devices, enabling them to measure and report pH, temperature, pressure, deliver drug payloads, and perform electrical/mechanical stimulation [1,4,35–36]. The stimulation/actuation can be performed upon localization of the ingested iMAG in the vicinity of the marker. The *in vivo* experiment using magnetic beads also demonstrates our system's robustness to field distortion caused by magnetic objects when located sufficiently away (>5cm in this case) from the devices being localized (Figs. 4.18–20). Sensing capabilities could enable iMAG to generate a spatiotemporal map for comprehensive patient diagnosis and assisting further in anatomic targeting using the pH and pressure profile. From a consumer electronics standpoint, iMAG offers the potential for non-invasive and location-specific measurement of physiological markers and vital parameters along the gut, which could be of interest in the field of fitness and smart-medicine [35].

4.7 Conclusions

Our system offers a high FOV, high spatial resolution in 3D, and fully wireless operation of the ingestible microdevices (Table 2.2). It also supports concurrent

multi-device usage. We use safe magnetic fields generated by non-obstructive planar electromagnets, and have demonstrated system functionality in large animals, illustrating its potential for use in non-clinical settings without the need for harmful radiation.

Prior magnetic tracking systems that localize a moving magnet inside the GI tract use an external array of magnetic sensors to reconstruct the magnet's position [14–18,37]. Since the reconstruction is based on the received magnetic field strength and direction at each sensor's location, it is susceptible to field distortions produced by nearby magnetic materials. As a result, these approaches lack scalability across the number of magnets due to the increasingly distorted field produced by each moving magnet when multiple of them are used simultaneously. For a single-magnet

System Specifications	This work	Nat. BME 2017 [13]	ASME 2016 [16]	Sensor 2014 [41]	ACMTG 2015 [43]	US Patent 2003 [55]	SIGCOMM 2018 [44]
Localization Modality	**Magnetic Field Gradient**	MRI Inspired	Magnetic Tracking	Magnetic Tracking	EM-Induction based Tracking	MRI Gradients	RF-based Backscatter
Localization Dimension	**3D**	2D	5D *	3D	6D *	6D *	3D
Mean Spatial Resolution	**1.5mm** **	0.5mm	2.1mm	5mm	< 5mm	2mm	14mm
Field of View	**40 x 40 x 40 cm^3** #	1.2cm ##	7 x 7 x 5 cm^3	20 x 20 x 20 cm^3	Hemi-sphere with 15cm radius	30cm from center	8cm $
Penetration Depth	**40cm** #	1.2cm	5cm	20cm	15cm	Sensor dependent $$	8cm
Temporal Resolution	**300ms**	N.R.	5ms	7.5ms	33ms *#	62.5ms *#	N.R.
Sampling Frequency	**Once per minute *$**	N.R.	200Hz	133Hz	30Hz	16Hz	N.R.
Sensor Size	**20mm length 8mm diameter**	1.8 x 1.2 x 0.3 mm^3	12.8mm length 6.4mm diameter	12mm length 6mm diameter	3x (15mm length, 4mm diameter)	N.R.	7.5cm long antenna
Sensor Communication	**Wireless**	Wireless	N/A	N/A	Wireless	Wired	Wireless
Sensor Power	**Battery**	Wired	N/A	N/A	N/A	Wired	N/A
Multi-Sensor Localization	**Yes**	Yes	No	No	Yes	No	Yes
Field Generator	**Planar Electromagnets (B≤15mT)**	Strong Permanent Magnets (0.2-1T)	N/A	N/A	Electromagnetic Coil with Modulated Current	Volume-enclosing MRI Gradient Coils (B>1T)	External Transmitter Array (830-870MHz)
System Safety	**Yes**	No (sub-Tesla level B)	Yes	Yes	Yes	No (strong B, invasive sensor)	Yes
System Evaluation	***in vivo* (large animal model)**	*in vivo* (small animal model)	Bench study (outside organisms)	*in vivo* (large animal model)	Bench study (outside organisms)	N.R.	Tissue phantoms and *ex vivo*

* Angular orientation is also reported (3D+2/3D)
** Scalable with gradient strength and sensor resolution
# Scalable with coils size and current
Reported for a single axis
$ Only depth-FOV is relevant for RF
$$ Depends on penetration depth of the wired sensor
*# Converted from the reported sampling frequency
*$ Sufficient for GI tract, can be increased to 3.3Hz
N.R.: Not Reported
N/A: Not Applicable

Table 2.2: Comparison with existing EM-based tracking methods.

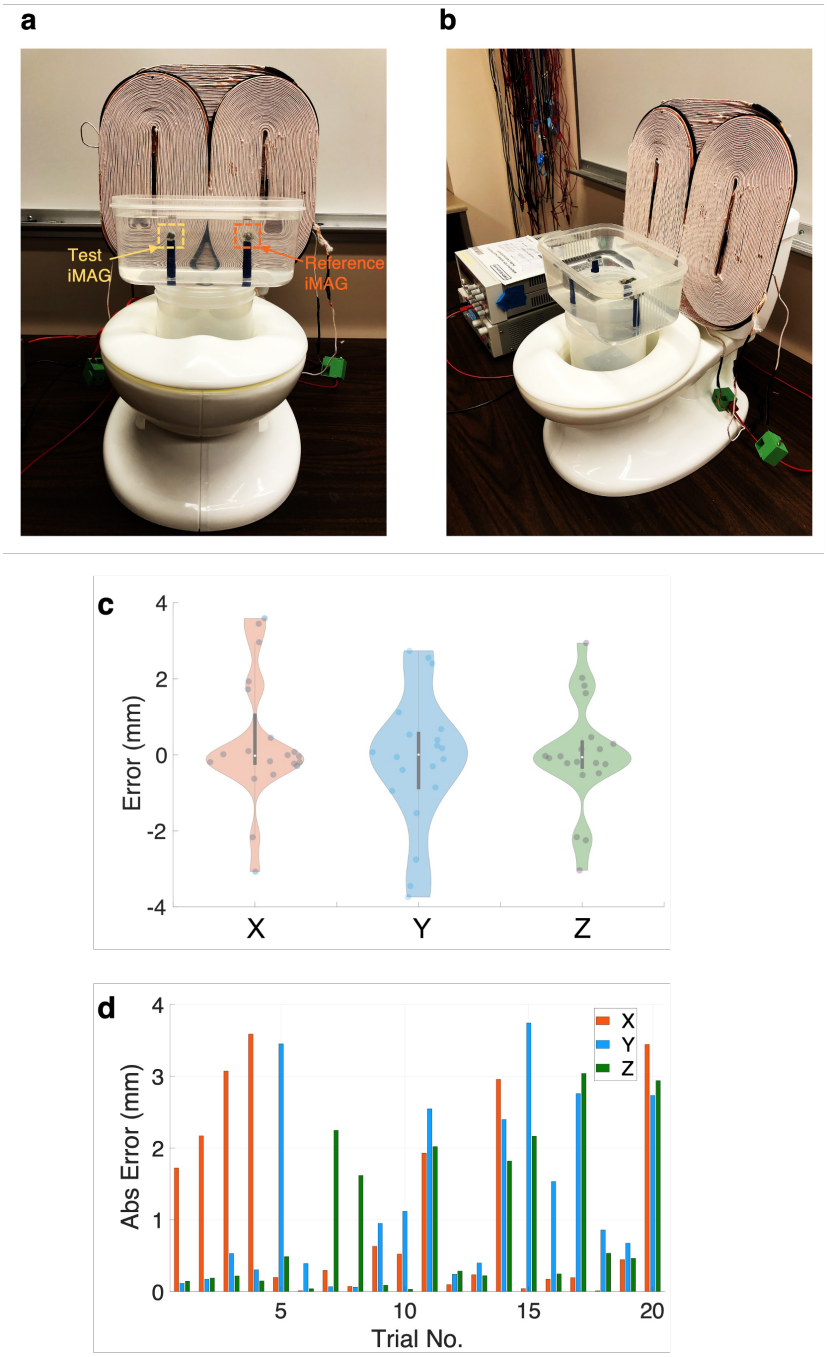

Fig. 4.22: iMAG for smart-toilets. (a) Front-view of the gradient coils assembly mounted on a toilet seat for continuous GI monitoring. (b) Side-view. Two iMAG devices are placed in a tank filled with saline solution to demonstrate 3D localization. The experiment is repeated for n=20 different locations of the iMAG devices in the FOV. (c) Error obtained at all the locations is clustered together and plotted. (d) Error at each location is plotted separately. Error reported as mean $\pm$ std: 1.09 $\pm$ 1.29mm (X), 1.25 $\pm$ 1.22mm (Y), 0.95 $\pm$ 1.05mm (Z). This prototype shows the ability of our technology to be deployed in common human-specific settings.

localization, the mean spatial resolution is around 5mm and rapidly degrades to more than 1cm as the distance from the sensor array is increased to more than 15cm, thus limiting the effective FOV [38–39]. Furthermore, the size of the magnet required to achieve cm-scale precision in a GI-FOV approaches that of a 000–capsule and is larger than the FDA-approved daily dosed osmotic controlled release oral delivery system (OROS), leaving little room for additional components (for actuation or stimulation) that can be fitted in an ingestible pill with minimal risk of obstruction [40–41].

An electromagnetic induction-based system has previously been reported to excite wireless LC coils (used as markers), using an externally located pickup coil array to track the markers [42]. A single marker is composed of three LC coils (each measuring 15 x ϕ4 mm^3) arranged in a ring-fashion to achieve 6D tracking, rendering a size that is unsuitable for an ingestible device. When a single LC coil is used as a marker to fit into an ingestible footprint, it only achieves 5D tracking and suffers from an inherent dead-angle problem [42], which makes tracking reliability uncertain. In contrast, iMAG is capable of achieving 6D tracking with the current footprint [25]. The system in [42] is also lacking *in vivo* evaluation and achieves a lower penetration depth than our work. Furthermore, RF-based localization methods have an order of magnitude lower resolution than our approach due to heavy dependence on body-tissue and multi-path effects [44]. Their penetration depth is also limited due to heavy attenuation of RF signals by body-tissue.

A current limitation of our system is the achievable distance of the receiver board (≤50 cm) when iMAG is located deep inside the GI tract. This is due to the thick gastric and intestinal walls that cause significant loss in the 2.4GHz RF signal strength. Future devices could use a lower frequency of 401–406MHz (MICS band) or 915MHz (ISM band) for communication to achieve a longer distance from the receiver board to the devices. Tissue absorption is attenuated at lower frequencies, leading to a higher signal strength at the receiver. The overall size of iMAG could

also be reduced by using a custom-designed ASIC that has 3D magnetic sensing and wireless communication capabilities. Such ASICs could be used to create highly miniaturized and low-power devices, which can exploit energy harvesting from the GI fluids and eliminate the need for batteries for power [45–47].

Future successful translation of our system will require extensive safety studies in large animal models to enable human trials. From a manufacturing perspective, iMAG can be mass-produced at a low cost per device since all components are off-the-shelf and inexpensive. With an ASIC implementation of iMAG, the cost can be further reduced. iMAG's 4-weeks of battery-life provides sufficient time for evaluation in chronic settings and can be further enhanced by using higher energy density batteries. The electromagnetic coils for gradient generation incur a single-time manufacturing cost and can be used repeatedly for iMAG monitoring. The FOV produced by the coils is scalable with the coil size, number of layers and the DC current used. The coils can also be customized for various patient-specific requirements (Fig. 4.1). For instance, a conformal coil structure can be made into a jacket or incorporated into a backpack and powered with batteries. The coils can also be attached to a toilet seat (Fig. 4.22) or mounted on a rigid wall for regular motility monitoring of patients not comfortable wearing or carrying the coils. This is especially useful for patients with pre-existing disabilities impeding movement and locomotion. Thanks to their complete planarity, the coils can easily slide beneath the bed for GI monitoring during sleep [10]. The iMAG technology could thus be used to advance current capabilities in GI tract monitoring, diagnosis and treatment.

4.8 Methods

iMAG assembly: The Printed Circuit Board (PCB) for iMAG was fabricated on a standard 4-layer 0.062" FR4 substrate, measuring 14mm x 7.2mm. The NRF BLE module (NRF52832-CIAA-R), the matching-network circuit, the 2.4GHz antenna (2450AT18B100) and the 32MHz crystal (CX2016DB32000D0WZRC1) were

soldered on top while the 3D magnetic sensor (AK09970N) and the 11mF storage capacitor (CPH3225A) were soldered on the bottom of the PCB. Two coin-cell batteries (SR626W) are stacked together is series and attached to one end of the PCB (closer to the antenna and away from the sensor). Matching network for interfacing between the NRF module and the antenna was designed using simulations in Microwave-Office software and later tuned in real time on the fabricated board (due to manufacturing variations) using a Microwave Vector Network Analyzer by Keysight (N9918A). The final matching network circuit for the NRF comprises a 1pF shunt capacitor and a 3.3nH series inductor, and the matching network circuit for the antenna comprises a 1pF shunt capacitor and a 4.7nH series inductor (Fig. 4.3). Since transmission through the antenna is the most power-hungry phase of the entire operation, it necessitates that the entire matching network circuit be very accurately tuned to avoid power losses from the NRF to the antenna.

The AKN 3D magnetic sensor is based on the Hall-effect, has a 16-bit data-out for each of the 3-axis magnetic components, high sensitivity (1.1–3.1μT/LSB) and measurement range (± 36mT), and a footprint of 3x3x0.75mm^3. It communicates with the NRF module over the I2C protocol. The sensor consumes 2.2mA of current for 850μs in the low-noise mode (1.1μT/LSB) and 1.5mA for 250μs in the low-power mode (3.1μT/LSB). For the iMAG device, the sensor is operated in the low-power mode. Given the high current consumption by the sensor during field measurements, it is imperative to use a high current-drive battery and a large storage capacitor, as done for iMAG. With future implementations of a low-power CMOS–integrated 3D magnetic sensor, both the power and the area of the iMAG pill can be significantly reduced.

The SR626W silver oxide batteries were chosen because of their compact size (6.8mm x 2.6mm) and high current-drive capacity (28mAh), which is sufficient to power the devices for two continuous weeks. For chronic tests, since we wanted to extend the battery life to four weeks, we used SR927W instead, which measures

9.5mm x 2.7mm and has a current drive capacity of 60mAh (>2x of SR626W). Additionally, the BLE antenna 2450AT18B100 (from Johanson Technology Inc.) was replaced by 0479480001 (from Molex) due to the latter's higher gain to help achieve higher signal strength during the chronic experiments. The resultant increase in the device size to 20mm x 12mm was still acceptable for an ingestible electronic.

iMAG configuration: The BLE software for the device was implemented as an event-driven application, with both the NRF and the magnetic sensor operated in ultra-low power modes at all times, except for the advertising and the magnetic fields measurement phases. A BLE custom service application for the sensor was developed to configure iMAG as a peripheral BLE server. The custom application initializes and instantiates all the necessary BLE service modules and advertising schemes, and reports four data values in a single notification-enabled GATT characteristic: (i) field data measured during X-gradient; (ii) field data measured during Y-gradient; (iii) field data measured during Z-gradient; and (iv) temperature value measured by the internal temperature sensor of the NRF IC.

An nRF52 Development Kit was used to program iMAG before encapsulation. The sensor was configured via the I2C interface to operate in the single-measurement mode, with measurement events processed and verified through the interrupt pin (ODINT). Furthermore, the RAM of iMAG's NRF chip was redefined to take into account the added GATT characteristics and services. The low-frequency oscillator configuration was also redefined to redirect all low-frequency operations to the internal 32.768kHz RC oscillator instead of the external 32.768kHz oscillator, which was omitted from the iMAG PCB to conserve space. For debugging, the sensor's measurements were logged through a UART terminal program via the UART connection on the nRF52 Development Kit, controlled externally from a smartphone. The debugging interface was disabled in iMAG before encapsulation with PDMS.

For a completely encapsulated iMAG, the peripheral BLE application first initializes the GATT interface, Generic Access Profile (GAP) parameters, BLE stack and custom service. It then initializes the 400kHz I2C interface with the sensor, applies a reset, and begins advertising. The TX power was set to 4dBm to ensure maximal connectivity with the external client (receiver board). To get a robust system, the speed and stability of the connection between the client and iMAG are of paramount importance. However, the high attenuation of 2.4GHz BLE signals by body tissue demands a high advertising rate and a faster connection interval in order to maximize the connection probability, resulting in a higher power consumption. For the batteries used with the current iMAG (SR626W), an advertising rate of 2.5s and a connection interval of 50ms was used to achieve two weeks of battery-life. Once a BLE connection is established, iMAG remains in the low-power mode until an external event/notification triggering a measurement is received.

Power optimization for iMAG: Power measurements indicate that iMAG consumed (i) 10μA in idle-mode; (ii) a maximum spike of 15mA during advertising-mode with an average of 440μA across all three BLE channel transmissions. When connected with the receiver board, iMAG consumed 120μA in standby mode, and an average of 250μA when requesting a measurement from the magnetic sensor. We minimized the power consumed by iMAG to ensure that the maximum continuous current was within the discharge limits of the battery. All non-necessary peripherals were deactivated, including the BLE GPIO pins, all interrupt pins, and the general Board Support Package (BSP) module. Furthermore, DC/DC mode power management was enabled on iMAG's NRF to make it switch automatically between the on-chip DC/DC regulator and the LDO regulator, depending on the instantaneous load. Such a regulation protocol is more power-efficient, particularly in the presence of the high-power TX radio spikes. The 10μH and 15nH inductors needed for the DC/DC mode power regulation mechanism were soldered onto the PCB in accordance with the regulator impedance requirements. This resulted in significant power-saving (Table 2.3). With the above configuration, iMAG consumed: (i) 8μA

iMAG's Operation Mode	DC/DC Regulator Disabled: Current Consumption	DC/DC Regulator Enabled: Current Consumption
System Off Idle-mode	0.3μA	0.3μA
System On Idle-mode	10μA	8μA
Peak Consumption during Advertising	15mA	8mA
Average Consumption during Advertising	440μA	230μA
Connection Mode Standby	120μA	80μA
Peak Consumption during I2C Data Transmission	13mA	6mA
Average Consumption during I2C Data Transmission	250μA	180μA

Table 2.3: iMAG's Power Consumption Summary. To make the iMAG highly power-efficient, the DC/DC regulator for the NRF BLE chipset is enabled which results in almost 2x power saving (comparing the right two columns in the above table).

in idle-mode, and (ii) a maximum spike of 8mA during advertising-mode with an average of 230μA across all three BLE channel transmissions. When connected with the receiver board, iMAG consumed 80μA in standby mode and an average of 180μA when requesting a measurement from the sensor.

Receiver board configuration: An nRF52 development board (called as the receiver board) is configured as a BLE client that scans, detects, and requests data from the target server (iMAG). Upon detecting the vendor-specific UUID service address associated with an iMAG, the central client automatically assigns all the handles representing the X-field, Y-field, Z-field, and the temperature GATT characteristics, and initializes all notification-based procedures. Furthermore, the central client application initializes simultaneous advertising events such that an external smart phone can connect to it and remotely activate event notifications (called as 'ping').

The ping signal is relayed by the central client board to the iMAG devices to trigger the magnetic field measurements at their appropriate times (Fig. 4.4). With its GPIO pins connected to the gradient coils' ENA (enable) switches, the central client activates the required sequence of coil combinations shown in Fig. 4.8 to generate the magnetic field gradients.

The receiver board is connected to a laptop via USB and using a simple UART protocol, the board displays the received field-data values in real time as they are streamed from the connected iMAGs. All GATT characteristic tables and byte array sizes were matched between the server and the client to ensure accurate transmission of all the data values. The central client is capable of requesting and receiving data from multiple IMAGs, each at a distinct location in the FOV.

Spatial resolution: The complete definition of the spatial localization resolution (Δx) obtained by our system, in each of the three dimensions, is given by Eq. (4.5) [25]:

$$\Delta x = \frac{\Delta B_{eff}}{G}\left\{1 + \sqrt{\left(\frac{\delta G_i}{G}\right)^2 + \left(\frac{\delta G_s}{G}\right)^2}\right\} \tag{4.5}$$

$$\Delta B_{eff} = \sqrt{(\Delta B_i)^2 + (\Delta B_j)^2 + (\Delta B_k)^2}\,. \tag{4.6}$$

ΔB_{eff} is the effective resolution that the sensor can achieve while performing a magnetic field measurement, as given by Eq. (4.6). G is the applied magnetic field gradient, which is determined by the current in the electromagnets and their geometrical structure. Two major noise sources have been identified in G: (i) δG_i—error caused by field interpolation; and (ii) δG_s—error caused by variations in supply current [25]. The goal is to keep the contributions by these two error sources below 5% so that RHS in Eq. (4.5) reduces to $\approx \Delta B_{eff}/G$.

Gradient coils design and assembly: The gradient required along each axis is described by Eq. (4.4). Using the coil-combinations described in Fig. 4.8 for the X, Y, and Z gradients, monotonically varying magnetic field magnitudes are generated in the FOV [25]. A single field measurement takes <1ms. However, to ensure that the ping signal is received by the iMAG device and the measured data is transmitted to the receiver over the Bluetooth protocol, a 50ms time-window is required. The 10ms rise and fall times are due to the L/R time constant of the coils and the switching requirement of the DC power supplies. The three gradient coils are assembled using a 50-stranded, 32 AWG Litz wire (Fig. 4.9). The Z-Coil consists of 2 layers, each with 80 turns. Each elongated half of the X and Y coils consists of 2 layers, with 68 turns/layer. Finally, the three coils are stacked together concentrically to give a single planar structure measuring 60x60x2cm^3. For applications requiring a bigger FOV, the physical dimensions can be correspondingly scaled for all the coils. More layers can be added to generate a proportionately higher FOV and/or gradient strength. The DC current is another parameter for scaling the FOV vertically. As the gradient G increases, the position resolution given in Eq. (4.1) improves.

Gradient coils characterization: The coils in this work were characterized using a setup comprising linear actuators that move in the X, Y, and Z directions and by measuring the magnetic field at every 1cm step (Fig. 4.23). Points in between the 1cm steps are interpolated in MATLAB. This results in a finely characterized FOV with steps of 1mm in X, Y, and Z, such that the interpolation error of δG_i described in Eq. (4.5), causes <5% variation in G. To reduce the effect of the sensor noise from 15μT_{pp} (measured in the lab) to ≤1μT_{PP}, the sensor averages 200 measurements at each location. The earth's ambient magnetic field is also measured at each location and subtracted from the gradient coil's field. The corrected field values are then stored in the LUT. Each step comprising all the measurements and the movement of the actuators takes <15s, requiring 10days to completely characterize the 40x40x40cm^3 FOV with 1cm increments. The technique for software-based characterization of the coils that requires a significantly less time is discussed in [25].

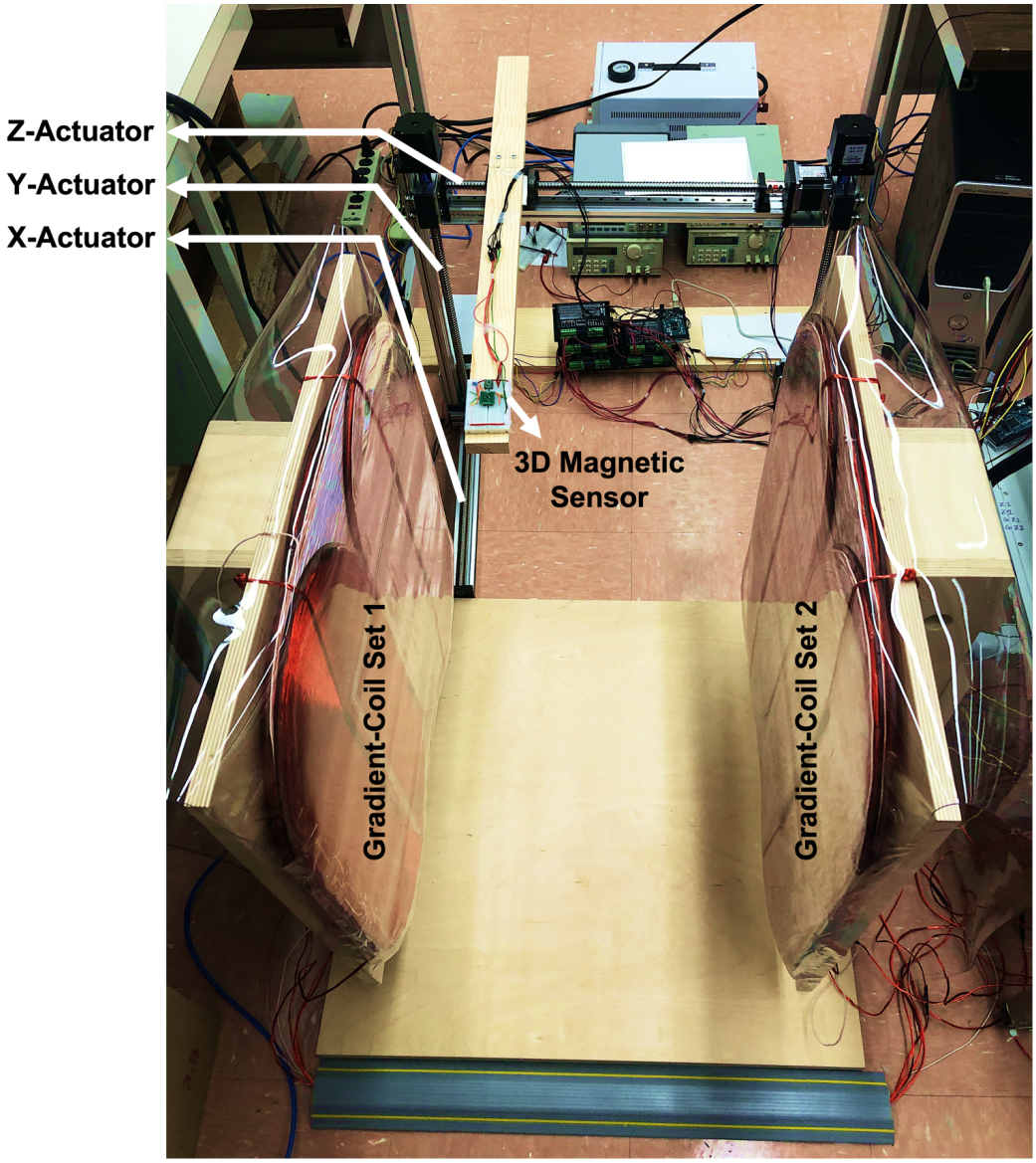

Fig. 4.23: Setup for characterizing the magnetic field gradients produced by the coils in the FOV. A 3D magnetic sensor mounted on a wooden arm is moved in the FOV in increments of 1cm in the X, Y and Z directions using three orthogonally connected linear actuators. The magnetic field data measured by the sensor at each step is stored, interpolated (to achieve 1mm resolution), and then used for creating an LUT for position decoding during the localization experiments.

Also, the entire characterization process needs to be performed *only once* for a given set of coils since the magnetic field values for an arbitrary DC current can be obtained

by linearly scaling the field values stored in the LUT.

Gradient coils controller board: It is crucial to have a constant DC current from the power supply into the coils to minimize δG_s in Eq. (4.5), which is achieved by designing a controller board. A top-level schematic of the board's circuit is shown in Fig. 4.24. V_{REF} and R_1 together set the value of the DC current since $I_{DC} = V_{REF}/R_1$. An N-channel MOSFET driver M_1 (FDL100N50F) rated for 500V and 100A is used for handling the high DC current coming into the coils. R_1 is chosen with high temperature stability (MP930-0.020-5%) to ensure a thermally stable current value.

Search algorithm: For each measurement, iMAG first measures the earth's magnetic field (±30μT to ±60μT) to cancel its effect from the gradient coil's field.

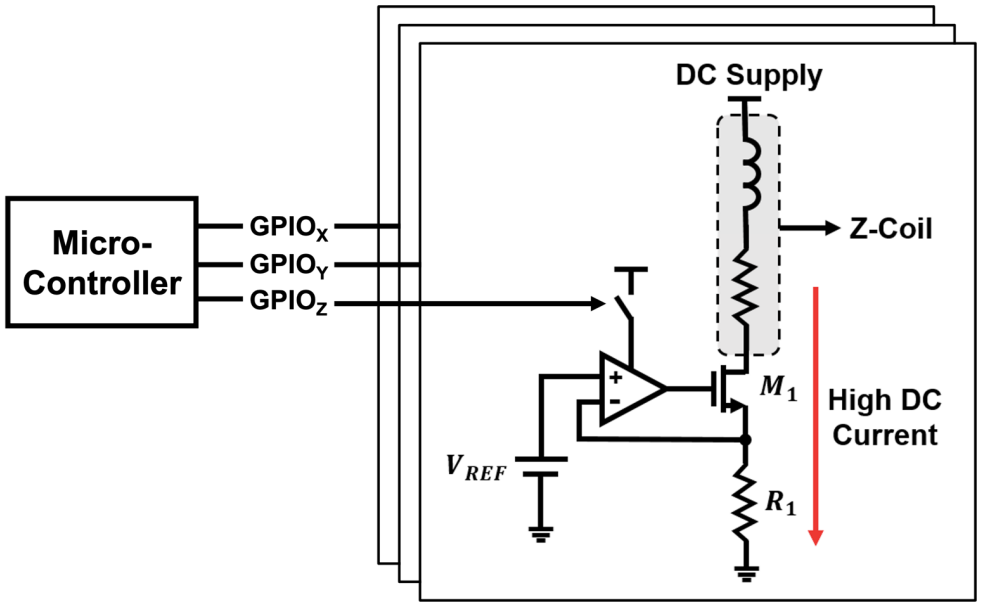

Fig. 4.24: Overview of the gradient coil controller circuit. V_{REF} and R_1 together set the value of the DC current since $I_{DC} = V_{REF}/R_1$. An N-channel MOSFET driver M_1 (FDL100N50F) rated for 500V and 100A is used for handling the high DC current coming into the coils. R_1 is chosen with high temperature stability (MP930-0.020-5%) to ensure a thermally stable current value. The coil control is established by the GPIO pins connected to a microcontroller (nRF52DK or Arduino) that serve as the coil enable (ENA) signals.

The corrected field values transmitted wirelessly by iMAG are received by the receiver board and given as input to the 3D search algorithm implemented in MATLAB, which outputs the corresponding closest position coordinate. The details of the algorithm are described in [25].

X-gradient variation in FOV: Variation of the X-gradient along the Z-axis is shown in Fig. 4.7 (b). Since the field strength gradually reduces as distance from the surface increases, G_X achieves the highest value of 25mT/m at Z = 4cm and reduces monotonically to 5.24mT/m at Z = 20cm. Variation of the X-gradient along the Y-axis is shown in Fig. 4.7 (c). The circular Z-Coil results in a field magnitude along the X-axis that is non-homogenous across Y-coordinates. The global coil-center (Y = 30cm) has the highest Z-gradient as well as the highest field magnitude, which gradually falls as Y is increased or decreased [25]. This effect also manifests in the field profile when both the X and Z coils are powered simultaneously, wherein the maximum G_X = 14.14mT/m occurs at Y = 32cm and falls to 5.65mT/m at Y = 0 (Fig. 4.7 (c)).

Communication range study: The communication range between iMAG and the receiver board is evaluated *in vitro* using different solutions (HCl, NaCl, SGF, SIF, porcine gastric fluid). The SGF is prepared as follows: 0.2% w/v NaCl, 0.7% v/v HCl, buffered to a pH of 1.28. The SIF contains more of Pancreatin enzyme (composition of Lipase, Amylase, Protease), as opposed to ionic salts and acids (Sodium Oleate, Sodium Taurocholate, Sodium Phosphate, NaCl) [53],[54]. For all the tests, a PDMS encapsulated iMAG is submerged in a cylindrical beaker such that the solution is uniformly distributed around it. The receiver board (nRF52-DK) is kept outside in air and moved as far as possible before losing connection with iMAG. All range values beyond 1m are denoted as 1.1m since the board is not required to be moved farther than 1m under any test scenario. For *in vivo* tests, iMAG was placed in the gastric cavity of a pig (Yorkshire Swine, 60kg) with an endoscope (Olympus). iMAG was held with an endoscopic snare, moved around the stomach to coat it with

gastric juice, and held in the stomach while communicating with the external receiver.

Communication time study: The communication time and long-term stability of the iMAG were first evaluated under *in vitro* settings. iMAG was submerged in an HCl solution (pH = 1.5) for two weeks and was communicated with within every few hours. The iMAG pill at the end of the two weeks was fully functional with no electrical or mechanical damages. This time study was done using HCl to mimic the harsh acidic environment of the stomach as it represents the most extreme case in the entire GI tract. We next performed time studies using other solutions such as SGF, SIF and porcine gastric juice, but those were conducted only for a few days (24–48 hours) since iMAG survived the HCl environment for two weeks.

***In vitro* testing**: During *in vitro* localization, a 20x20x15cm^3 of saline (9g NaCl per liter of water) tank is placed on top of the gradient coil-stack (Fig. 4.13 (a), (d)). While localizing the iMAG relative to the global-origin (0,0,0 in Fig. 4.6), the error plots in Fig. 4.13 (b), (e) show that the error values occur in increments of 1mm. This is because the LUT (created during characterization) stores field values corresponding to spatial coordinates that are 1mm apart. For relative localization using another iMAG, the error is computed by subtracting the X, Y, and Z components of the decoded distance vector from the ground truth vector, which results in non-integer values (Fig. 4.13 (c), (f)) with peak <5mm.

***In vivo* testing:** All experiments were conducted in accordance with the procedures approved by the Massachusetts Institute of Technology Committee on Animal Care. We chose a swine model due to anatomical similarities of their GI tract to humans as well as their wide usage in GI tract device evaluation [31]. We observed no adverse effects during the experiments. We administered the iMAG to female Yorkshire swine, 35kg to 65kg (Tufts, Medford USA). To deliver the iMAG, we placed the swine on a liquid diet 24 hours before the procedure and fasted the swine overnight.

We sedated them with intramuscular injection of Telazol (tiletamine/zolazepam) (5mg/kg), xylazine (2mg/kg), and atropine (0.05mg/kg) and if needed supplemental isoflurane (1-3% in oxygen) via a face mask. An orogastric tube or overtube was placed with guidance of a gastric endoscope and remained in the esophagus to ease the passage of the device. In the first experiment, two iMAG devices placed a known distance apart were passed through the overtube and placed into the insufflated stomach (Fig. 4.14). Although the swine were fasted, some of them still possessed food in their stomach during the iMAG delivery. In a second experiment, an iMAG was inserted into the insufflated stomach through the overtube and left to pass through the GI tract (Fig. 4.15). Magnetic field measurements were made in the chute followed by an X-ray scan to determine residency time of the devices as well as for any evidence of gastrointestinal perforation (pneumoperitoneum). This was repeated on all the subsequent test days (M/W/F) until the ingested iMAG was excreted. Additionally, during retention of the devices the animals were evaluated clinically for normal feeding and stooling patterns. No evidence of pneumoperitoneum on X-ray nor any changes in feeding or stooling patterns were observed. In a third experiment to validate our fecal incontinence model (Fig. 4.16), an iMAG was tethered on the tip of a catheter and placed into the rectum. The iMAG's location was scanned repeatedly (using both magnetic field measurements and X-rays) as the device was gradually pulled out in 1–2cm increments. Similar steps were executed during the final experiment to examine the potential interference caused by magnetic materials surrounding iMAG (Fig. 4.18), with magnetic beads placed in the rectum prior to iMAG's insertion.

During all the *in vivo* tests, the receiver board was kept close to the animal's abdominal region, connected to a computer displaying the received magnetic field values from the iMAG devices. Animals also had a reference iMAG secured on the skin using a Tegaderm™ patch. After performing magnetic field measurements in the chute (Fig. 4.14 (a)), the animal was physically carried to the X-ray scanner every time a scan was required. During this motion, it was hard to keep the position of the

iMAGs intact due to the relative movement of the animal's organs. Additionally, to get two orthogonal X-ray scans to compute the 3D inter-device distance, the animal was manually rotated by 90^0, which does not result in perfect orthogonality. Therefore, comparisons with X-ray scans show a difference of >5mm for localization in the colon (Fig. 4.15 (d)), which is an artifact resulting from the X-ray acquisition methodology.

Software: J-Link RTT Viewer was used for collecting the raw magnetic field values from the iMAG pills and the nRF receiver. MATLAB was used for position decoding using the field values. Arduino Mega 2560 and the Arduino IDE were used for FOV characterization and LUT creation. MATLAB and GraphPad Prism were used for data analysis and plotting. Illustrations were made in Adobe Illustrator and Microsoft PowerPoint.

Chapter 5

A LOW-POWER AND MINIATURIZED 3D MAGNETIC SENSOR IN CMOS WITH HIGH SENSITIVITY

Magnetic sensors have become increasingly ubiquitous as they constitute an integral part of several fast-growing sectors such as automotive, navigation, robotics, medical devices, power grids, industrial applications, consumer electronics and space equipment [1]–[11]. Many different types of magnetic sensors such as Hall sensors, semiconducting magneto-resistors, fluxgate sensors, resonant sensors, induction-based magnetometers and superconducting quantum interference devices (SQUID) have been developed for these applications [8]–[24]. Due to their compatibility with the standard low-cost complementary metal-oxide-semiconductor (CMOS) process, Hall sensors are one of the most widely used types of magnetic sensors [8]–[16]. More recently, Hall sensors have been used for magnetic gradient based navigation and tracking of miniaturized devices in different biomedical applications (Fig. 5.1) [25]–[28]. However, one of the key challenges of CMOS-based Hall sensors is their relatively low sensitivity, which is inevitable given the low Hall coefficient of silicon [1]. To achieve better sensitivity, Hall sensors need to be biased at higher current levels, which hinders their widescale use in low-power bioelectronics and other power-constrained applications. Another challenge is the difficulty in implementing high-sensitivity 3D Hall sensors in the standard CMOS process. This is often overcome by using ferromagnetic material that require additional and expensive steps during fabrication, thus increasing the cost [8],[9],[16]–[19].

In this work, we propose a new 3D magnetic sensor that is fully CMOS compatible and achieves high sensitivity with only μW-level power budget. The core sensing elements are three highly dense coils that are orthogonal to each other and produce an induced electromotive force (EMF) in response to the changing magnetic flux along each coil's axis. The 3D coils are implemented using the available metal stack

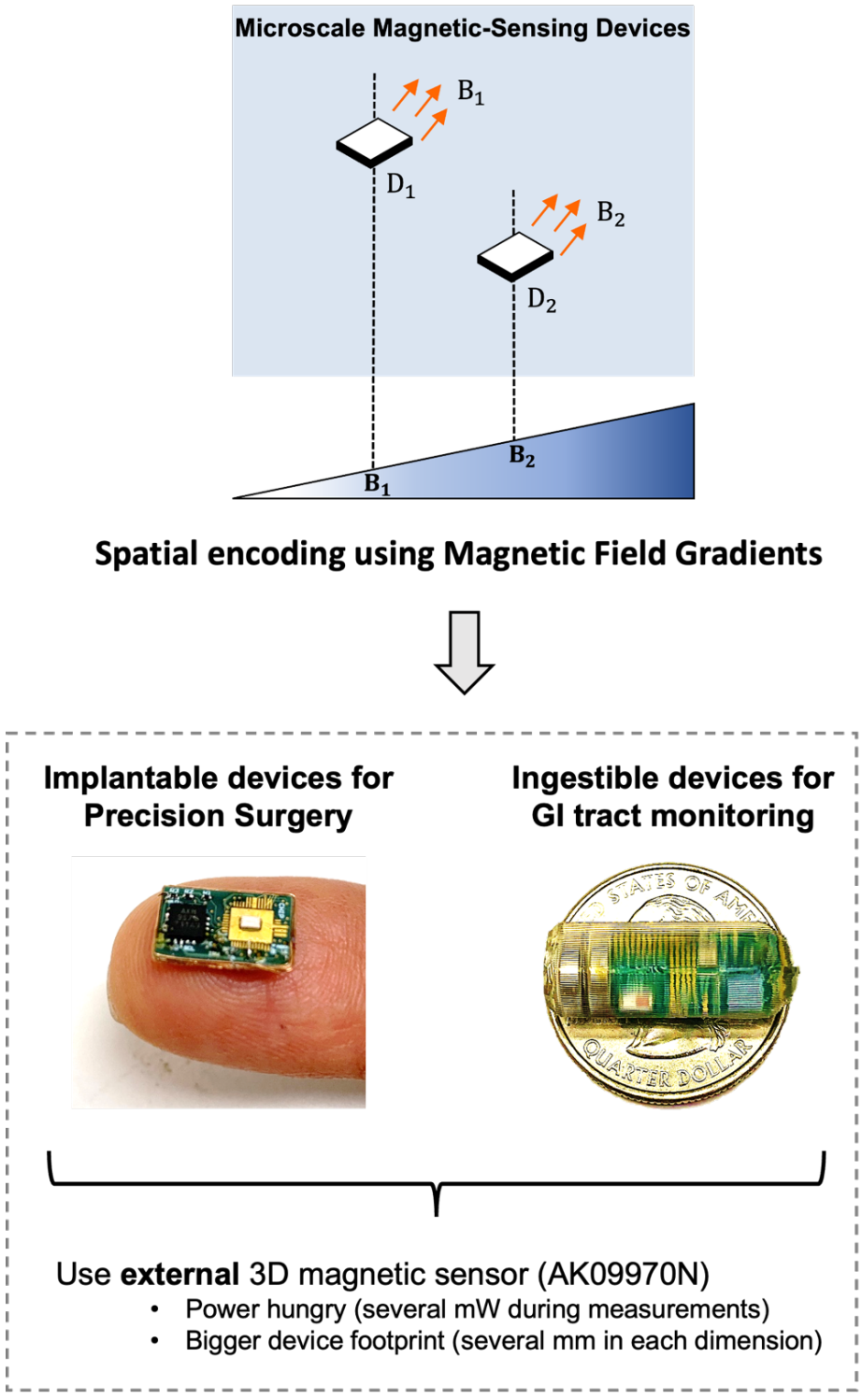

Fig. 5.1: MRI inspired spatial encoding adopted in this work (top) and its implementation for implantable and ingestible devices (bottom) for different biomedical applications.

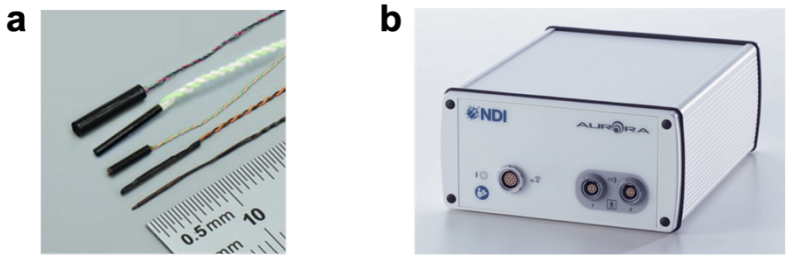

Fig. 5.2: Electromagnetic based tracking solution by NDI Aurora comprising of (a) wired coil-based magnetic sensor, and (b) stand-alone processing circuit block.

in standard CMOS process and do not require any additional processing steps during fabrication. Although coil-based magnetic sensors have been reported by NDI Aurora and others [3]–[6],[22]–[24] for electromagnetic tracking in clinical settings (Fig. 5.2), these sensors are not CMOS-integrated and are at least several mm long. They also lack the capability for wireless operation as the interface and control circuit unit is located far from the sensing coils and requires a wired connection to the coils. As a result, the use of these sensors is limited. By incorporating the 3D coils and all the processing circuitry on a monolithic CMOS chip, as done in this work, the sensor footprint can be significantly reduced and the sensitivity can be enhanced. Furthermore, the µW-level power required by our sensor can be easily delivered wirelessly or harvested locally from bio-fluids [29], thus eliminating the need for wired sensors. Such highly miniaturized, ultra-low power and wireless magnetic sensors can be of significant benefit for several applications, particularly for bioelectronics.

5.1 System Overview

To sense the 3D components of the alternating (AC) magnetic field (Fig. 5.3) through electromagnetic induction, the sensor needs three orthogonal coils. For sensing the in-plane components of the magnetic field to the CMOS chip (X and Y axis), we need on-chip coils in the X and Y planes that are orthogonal to the chip's plane (Z).

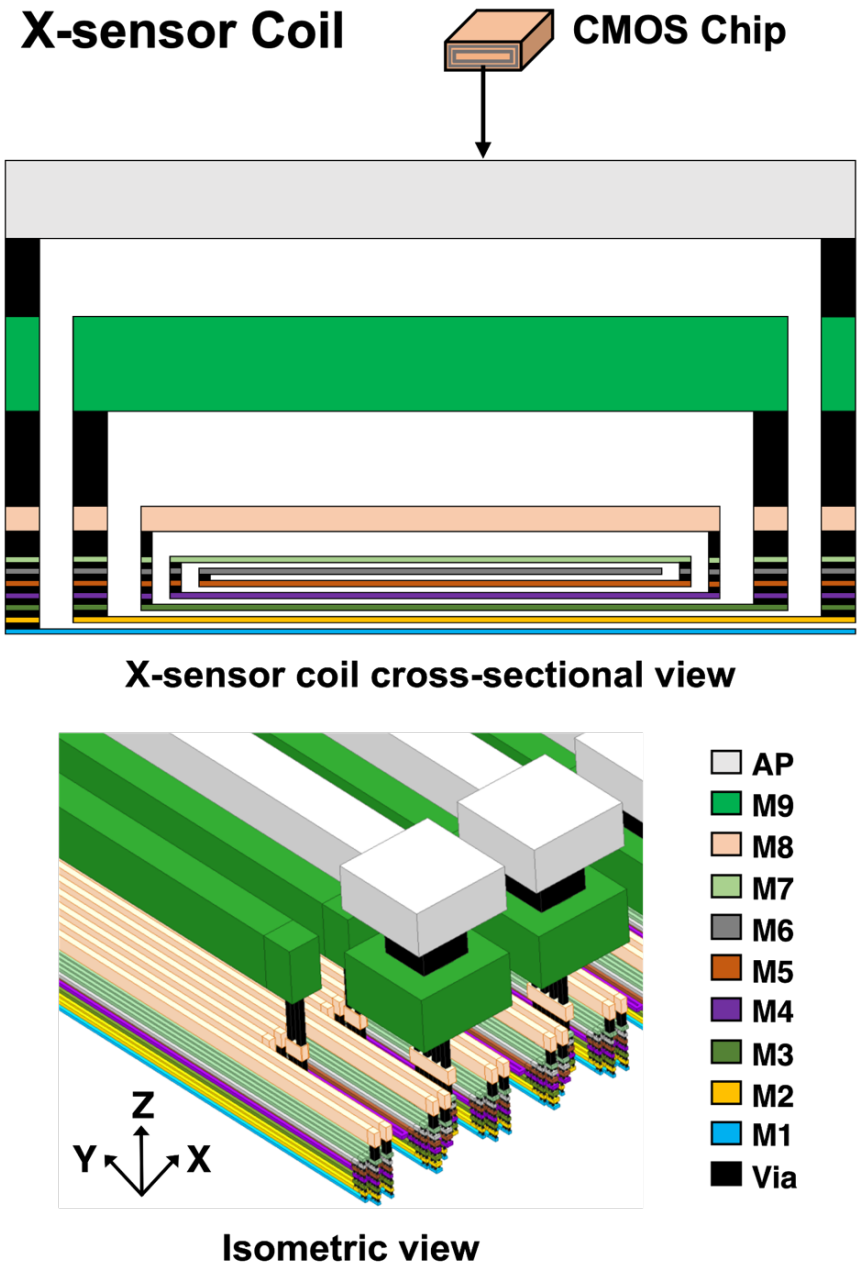

Fig. 5.3: The X (and Y) sensor is realized as a spiral coil in the vertical dimension of the 65nm CMOS process. The outermost loop of the spiral is made by connecting the lowest metal layer M1 to the highest metal layer AP through all the intermediate metal layers and vias. The second loop is made by connecting M2 to M9, and so on until all the metal options are exhausted. The isometric view of the coil shows a much larger number of lower metal spirals (M1-M7), which is a result of using minimum width and spacing DRC specifications for all the metal layers to obtain highly dense coils.

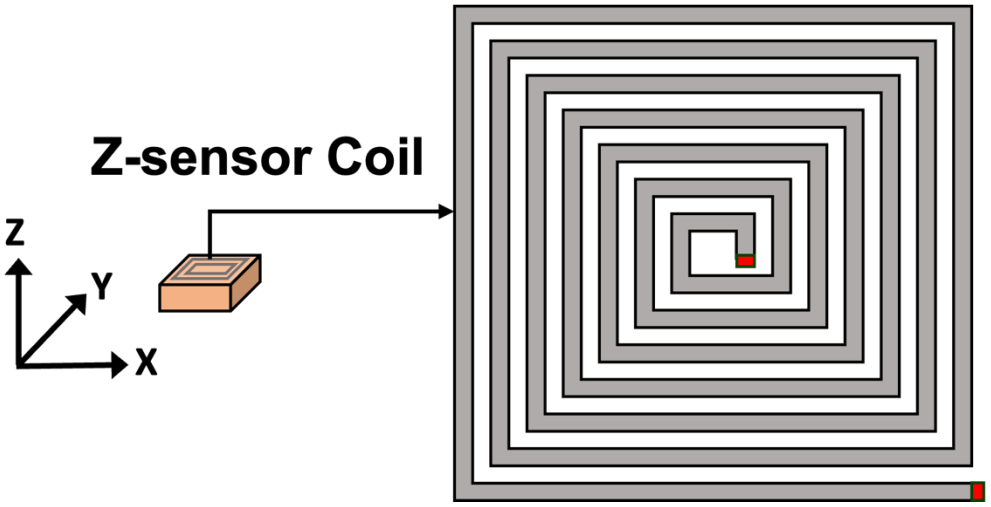

Fig. 5.4: A single spiral loop of the on-chip Z-sensor coil is shown that is implemented using one of the several metal options available in the 65nm CMOS processes. Each of the ten metal layers in the 65nm node is used for creating a spiral loop in the plane of the metal and all the spirals are connected together using vias (at the red terminal locations) to yield a single multi-layer spiral spanning from the lowest metal layer (M1) to the highest metal layer (AP).

Realizing such coils is difficult due to lack of any dedicated metal layer in these planes in standard CMOS processes. We overcame this challenge and realized the X and Y sensor coils in 65nm CMOS by using the interconnect vias as part of the coil structure. As shown in Fig. 5.3, the outermost spiral of the X-sensor coil is made by connecting the lowermost metal M1 to the topmost metal AP (aluminum) through intermediate metals and vias. The second spiral is realized by connecting M2 to M9. This process is repeated until all the metal options are exhausted, thus leveraging them to maximum utilization for coupling with the X-axis magnetic flux. To further increase the coupling, we follow minimum design-rule-check (DRC) specification for both width and spacing for each metal layer to realize highly dense coils. An inherent challenge here is the height from M1 to AP which is dictated by the fabrication process (<20μm in 65nm) and cannot be changed. To alleviate that, we adopt two techniques: (i) the length of the coil is kept much larger than the height of the coil-stack, and is chosen to be close to one of the dimensions of the chip

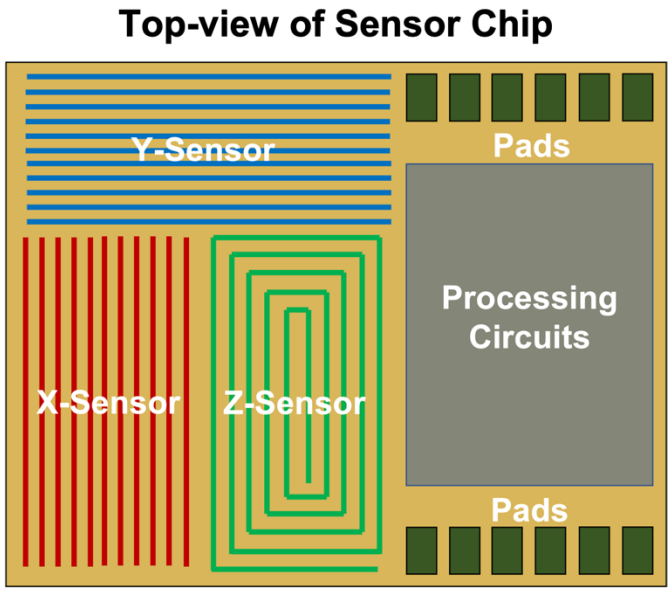

Fig. 5.5: Top view of the integrated CMOS chip with the 3D magnetic sensor coils and the processing circuitry.

(1.45mm); and (ii) multiple coil spirals are cascaded to increase the effective coupling area (Fig. 5.3, isometric view). The resultant large number of spirals come at the cost of an increased coil resistance (R_{Coil}) which leads to a high noise floor, necessitating the design of low-noise front-end circuitry for amplification, sharp bandpass filtering and high-resolution digitization, as discussed later, to achieve a high signal-to-noise ratio (SNR). The Y-sensor coil is realized identically to X but is shifted by 90^0. The Z-sensor coil is implemented in the plane of the CMOS chip as a multi-layer spiral realized using all the ten metal layers (M1-M9 and AP) offered in the 65nm node and connected using vias (Fig. 5.4). Since both the dimensions for the Z-coil can be controlled independently and are not constrained by the process, they are designed with a more regular aspect ratio unlike the X/Y coils. As a result, the Z-coil achieves almost 100x more coupling compared to the X/Y coils for a given area, as detailed later. A top-view image of the integrated 3D magnetic sensing coils sitting next to the processing circuitry on a CMOS chip is shown in Fig. 5.5.

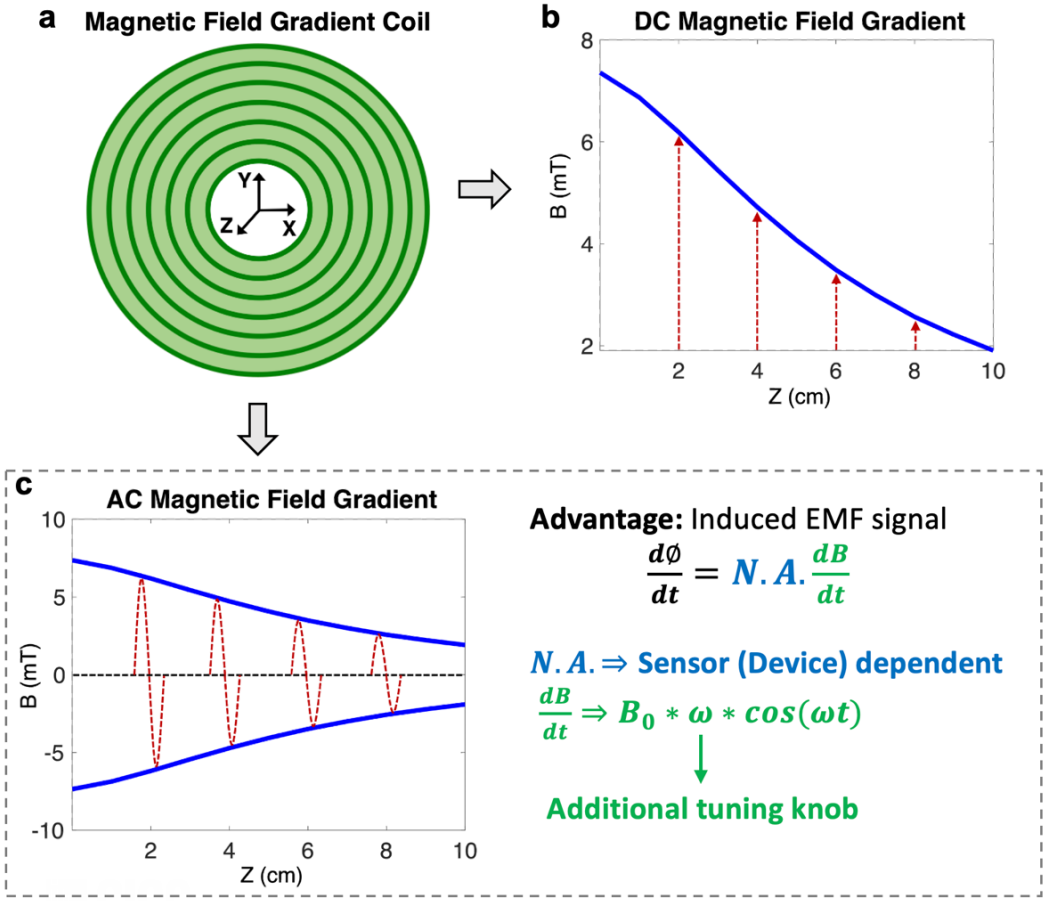

Fig. 5.6: Replacing DC gradients with AC. (a) Electromagnetic gradient generating coil (30cm diameter). (b) DC magnetic field gradient produced by the coil when using a DC input current source. (c) When the current type is changed to AC, the peak gradient value is identical to DC but with an additional feature of each point exhibiting a sinusoidal variation, thus creating an AC magnetic field gradient. This provides an additional tuning knob of frequency ω that can be used to enhance the signal while keeping the current constant, thus making this approach more power efficient than DC excitation.

Our tri-axial CMOS magnetic sensor can be used in a variety of applications that require AC field sensing from 100Hz to a few kHz given the current processing circuitry, which can be modified to accommodate higher frequencies. In this work, we aim to use the sensor for 3D localization using the magnetic field gradient based spatial encoding scheme described by the authors in [26] (Fig. 5.1). The Z-coil used

in [26] is powered by a DC current that produces a decaying magnitude of the magnetic field as the distance from the coil is increased, resulting in a Z-axis gradient (Fig. 5.6). By changing the current from DC to AC for use in this work, an identical gradient can be generated with an additional feature of exhibiting a sinusoidal variation at each point along the gradient. Similarly, the X and Y gradients in [26] can also be changed to AC. Since the peak magnetic field value at each point along the AC gradient remains the same as DC (Fig. 5.6), the spatial localization algorithm used in [26] can be used with AC gradients as well.

The induced EMF in the sensor coil is a product of the sensor's effective cross section area and the rate of change of the magnetic field which is given by:

$$dB/dt = B_0 * \omega * cos\ (\omega t) \tag{5.1}$$

where $B_0 * sin\ (\omega t)$ is the magnetic field at the sensor's location. Eq. (5.1) illustrates that we now have another parameter for enhancing the signal at the sensor—the

Component	DC Electromagnetic Localization	AC Electromagnetic Localization
Gradient Coils	Peak current I_0 ⇒ **I_0^2R heat loss**	Peak current I_0 ⇒ **$I_0^2R/2$ heat loss**
Gradient Coils	High signal ⇒ High current ⇒ **I^2R loss increases quadratically**	High signal ⇒ High frequency (ω) ⇒ **I^2R loss constant**
Gradient Coils	Need **DC power supply**	Need **AC power supply**
Gradient Coils & Microdevice	**Affected** by earth's ambient magnetic field	**No effect** from earth's field
Microdevice	Needs Hall-based sensors ⇒ **Higher sensitivity needs higher power Not high chip area**	Needs passive coil-based sensors ⇒ **Higher sensitivity does not need higher power Needs higher chip area**
Microdevice	**DC offsets** severely affect the sensor readout	**No effect** of DC offsets
Microdevice	Sensor has **low-frequency noise** components	All low-frequency and out-of-band **noise can be filtered**
Microdevice	High sensitivity Hall-sensors using ferromagnetic material are **not compatible with CMOS**	3D sensing-coils can be **integrated in CMOS process**

Table 3.1: Comparison table illustrating the advantages offered by AC electromagnetic localization and navigation system over the DC counterpart.

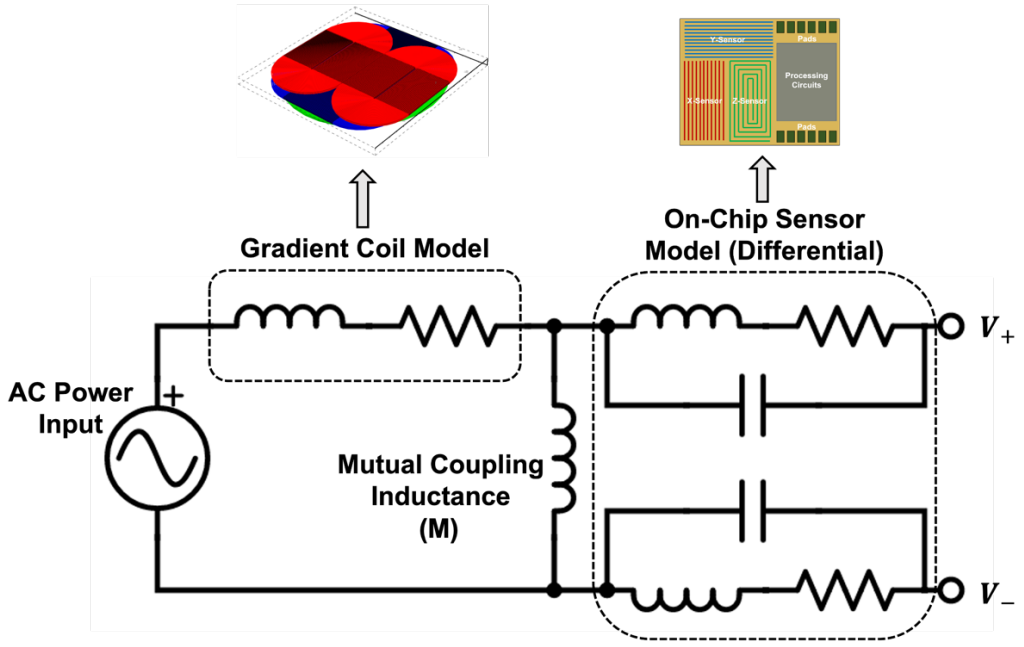

Fig. 5.7: Complete simulation model of the coupled coils with the external magnetic field gradient coil serving as the primary and the on-chip sensor coil serving as the secondary. Since the front-end circuit interfacing with the sensor coil is differential in nature, the sensing coil is also modelled in a differential manner to generate V+ and V- components of the induced EMF voltage.

frequency ω of the magnetic field. Compared to the DC gradients in [26] where the signal at the sensor can be enhanced only by increasing B_0, which requires a higher current in the gradient coils or more number of turns, the AC gradients offer a more power efficient way by increasing the frequency of operation while keeping the current (and hence B_0) constant. Higher power efficiency is also achieved for the sensor as the 3D coil-based sensing requires only µW-level power consumption by the processing circuitry, which is orders of magnitude smaller than the mW-level power consumed by the Hall sensors for sensing DC gradients in [25]–[27]. A detailed comparison between AC and DC gradients is shown in Table 3.1. A slight downside of the 3D coil-based sensing is the chip area occupied by the coils, which can be overcome in the future versions by releasing the lower metal layers (M1-M3) from the coil-stack as they do not contribute heavily to the X/Y coupling due to their

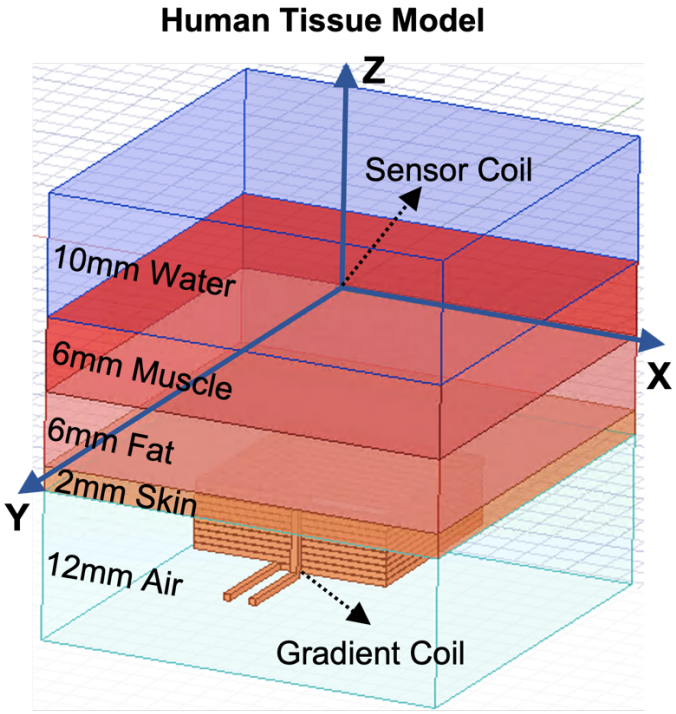

Environment	Mutual Inductance (nH)	
	X/Y	Z
Air	1.401	87.84
Fresh water (0.01 S/m)	1.395	87.55
Sea water (4 S/m)	1.408	87.98
Tissue model	1.415	88.46

Frequency (Hz)	Mutual Inductance (nH)	
	X/Y	Z
100	1.405	87.97
250	1.405	87.97
500	1.405	87.97
750	1.405	87.97
1000	1.405	87.97

Fig. 5.8: Coupled coils simulations in the presence of human tissue. The complex human tissue is modelled using multiple layers—skin, fat, muscle and water (top). It can be seen that the value of the mutual inductance M does not change from the all-water configuration to the tissue configuration, which demonstrates immunity to the presence of human tissue between the two coils (bottom). Frequency sweep from 100Hz to 1000Hz also indicates independence against frequency variations.

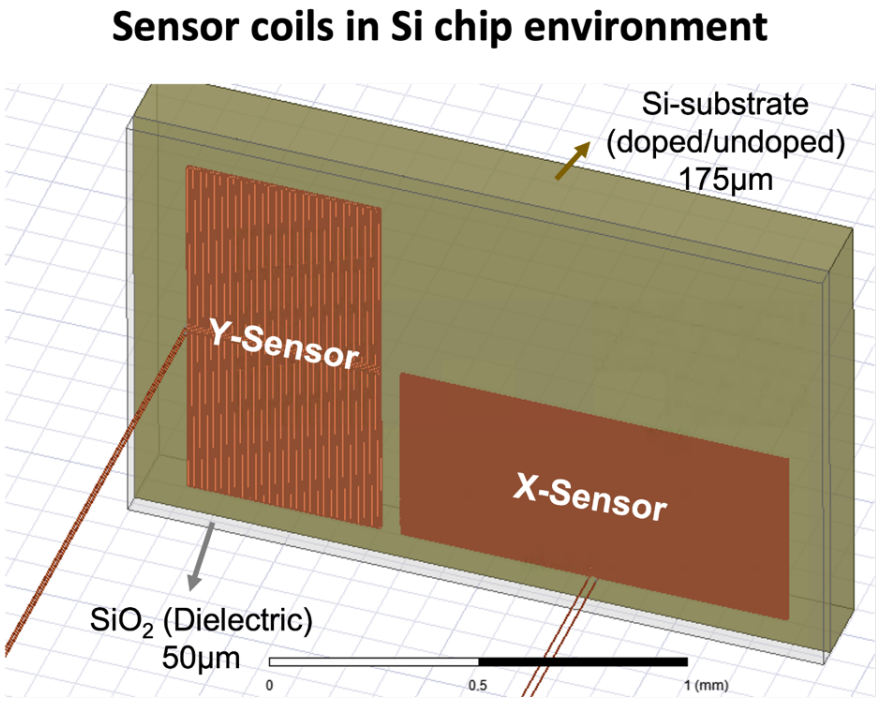

Environment	Mutual Inductance (nH)
Only SiO_2	1.394
SiO_2 + Doped Si-Sub	1.401
SiO_2 + Undoped Si-Sub	1.412

Frequency (Hz)	Mutual Inductance (nH)
100	1.398
250	1.398
500	1.398
750	1.398
1000	1.398

Fig. 5.9: EM simulations with the X/Y sensor coils (top) enclosed in the silicon chip environment to see variation in M due to presence of Si media around the coils. The value of M stays relatively constant as the conductivity of the media is varied and also during frequency sweep up to 1kHz (bottom).

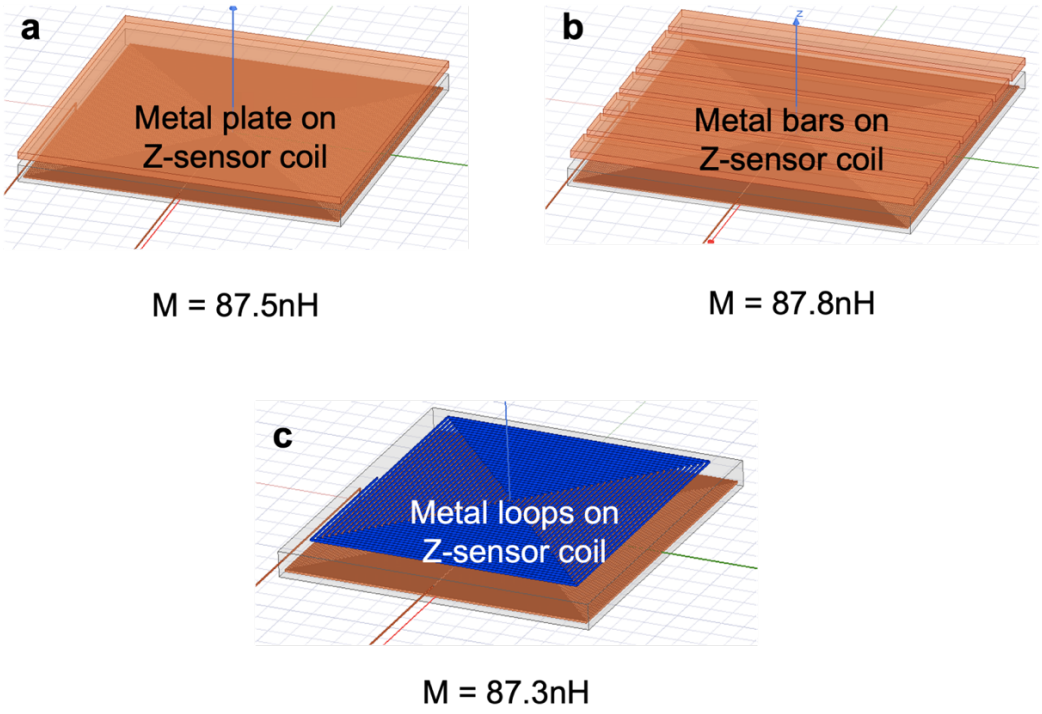

Fig. 5.10: EM simulations to study the effect of eddy currents on the value of M for the Z-sensor coil, which is due to the presence of conductive media (doped Si substrate) directly below the Z-sensor. This is modelled as: (a) conductive plate placed above the sensor coil, (b) conductive bars placed above the sensor coil, and (c) conductive loop placed above the sensor coil. It is observed that the value of M stays constant across these simulations, confirming immunity against eddy current induced effects

low thickness and vertical spacing. Instead, these can be used for routing of components (transistors, resistors etc.) located in the active silicon area beneath the coils, which will help avoid any unused chip area.

For selecting the excitation frequency ω, Eq. (5.1) indicates that a higher value of ω leads to a higher EMF signal. However, the external gradient coil's reactive impedance ($jL\omega$) also increases with ω, requiring a higher voltage AC power supply unit for the same current. The gradient coils are powered at 500Hz which is the maximum available frequency of the AC power supply used in this work (see

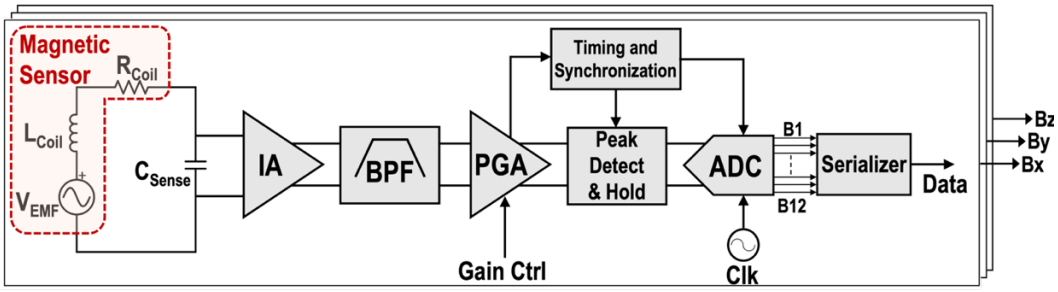

Fig. 5.11: Block-level diagram of the 3D magnetic sensor and the processing circuitry comprising the instrumentation amplifier (IA), band-pass filter (BPF), programmable gain amplifier (PGA), peak detect and hold (PDH) circuit, timing and synchronization, 12-bit SAR ADC and a serializer.

Methods). The value of ω should be high enough to avoid electromagnetic interference from the surroundings, most common being the 50/60Hz components caused by the power grid. Extensive electromagnetic simulations are performed using ANSYS Maxwell to evaluate the mutual inductance M between the on-chip sensor coils and the external gradient coils, and to study the effect of frequency variation, eddy currents, and tissue absorption on the value of M (Fig. 5.7–5.10).

5.2 Circuit Design and Measurement Results

An overview of the processing circuit blocks for the sensor is shown in Fig. 5.11. The coil-resistance R_{Coil} is an inevitable parasitic that introduces a wideband noise of $\sqrt{4kTR}$ V/$\sqrt{Hz}$. By using a sensing capacitor C_{Sense}, the noise can be limited to $\sqrt{kT/C}$. C_{Sense} cannot be arbitrarily large for noise suppression since the RC lowpass frequency should be higher than the EMF signal's frequency of 500Hz. R_{Coil} is 8MΩ for the X/Y sensors and 5.4MΩ for the Z-sensor, resulting in a thermal noise floor of 364nV/$\sqrt{Hz}$ and 300nV/$\sqrt{Hz}$, respectively. As the desired magnetic field resolution of the sensor is ≤10μT in each axis, the sensor coils are simulated with 10μT at 500Hz which determines the tolerable noise floor for the front-end circuit blocks. The X/Y sensors generate 660nV while the Z-sensor generates 40μV of EMF in response to

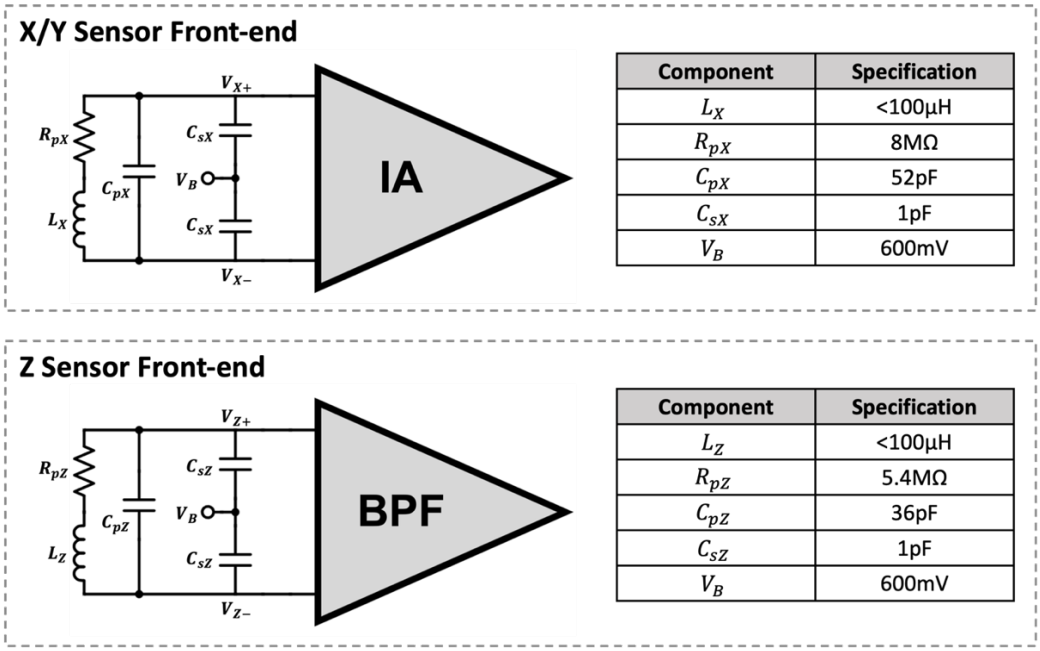

Fig. 5.12: Detailed front-end schematic of the on-chip X and Z sensor coils showing the connections and the values of the components (including parasitic components R_p and C_p). The low-noise IA is used at the front-end of the X (and Y) sensor due to the high thermal noise floor caused by the parasitic resistance (R_{pX}). For the Z-sensor, the value of the parasitic resistance (R_{pZ}) is lower and the value of the induced EMF is higher compared to X, which obviates the need for using a low-noise IA at the front-end. Hence, the Z-sensor coil is directly connected to the BPF circuit.

the 10µT field. Since the X/Y sensors' output is close to their thermal noise floor, it is imperative to design the front-end instrumentation amplifier (IA) with 8-10x lower input-referred noise (IRN) floor, i.e., ≈40nV/$\sqrt{Hz}$, as detailed below. The Z sensor does not require a low-noise IA at the front-end and can be directly connected to the BPF (Fig. 5.12). Additional details of all the circuit blocks are included in the Methods section.

5.2.1 Instrumentation Amplifier (IA)

The IA is capacitively coupled to the input to avoid DC offsets and low frequency noise (Fig. 5.13) [30]. It is implemented in a fully-differential closed-loop architecture to achieve high common-mode noise rejection and ensure sufficient linearity. The input coupling capacitor C_1 is $25 * C_2$, where C_2 is a 230fF metal-oxide-metal (MOM) capacitor, rendering a total closed-loop gain of 50V/V. The gain is not kept to be very high to avoid amplifying the input noise. Pseudo-resistors realized using transistors are added in the feedback path of the IA to provide GΩ-level impedance, which is needed to control the high-pass corner frequency to be within 10-100Hz. The low-pass corner frequency of the IA is determined by the output impedance of G_{m1} and the load capacitor C_L (25pF). The G_{m1} block is implemented as a cascade of two current-reuse stages (Fig. 5.13) [31]–[34]. Since both M_3 (M_4) and M_5 (M_6) carry the same current, the IRN of the first stage is given by:

$$\text{Input Referred Noise } (V^2/Hz): \frac{16kT}{3} * \frac{1}{g_{m3} + g_{m5}} \tag{5.2}$$

where k is Boltzmann's constant, T is the absolute temperature, g_{m3} and g_{m5} are the transconductances of M_3 and M_5, respectively. In the absence of the current-reuse topology, the last term in Eq. (5.2) reduces to $1/g_{m3}$ (or $1/g_{m5}$), illustrating that this topology helps reduce the noise power by half. Due to the high g_m requirement of stage-1 for achieving low noise, it is the most power-hungry block in the entire design with a bias current of 800nA flowing through M_2 from a supply voltage (Vdd) of 1.2V. The bias current in stage-2 is 10x lower. The total power consumption of the IA is 1.3µW. 2.5V thick-oxide transistors are used everywhere to minimize gate leakage and are operated in the sub-threshold regime to further reduce the noise. To reduce the 1/f flicker noise, input stage transistors (M_3–M_6) are designed with a large gate area with each having a width of 400µm. The measured IRN of the IA (Fig.

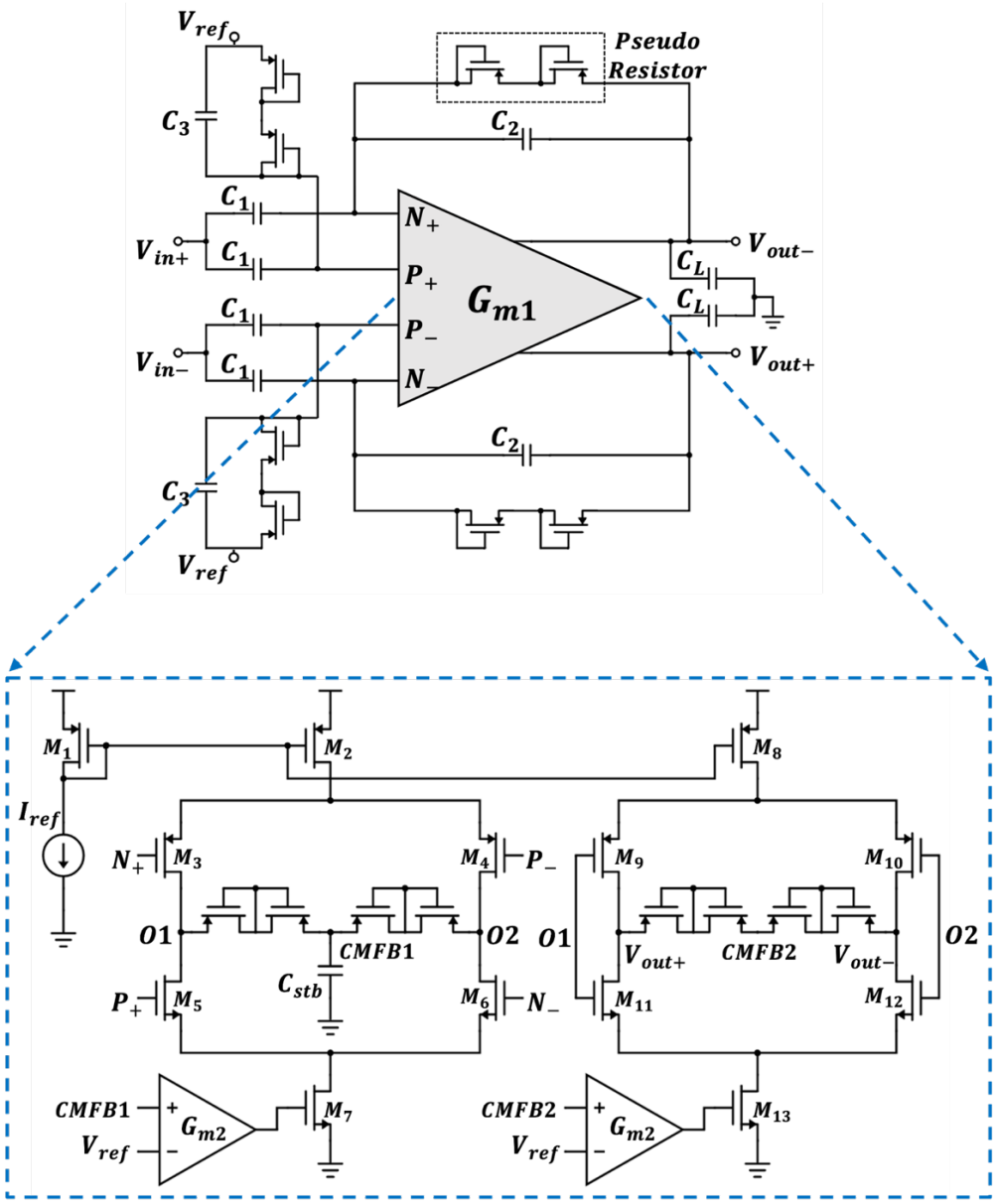

Fig. 5.13: Circuit schematic of the instrumentation amplifier (IA) is shown. It is capacitively coupled to the input and is implemented in a fully-differential closed-loop architecture with a gain of 50V/V. High impedance pseudo-resistors are used in the feedback network to help achieve the desired frequency response. Transistor-level implementation of the G_{m1} block is also shown. It comprises of two current-reuse stages cascaded together for achieving low noise. Operation in sub-threshold regime further reduces the noise. Common-mode feedback (CMFB) is implemented to bias the output nodes of each stage at V_{ref}, chosen to be Vdd/2 (600mV).

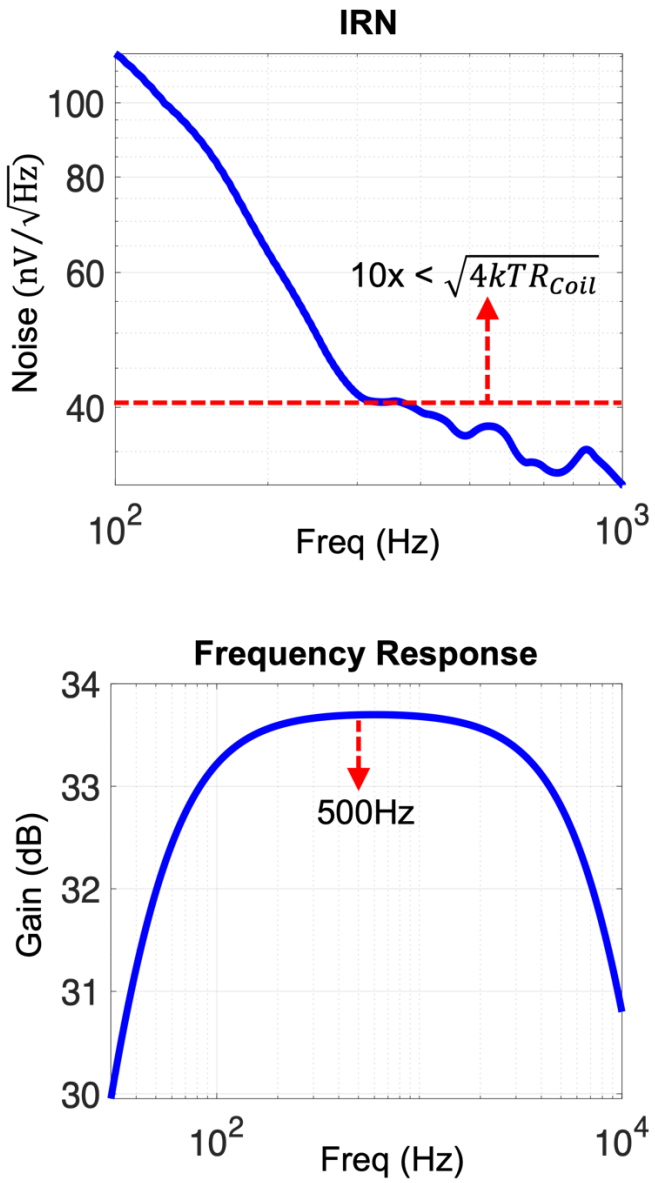

Fig. 5.14: Measured input-referred noise (IRN) of the IA (top) demonstrating ≤ 40nV/$\sqrt{Hz}$ of IRN when the frequency is ≥ 300Hz, which satisfies the low-noise amplification requirement for the EMF signal. Measured frequency response of the IA (bottom) showing a relatively flat gain of 33.7dB around 500Hz which is the EMF signal's frequency.

5.14) is lower than $40nV/\sqrt{Hz}$ at and near the EMF signal's frequency of 500Hz. The measured frequency response of the IA (Fig. 5.14) shows that 500Hz is well

within the pass-band. The IA is used at the front-end of the X and Y sensors due to their stringent noise requirement compared to the Z-sensor which is directly connected to the band-pass filter (BPF) described below.

5.2.2 Band-Pass Filter (BPF)

After the low-noise amplification of the EMF signal using the IA, it is imperative to filter the signal to eliminate the excessive out-of-band noise and improve the SNR. This is accomplished using the BPF (Fig. 5.15) which is also implemented as a capacitively-coupled, fully-differential and closed-loop architecture. To achieve a very sharp BPF response, the low-pass corner frequency should be lower than the high-pass corner, resulting in intersection of the two responses in their steep slope regions (Fig. 5.16) to yield a sharp filter response (Fig. 5.17). A slight disadvantage of this is less than unity gain at the output, as seen to be 0.4V/V at the center frequency of 500Hz in Fig. 5.17, which is not problematic since the gain can be compensated by the following block. Fig. 5.13 shows the implementation of the BPF's G_{m1} stage. Since the output impedance of G_{m1} helps control the filter response, the biasing node of the output stage (gate of M_8) is controlled externally by a tunable DC voltage and not by the on-chip current I_{ref}. This is crucial to adjust the filter response post-fabrication (Fig. 5.17), especially because the transistors are operated in sub-threshold regime which is more susceptible to process variations. The values of the passive components used in the BPF are: C_a=1pF, C_b=15pF, C_c=1pF, C_d=1pF, C_e=106pF, R_a=10.4kΩ and R_b=105.5kΩ. The resistors R_a and R_b are not implemented as pseudo-resistors as those are more prone to process variations, which are undesirable for the BPF. V_{ref} is chosen as Vdd/2 which is 600mV.

5.2.3 Programmable Gain Amplifier (PGA)

The PGA's function is to amplify the EMF signal sufficiently for the ADC to process. The PGA is also implemented as a capacitively-coupled and fully-differential

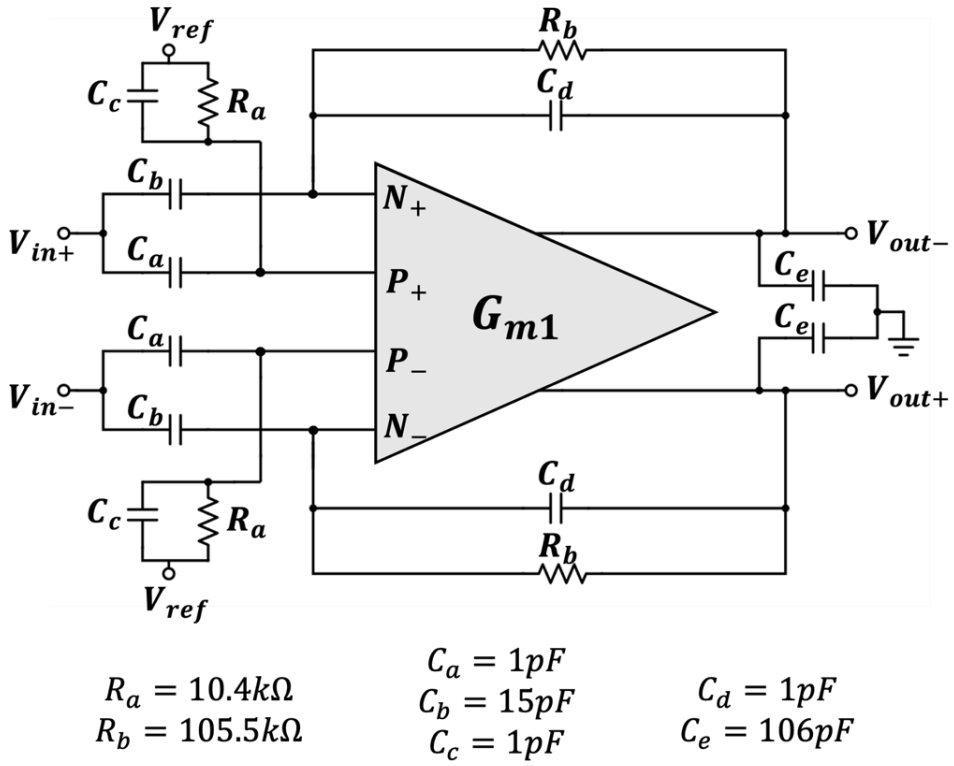

Fig. 5.15: Circuit schematic of the band-pass filter (BPF) showing its capacitively coupled, fully-differential and closed-loop architecture. A very sharp filter response is required around 500Hz to eliminate the excessive out-of-band noise in the EMF signal caused by the coil's resistance.

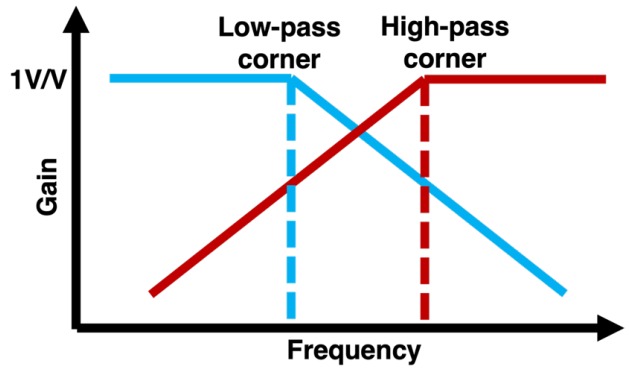

Fig. 5.16: Conceptual diagram showing the design consideration for the band pass filter's (BPF) frequency selection. To achieve a very sharp BPF response, it is desired to have the low-pass corner frequency to be lower than the high-pass corner, resulting in the intersection of the two responses in their steep slope regions.

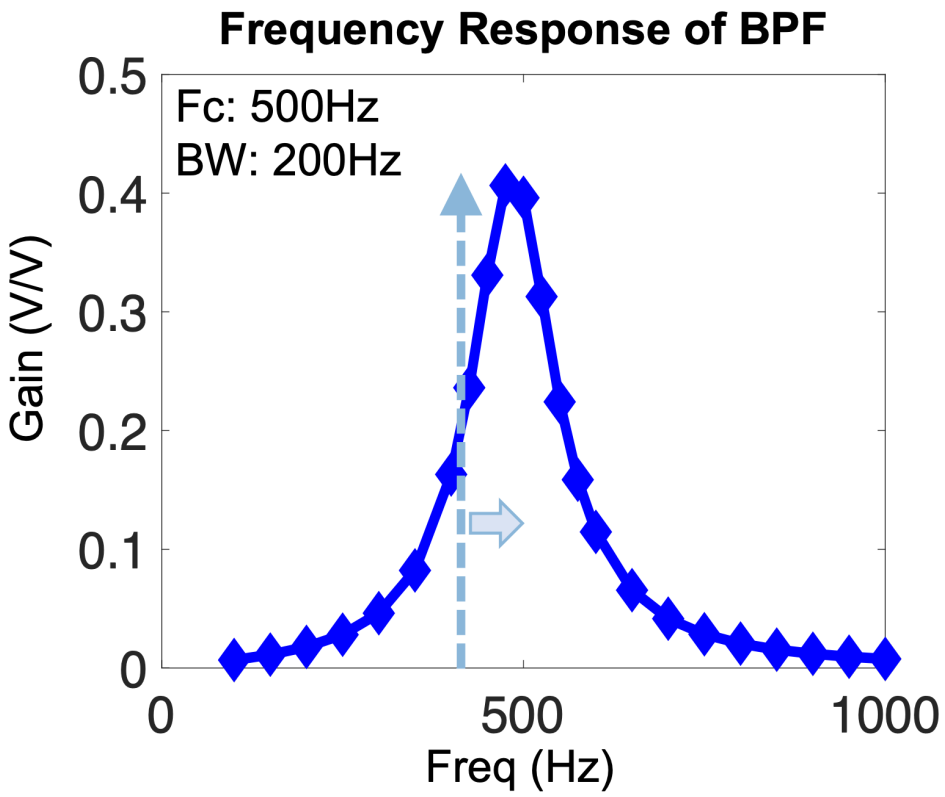

Fig. 5.17: Measured frequency response of the BPF shows 200Hz of bandwidth around the center frequency of 500Hz. The post-fabrication center frequency is initially around 420Hz (pale blue), which is shifted to the desired 500Hz by finding the optimum bias point. The overall SNR is enhanced at the output of BPF but the signal amplitude is reduced due to the less than unity gain at 500Hz.

architecture (Fig. 5.18) but with its $N_+ - P_+$ and $N_- - P_-$ nodes tied together, unlike the IA and the BPF. At the input of the PGA, a 3-bit tunable capacitive network is implemented to control the gain of the PGA from 40V/V to 280V/V in steps of 40V/V. The tunability is necessary to accommodate the varying range of the EMF signal due to the varying peak field magnitude produced by the gradient coils throughout the FOV. The feedback capacitor C_g is chosen to be 44.6fF. The switches $S_1 - S_3$ are implemented using pass transistor logic and driven using inverter-based drivers. The G_{m1} stage is implemented as shown in Fig. 5.13. The FFT of the measured signal output of the PGA and the time domain waveform are shown in Fig.

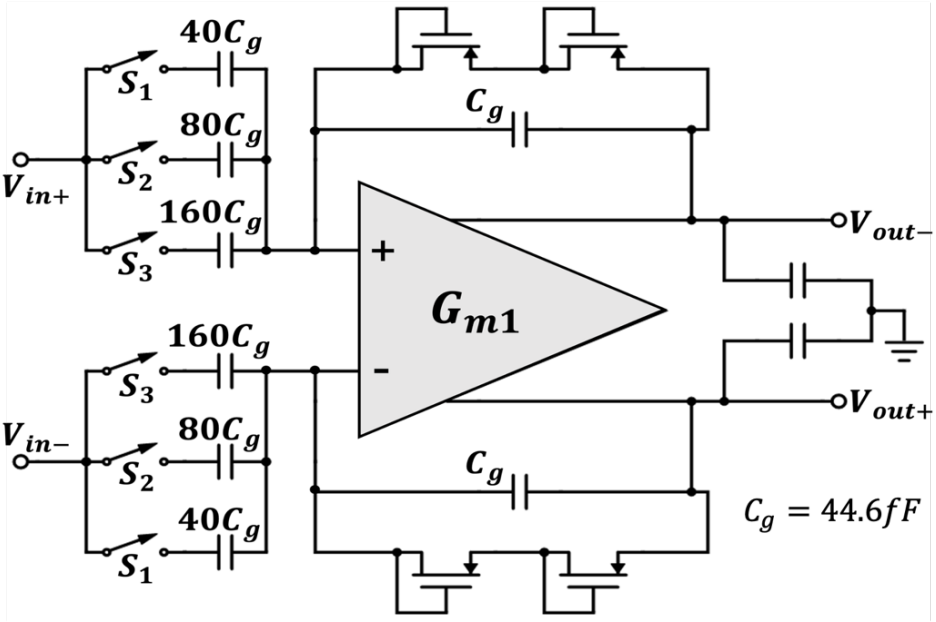

Fig. 5.18: Programmable gain amplifier (PGA) schematic is shown. The purpose of PGA is to provide sufficient gain to the EMF signal to compensate for the loss due to BPF and to make it compatible for the ADC to process. The tunability at the input of the PGA is essential to accommodate for the variations in the EMF signal level when the sensor is located in different regions of the FOV.

5.19. The total integrated noise at the output of the PGA is 8mV_{rms} for the X/Y sensors and 1mV_{rms} for the Z-sensor, which translates to a raw magnetic field resolution of $64\mu\text{T}_{\text{rms}}$ and $8\mu\text{T}_{\text{rms}}$, respectively. The resolution is further improved by averaging several consecutive samples, as discussed later.

5.2.4 Peak Detect and Hold (PDH) circuit

As mentioned earlier, the peak magnitude of the sinusoidal magnetic field at any given point of interest in the FOV is the only necessary signal for the purpose of position decoding. This relaxes the constraint on the ADC which is required to digitize only the peak values and not operate in continuous mode, thus saving power significantly. To extract the peak magnitude from the differential outputs of the PGA,

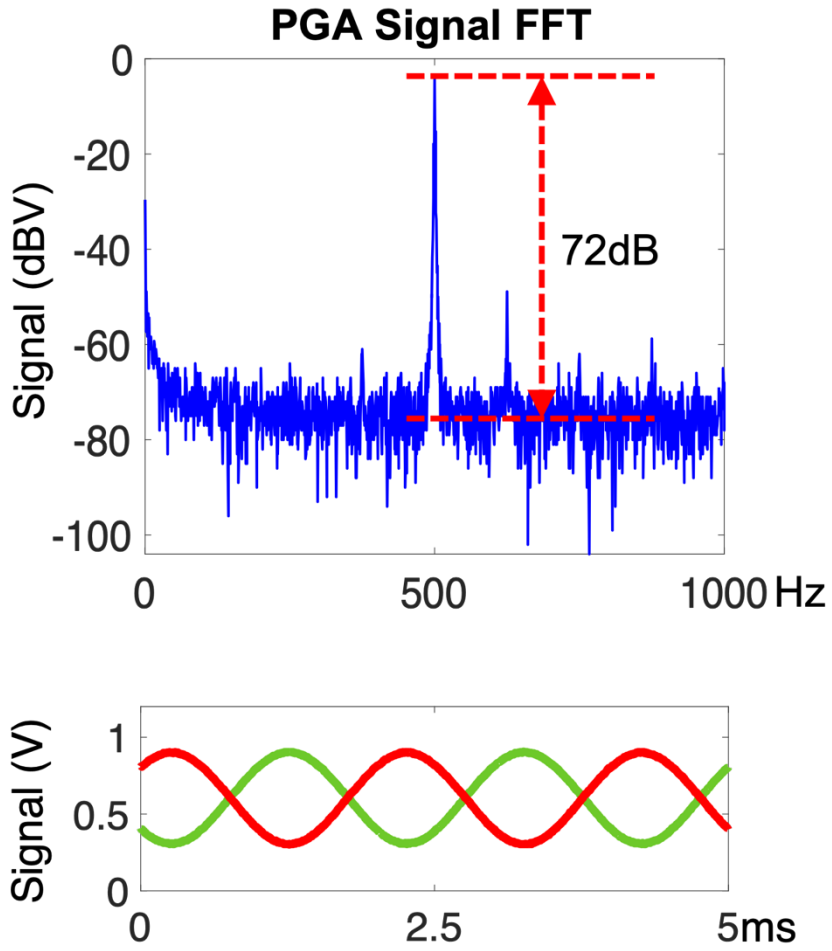

Fig. 5.19: Measured spectrum of the PGA signal output, showing an SNR of 72dB. The time domain differential outputs are shown below, highlighting an output voltage swing of 600mV$_{pp}$ in response to a mid-range magnetic field input.

a differential PDH circuit is implemented for both positive and negative peak extraction [35]–[38], as shown in Fig. 5.20. The PDH circuit operates in three modes: peak detect, peak hold, and reset. For the positive PDH circuit shown in Fig. 5.20, as V_{in+} increases, the output of G_{m3} decreases, leading to an increased current in the current-mirror pair which causes V_{out+} to increase until a positive peak is detected. When V_{in+} starts decreasing, V_{out+} is unable to follow as the hold capacitor C_p (15pF) cannot discharge from the current-mirror transistor on top, thus holding the previous peak value. After the ADC performs digitization of the peak value stored

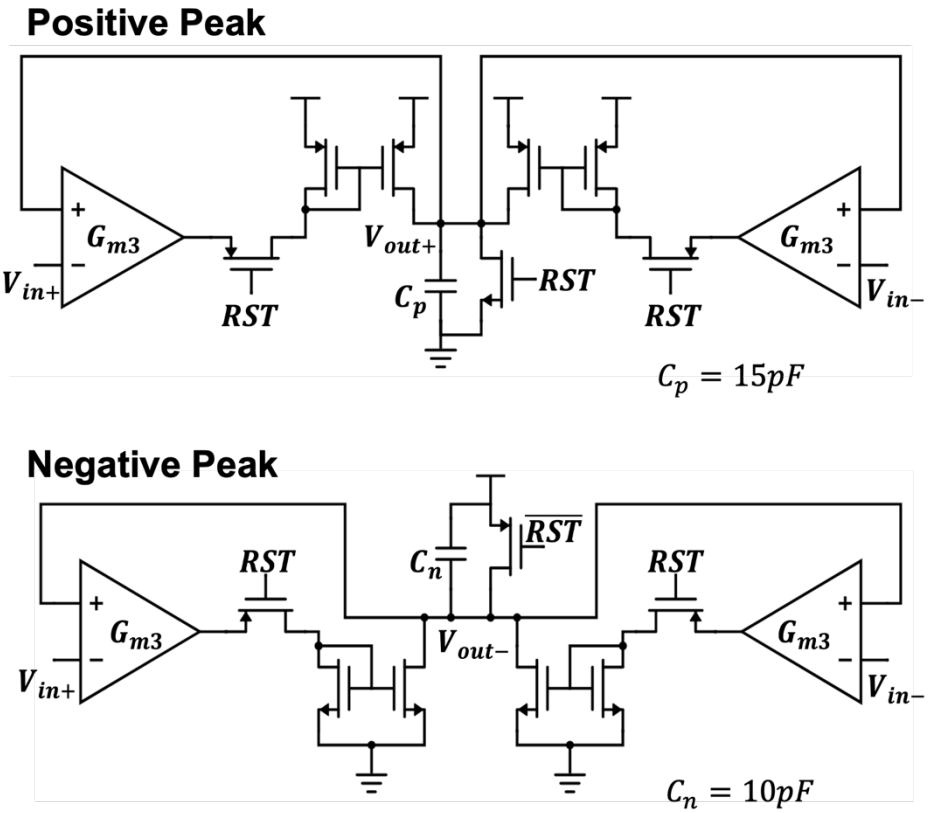

Fig. 5.20: The peak detect and hold (PDH) circuit schematic is shown. The positive PDH (top) extracts the positive peak voltage from the differential input EMF signals V_{in+} and V_{in-}. As a result of the feedback action, the output V_{out+} follows the inputs during their rising phase and holds the peak value (until reset) as the inputs start decreasing. Analogous to the positive PDH, a negative PDH circuit is realized to track and hold the negative peaks (bottom) since both positive and negative peak values are required for the differential-input ADC.

on C_p, the reset transistor at V_{out+} (RST) discharges C_p immediately for the next cycle. Since the input to the PDH is differential, an identical circuit is used to extract the positive peaks from V_{in-} and its output is connected to V_{out+}. A similar operation takes place for negative peak extraction (Fig. 5.20). The measured positive and negative peaks are plotted in Fig. 5.21. For the ADC to digitize the outputs of the PDH, a sampling clock is generated that is synchronized with the peaks of the EMF

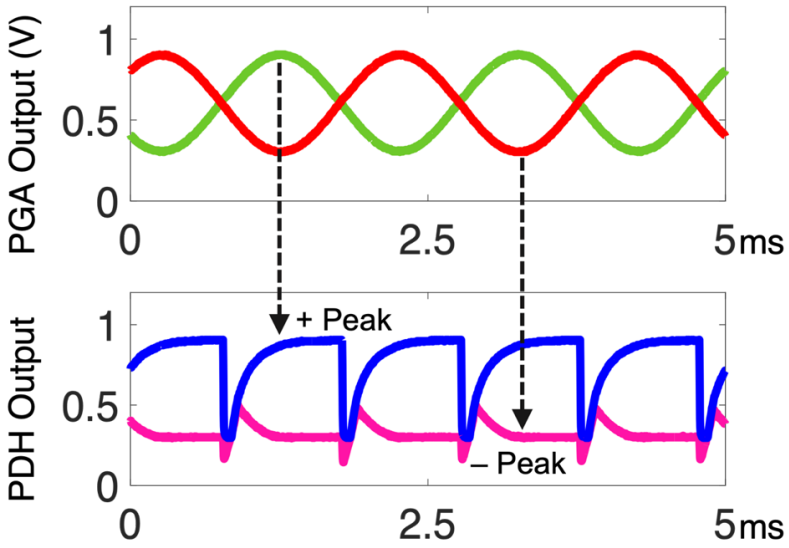

Fig. 5.21: Measured waveforms for the positive and negative PDH circuit outputs. The inputs are tracked until the respective peaks are reached and the peak value is held until the next cycle begins.

signal (see Methods). The power consumption of the complete PDH block is 1.14µW.

5.2.5 Analog-to-Digital Converter (ADC)

The differential outputs of the PDH are fed to a 12-bit differential-input successive approximation register (SAR) based ADC (Fig. 5.22). The high power-efficiency of SAR ADCs for the relatively low sampling rate of 20kS/s required in this work makes them a preferred choice over other ADC architectures [39]–[43]. By adopting the monotonic capacitor switching procedure for our ADC, the power and area requirements are further reduced [39]. The ADC consists of four major blocks—comparator, capacitive digital-to-analog converter (DAC), SAR logic block, and bootstrapped switches. The input is first sampled on the top plates of the capacitors via the boot-strapped switches while all the bottom plates are connected to V_{refP}

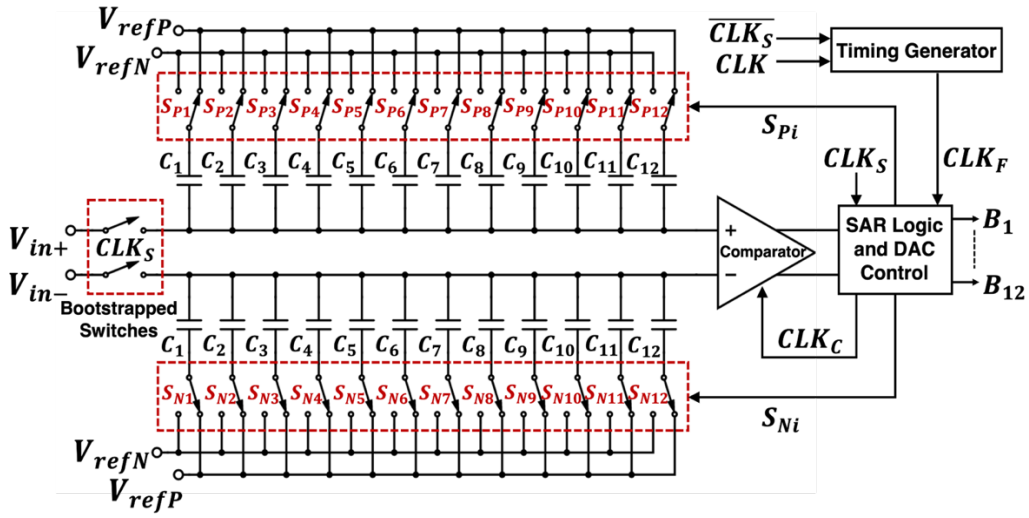

Fig. 5.22: Top-level schematic of the 12-bit SAR ADC showing all the major blocks—comparator, 12-bit capacitive DAC, SAR logic and DAC control block, and bootstrapped switches for input sampling.

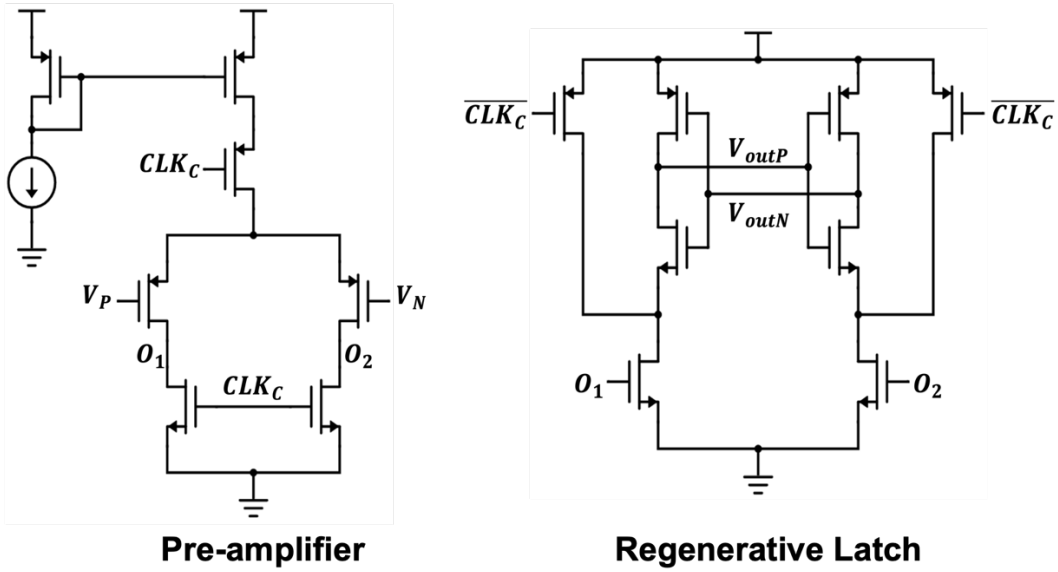

Fig. 5.23: Two-stage dynamic comparator consisting of a pre-amplifier followed by a regenerative latch. The pre-amplifier's input transistors are biased in sub-threshold to achieve low noise and high power-efficiency.

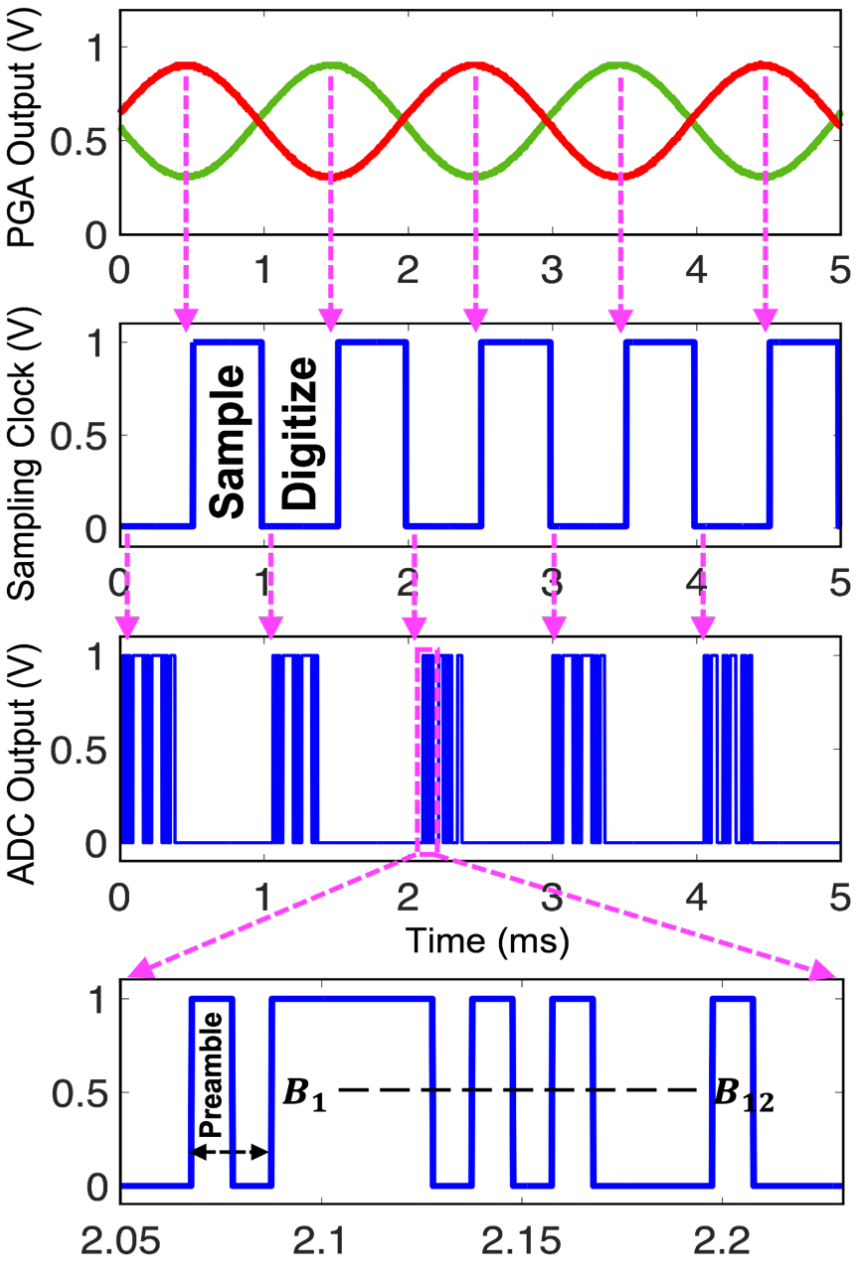

Fig. 5.24: Measurement results showing asynchronously generated sampling clock from the sinusoidal EMF signal for ADC operation. The sampling clock is high for the duration of the peak hold time, which spans from the peak of the sinusoid to the common-mode (600mV) crossing. The 12-bit digital data stream generated for each of the three sensors is serialized together to be read from a single digital pad on the chip. A zoomed version of the 12-bit data output for one of the sensors is shown with the preamble bits present at the beginning for identification.

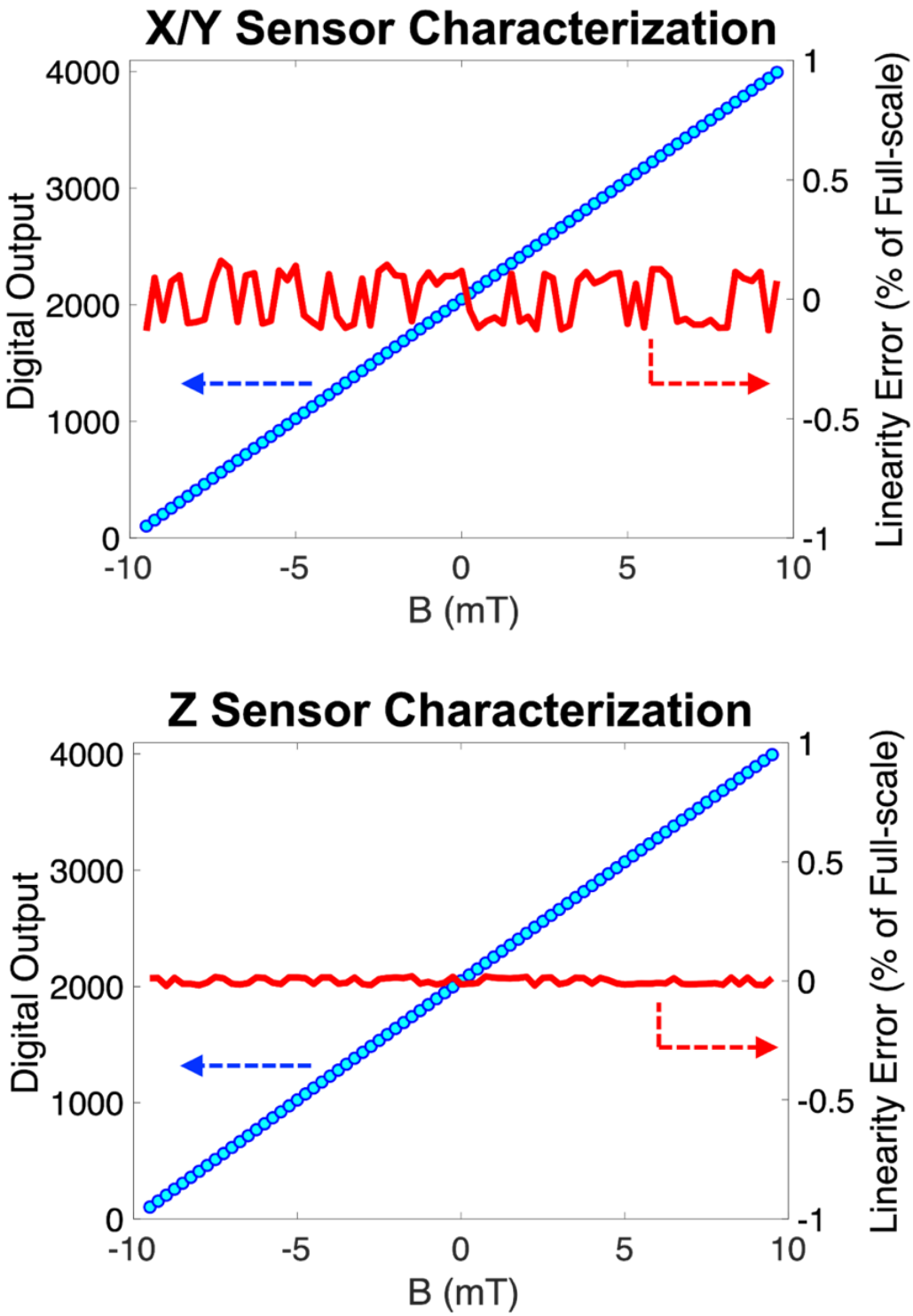

Fig. 5.25: End-to-end characterization for the X/Y sensor (top) and the Z sensor (bottom) showing <0.2% linearity error for both the sensor types.

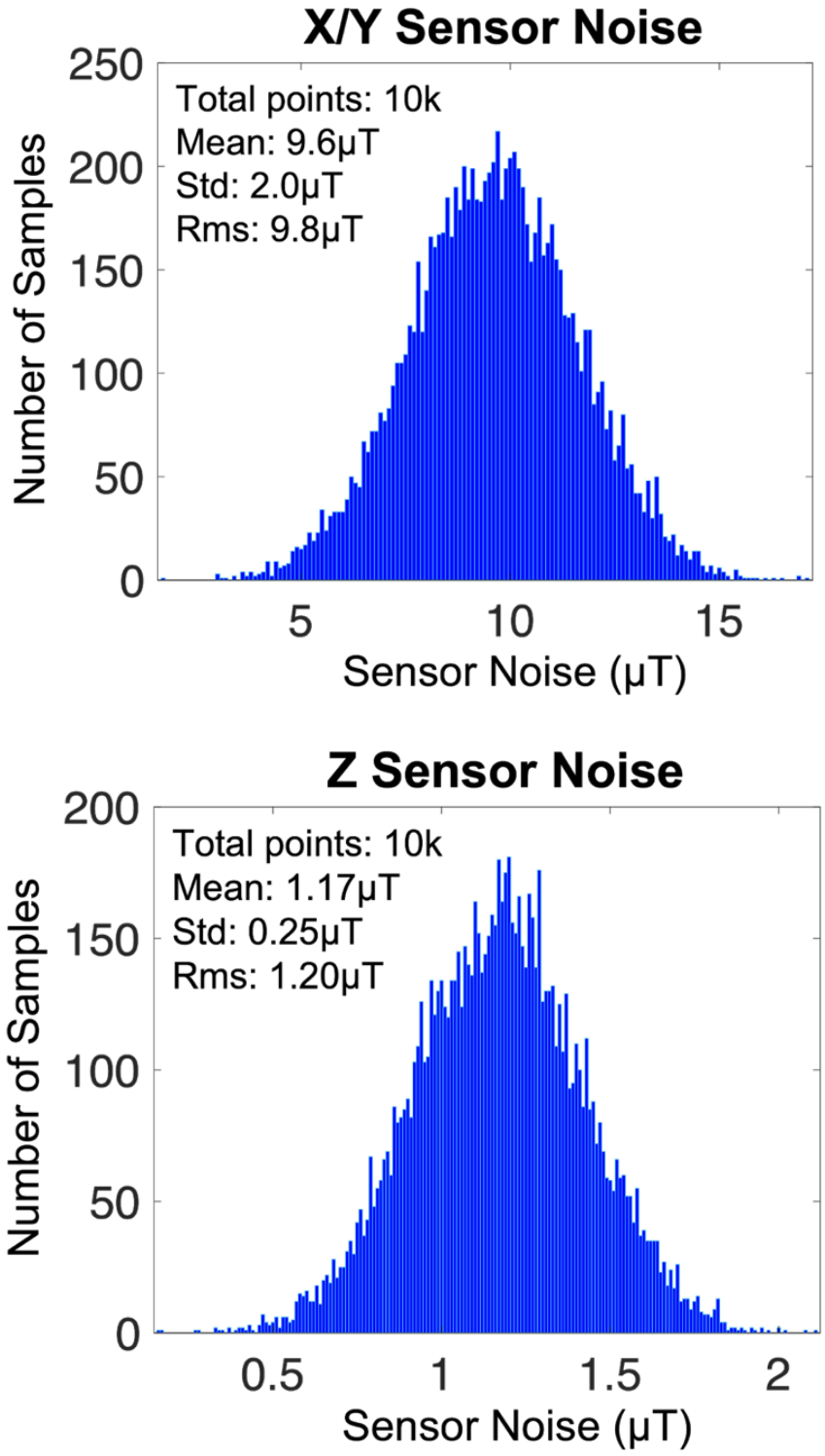

Fig. 5.26: Sensor noise performance showing the noise statistics for 10k sample points collected from 5 different chips. The X/Y sensor exhibits 9.8μT_{rms} noise whereas the Z sensor exhibits 1.2μT_{rms} noise.

(1.2V). When the boot-strapped switches are turned off, the comparator performs the first comparison without switching any capacitor. If the comparator output is high (MSB = 1), capacitor C_1 on the higher voltage side (V_{in+}) is switched to V_{refN} (0V) and the C_1 on the lower voltage side (V_{in-}) remains unchanged. An opposite scenario is executed if MSB = 0. This process is repeated until the LSB is computed. As evident, there is only one capacitor switching per bit computation, which reduces the charge transfer in the DAC and the control logic, resulting in significant power saving. The DAC capacitors are binary weighted with $C_i = 2 * C_{i+1}$ for $i \in (1, 10)$ and $C_{11} = C_{12} = 4$fF.

The comparator (Fig. 5.23) consists of a pre-amplifier followed by a regenerative latch for optimum performance [41]–[43]. The dynamic nature of the comparator ensures no static power consumption. When the ADC clock (CLK) is high, the outputs O_1 and O_2 are reset. When the clock is low, V_P and V_N are compared by the pre-amplifier and the result is fed to the regenerative latch to produce a digital output. By biasing the pre-amplifier's input transistors in sub-threshold regime using the current mirror on top, we achieve low noise and high power-efficiency. The SAR logic and DAC control block (Fig. 5.22) generate all the necessary controls and clock signals using an external 50kHz clock (see Methods). The 12-bit output of the ADC is serialized to produce a single stream of the X, Y, and Z sensor data, a zoomed version of which is shown in Fig. 5.24. The ADC consumes a total power of 2.26µW. The end-to-end sensor characterization results are shown in Fig. 5.25, when the input (X-axis) is swept from -10mT to 10mT and the digital output of the ADC is plotted on the Y axis. The linearity error for the two sensor types is <0.2%. The noise statistics measured across 5 different chips are plotted in Fig. 5.26, highlighting <10µT_{rms} noise for both the sensor types.

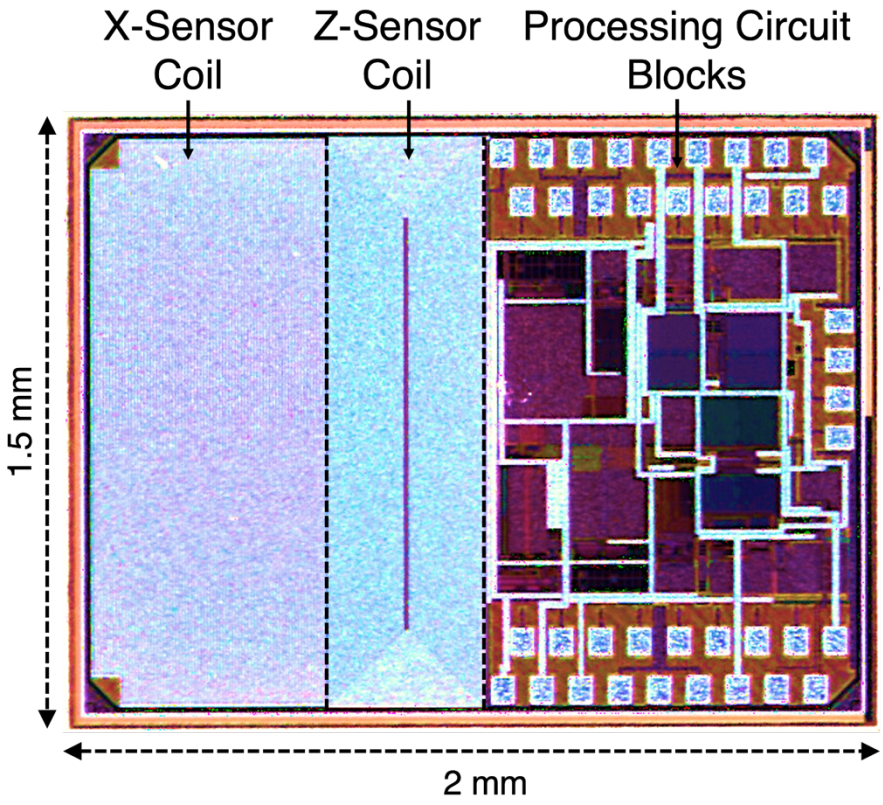

Fig. 5.27: Chip micrograph of the 3D magnetic sensor in 65nm CMOS process is shown. The X and Z sensor coils measure 1.45x0.6mm^2 and 1.45x0.4mm^2, respectively, and the remaining chip area of 1.45x1mm^2 is occupied by the processing circuit blocks. To reduce the fabrication cost of the prototype chips, Y sensor is realized using the X sensor of another identical chip by orthogonal placement, which won't be necessary during mass fabrication as the cost would be significantly lower.

5.2.6 3D Localization of Catheters

The 3D magnetic sensor (Fig. 5.27) is fabricated in the 65nm CMOS process. Since the coils occupy 50% of the chip area, the Y-sensor is realized using the X-sensor of another chip placed orthogonally to the first one (Fig. 5.28). This is done only to reduce the area and cost of these prototype chips and is not necessary for mass fabrication where the cost would be significantly lower. To illustrate the use of our

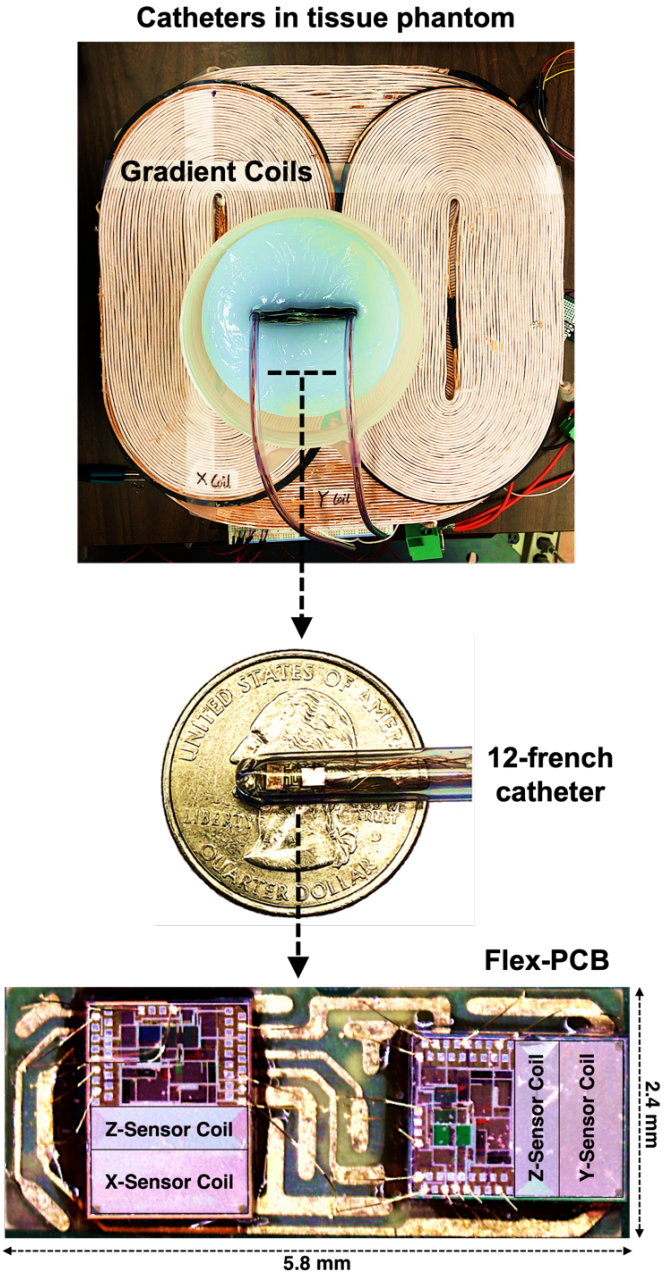

Fig. 5.28: Two sensor chips are assembled on a flex-PCB measuring 2.4x5.8mm^2, which is intentionally designed to be rectangular to fit into the tip of a 12-french catheter that has an inner diameter of 2.8mm. The chip pads for supply voltages, clock input and data readout are wire-bonded to the PCB traces. Thin copper wires (38 AWG) are soldered to the traces and guided through the catheter tube for external access. Two catheter-enclosed devices are attached to a test fixture with a known distance between the catheter tips for relative localization of one device with respect to another. The fixture is submerged in a phantom and placed on top of the magnetic field gradient generating coils for 3D localization.

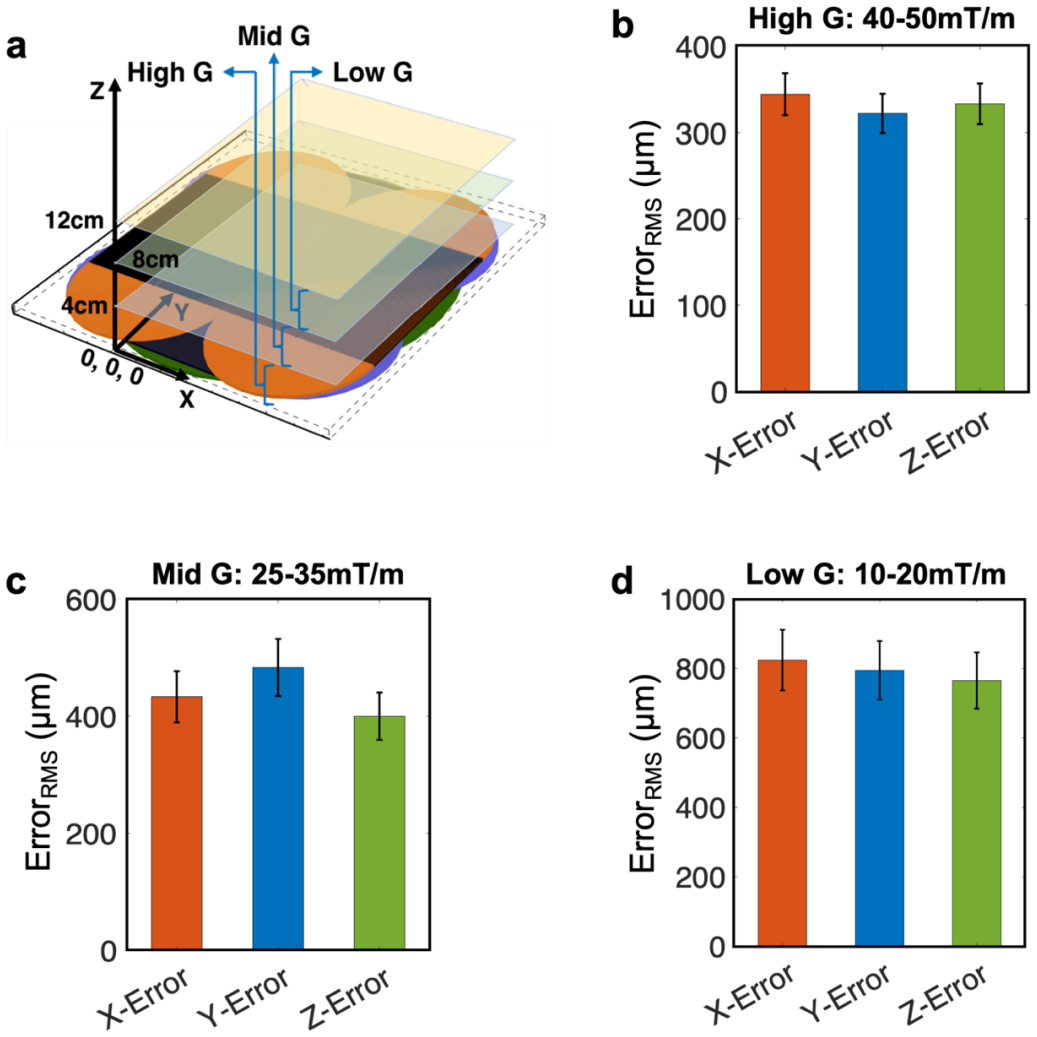

Fig. 5.29: 3D localization results. (a) The 22x22x12cm^3 of FOV produced by the gradient coils is shown where the first 4cm along the Z-axis constitute the high gradient region with G ∈ (40, 50mT/m), the next 4cm correspond to mid gradient with G ∈ (25, 35mT/m) and the last 4cm correspond to low gradient with G ∈ (10, 20mT/m). Error values in the measured distance between the two devices are plotted for 10 different locations each in the (b) high, (c) mid, and (d) low gradient regions. At any given location, 40 consecutive measurements are averaged for each sensor to reduce the noise in raw field values, resulting in a position update rate of 25Hz for 500Hz of EMF signal. The mean error varies from 350µm (high gradient) to 800µm (low gradient) and has a volume-averaged value of 500µm in the FOV.

sensor for 3D localization in clinical settings, two sensor chips are assembled on a flex-PCB and fitted into the tip of a 12-french catheter (Fig. 5.28). Two such catheter-enclosed devices are attached to a test fixture with a known distance between them and submerged in a phantom to perform relative localization. The magnetic field gradient coils are placed beneath the phantom to produce the required gradient during measurements. At a given location, 40 consecutive measurements are averaged to obtain an equivalent magnetic field resolution (ΔB) of 9.8μT_{rms} for the X/Y sensors and 1.2μT_{rms} for the Z-sensor (Fig. 5.26). Given the EMF frequency of 500Hz that results in 1000 data points per second thanks to the differential PDH circuit, an update rate of 25Hz is achieved for the device location. Due to variations in the gradient profile in the FOV, the localization experiment is performed in three different regions—high (40–50mT/m), mid (25–35mT/m), and low (10–20mT/m) gradient (Fig. 5.29). The error in the measured distance between the two devices varies from a mean value of 350µm (high gradient) to 800µm (low gradient), while staying below 1mm throughout the FOV.

5.3 Conclusion

Table 3.2 shows that our magnetic sensor is the first of its kind that is capable of sensing 3D magnetic fields using standard CMOS technology. By employing the technique of EMF induction in passive coils, the sensor consumes no power by itself which is in sharp contrast with the power-hungry Hall and Fluxgate sensors that require mW-level power [9]–[11],[14]–[20]. The processing circuitry has been carefully designed to achieve low-noise operation while consuming 14.8µW of total power which is orders of magnitude smaller than prior works. Our induction-based sensor also enjoys immunity to DC offsets and low-frequency noise which are always present in Hall and Fluxgate sensors, requiring dedicated circuitry for minimization and cancellation [9]–[20]. The current sensor noise of 9.8μT_{rms} (X, Y) and 1.2μT_{rms} (Z) is obtained after averaging 40 measurements per sample at 500Hz of EMF, resulting in an update rate of 25Hz. The averaging window and the EMF signal's

	This work	ISSCC 2020 [25]	NBME 2017 [28]	JSSC 2017 [15]	ISSCC 2015 [17]	JSSC 2007 [9]
Sensing Mechanism	**EMF Induction**	Hall Effect	Hall Effect	Hall Effect + EMF Induction	Fluxgate	Hall Effect
Sensing Dimensions	**3D**	3D	1D	1D	2D	3D
CMOS Technology	**Yes (65nm CMOS)**	No	Yes (0.18μm CMOS)	Yes (0.18μm CMOS)	Yes (0.6μm CMOS)	Yes (0.35μm CMOS)
Ferromagnetic Material	**No**	N.R.	No	No	Yes	Yes
Sensor Noise (X, Y, Z)	**9.8μT_{rms} (X, Y) 1.2μT_{rms} (Z) ***	5μT_{rms} (X, Y, Z)	625μT (Z)	210μT_{rms}	0.2μT_{rms}	0.1μT (X, Y) 0.6μT (Z) &&
DC Offset	**No**	Yes	Yes	Yes (40μT)	Yes (0.9μT)	Yes (1.5μT) &&
Range	**±10mT**	±36mT	40-170mT	±7.8mT	±1.32mT	±200μT
Power	**14.8μW**	1mW	339μW	13.86mW #	280mW #	30mW
Supply Voltage	**1.2V**	2.5V	1.8V	1.8V	5V	2.2 – 3.6V
Update Frequency	**25Hz ***	7Hz	763Hz	<3MHz ##	<15kHz &	11.76Hz $
B-field Frequency	**100 – 1kHz**	DC	DC	DC – 3MHz ##	DC – 75kHz ##	DC
Digitization	**Yes (12-bit SAR ADC)**	Yes (16-bit ADC)	Off-chip	No	Yes (13.5-bit ADC)	Yes (12-bit ΣΔ ADC)
Device Dimensions	**4mm^2 ****	108x68mm^2	1.8x1.2mm^2	3.5x2.5mm^2	9.8mm^2	2.3x2.8mm^2

* Obtained by averaging 40 consecutive samples
** Estimated for a single 3D sensing chip based on the current prototype measuring 3mm^2
& Calculated from the ADC sample rate (200kS/s) and ENOB (13.5)
&& Calculated from the reported value in LSB/μT
# Calculated from the reported current and voltage
Calculated from the reported sensor bandwidth
$ Calculated from the reported refresh time
N.R. – Not reported

Table 3.2: Comparison with state-of-the-art. Our CMOS-integrated 3D magnetic sensor has the lowest reported power, <10μT_{rms} noise, ±10mT range, and immunity to DC offsets and low-frequency noise.

frequency can be chosen accordingly to yield the desired noise and update rate for a given application. The current processing circuitry is capable of handling B-field from 100Hz to 1kHz, which can be easily modified in future versions to accommodate the desired range of frequency. Wireless power and data telemetry can also be integrated in the future to achieve fully-autonomous sensing [29].

Our 3D magnetic sensor is especially useful for bioelectronics and biomedical applications. As shown in Fig. 5.28–5.29, the sensor can be enclosed in tips of catheters and guidewires to achieve real-time navigation and tracking with ≈500μm of volume-averaged mean position error. This could be of significant clinical benefit in tracking catheters and guidewires used in endovascular procedures such as renal

denervation, liver lesion resection, stent and shunt placement, and abdominal aortic aneurysm repair [3]–[6],[44]. Such guidance assistance is also crucial for minimally invasive surgery (MIS) where the procedure is performed through small openings in the body to reduce patient discomfort, healing time, risk of complications, and achieve better patient outcomes. Typical examples of MIS are neurosurgery, ENT surgery, interventional radiology, cardiac surgery and robotic surgery [45]. The 3D magnetic sensor can also be used as a fiducial marker during preoperative planning for image guided surgery. Currently used fiducial markers are mostly passive and bulky—implanted spheres, bone screws and adhesive skin markers, which suffer from a poor localization error in sub-cm scale [46],[47]. This is particularly important for soft tissue organs like liver as they complicate the intraoperative registration due to their inherent deformability and respiratory-related motion. Thanks to the small size and low-power operation of our magnetic sensor, several of them can be attached as anatomical landmarks around the liver lesion and on the surgical tool to achieve dynamic tracking with high precision [48]. The use of our sensor as anatomical landmark can also benefit targeted radiotherapy used in cancer tumor treatment which heavily relies on the precision of targeting for maximum efficacy [49],[50]. For the more recently reported magnetic gradient based localization of devices in precision surgeries [25],[26] and for GI tract monitoring [27],[2], the bulky, power-hungry and off-chip Hall sensor can be replaced by the current CMOS-based sensor to yield a much smaller, low-power and integrated device that enhances the performance and usefulness of these systems.

5.4 Methods

Z-sensor coil implementation: The Z-sensor coil is implemented by creating a spiral loop of metal that lies in the plane of the CMOS chip, an illustration of which is shown in Fig. 5.4. The induced EMF, which is an indirect measure of the magnetic field produced by the external gradient coils, is given by:

$$EMF = d\phi/dt = N.A.dB/dt \quad (5.3)$$

where *N.A.* is the sensor dependent geometric factor and dB/dt is the AC gradient dependent factor. For a sinusoidal magnetic field produced by the gradient coils:

$$B = B_0 * sin(\omega t) \quad (5.4)$$

$$dB/dt = B_0 * \omega * cos(\omega t). \quad (5.5)$$

From the gradient coils side, both B_0 and ω can be used to enhance the EMF given by Eq. (5.3). From the sensor side, the geometrical factor of *N.A.* can be increased to control the amount of induced voltage. It is to be noted that *A* is the effective cross-section area of the coil-sensor that is perpendicular to the incoming magnetic field flux, and *N* is the total number of turns of the coil-sensor in the direction of the incoming flux. For the spiral Z-sensor coil's detailed diagram shown in Fig. 5.30, the equivalent definition of $N.A.$ in Eq. (5.3) changes to:

$$N.A. = A1 + A2 + \cdots An \quad (5.6)$$

where $A1$ denotes the area of the outer-most loop, $A2$ denotes the area of the second loop, and so on. An illustration is shown in the Fig. 5.30 (b), where the multi-turn coil can be divided into several single-turn coils and the effective area of each can be calculated. The value of n used for illustration in Fig. 5.30 is 7, but the actual n used for the Z-sensor coil is significantly higher (Table 3.3).

As evident from Eq. (5.6), a multi-turn spiral coil would produce a correspondingly large EMF. To achieve that, the Z-sensor coil is designed with minimum width and spacing requirements set by the DRC in order to achieve the maximum number of turns for a given area. To achieve a further increase in the effective area, identical coils are implemented in all the metal layers from M1 on bottom to AP on top, and

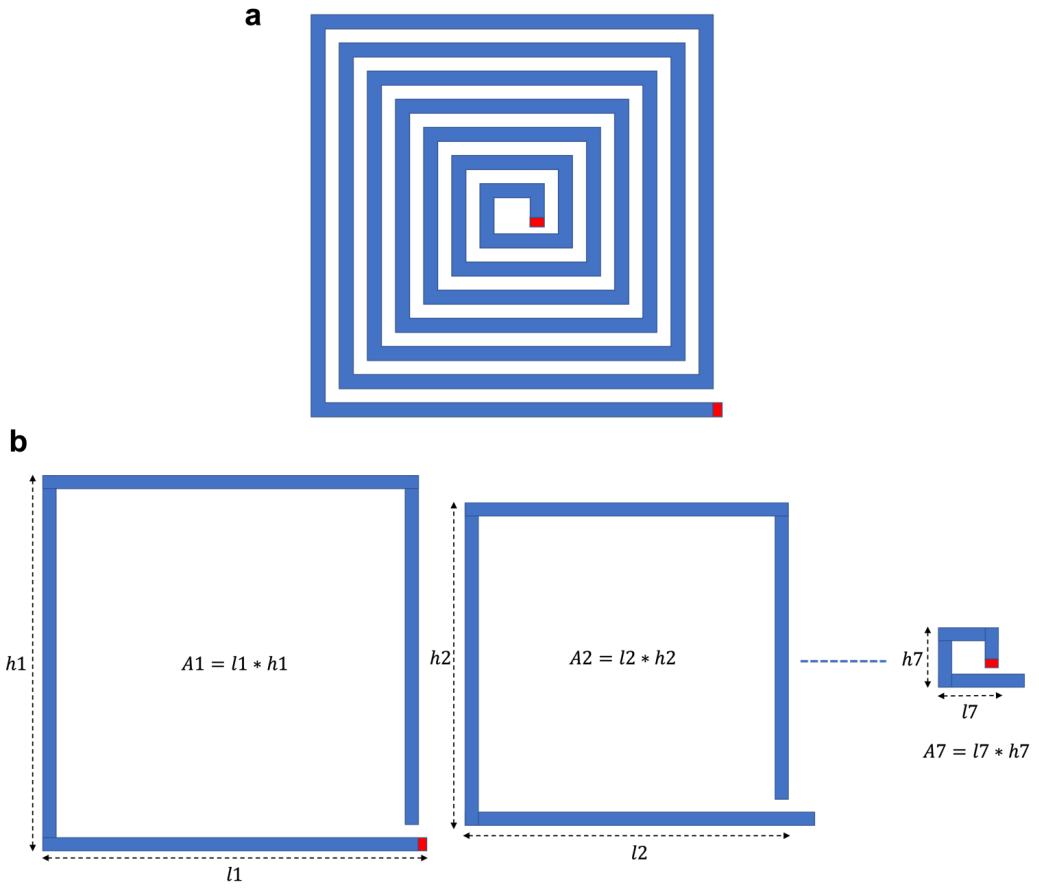

Fig. 30: Z-sensor coil. (a) A single spiral loop of the on-chip Z-sensor coil is shown that is implemented using one of the several metal options available in the 65nm CMOS processes. Each of the ten metal layers in the 65nm node is used for creating a spiral loop in the plane of the metal and all the spirals are connected together using vias (at the red terminal locations) to yield a single multi-layer spiral spanning from the lowest metal layer (M1) to the highest metal layer (AP). (b) The spiral loop shown in (a) is split into several single-turn loops for evaluating the expression described in Eq. (5.6).

are stacked together to form a single spiral spanning all the available metal layers in the 65nm node.

Parameter	X/Y Sensor Coil	Z Sensor Coil
Chip Area	1.45 x 0.6 mm^2	1.45 x 0.4 mm^2
Number of Turns	M1-M7: 1200 M1-M8: 600 M1-M9: 75 M1-AP: 75	M1-M7: 666 M8: 249 M9: 49 AP: 39
Coil Resistance	8MΩ	5.4MΩ
Coil Inductance	<100μH	<100μH
Parasitic Capacitance (with p-sub)	52pF	36pF

Table 3.3: Details of the number of turns for each sensor coil and their different components. The values of the coil resistance, inductance, and parasitic capacitance are also shown.

Mutual inductance between gradient coil and on-chip sensor coil: For two coils that have a mutual inductance M between them, the induced EMF in one (secondary) due to changing current I in the other (primary) is given by:

$$EMF = M * dI/dt. \tag{5.7}$$

M depends on various factors: (i) the area and number of turns in both the primary and the secondary coils; (ii) the distance between the two coils; (iii) the relative orientation of the two coils; and (iv) the media between the two coils. Hence, the best way to evaluate M is through electromagnetic simulations and then verifying the simulated outcome by comparison with theoretical calculations. For the purpose of calculation of M, we make use of another equation:

$$EMF = N * A * dB/dt \tag{5.8}$$

which describes the induced EMF in the secondary coil as a function of the secondary coil's number of turns (N), cross-section area (A) perpendicular to the magnetic flux B, and the rate of change of the magnetic flux. By equating (5.7) and (5.8), we obtain:

$$M = N * A * (dB/dt)/(dI/dt) \tag{5.9}$$

where I is the current in the primary coil and B is the magnetic field at the location of the secondary coil. For a sinusoidal current I given by:

$$I = I_0 * \sin(\omega * t). \tag{5.10}$$

The magnetic field B at the location of the secondary coil is given by:

$$B = B_0 * \sin(\omega * t). \tag{5.11}$$

Plugging I and B from Eq. (5.10) and (5.11), respectively, in Eq. (5.9), we get:

$$M = N * A * B_0/I_0 \tag{12}$$

where I_0 is the peak current used to excite the primary coil and B_0 is the peak magnetic field observed at the secondary coil's location. For simple coil structures, B_0 can be calculated theoretically from I_0 using the Biot-Savart law since both are peak (hence can be considered DC for calculation purpose) values. For more complex geometries such as the gradient coils used in this work, the value of B_0 for a given I_0 is found experimentally and also through magnetostatic simulations in Maxwell. Once the ratio B_0/I_0 is found, we can plug it in Eq. (5.12) and use the geometrical parameters N and A of the secondary coil to calculate the mutual inductance M. This theoretical value of M can be compared with its simulated value from magnetostatic simulations in Maxwell and gives us a higher degree of confidence in the effective

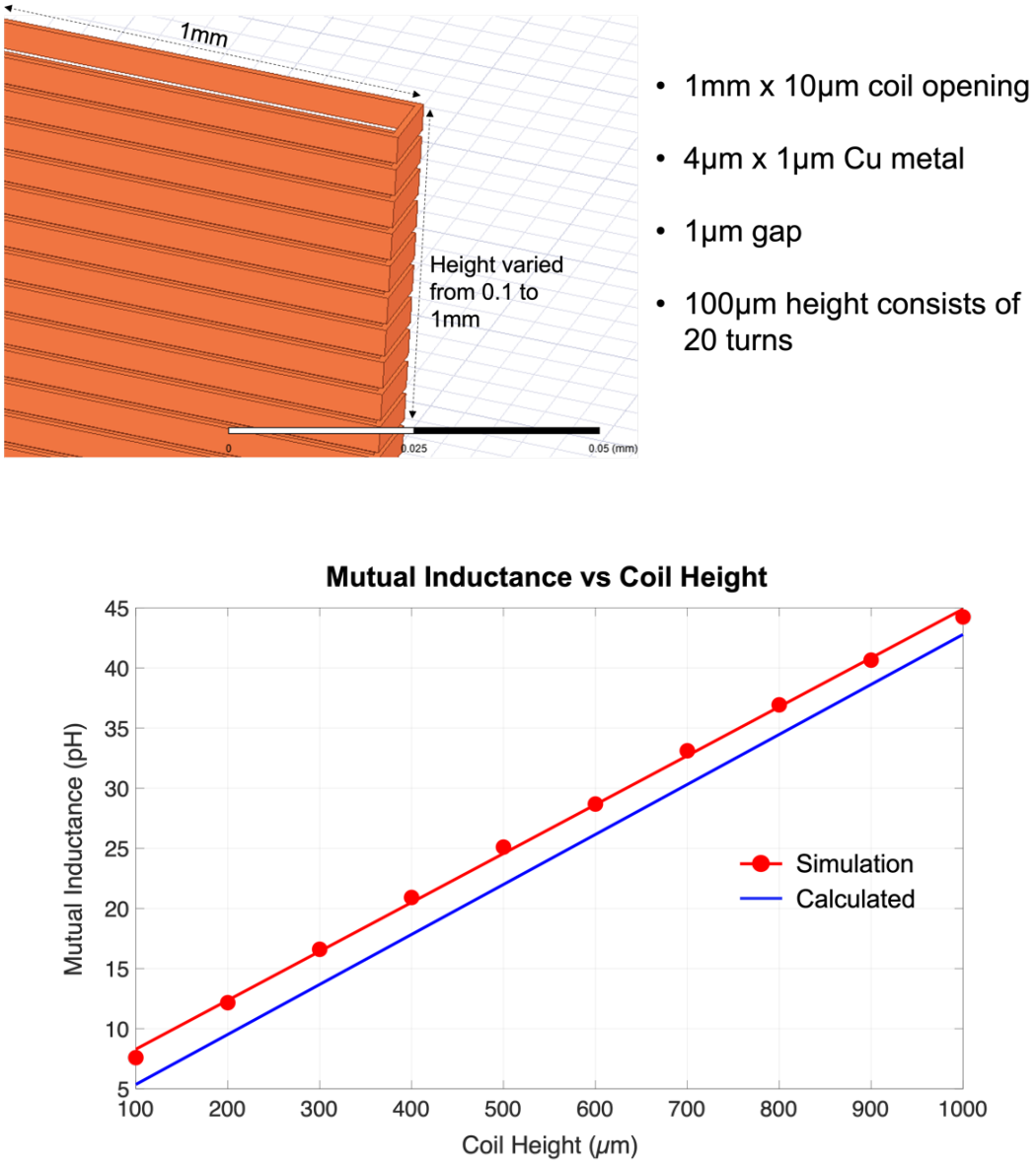

Fig. 5.31: Mutual inductance verification in ANSYS Maxwell. The secondary coil (on-chip sensor coil) is shown in the top panel with the used parameters for simulation. The mutual coupling between the secondary and the primary coil (external gradient coil) is simulated while varying the number of turns (hence the effective coupling area) of the secondary coil. The simulated value is then compared with the theoretically calculated value (bottom panel) to confirm a good matching between the two. These simulations are carried out for both the X and Z sensor coils to confirm the consistency of the trend.

coupling that will occur between the two coils in the final real-world scenario. Fig. 5.31 shows that we obtained good agreement between the theoretical and the simulated values of M. For a comprehensive study, the value of M is evaluated under different settings: silicon chip environment, frequency variation, eddy currents, and presence of human tissue (Fig. 5.7–5.10).

Advantages of using AC gradient: There are several advantages to using an AC magnetic field gradient instead of DC for localization of magnetic-field sensing microdevices. First, for a gradient G_0 that corresponds to a DC current of I_0, the same gradient in AC domain would require a current excitation of $I_0 sin(\omega_0 t)$. The power loss due to heating in the coils, which can be quite significant for continuous operation, would be $I_0^2 R$ for DC excitation and $I_0^2 R/2$ for AC excitation. Thus, the power loss is reduced by half for AC gradients.

Second, for an AC gradient based localization system, the magnetic-field sensing microdevice is not constrained to employ a Hall-effect based magnetic sensor for high resolution, as was done in [25]–[28]. Instead, a coil-based sensor capable of sensing the induced EMF due to the AC magnetic field produced by the gradient coils, would suffice. As shown by Eq. (5.13), the position resolution Δx obtained by using a DC gradient *G* and a magnetic sensor with resolution ΔB, can be improved by increasing the value of *G* which scales linearly with the DC current (for a given sensor and coil geometry).

$$\Delta x = \Delta B / G \tag{5.13}$$

Thus, a lower Δx implies a higher *G* which requires a higher *I*. On the other hand, while using the AC gradient, the induced EMF is given by:

$$EMF = d\phi/dt = N.A.dB/dt \tag{5.14}$$

where *N.A.* is the sensor dependent geometric factor and dB/dt is the AC gradient dependent factor. For a sinusoidal magnetic field produced by the gradient coils:

$$B = B_0 * sin\,(\omega t) \tag{5.15}$$

$$dB/dt = B_0 * \omega * cos\,(\omega t). \tag{5.16}$$

As seen from Eq. (5.16), dB/dt not only depends on B_0 which is the peak magnetic field value that depends on the peak current in the coils, but also on the frequency component ω. Thus, we now have an additional tuning knob of frequency ω to enhance the sensitivity of the sensor, thus reducing ΔB in Eq. (5.13). This improves Δx without having to ramp up the current to yield a higher G. If the current I in the gradient coils stays the same while the frequency is changed, the I^2R heat loss also stays the same, unlike the DC gradients that increase the current linearly and result in a quadratic increase in the I^2R loss. This results in a more power efficient system.

Third, the sensor for the AC gradient based localization can be replaced by a passive EMF-sensing inductor coil that does not consume any active power during the EMF sensing mechanism. The processing of the EMF can easily be done within a few μW of power, as described in the circuit design sections above. The complete end-to-end power of the coil-based sensor and processing circuits in this work is <15μW, which is significantly less than the milliwatt-level power consumed by the power-hungry Hall sensors used in [25]–[28]. It is also to be noted that the sensitivity of Hall sensors directly depends on the current used in Hall elements, implying that a higher sensitivity comes at the cost of higher power. However, for the passive coil-based sensor, the sensitivity can be enhanced by either using a higher frequency on the gradient coils side, or using a higher geometrical factor on the sensor side. As discussed before, a higher frequency does not lead to more power loss for the gradient

coils. Thus, the AC gradient based localization system is more power efficient both from the gradient coils side and the sensor side.

The AC gradient based system is also more robust to DC offsets, ambient earth's magnetic field, and avoids low-frequency noise problems. Table 3.1 summarizes all the major advantages achieved by the AC gradients over DC.

AC power supply: The AC power supply used in this work is model number AC6803B by Keysight. It provides a maximum output power of 2000W, maximum RMS current of 20A, and allows monitoring of the AC voltage, current and power with <1% precision. It has a tunable frequency range for 40Hz to 500Hz with an accuracy of 0.02%. The output voltage is stable up to 100 ppm/^{0}C, has a typical response time of 150µs, and has ±15% of full scale line regulation.

Circuit blocks: For the IA, the relatively low gain is compensated later in the chain using the PGA after the sensitive EMF signal is filtered by the bandpass filter following the IA. Pseudo-resistors are used in the IA to also bias the non-feedback

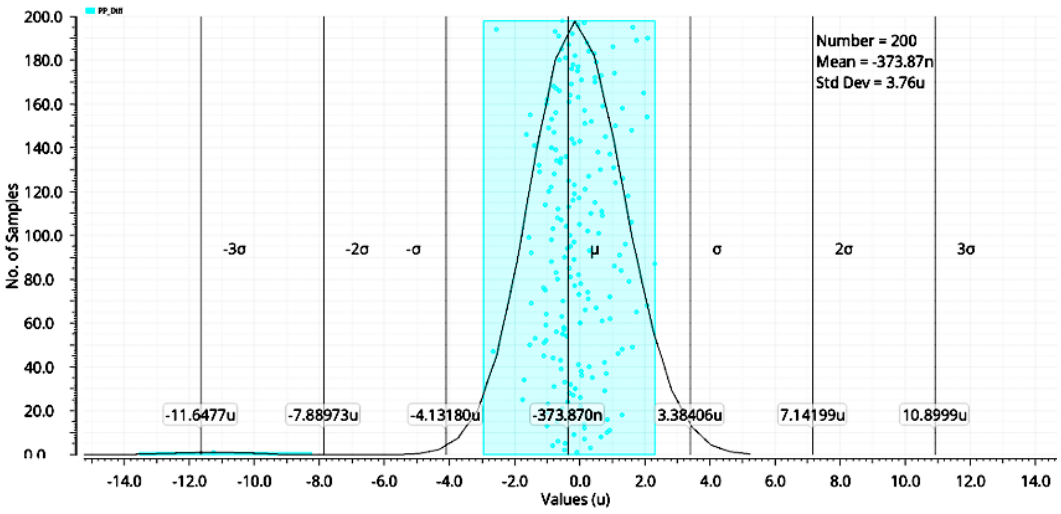

Fig. 5.32: Monte Carlo simulation results for the IA showing the value of offset voltage to be -0.37 ± 3.76 µV, which is well within the acceptable range.

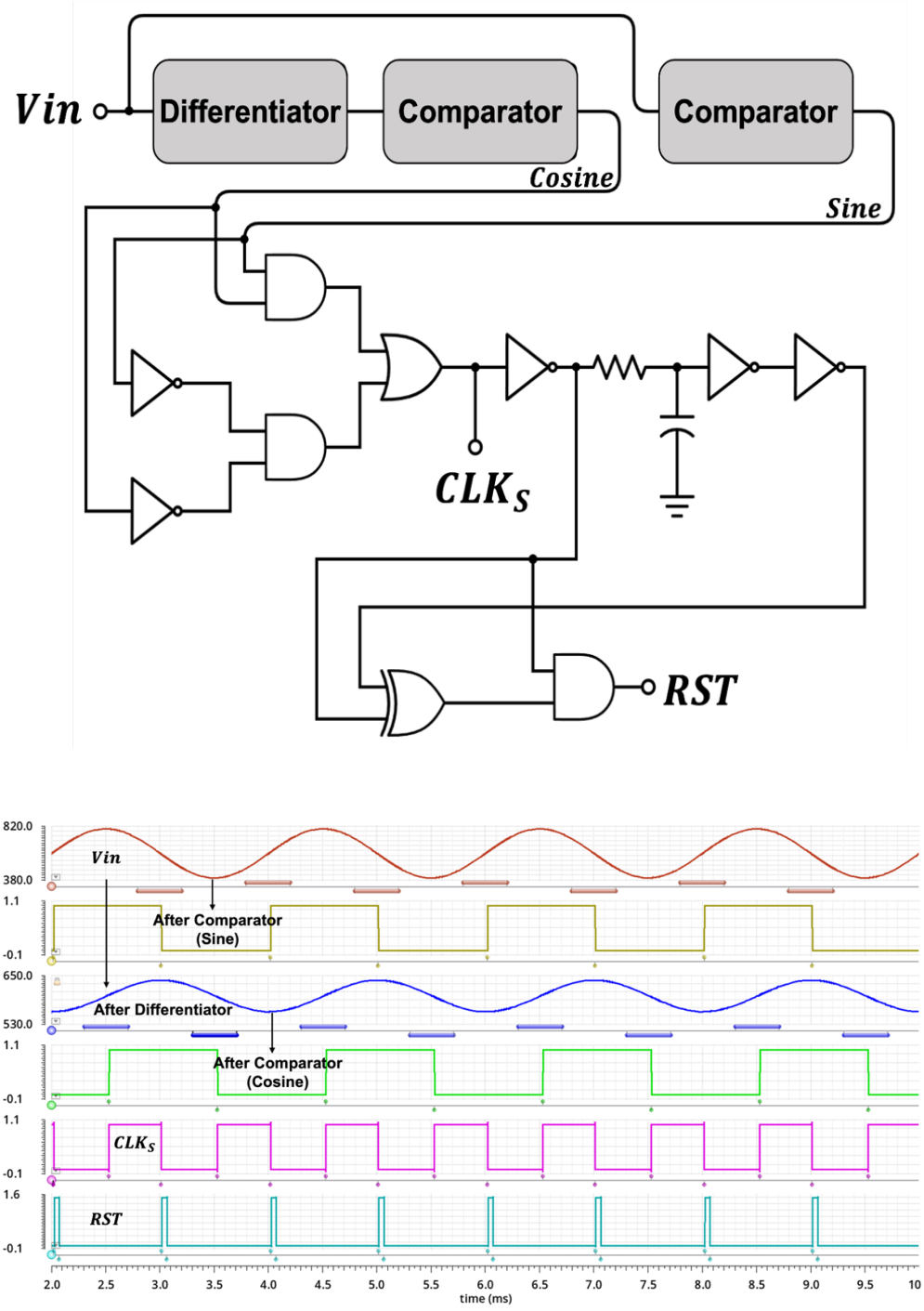

Fig. 5.33: Overview of the timing block (top) that generates the ADC sampling clock (CLK_S) and the PDH reset signal (RST) using the output of the PGA (V_{in}). Signal waveforms at relevant nodes of this block are shown in the bottom panel.

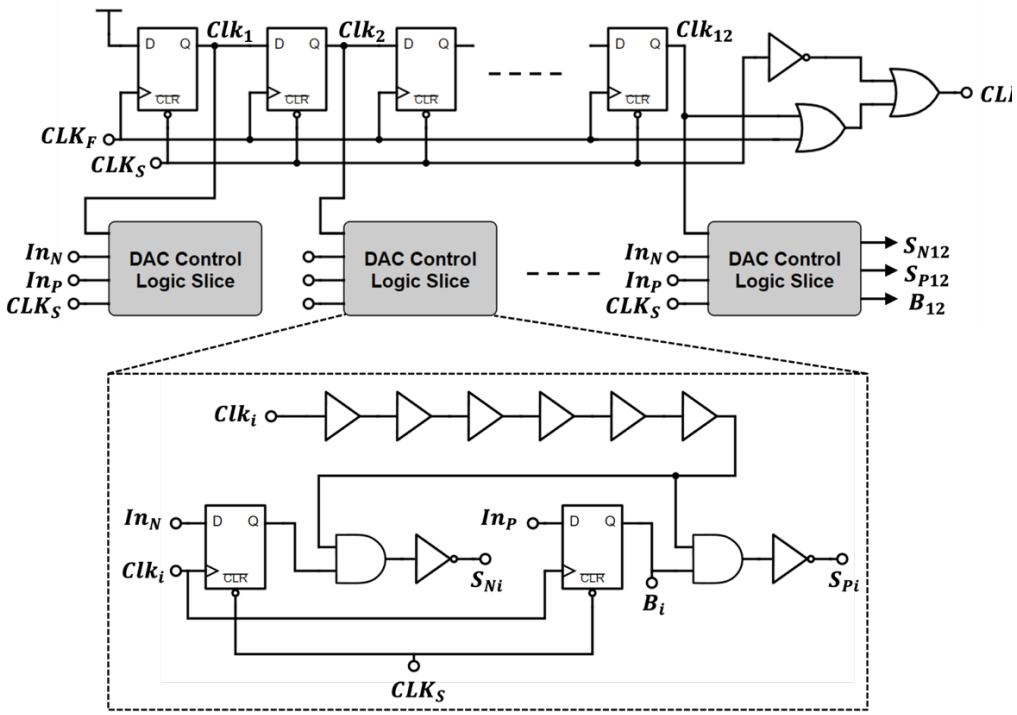

Fig. 5.34: Block level overview of the SAR Logic and DAC Control block used in the ADC.

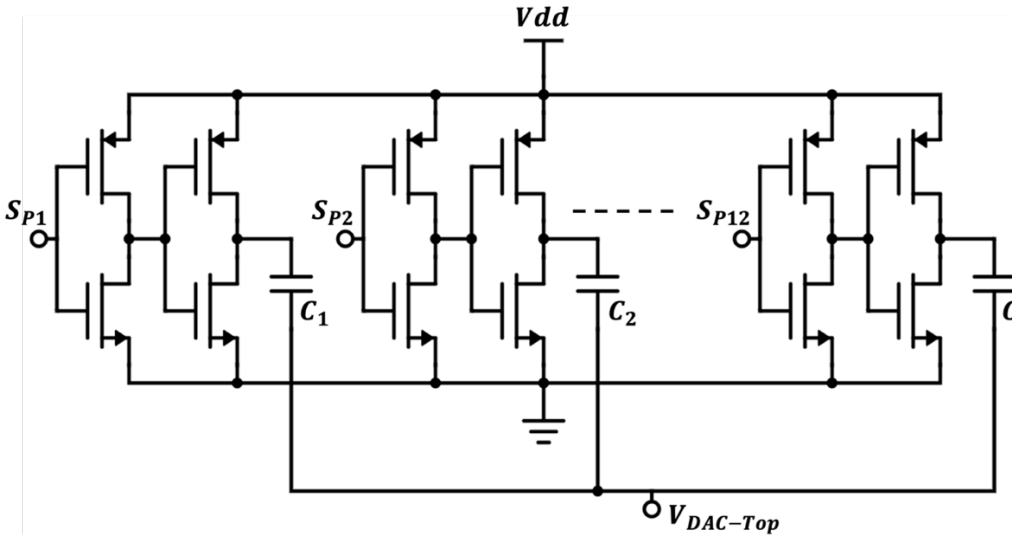

Fig. 5.35: DAC overview showing the switching signals (S_{P1}-S_{P12}), inverter-based drivers for switching the capacitors, and the DAC capacitors (C_1-C_{12}).

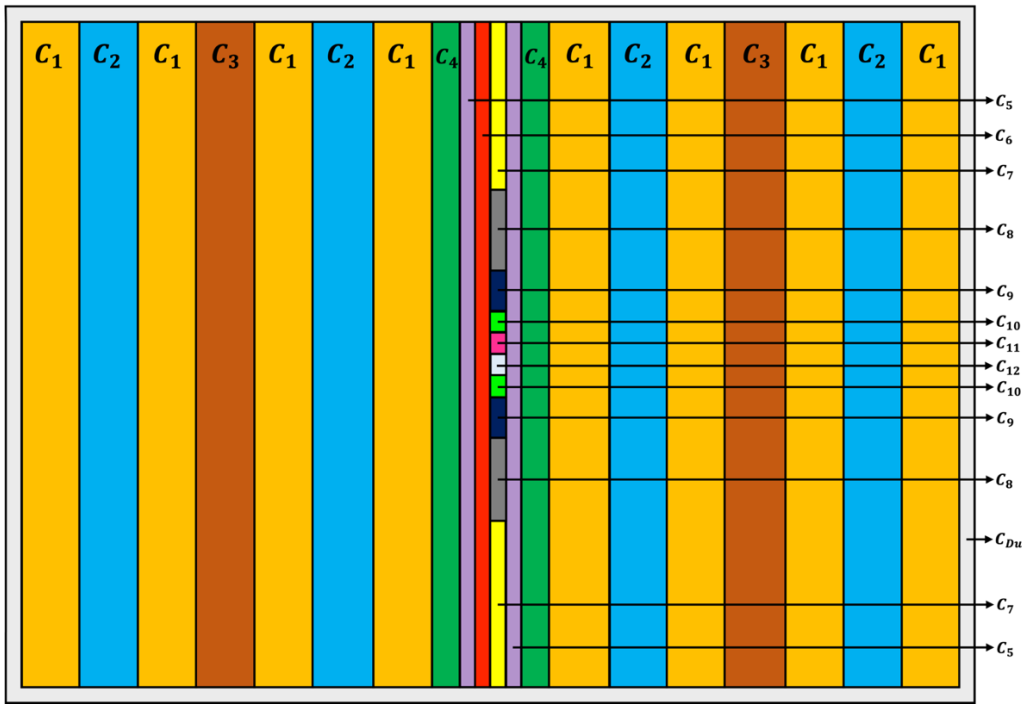

Fig. 5.36: Layout of the DAC capacitors showing a highly common-centroid floorplan.

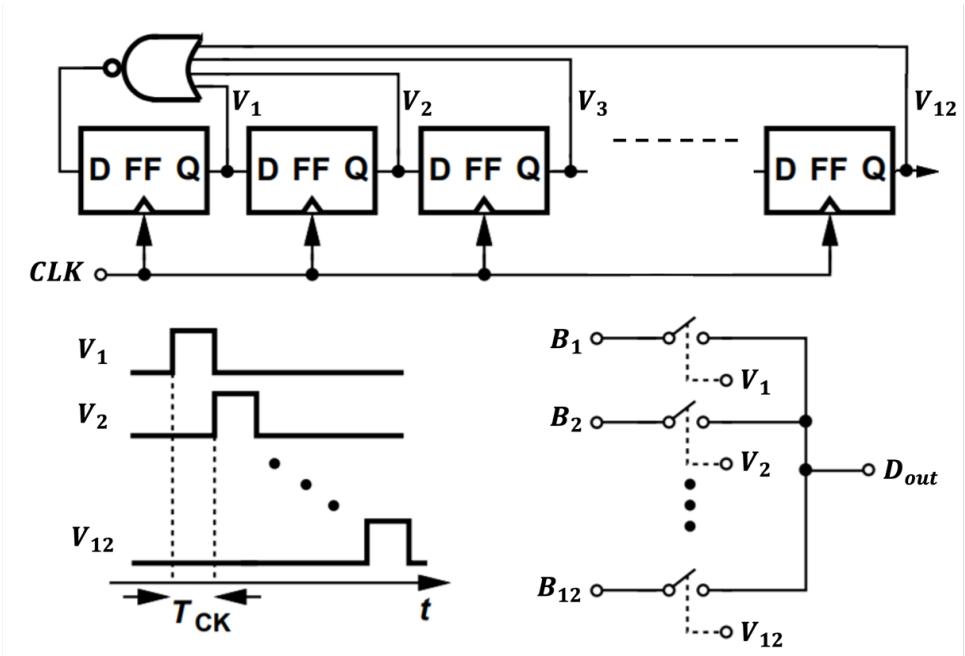

Fig. 5.37: Overview of the serializer block showing the architecture (top) and its operation (bottom).

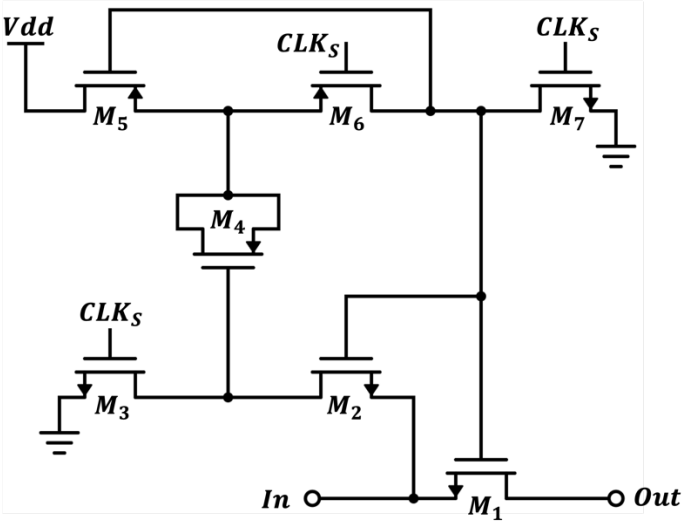

Fig. 5.38: Circuit schematic of the bootstrapped switch.

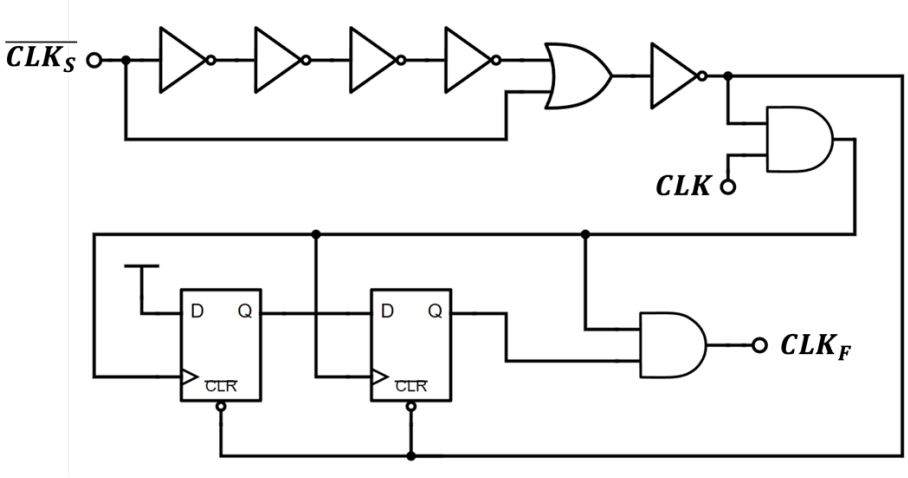

Fig. 5.39: Block level overview of the timing generator block used in the ADC.

nodes P_+ and P_- to V_{ref} which is chosen to be Vdd/2 (Fig. 5.13). By separating the biasing of the N_+ and P_+ nodes (and similarly N_- and P_- nodes), the two can be biased independently to drive both NMOS and PMOS transistors using the same input signal V_{in+} (and similarly V_{in-}) [31]. The common mode voltage at the output of each stage of the IA is set to V_{ref} (chosen as Vdd/2) using G_{m2}, which can be

chosen independently of the V_{ref} used for biasing the non-feedback path. Monte Carlo simulations of the IA are shown in Fig. 5.32. The differential outputs of the PGA are also centered around a common mode voltage of Vdd/2 = 600mV on the chip, which is shifted to 0V when observing through the AC coupled mode of the oscilloscope.

For the ADC to digitize the outputs of the PDH circuit, a sampling clock needs to be generated that is synchronized with the peaks of the sinusoidal EMF signal (Fig. 5.24). The sampling clock needs to be high for the duration of the peak hold time, which spans from the peak of the sinusoid to the common mode (600mV) crossing. This is accomplished by converting the sine signal to rail-to-rail digital voltage using a comparator whose other input is connected to 600mV (Fig. 5.33). A cosine waveform is generated by differentiating the sine signal and is also converted to rail-to-rail digital voltage. By using an XOR operation on these two digital signals, we obtain the sampling clock shown in Fig. 5.24. The reset (RST) signal for the PDH circuit in Fig. 5.20 is also obtained using the digital sine signal and some logic blocks (Fig. 5.33).

For the monotonic capacitor switching procedure adopted for the SAR ADC, a downward switching procedure is implemented for the DAC network as discharging through NMOS transistors is faster compared to PMOS. The ADC DAC capacitors are implemented through the metal-oxide-metal (MOM) technique using metal layers 3 and 7. For the dynamic comparator circuit of the ADC, PMOS transistors are used at the input of the pre-amplifier due to the downward switching procedure which eventually drives the comparator inputs to 0V. Additional details of the different circuit blocks used in the ADC are described in Figs. 5.34–5.39.

Flexible PCB Design: The PCB was designed as a single layer flex board with Polyimide (PI) substrate and a conducting copper layer. Polyimide is used due to its greater heat resistance compared to the cheaper polyester materials. In addition, an

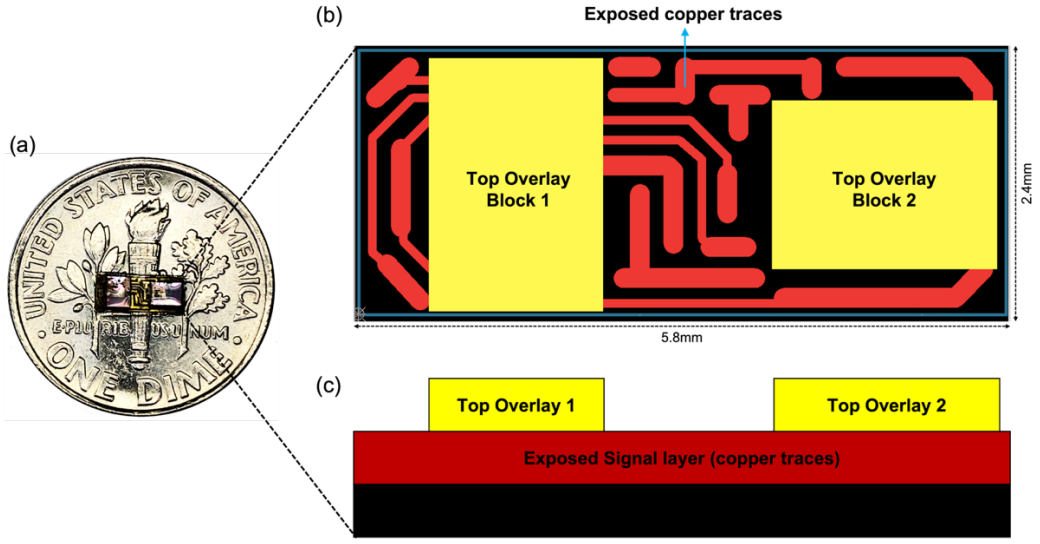

Fig. 5.40: Assembled device on the flex PCB board. (a) Shown on top of a US dime for perspective. (b) Top-view of the flex PCB design showing the two Overlay blocks for placements of the two chips and the exposed copper traces for wire-bonding. The vertical dimension of the PCB was kept as small as possible to maintain compatibility for implantation in most commercial catheters. (c) Side-view of the PCB design.

ENEPIG (Electroless Nickel Electroless Palladium Immersion Gold) surface finish was applied, as is typically recommended for boards requiring gold wire bonding. The flexible PCB was completed in Altium Designer version 16.1 (Altium Ltd.). Fig. 5.40 shows the final layout of the design. The layout of the PCB was motivated primarily by the size requirements of the prototype and optimized to reduce possible challenges with wire bonding. Specifically, the vertical dimension of the PCB was restricted to a range between 2–2.4mm to maintain compatibility for implantation in most commercial catheters. The thinnest trace width and spacing used in this design is 0.075 mm, which is dictated by the requirements set by the manufacturing companies. Traces widths for power lines and for pads requiring many wire bond connections were set to be larger: (i) 0.2mm width was used for VDD and ground pads, and (ii) 0.1mm width was used in other cases. The final system dimensions are 5.8x2.4x0.8mm^3. The finalized design is compatible with the dimensions of typical

commercial catheters and can be fabricated within standard manufacturing capabilities. For the prototype assembly, two magnetic sensor chips are mounted on the flex PCB board. The on-chip pads for supply voltages, clock input and data readout are wire-bonded to the PCB traces. Thin copper wires (38 AWG) are soldered to the traces and guided through the catheter tube for external access.

Magnetic FOV characterization: To perform spatial mapping using the magnetic field measurements by the CMOS chip sensor, we need to characterize the 500Hz AC magnetic field in the FOV of the planar gradient coils. However, there were no commercially available sensors that could measure a 500Hz magnetic field with a resolution of <10μT while maintaining a 10-15mT range. This presented a challenge in taking magnetic field measurements of the desired 500 Hz signal using sensors that had too low of an output data rate, and would thus alias the frequency content of the magnetic field. We hypothesized that we could exploit the frequency-independent nature of the peak values of the sinusoidal magnetic field to predict the peak values at 500Hz without needing to measure a full 500Hz signal. To accomplish that, magnetic field measurements at lower frequencies were taken to find a scaling or cross-correlation factor that could reliably predict the measurements at the desired frequency of 500Hz.

The AK09970N sensor was chosen to perform the magnetic field measurements, given its low-noise performance. The sensor was mounted on an automated 3D stage consisting of X, Y, and Z linear actuators, positioned above the stacked X, Y, and Z gradient coils. Table 3.4 shows the Z-gradient measurements from 0-5cm in increments of 1cm. These measurements are performed at several low frequency values ranging 47Hz to 251Hz. At each position for a given frequency, 150 measurements are averaged to calculate the peak field magnitude. As seen from Table 3.4, the sensor's peak magnetic field measurements are independent of frequency and the peak field magnitude stays consistent around a mean value (with some standard

Freq \ Position	0cm	1cm	2cm	3cm	4cm	5cm
47Hz	511.4163554	437.6612825	376.274513	323.11551	275.8697759	240.0128612
67Hz	512.8752977	457.5796322	373.7314577	324.559324	281.4355911	238.4765404
89Hz	506.1606607	437.7787621	376.8611889	319.8899652	275.7860983	239.4587655
109Hz	509.5092028	437.6424756	376.7612741	324.2789647	278.5032454	242.989645
131Hz	508.3633781	437.3752974	375.1060144	323.2177567	278.0030879	241.3377136
151Hz	506.9946768	438.4537472	378.6281832	325.423659	283.5807822	244.1256699
173Hz	508.4966853	435.3955076	375.2209782	324.6742164	282.4619893	243.475114
211Hz	507.3632876	435.3831402	379.3313245	326.4804094	283.3015778	251.6962592
251Hz	500.2628096	436.4340026	374.7748613	328.1076269	287.8809746	250.2929233
Avg. Value	507.9380393	439.3004275	376.2988662	324.4163814	280.7581247	243.5406102

Table 3.4: Z-coil magnetic field measurements along the Z-axis from 0–5cm and repeated from 47–251Hz in order to study the frequency dependence of the magnetic field values. It can be seen that the peak values are independent of the frequency and the 10–20μT of variation in the values is due to the sensor noise. This allows us to characterize the magnetic field-of-view (FOV) at a much lower frequency without compromising the accuracy and use the collected data for higher frequency measurements.

deviation) for each fixed point along the Z-axis. The margin of error can be attributed to the 10-20μT of sensor noise. This observation gave us the ability to characterize high-frequency magnetic fields (still under 1kHz) without needing to actually create the high-frequency signal for characterization purposes. During the actual characterization phase, the sensor is mounted on the automated 3D stage and is moved in the 20x20x10cm^3 of FOV in increments of 1mm. At each step, magnetic field measurements are made and stored in a look-up table (LUT) for position decoding later. The search algorithm to retrieve the 3D position coordinates from the LUT using the magnetic field values obtained during localization experiments, is described in [26].

Angular sensing implementation: The three magnetic field vectors obtained during the measurements are: (i) Bxx, Bxy, Bxz (measured when X-gradient on), (ii) Byx, Byy, Byz (measured when Y-gradient on), and (iii) Bzx, Bzy, Bzz (measured when

Z-gradient on). These nine values can be compared with the values stored in the LUT during the characterization phase and can be used to decode the angular orientation of the microdevice relative to the known orientation used during characterization. The vrrotvec() function in MATLAB was chosen to find the angular transformation between the measured magnetic field vectors and the reference dataset from the LUT. It returns an axis-angle representation of the rotation transformation, which can then be converted into other types such as rotation matrix, Euler angle, or quaternion forms.

Tissue phantom preparation: The tissue-mimicking phantom was prepared by embedding the catheter-fixture in 1% (w/v) agarose hydrogel. Agarose powder (Bio-Rad Laboratories) was mixed in milliQ water, heated to dissolve, and maintained at 65°C before use. The agarose solution was casted around the fixture inside a custom phantom holder and cooled to room temperature to form a hydrogel phantom.

Chapter 6

CONCLUSION

Advances in medical electronics have led to highly miniaturized and low-power devices being used for a myriad of application, both inside and outside the clinic. These remarkable breakthroughs in medical electronics have been made possible by relentless research and development in different areas including integrated circuits technology, data science, material science, biological and chemical engineering, and advanced packaging to name a few. However, there are many challenges that are yet to be overcome in order to makes these devices more smart, efficient, compact, fully-wireless, low-power and hopefully fully-autonomous. One such challenge is to be able to locate these devices *in vivo* with high precision, which can obviate the need for using potentially harmful X-ray radiation or bulky setups like those used in MRI, which remain to be the gold-standard for achieving high-precision localization. In this thesis, we present a radiation-free system for localizing and tracking miniaturized wireless devices *in vivo* with high accuracy, using harmless magnetic field gradients. Our system overcomes several challenges faced by existing localization and tracking methods, and has the potential to replace harmful X-ray radiation used routinely for locating sensors and devices *in vivo*.

In the first part, we presented a high-resolution 3D navigation and tracking system using magnetic field gradients, that can replace X-Ray fluoroscopy in high-precision surgeries. Monotonically varying magnetic fields in X, Y, and Z directions are created in the field-of-view to produce magnetic field gradients, which encode each spatial point uniquely. Highly miniaturized, wireless and battery-less devices, capable of measuring their local magnetic field, are designed to sense the gradient field. One such device can be attached to an implant inside the body and another to a surgical tool, such that both can simultaneously measure and communicate the magnetic field at their respective locations to an external receiver. The relative

location of the two devices on a real-time display can enable precise surgical navigation without using X-Rays. A prototype device is designed consisting of a micro-chip fabricated in 65nm CMOS technology, a 3D magnetic sensor and an inductor-coil. Planar electro-magnetic coils are designed for creating the 3D magnetic field gradients in a 20x20x10cm^3 of scalable FOV. The system is tested *in vitro* to demonstrate a localization accuracy of <100μm in 3D.

In the second part, we demonstrated 3D localization and tracking of wireless ingestible microdevices in the GI tract of large animals in real time and with millimeter-scale resolution. This was achieved by generating 3D magnetic field gradients in the GI field-of-view using high-efficiency planar electromagnetic coils that encode each spatial point with a distinct magnetic field magnitude. The field magnitude is measured and transmitted by the miniaturized, low-power and wireless microdevices to decode their location as they travel through the GI tract. Our system offers a high FOV (40x40x40cm^3), high spatial resolution in 3D (1.5mm), and fully wireless operation of the ingestible microdevices. It also supports concurrent multi-device usage. We use safe magnetic fields generated by non-obstructive planar electromagnets, and have demonstrated system functionality in large animals, illustrating its potential for use in non-clinical settings without the need for harmful radiation. This system could be useful for quantitative assessment of the GI transit-time, precision targeting of therapeutic interventions, and minimally invasive procedures.

In the final part of this thesis, we focused on the design of on-chip 3D magnetic sensors as they are of significant importance not only for medical electronics, but also for applications related to automotives, navigation, industrial use and consumer products. Our proposed novel 3D magnetic sensor is realized in the standard CMOS process and achieves high sensitivity and ultra-low power operation. The sensor is comprised of three orthogonal and highly dense metal coils implemented in the 65nm node, which generate a voltage in response to AC magnetic fields by electromagnetic

induction. The Z sensor coil is realized in the plane of the CMOS chip, whereas the X and Y sensor coils are realized in the vertical plane by using the interconnect vias as part of the coil structure. The EMF voltage signal is processed by on-chip circuitry that performs low-noise amplification, filtering, peak detection and 12-bit digitization while consuming only 14.8μW to yield μT-level sensitivity. The 3D magnetic field measurements by the sensor when enclosed in a catheter, are used for spatial localization of the sensor with 500μm mean accuracy. This demonstrates potential toward miniaturized wireless navigation and tracking in medical applications and other areas that require low-power and high-resolution 3D magnetic sensing.

BIBLIOGRAPHY

1.1. W. Gao *et al.*, "Fully integrated wearable sensor arrays for multiplexed in situ perspiration analysis," *Nature*, vol. 529, no. 7587, pp. 509-514, Jan. 2016.

1.2. C. Steiger *et al*., "Ingestible electronics for diagnostics and therapy," *Nature Reviews Materials,* vol. 4, no.2, pp. 83-98, Feb. 2019.

1.3. A. Wang *et al.*, "Wireless capsule endoscopy," *Gastrointestinal Endoscopy,* vol. 78, no.6, pp. 805-815, 2013.

1.4. Y. L. Kong *et al.*, "3D-printed gastric resident electronics," *Advanced Materials Technologies,* vol. 4, no.3, 2019.

1.5. D. K. Piech *et al*., "A wireless millimetre-scale implantable neural stimulator with ultrasonically powered bidirectional communication," *Nature Biomedical Engineering,* vol. 4, no. 2, pp. 207-222, Feb. 2020.

1.6. U. Mezger *et al*., "Navigation in surgery," *Langenbeck's Archives of Surgery,* vol. 398, pp. 501-514, 2013.

1.7. W. M. Ricci *et al.*, "Intramedullary nailing of femoral shaft fractures: Current concepts," *JAAOS-Journal of the American Academy of Orthopaedic Surgeons,* vol. 17, no.5, pp. 296-305, 2009.

1.8. P. Nadeau *et al*., "Prolonged energy harvesting for ingestible devices," *Nature Biomedical Engineering,* vol. 1, no. 3, Feb. 2017.

1.9. M. M. Waldrop, "More than Moore," *Nature,* vol. 530, no. 7589, pp.144-148, Feb. 2016.

1.10. M. Roser *et al.*, "Our World in Data," 2023. https://ourworldindata.org/moores-law

1.11. M. T. Bohr and I. A. Young, "CMOS scaling trends and beyond," *IEEE Micro,* vol. 37, no.6, pp. 20-29, Dec. 2017.

1.12. K. Agarwal *et al*., "Wireless power transfer strategies for implantable bioelectronics," *IEEE Reviews in Biomedical Engineering,* vol. 10, pp. 136-161, 2017.

1.13. E. Falkenstein *et al*., "Low-power wireless power delivery," *IEEE Transactions on Microwave Theory and Techniques,* vol. 60, no.7, pp. 2277-2286, Jul. 2012.

1.14. J. Gardner, "A history of deep brain stimulation: Technological innovation and the role of clinical assessment tool," *Social Studies of Science,* vol. 43, no. 5, pp. 707-728, 2013.

1.15. S. S. C. Rao *et al*., "Evaluation of gastrointestinal transit in clinical practice: Position paper of the American and European Neurogastroenterology and Motility Societies," *Neurogastroenterology & Motility,* vol. 23, no.1, pp. 8-23, Sep. 2010.

1.16. A. M. Franz *et al*., "Electromagnetic tracking in medicine—A review of technology, validation, and applications," *IEEE Transactions on Medical Imaging,* vol. 33, no. 8, pp. 1702-1725, Aug. 2014.

1.17. C. E. Brinck *et al*., "Magnetic tracking of gastrointestinal motility," *Physiological Measurement,* vol. 41, no. 12, Dec. 2020.

1.18. D. Vasisht *et al*., "In-body backscatter communication and localization," *Proceedings of the 2018 Conference of the ACM Special Interest Group on Data Communication*, Aug. 2018.

1.19. R. W. Cootney, "Ultrasound imaging: Principles and applications in rodent research," *Ilar Journal,* vol. 42, no.3, pp. 233-247, 2001.

1.20. N. Ji, "The practical and fundamental limits of optical imaging in mammalian brains," *Neuron,* vol. 83, no. 6, pp. 1242-1245, Sep. 2014.

1.21. V. P. B. Grover *et al*., "Magnetic resonance imaging: Principles and techniques: lessons for clinicians," *Journal of Clinical and Experimental Hepatology,* vol. 5, no. 3, pp. 246-255, Sep. 2015.

1.22. J. P. Marques *et al*., "Low-field MRI: An MR physics perspective," *Journal of Magnetic Resonance Imaging,* vol. 49, no. 6, pp. 1528-1542, Jun. 2019.

1.23. S. Sharma *et al*., "Wireless 3D surgical navigation and tracking system with 100μm accuracy using magnetic-field gradient-based localization," *IEEE Transactions on Medical Imaging,* vol. 40, no. 8, pp. 2066-2079, Aug. 2021.

1.24. S. Sharma *et al*., "20.4 3D surgical alignment with 100µm resolution using magnetic-field gradient-based localization," *2020 IEEE International Solid-State Circuits Conference (ISSCC)*. IEEE, 2020.

1.25. S. Sharma *et al*., "Location-aware ingestible microdevices for wireless monitoring of gastrointestinal dynamics," *Nature Electronics,* vol. 6, pp. 242-256, Feb. 2023.

1.26. S. Sharma, H. Melton, L. Edmonds, O. Addington, M. G. Shapiro, A. Emami, "A monolithic 3D magnetic sensor in 65nm CMOS with <10µT_{rms} noise and 14.8µW power," *2023 IEEE Custom Integrated Circuits Conference - (CICC)*, San Antonio, TX, USA, 2023, pp. 1-2.

1.27. M. A. Khan et al., "Magnetic sensors—A review and recent technologies," *Engineering Research Express*, vol. 3, no. 2, 2021.

1.28. S. Zuo et al., "Miniaturized magnetic sensors for implantable magnetomyography," *Advanced Materials Technologies*, vol. 5, no. 6, 2020.

1.29. C. Schott et al., "CMOS single-chip electronic compass with microcontroller," *IEEE Journal of Solid-State Circuits*, vol. 42, no. 12, pp. 2923-33, 2007.

2.1. S.E. Forshult, "*Magnetic Resonance Imaging—MRI—An Overview,"* Research Report, Karlstad University Studies 2007:22; Karlstad University: Karlstad Sweden, 2007.

2.2. D. Formica and S. Silvestri, "Biological effects of exposure to magnetic resonance imaging: An overview," *Biomedical Engineering Online*, vol. 3, pp. 1-12, Apr. 2004.

2.3. V. P. B. Grover et al., "Magnetic resonance imaging: principles and techniques: Lessons for clinicians," *Journal of Clinical and Experimental Hepatology*, vol. 5, no. 3 pp. 246-255, Sep. 2015.

2.4. S.S. Hidalgo-Tobon, "Theory of gradient coil design methods for magnetic resonance imaging," *Concepts in Magnetic Resonance Part A,* vol. 36, no. 4, pp: 223-242, Jun. 2010.

2.5. N. Gudino *et al.*, “Advancements in Gradient System Performance for Clinical and Research MRI,” *Journal of Magnetic Resonance Imaging*, vol. 57, no. 1, pp. 57-70, 2023.

2.6. R. Ansorge and M. Graves, ”*The physics and mathematics of MRI,”* Morgan & Claypool Publishers, 2016.

2.7. P. Golland, “Spatial encoding in MRI and how to make it faster,” Massachusetts Institute of Technology, Boston (2000).

2.8. R. S. Popovic, “Hall effect devices,” CRC Press, 2003.

2.9. C. Chien, “The Hall effect and its applications,” Springer Science & Business Media, 2013.

3.1. W. M. Ricci *et al.*, “Intramedullary nailing of femoral shaft fractures: Current concepts,” *JAAOS-Journal of the American Academy of Orthopaedic Surgeons*, vol. 17, no. 5, pp. 296-305, 2009.

3.2. A. Wang *et al.*, “Wireless capsule endoscopy,” *Gastrointestinal Endoscopy*, vol. 78, no. 6, pp. 805-815, 2013.

3.3. U. Mezger *et al.*, “Navigation in surgery,” *Langenbeck's Archives of Surgery,* vol. 398, no. 4, pp. 501-514, 2013.

3.4. H. Chen *et al.*, “Advances in functional X-ray imaging techniques and contrast agents,” *Physical Chemistry Chemical Physics: PCCP,* vol. 14, no. 39, pp. 13469-86, 2012.

3.5. H. M. Kremers *et al*., “Prevalence of total hip and knee replacement in the united states,” *The Journal of Bone and Joint Surgery,* vol. 97, no. 17, pp. 1386-97, 2015.

3.6. B.A. Schueler, “The AAPM/RSNA physics tutorial for residents general overview of fluoroscopic imaging,” *RadioGraphics*, vol. 20, no. 4, pp. 1115-26, 2000.

3.7. T. Leloup *et al.,* “A novel technique for distal locking of intramedullary nail based on two non-constrained fluoroscopic images and navigation,” *IEEE Transactions on Medical Imaging,* vol. 27, no. 9, pp. 1202-12, 2008.

3.8. M. Monge *et al.*, "Localization of microscale devices in vivo using addressable transmitters operated as magnetic spins," *Nature Biomedical Engineering*, pp. 736-744, 2017.

3.9. A. M. Franz *et al.*, "Electromagnetic tracking in medicine—A review of technology, validation, and applications," *IEEE Transactions on Medical Imaging*, vol. 33, no. 8, pp. 1702-25, Aug. 2014.

3.10. S. Sharma *et al.*, "Surgical alignment by magnetic field gradient localization," US patent, 11,399,848 B2, 2022.

3.11. S. Sharma *et al.*, "20.4 3D surgical alignment with 100µm resolution using magnetic-field gradient-based localization," *2020 IEEE International Solid-State Circuits Conference - (ISSCC)*, San Francisco, CA, USA, 2020, pp. 318-320.

3.12. S. Guo *et al.*, "An efficiency-enhanced CMOS rectifier with unbalanced-biased comparators for transcutaneous-powered high-current implants," *IEEE Journal of Solid-State Circuits*, vol. 44, no. 6, pp. 1796-1804, 2009.

3.13. M. Monge *et al*., "A fully intraocular high-density self-calibrating epiretinal prosthesis," *IEEE Transactions on Biomedical Circuits and Systems*, vol. 7, no. 6, pp. 747-760, 2013.

3.14. T. Ying *et al.*, "Area-efficient CMOS charge pumps for LCD drivers," *IEEE Journal of Solid-State Circuits*, vol. 38, no. 10, pp. 1721-25, 2003

3.15. X. Liu *et al.*, "An 86% efficiency 12µW self-sustaining PV energy harvesting system with hysteresis regulation and time-domain MPPT for IOT smart nodes," *IEEE Journal of Solid-State Circuits*, vol. 50, no. 6, pp. 1424-37, 2015.

3.16. X. Liu *et al.,* "A switched capacitor energy harvester based on a single-cycle criterion for MPPT to eliminate storage capacitor," *IEEE Transactions on Circuits and Systems I: Regular Papers*, vol. 65, no. 2, pp. 793-803, 2018.

3.17. M. H. Nazari *et al*., "An implantable continuous glucose monitoring microsystem in 0.18µm CMOS," *2014 Symposium on VLSI Circuits Digest of Technical Papers*, Honolulu, HI, 2014, pp. 1-2.

3.18. B. Razavi, “Design of analog CMOS integrated circuits,” McGraw-Hill, Boston, 2001.

3.19. M. M. Ahmadi *et al.*, “A wireless-implantable microsystem for continuous blood glucose monitoring,” *IEEE Transactions on Biomedical Circuits and Systems*, vol. 3, no. 3, pp. 169-180, 2009.

3.20. R. Turner, “Gradient coil design: A review of methods,” *Magnetic Resonance Imaging*, vol. 11, no. 7, pp 903-920, 1993.

3.21. S. S. Hidalgo-Tobon, “Theory of gradient coil design methods for magnetic resonance imaging,” *Concepts in Magnetic Resonance*, vol. 36A, no. 4, pp 223-242, 2010.

3.22. J. Marques *et al.*, “Low-field MRI: An MR physics perspective,” *Journal of Magnetic Resonance Imaging,* vol. 49, no. 6, pp. 1528-42, 2019.

3.23. N5700 Series System DC Power Supplies by Keysight, Datasheet.

3.24. N8700 Series System DC Power Supplies by Keysight, Datasheet.

3.25. S. H. Kim *et al.*, “Flexible, stretchable and implantable PDMS encapsulated cable for implantable medical device,” *Biomedical Engineering Letters*, vol. 1, no. 199, 2011.

3.26. J. A. Nyenhuis *et al.*, “MRI and implanted medical devices: Basic interactions with an emphasis on heating,” *IEEE Transactions on Device and Materials Reliability*, vol. 5, no. 3, pp. 467-480, 2005.

3.27. *Standard Test Method for Measurement of Magnetically Induced Torque on Medical Devices in the Magnetic Resonance Environment*, Standard F2213-17, ASTM International, 2017.

3.28. C. L. G. Ham *et al.*, “Peripheral nerve stimulation during MRI: Effects of high gradient amplitudes and switching rates,” *Journal of Magnetic Resonance Imaging*, vol. 7, no. 5, pp. 933-937, 1997.

3.29. D. J. Schaefer *et al.*, “Review of patient safety in time-varying gradient fields,” *Journal of Magnetic Resonance Imaging*, vol. 20, no. 1, pp. 20-29, 2000.

3.30. V. Klein *et al.*, “Investigating cardiac stimulation limits of MRI gradient coils using electromagnetic and electrophysiological simulations in human and

canine body models," *Magnetic Resonance in Medicine*, vol. 85, no.2 pp. 1047-61, 2021.

3.31. D. Son *et al.*, "A 5-D localization method for a magnetically manipulated untethered robot using a 2-D Array of Hall-effect sensors," *IEEE/ASME Transactions on Mechatronics*, vol. 21, no. 2, pp. 708-716, 2016.

3.32. E. Nevo, "Method and apparatus to estimate location and orientation of objects during magnetic resonance imaging," US patent 6,516,213 B1, 2003.

3.33. L. Pan *et al.*, "Integration and evaluation of a gradient-based needle navigation system for percutaneous MR-guided interventions," *PloS One,* vol. 15, no. 7, July 2020.

3.34. M. N. Oosterom, "Extending the hybrid surgical guidance concept with freehand fluorescence tomography," *IEEE Transactions on Medical Imaging*, vol. 39, no. 1, pp. 226-235, 2020.

3.35. F. Parent *et al.*, "Intra-arterial image guidance with optical frequency domain reflectometry shape sensing," *IEEE Transactions on Medical Imaging*, vol. 38, no. 2, pp. 482-492, 2019.

3.36. D. Vasisht *et al.*, "In-body backscatter communication and localization," *Proceedings of the 2018 Conference of the ACM Special Interest Group on Data Communication* (*SIGCOMM '18*). Association for Computing Machinery, New York, NY, USA, pp. 132–146.

3.37. F. Chen *et al.*, "3D catheter shape determination for endovascular navigation using a two-step particle filter and ultrasound scanning," *IEEE Transactions on Medical Imaging*, vol. 36, no. 3, pp. 685-695, 2017.

3.38. A. L. Simpson *et al.*, "Comparison study of intraoperative surface acquisition methods for surgical navigation," *IEEE Transactions on Biomedical Engineering*, vol. 60, no. 4, pp 1090-99, 2013.

4.1. C. Steiger *et al.,* "Ingestible electronics for diagnostics and therapy," *Nature Reviews Materials,* vol. 4, pp. 83-98, 2019.

4.2. J. Keller *et al.,* "Advances in the diagnosis and classification of gastric and intestinal motility disorders," *Nature Reviews Gastroenterology & Hepatology*, vol. 15, pp. 291-308, 2018.

4.3. S. S. C. Rao *et al.,* "Evaluation of gastrointestinal transit in clinical practice: Position paper of the American and European Neurogastroenterology and Motility Societies," *Neurogastroenterology & Motility*, vol. 23, no. 1, pp. 8–23, 2011.

4.4. M. Mimee *et al.,* "An ingestible bacterial-electronic system to monitor gastrointestinal health," *Science*, vol. 360, no. 6391, pp. 915-918, 2018.

4.5. B. Kuo *et al.,* "Comparison of gastric emptying of a nondigestible capsule to a radio-labelled meal in healthy and gastroparetic subjects," *Alimentary Pharmacology & Therapeutics*, vol. 27, no. 2, pp. 186–196, 2008.

4.6. A. Wang *et al.,* "Wireless capsule endoscopy," *Gastrointestinal Endoscopy*, vol. 78, no. 6, pp. 805-815, 2013.

4.7. R. A. Hejazi *et al.*, "Video capsule endoscopy: A tool for the assessment of small bowel transit time," *Frontiers in Medicine,* vol. 3, no. 6, 2016.

4.8. S. Maqbool *et al.*, "Wireless capsule motility: Comparison of the SmartPill GI monitoring system with scintigraphy for measuring whole gut transit," *Digestive Diseases and Sciences*, vol. 54, no. 10, pp. 2167-74, 2009.

4.9. C. Dagdeviren *et al.*, "Flexible piezoelectric devices for gastrointestinal motility sensing," *Nature Biomedical Engineering,* vol. 1, pp. 807–817, 2017.

4.10. A. M. Haase *et al.*, "Gastrointestinal motility during sleep assessed by tracking of telemetric capsules combined with polysomnography—A pilot study," *Clinical and Experimental Gastroenterology,* vol. 8, pp. 327-332, 2015.

4.11. A. A. Gharibans *et al.*, "Artifact rejection methodology enables continuous, noninvasive measurement of gastric myoelectric activity in ambulatory subjects," *Scientific Reports,* vol. 8, 2018.

4.12. H. Chen *et al.*, "Advances in functional X-ray imaging techniques and contrast agents," *Physical Chemistry Chemical Physics: PCCP,* vol. 14, no. 39, pp. 13469-86, 2012.

4.13. M. Monge *et al.*, "Localization of microscale devices in vivo using addressable transmitters operated as magnetic spins," *Nature Biomedical Engineering*, vol. 1, pp. 736-744, 2017.

4.14. J. Worsøe *et al.*, "Gastric transit and small intestinal transit time and motility assessed by a magnet tracking system," *BMC Gastroenterology*, vol. 11, no. 145, 2011.

4.15. W. Andrä *et al.*, "A novel method for real-time magnetic marker monitoring in the gastrointestinal tract," *Physics in Medicine and Biology*, vol. 45, no. 10, pp. 3081-93, 2000.

4.16. D. Son *et al.*, "A 5-D localization method for a magnetically manipulated untethered robot using a 2-D array of Hall-effect sensors," *IEEE/ASME Transactions on Mechatronics*, vol. 21, no. 2, pp. 708-716, 2016.

4.17. M. Pourhomayoun *et al.*, "Accurate localization of in-body medical implants based on spatial sparsity," *IEEE Transactions on Biomedical Engineering*, vol. 61, no. 2, pp. 590-597, 2014.

4.18. W. Weitschies *et al.*, "Magnetic marker monitoring: High resolution real-time tracking of oral solid dosage forms in the gastrointestinal tract," *European Journal of Pharmaceutics and Biopharmaceutics*, vol. 74, no. 1, pp. 93-101, 2010.

4.19. A. M. Franz *et al.*, "Electromagnetic tracking in medicine—A review of technology, validation, and applications," *IEEE Transactions on Medical Imaging*, vol. 33, no. 8, pp. 1702-25, Aug. 2014.

4.20. C. E. Brink *et al.*, "Magnetic tracking of gastrointestinal motility," *Physiological Measurement*, vol. 41, no. 12, pp. 12TR01, 2020.

4.21. J. Baker-Jarvis and Sung Kim, "The interaction of radio-frequency fields with dielectric materials at macroscopic to mesoscopic scales," *Journal of Research of the National Institute of Standards and Technology,* vol. 117, pp. 1-60, 2012.

4.22. C. Schiller *et al.*, "Intestinal fluid volumes and transit of dosage forms as assessed by magnetic resonance imaging," *Alimentary Pharmacology & Therapeutics*, vol. 22, no. 10, pp. 971–979, 2005.

4.23. D. M. Mudie *et al.*, "Physiological parameters for oral delivery and in vitro testing," *Molecular Pharmaceutics*, vol. 7, no. 5, pp. 1388-1405, 2010.

4.24. I. Dove, "Analysis of radio propagation inside the human body for in-body localization purposes," 2014.

4.25. S. Sharma *et al.,* "Wireless 3D surgical navigation and tracking system with 100µm accuracy using magnetic-field gradient-based localization," *IEEE Transactions on Medical Imaging*, vol. 40, no. 8, pp. 2066-79, 2021.

4.26. C. L. G. Ham *et al.*, "Peripheral nerve stimulation during MRI: Effects of high gradient amplitudes and switching rates," *Journal of Magnetic Resonance Imaging*, vol. 7, no. 5, pp. 933-937, 1997.

4.27. D. J. Schaefer *et al.*, "Review of patient safety in time-varying gradient fields," *Journal of Magnetic Resonance Imaging*, vol. 20, no. 1, pp. 20-29, 2000.

4.28. V. Klein *et al.*, "Investigating cardiac stimulation limits of MRI gradient coils using electromagnetic and electrophysiological simulations in human and canine body models," *Magnetic Resonance in Medicine*, vol. 85, no.2 pp. 1047-61, 2021.

4.29. S. Sharma *et al.*, "20.4 3D surgical alignment with 100µm resolution using magnetic-field gradient-based localization," *2020 IEEE International Solid-State Circuits Conference - (ISSCC)*, San Francisco, CA, USA, 2020, pp. 318-320.

4.30. F. Mostafaei *et al.*, "Variations of MRI-assessed peristaltic motions during radiation therapy," *Plos One*, vol. 13, no. 10, pp. 1-12, 2018.

4.31. M. M. Swindle *et al.*, "Swine as models in biomedical research and toxicology testing," *Veterinary Pathology*, vol. 49, no. 2, pp. 344-356, 2012.

4.32. N. S. Ruiz *et al.*, "Fecal incontinence - Challenges and solutions," *World Journal of Gastroenterology* vol. 23, no. 1, pp. 11-24, 2017.

4.33. Y. K. Lo *et al.*, "A wireless implant for gastrointestinal motility disorders," *Micromachines*, vol. 9, no. 17, 2018.

4.34. Y. L. Kong *et al.*, "3D-printed gastric resident electronics," *Advanced Materials Technologies,* 2019, 4, 1800490.

4.35. G. Traverso *et al.*, "Physiologic status monitoring via the gastrointestinal tract," *Plos One*, vol. 10, no. 11, pp. 1-13, 2015.

4.36. A. Menciassi *et al.*, "Clamping tools of a capsule for monitoring the gastrointestinal tract problem analysis and preliminary technological activity," *2005 IEEE International Conference on Robotics and Automation*, 2005, pp. 1309-14.

4.37. T. D. Than *et al.,* "A review of localization systems for robotic endoscopic capsules," *IEEE Transactions on Biomedical Engineering*, vol. 59, no. 9, pp. 2387-99, 2012.

4.38. S. Su *et al.*, "Investigation of the relationship between tracking accuracy and tracking distance of a novel magnetic tracking system," *IEEE Sensors Journal*, vol. 17, no. 15, pp. 4928-37, 2017.

4.39. F. Bianchi *et al.*, "Localization strategies for robotic endoscopic capsules: A review," *Expert Review of Medical Devices*, vol. 16, no. 5, pp. 381-403, 2019.

4.40. D. M. Pham *et al.*, "A real-time localization system for an endoscopic capsule using magnetic sensors," *Sensors (Basel, Switzerland)* vol. 14, no. 11 20910-29, 2014.

4.41. D. M. Bass *et al*., "Gastrointestinal safety of an extended-release, nondeformable, oral dosage form (OROS®)[1]," *Drug-Safety,* vol. 25, no. 14, 1021–33, 2002.

4.42. J. Huang *et al.*, "IM6D: Magnetic tracking system with 6-DOF passive markers for dexterous 3D interaction and motion," *ACM Transactions on Graphics*, vol. 34, no. 6, pp. 1-10, 2015.

4.43. E. Nevo *et al.*, "Method and apparatus to estimate location and orientation of objects during magnetic resonance imaging," US patent 6516213 B1, 2003.

4.44. D. Vasisht *et al.*, "In-body backscatter communication and localization," *2018 Conference of the ACM Special Interest Group on Data Communication*, New York, NY, USA, 2018, pp. 132–146.

4.45. P. Nadeau *et al.*, "Prolonged energy harvesting for ingestible devices," *Nature Biomedical Engineering,* vol. 1, 2017.

4.46. A. H. Talkhooncheh *et al.*, "A fully-integrated biofuel-cell-based energy harvester with 86% peak efficiency and 0.25V minimum input voltage using source-adaptive MPPT," *2020 IEEE Custom Integrated Circuits Conference (CICC)*, 2020, pp. 1-4.

4.47. A. H. Talkhooncheh *et al.*, "A biofuel-cell-based energy harvester with 86% peak efficiency and 0.25-V minimum input voltage using source-adaptive MPPT", *IEEE Journal of Solid-State Circuits*, vol. 56, no. 3, pp. 715-728, March 2021.

4.48. R. Turner, "Gradient coil design: A review of methods," *Magnetic Resonance Imaging*, vol. 11, no. 7, pp 903-920, 1993.

4.49. S. S. Hidalgo-Tobon, "Theory of gradient coil design methods for magnetic resonance imaging," *Concepts in Magnetic Resonance*, vol. 36A, no. 4, pp 223-242, 2010.

4.50. S. Sharma *et al.,* "Electromagnet gradient coil apparatus for micro-device localization," US patent 11,457,835 B2, 2022.

4.51. S. Sharma *et al.*, "In-vivo monitoring of an internal volume of a mammal using magnetic field gradients," US patent 20,210,137,412, 2021.

4.52. S. Sharma *et al.,* "Surgical alignment by magnetic field gradient localization," US patent 11,399,848 B2, 2022.

4.53. I. Khadra *et al*., "Statistical investigation of simulated intestinal fluid composition on the equilibrium solubility of biopharmaceutics classification system class II drugs," *European Journal of Pharmaceutical Sciences*, vol. 25, no. 67, pp. 65-75, 2015.

4.54. M. Vertzoni *et al.,* "Dissolution media simulating the intralumenal composition of the small intestine: Physiological issues and practical aspects," *Journal of Pharmacy and Pharmacology*, vol. 56, no. 4, pp. 453-62, 2004.

4.55. E. Nevo, "Method and apparatus to estimate location and orientation of objects during magnetic resonance imaging," US patent 6,516,213 B1, 2003.

5.1. M. A. Khan *et al.*, "Magnetic sensors—A review and recent technologies," *Engineering Research Express*, vol. 3, no. 2, 2021.

5.2. C. E. Brink *et al.*, "Magnetic tracking of gastrointestinal motility," *Physiological Measurement*, vol. 41, no. 12, pp. 12TR01, 2020.

5.3. A. M. Franz *et al.*, "Electromagnetic tracking in medicine—A review of technology, validation, and applications," *IEEE Transactions on Medical Imaging,* vol. 33, no. 8, pp. 1702-25, 2014.

5.4. E. Lugez *et al.*, "Electromagnetic tracking in surgical and interventional environments: Usability study," *International Journal of Computer Assisted Radiology and Surgery*, vol. 10, no. 3, pp. 253-62, 2015.

5.5. Z. Yaniv and E. Wilson, "Electromagnetic tracking in the clinical environment," *Medical Physics,* vol. 36, no. 3, pp. 876-892, 2009.

5.6. Electromagnetic Tracking Education Guide – NDI, August 2021.

5.7. X. Zhou, M. Sveiven and D. A. Hall, "A CMOS magnetoresistive sensor front-end with mismatch-tolerance and sub-ppm sensitivity for magnetic immunoassays," *IEEE Transactions on Biomedical Circuits and Systems*, vol. 13, no. 6, pp. 1254-63, 2019.

5.8. S. Zuo *et al.*, "Miniaturized magnetic sensors for implantable magnetomyography," *Advanced Materials Technologies*, vol. 5, no. 6, 2020.

5.9. C. Schott *et al.*, "CMOS single-chip electronic compass with microcontroller," *IEEE Journal of Solid-State Circuits*, vol. 42, no. 12, pp. 2923-33, 2007.

5.10. J. C. van der Meer *et al.*, "A fully integrated CMOS Hall sensor with a 3.65μT 3σ offset for compass applications," *IEEE International Solid-State Circuits Conference,* pp. 246-247, 2005.

5.11. V. Frick *et al.*, "CMOS microsystem for AC current measurement with galvanic isolation," *IEEE Sensors Journal*, vol. 3, no. 6, pp. 752-760, 2003.

5.12. H. Heidari *et al.*, "CMOS vertical Hall magnetic sensors on flexible substrate," *IEEE Sensors Journal*, vol. 16, no. 24, pp. 8736-43, 2016.

5.13. H. Heidari *et al.*, "A CMOS current-mode magnetic Hall sensor with integrated front-end," *IEEE Transactions on Circuits and Systems I: Regular Papers*, vol. 62, no. 5, pp. 1270-78, 2015.

5.14. J. Jiang, W. J. Kindt and K. A. A. Makinwa, "A continuous-time ripple reduction technique for spinning-current Hall sensors," *IEEE Journal of Solid-State Circuits*, vol. 49, no. 7, pp. 1525-34, 2014.

5.15. J. Jiang and K. A. A. Makinwa, "Multipath wide-bandwidth CMOS magnetic sensors," *IEEE Journal of Solid-State Circuits*, vol. 52, no. 1, pp. 198-209, 2017.

5.16. R. S. Popovic, "High resolution Hall magnetic sensors," *29th International Conference on Microelectronics Proceedings - MIEL 2014*, pp. 69-74, 2014.

5.17. M. Kashmiri *et al.*, "27.9 A 200kS/s 13.5b integrated-fluxgate differential-magnetic-to-digital converter with an oversampling compensation loop for contactless current sensing," *2015 IEEE International Solid-State Circuits Conference - (ISSCC) Digest of Technical Papers*, 2015, pp. 1-3.

5.18. P. M. Drljaca *et al*., "Low-power 2-D fully integrated CMOS fluxgate magnetometer," *IEEE Sensors Journal*, vol. 5, no. 5, pp. 909-915, 2005.

5.19. S. Kawahito *et al*., "A 2D CMOS microfluxgate sensor system for digital detection of weak magnetic fields," *IEEE Journal of Solid-State Circuits*, vol. 34, no. 12, pp. 1843-51, 1999.

5.20. V. Beroulle *et al.*, "Monolithic piezoresistive CMOS magnetic field sensors," *Sensors and Actuators A: Physical*, vol. 103, no. 1–2, pp. 23-32, 2003.

5.21. B. Bahreyni and C. Shafai, "A resonant micromachined magnetic field sensor," *IEEE Sensors Journal*, vol. 7, no. 9, pp. 1326-34, 2007.

5.22. E. Nevo, "Method and apparatus to estimate location and orientation of objects during magnetic resonance imaging," U.S. patent 6516213B1, 2003.

5.23. M. Cavaliere *et al*., "Inductive sensor design for electromagnetic tracking in image guided interventions," *IEEE Sensors Journal*, vol. 20, no. 15, pp. 8623-30, 2020.

5.24. M. Cavaliere *et al.*, "Planar body-mounted sensors for electromagnetic tracking," *Sensors,* vol. 21, no. 8, 2021.

5.25. S. Sharma *et al.,* "20.4 3D surgical alignment with 100μm resolution using magnetic-field gradient-based localization," *2020 IEEE International Solid-State Circuits Conference - (ISSCC)*, 2020, pp. 318-320.

5.26. S. Sharma *et al.*, "Wireless 3D surgical navigation and tracking system with 100μm accuracy using magnetic-field gradient-based localization," *IEEE Transactions on Medical Imaging*, vol. 40, no. 8, pp. 2066-79, 2021.

5.27. S. Sharma *et al.*, "Location-aware smart-pills for wireless monitoring of gastrointestinal dynamics," *Nature Electronics*, vol. 6, pp. 242-256, 2023.

5.28. M. Monge *et al.*, "Localization of microscale devices in vivo using addressable transmitters operated as magnetic spins," *Nature Biomedical Engineering,* vol. 1, pp. 736–744, 2017.

5.29. A. H. Talkhooncheh *et al.*, "A biofuel-cell-based energy harvester with 86% peak efficiency and 0.25-V minimum input voltage using source-adaptive MPPT," *IEEE Journal of Solid-State Circuits*, vol. 56, no. 3, pp. 715-728, 2021.

5.30. R. R. Harrison and C. Charles, "A low-power low-noise CMOS amplifier for neural recording applications," *IEEE Journal of Solid-State Circuits*, vol. 38, no. 6, pp. 958-965, 2003.

5.31. S. Rai *et al.,* "A 500μW neural tag with 2μVrms AFE and frequency-multiplying MICS/ISM FSK transmitter," *2009 IEEE International Solid-State Circuits Conference - Digest of Technical Papers*, 2009, pp. 212-213.

5.32. D. Han *et al.*, "A 0.45 V 100-channel neural-recording IC with sub-μW/channel consumption in 0.18μm CMOS," *IEEE Transactions on Biomedical Circuits and Systems*, vol. 7, no. 6, pp. 735-746, 2013.

5.33. L. Fang and P. Gui, "A 14nV/√Hz 14μW chopper instrumentation amplifier with dynamic offset zeroing (DOZ) technique for ripple reduction," *2019 IEEE Custom Integrated Circuits Conference (CICC)*, 2019, pp. 1-4.

5.34. A. Uran *et al.*, "An AC-coupled wideband neural recording front-end with sub-1 mm^2×fJ/conv-step efficiency and 0.97 NEF," *IEEE Solid-State Circuits Letters*, vol. 3, pp. 258-261, 2020.

5.35. M. W. Kruiskamp and D. M. W. Leenaerts, “A CMOS peak detect sample and hold circuit,” *IEEE Transactions on Nuclear Science*, vol. 41, no. 1, pp. 295-298, 1994.

5.36. Seok-Bae Park, J. E. Wilson and M. Ismail, “The CHIP - Peak detectors for multistandard wireless receivers,” *IEEE Circuits and Devices Magazine*, vol. 22, no. 6, pp. 6-9, 2006.

5.37. X. Fang *et al*., “Design and integration of a high accuracy multichannel analog CMOS peak detect and hold circuit for APD-based PET imaging,” *IEEE Transactions on Biomedical Circuits and Systems*, vol. 6, no. 2, pp. 179-187, 2012.

5.38. H. Zheng *et al*., “A CMOS peak detect and hold circuit with auto-adjust charging current for NS-Scale pulse ToF lidar application,” *IEEE Transactions on Circuits and Systems I: Regular Papers*, vol. 67, no. 12, pp. 4409-19, 2020.

5.39. C. Liu *et al*., “A 10-bit 50-MS/s SAR ADC with a monotonic capacitor switching procedure,” *IEEE Journal of Solid-State Circuits*, vol. 45, no. 4, pp. 731-740, 2010.

5.40. D. Zhang, A. Bhide and A. Alvandpour, “A 53-nW 9.1-ENOB 1-kS/s SAR ADC in 0.13-µm CMOS for medical implant devices,” *IEEE Journal of Solid-State Circuits*, vol. 47, no. 7, pp. 1585-1593, 2012.

5.41. M. van Elzakker *et al*., “A 10-bit charge-redistribution ADC consuming 1.9µW at 1 MS/s,” *IEEE Journal of Solid-State Circuits*, vol. 45, no. 5, pp. 1007-15, 2010.

5.42. P. Harpe, E. Cantatore and A. van Roermund, “A 10b/12b 40 kS/s SAR ADC with data-driven noise reduction achieving up to 10.1b ENOB at 2.2 fJ/conversion-step,” *IEEE Journal of Solid-State Circuits*, vol. 48, no. 12, pp. 3011-18, 2013.

5.43. C. Liu, C. Kuo and Y. Lin, “A 10 bit 320 MS/s low-cost SAR ADC for IEEE 802.11ac applications in 20 nm CMOS,” *IEEE Journal of Solid-State Circuits*, vol. 50, no. 11, pp. 2645-54, 2015.

5.44. E. Lugez *et al.*, "Improved electromagnetic tracking for catheter path reconstruction with application in high-dose-rate brachytherapy," *International Journal of Computer Assisted Radiology and Surgery*, vol. 12, no. 4, pp. 681-689, 2017.

5.45. U. Mezger, C. Jendrewski and M. Bartels, "Navigation in surgery," *Langenbeck's Archives of Surgery* vol. 398, no. 4, pp. 501-14, 2013.

5.46. R. R. Shamir, L. Joskowicz and Y. Shoshan, "Fiducial optimization for minimal target registration error in image-guided neurosurgery," *IEEE Transactions on Medical Imaging*, vol. 31, no. 3, pp. 725-737, 2012.

5.47. D. Habermehl *et al.*, "Evaluation of different fiducial markers for image-guided radiotherapy and particle therapy," *Journal of Radiation Research*, vol. 54, no. 1, pp. 61-68, 2013.

5.48. H. Zhang *et al.*, "Electromagnetic tracking for abdominal interventions in computer aided surgery," *Computer Aided Surgery*, vol. 11, no. 3, pp. 127-136, 2006.

5.49. A. P. Shah *et al.*, "Expanding the use of real-time electromagnetic tracking in radiation oncology," *Journal of Applied Clinical Medical Physics*, vol. 12, no. 4, pp. 34-49, 2011.

5.50. M. Kellermeier *et al.*, "Electromagnetic tracking (EMT) technology for improved treatment quality assurance in interstitial brachytherapy," *Journal of Applied Clinical Medical Physics*, vol. 18, no. 1, pp. 211-222, 2017.